OZONE AND WATER VAPOR MEASUREMENTS BY RAMAN LIDAR IN THE PLANETARY BOUNDARY LAYER

THÈSE N^{O} 2351 (2001)

PRÉSENTÉE AU DÉPARTEMENT DE GÉNIE RURAL

ÉCOLE POLYTECHNIQUE FÉDÉRALE DE LAUSANNE

POUR L'OBTENTION DU GRADE DE DOCTEUR ÈS SCIENCES TECHNIQUES

PAR

Benoît LAZZAROTTO
Ingénieur physicien diplômé EPF
de nationalités suisse et française et originaire de Saint-Aubin (FR)

acceptée sur proposition du jury:

Prof. B. Calpini, directeur de thèse
Dr I. Archinov, rapporteur
Prof. R. Monot, rapporteur
M. V. Simeonov, rapporteur
Prof. B. Vittoz, rapporteur
Prof. H. van den Bergh, rapporteur

Lausanne, EPFL
2001

Des chercheurs qui cherchent on en trouve

mais

des chercheurs qui trouvent on en cherche....

Coluche

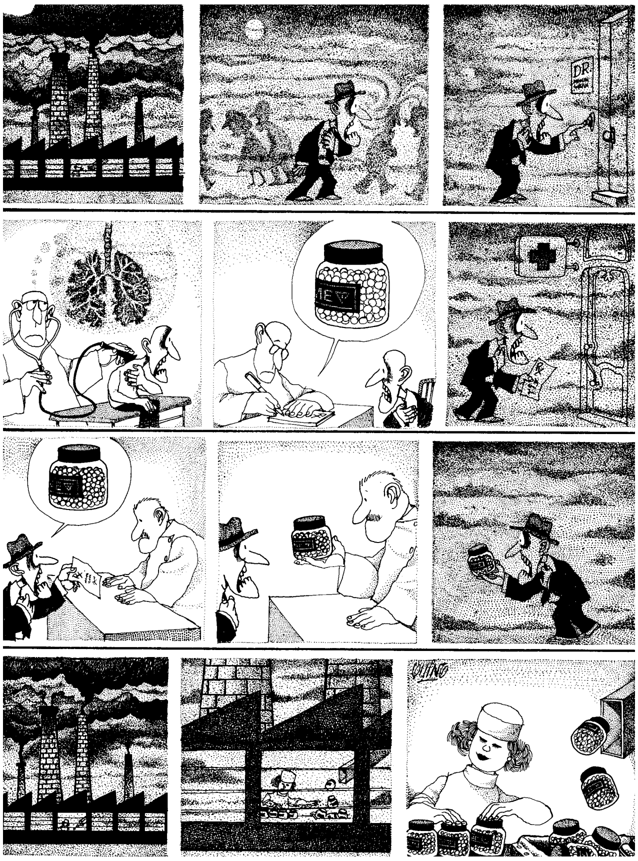

Air pollution, its origin and how to solve the problem...
by QUINO

Table of Contents

Preface

My Ph.D. student life can be mainly divided into two periods.
The first part lasted about one year and was shared between the Neuchâtel observatory, the EPFL and the Finnish Meteorological Institute based near Sodankylä, a small town beyond the Polar Circle. This last duty was carried out as part of the European project called SAONAS (Stratospheric Aerosol and Ozone in the Northern and Southern Hemispheres). I had the chance and the opportunity to work with an international team to build, install and make operational a stratospheric lidar dedicated to study the mechanisms of the Polar Stratospheric Clouds (PSC) and their possible relation with the ozone destruction on the both poles. I enjoyed an exterior lab life and the meeting of many people from different countries and universities exchanging professional experiences and ideas. I took the advantage of this long winter first stay (4 months) to go cross-country skiing, appreciate the relaxing finnish sauna, admire the fantastic northern lights and the beautiful sceneries of this snow covered cold lands.
The second one was spent within the EPFL. There I developed, with the help of other people from the lidar group, this "Raman project", purpose of the present thesis. During this period, that lasted three years, each year I took part to a measurement campaign in Finland, Switzerland, Italy, Crete, actively participating to what it involves before and after. As for my finnish experience, I keep good memories of those sometimes hard but wonderful days. The Raman project was developed during two years using the EPFL lidar moving truck, and the last year in a laboratory with its incomparable technical facilities in respect to the field campaign solution.

As an introduction, I just would like to explain in few words the organization of this manuscript, written in "US English" (for example water vapor is used rather than water vapour in "UK English").
- The introduction gives a general approach of the problem, with a global view on the interlinked aspects of the treated matter.
- The theory develops all the formalism needed to analyze, correct the signals and retrieve the quantities of interest.
- The experimental part gives an extensive description of the system, several tests and procedure to make and improve such a system.
- The corrections and errors analysis explains which approximations can be reasonably made in the different terms taken during the theory elaboration. Signal to Noise ratio of the Raman signals and statistical errors are discussed.
- The main idea was then to export all this knowledge in articles, placed in dedicated chapters. In contrast to the corrections and errors analysis chapter, where I focused on a signal or an averaged signal of 30 min., the concept was there to have as many as possible temporal series,

comparison with other measurements like sonde balloon, tethered balloon or numerical simulations.
- The annex consists in an investigation on the backscattered aerosol coefficient calculation, some useful tables and calculations, and description of our programs.

Acknowledgments

Because everything is always the fruit of a team!.

I wish to convey my appreciation and gratitude to the following people:

Prof. Hubert van den Bergh, head of the EPFL laboratory of environmental engineering, who accepted me in his team a few years ago.
Prof. Bertrand Calpini, head of the lidar group and my thesis director. An endless enthusiasm, a will to always go further and a capability to sleep only two hours a night.
Prof. François Golay, Prof. Bernard Vittoz, Prof. René Monot, Dr. Iouri Archinov to whom I express my sincere thanks for having accepted to act as referees for my thesis.
All the guys from the lidar group, members of this very nice and international team, with whom I don´t just share office hours but all what can happen in memorable field campaigns. Gilles Larchevêque, Mr. informatic who was always ready to help for making the machines work, François Jeanneret my first - three years - office colleague, Valentin Simeonov for his help in the experimental hours, Philippe Quaglia our clown, "Mr. Roumanian President" Jean Balin and Rodrigo Jimenez who brings the sun from his country.
Those from the LPAS, past and present, who were always here to help. A special thanks to Olivier Couach, from the LPAS numerical group, and one of my two colleagues from the "gyrotron kitchen team".
Flavio Comino, our LPAS (super) mechanician and his early colleague Manuel Santos, who taught me a lot of things and tricks about mechanics.
The EPFL doorkeepers, Alexandre Di Santolo and Denis Monnet, who helped me finding the right piece that was missing. And also all those people from the EPFL who participate to make this wonderful institution run.
Care is taken here not to forget the persons from the early times:
Valentin Mitev, Renaud Matthey, Patrick Weibel from the Neuchâtel observatory.
Esko Kiro, Rigel Kivi, Yuha Kahru, Kaisa Masson, Timo and Ritta Pirttijarvi, Yolanda Rumukainen, Mauri Nakkula... from the Finnish Meteorological Institute in Sodankylä.
And the other persons from different universities who shared with me the finnish period in this far off country above the polar circle.
For sure all the living members of my family, specially my parents that always encouraged me and stood by me when I needed.
I don't forget those looking at me from the heaven: my four grand-parents, with a special thought to my father's mother, "la Nonna" who I knew for a longer time and for whom I was her "cocolon", Théa my "second" mother and Charles my uncle that left us only few months ago.
All my friends with whom I have so much good time and, as I don't want to take the risk of for-

getting anyone, I don't make a list!
The correcting and helping team for my poor english, Penny, Suzan, Michel.
And last but not least, my beloved two women. My wife for her constant kindness and patience with a kind of (wild) bear like me, and for having endured such a strange timing during the last year... and for sure my little daughter who emits more light in my life than the most powerful laser ever available.

Thanks to all.

Résumé

L'extraction d'information spatiale et temporelle de la concentration d’ozone (O_3) et du rapport de mélange de la vapeur d’eau (H_2O) dans la troposphère revêt un intérêt essentiel. Contrairement au cas stratosphérique, l’ozone troposphérique peut avoir un impact dangereux, de par son effet toxique, sur les humains et la végétation, en provoquant une dégradation accélérée des minéraux, et en participant au problème de l’effet de serre. En ce qui concerne la vapeur d’eau, la connaissance de sa concentration fortement variable est essentielle à la fois à la chimie de la troposphère ($O(^1D) + H_2O$ -> 2OH) dans laquelle elle participe entre autre à la formation du radical hydroxyle (OH), ainsi qu’à la météorologie. La vapeur d’eau est le gaz à effet de serre le plus important, il joue un rôle prépondérant dans la chimie atmosphérique. La conversion et le transport d’eau dans l'atmosphère est le point clé du budget radiatif sur terre.
Du fait de la complexité et de la non linéarité du système de pollution de l’air, qui inclut les émissions, la chimie, la radiation thermique, le transport et la déposition, les stratégies de réduction de la pollution ne peuvent être correctement établies qu’en utilisant un modèle tridimensionnel eulérien de transport photochimique à grande échelle. Pour vérifier de tels modèles, des campagnes de mesures sont réalisées, au cours desquelles de nombreux paramètres physiques (vent, température, H_2O, etc.) et chimiques (émissions et immissions) sont mesurés en diverses parties de l’atmosphère.
Le LIDAR (LIght Detection And Ranging: détection de lumière résolue en distance), qui est une méthode de mesure in-situ et en temps réel des polluants atmosphériques, est un des meilleurs outils pour mesurer en 3-D les concentrations de gaz tels que O_3, H_2O et autres. Contrairement aux systèmes de mesures basés au sol, qui sont hautement sensibles aux conditions locales, la sensibilité et la résolution du lidar dans l’espace et le temps sont optimales pour obtenir des mesures, pour comparer ou fournir les valeurs d’initialisation pour les modèles. Au cours des trente dernières années , le lidar à absorption différentielle (DIfferential Absorption Lidar: DIAL) basé sur la rétrodiffusion élastique a été reconnu comme un outil commode de contrôle tridimensionnel en temps réel des concentrations des polluants de l’air [*Measures*, 1992], [*Schoulepnikoff et al.*, 1998]. Cependant l'appareil DIAL a montré des limites : - le fonctionnement dans des atmosphères avec d'importantes quantités d'aérosols, comme dans la couche limite planétaire (Planetary Boundary Layer: PBL), où elles sont hautement variables - l'impossibilité de détecter simultanément plusieurs composants ou polluants atmosphériques [*Bösenberg*, 1996] - la difficulté de détection à courte distance due à sa grande dynamique. De plus, du fait de son spectre et de la forte influence d'autres éléments, la vapeur d'eau ne peut pas être facilement mesurée dans l'UV avec les systèmes classiques DIAL.

Le but de ce travail a été de développer une méthode pour mesurer simultanément, dans la

PBL, la concentration absolue d'ozone ainsi que le rapport de mélange de la vapeur d'eau. Des mesures avec des lasers Nd : YAG et KrF ont été menées en parallèle à l'utilisation des techniques analogiques et de comptage des photons, permettant une augmentation de la gamme dynamique.

Pour établir le profil de concentration de l'ozone, nous avons tiré profit de la simultanéité de la rétrodiffusion induite pat l'effet Raman spontané sur les molécules d'azote (N_2) et d'oxygène (O_2), qui ont des sections efficaces d'absorption différentes pour l'ozone. Ainsi, avec une technique DIAL modifiée, la concentration d'ozone peut être mesurée en évitant la plupart des interférences dues à la rétrodiffusion, mal connue, des particules. Le profil du rapport de mélange de la vapeur d'eau peut aussi être obtenu avec un ensemble de trois signaux Raman rétrodiffusés, détectés simultanément, à partir des molécules de H_2O, N_2 et O_2. Le principal avantage de ce système Raman est sa "quasi" indépendance aux problèmes de rétrodiffusion dépendant de la longueur d'onde, tels qu'induits par les aérosols, et le fait que les concentrations de N_2 et O_2, ainsi que les sections efficaces Raman d'intérêt, sont bien connues. Bien que les sections efficaces Raman soient de deux à trois ordres de grandeur inférieurs aux sections efficaces de rétrodiffusion élastique, elles sont compensées par les concentrations proportionnellement beaucoup plus élevées de O_2, N_2 et H_2O vis à vis des gaz traces tels que O_3.

Le développement de la méthode Raman-DIAL pour les mesures atmosphériques dans la PBL présente plusieurs défis. L'un d'eux est le développement de systèmes lidar à haute sensibilité, en particulier le système de réception optique, le spectromètre et l'acquisition de la partie Raman du signal du système Raman-DIAL. L'autre concerne la procédure de traitement des données évaluant simultanément les profils d'ozone et de la vapeur d'eau. L'un comme l'autre de ces deux challenges présente un certain nombre de possibilités théoriques et pratiques qui sont traitées et examinées dans cette étude.

Summary

The temporal and spatial retrieve of ozone (O_3) concentration and water vapor (H_2O) mixing ratio in the troposphere is of essential interest. Contrary to the stratospheric case, the tropospheric ozone can have a harmful impact, with its toxic effect, on humans and vegetation, accelerating the degradation of the minerals and participating in the green-house problem. Concerning the water vapor, knowledge of its highly variable concentration is essential to both the chemistry of the troposphere ($O(^1D) + H_2O \rightarrow 2\ OH$) where it participates, among others, in the generation of the hydroxyl radical (OH) and to the meteorology. Water vapor is the dominant green-house gas, it plays an important role in the atmospheric chemistry. The conversion and transport of water in the atmosphere is the essential point in the earth's radiation budget.

Due to the complexity and the non-linearity of the air pollution system including emissions, chemistry, thermal radiation, transport and deposition, pollution abatement strategies can only be designed rightly by the use of a three-dimensional mesoscale Eulerian photochemical transport model. To check such models, measurement campaigns are undertaken, in which many physical (wind, temperature, H_2O, etc.) and chemical parameters (emissions and imissions) are measured at different parts of the atmosphere.

LIDAR (LIght Detection And Ranging), which is a real-time method for measuring air pollutants in situ, is one of the best tools to make 3-D measurements of gases concentrations like O_3, H_2O and others. Contrary to the ground based measurements that are highly sensitive to the very local conditions, lidar sensitivity and resolution in space and time is optimal to obtain measurements and to compare or give some input data for the models. During the last thirty years, (elastic backscatter) Differential Absorption Lidar (DIAL) has been established as a convenient tool for the monitoring of the three dimensional real time concentrations of air pollutants [*Measures*, 1992], [*Schoulepnikoff et al.*, 1998]. But the DIAL apparatus has shown limitations: - the operation in layers with high aerosol loading like in the Planetary Boundary Layer (PBL) where they are highly variable - the simultaneous detection of several atmospheric components or pollutants is impossible [*Bösenberg*, 1996] - the detection at short range is difficult due to the high dynamics. Furthermore, due to its spectrum and the strong influence from other elements, the water vapor can not be easily measured in the UV with classical DIAL systems.

The goal of this work was to develop a method to simultaneously measure the ozone absolute concentration and the water vapor mixing ratio in the PBL. Experiments with Nd : YAG and KrF lasers were made and utilization of both analog and photon counting techniques, increasing the dynamic range, were investigated.

To retrieve the ozone concentration profile, we take advantage of the simultaneous spontane-

ous Raman backscattering on the molecules of nitrogen (N_2) and oxygen (O_2) that have different ozone absorption cross-sections. Thus with a modified DIAL technique, the ozone concentration can be measured without most of the interference from poorly known backscatter by particles. Water vapor mixing ratio profile can also be obtained with a set of three Raman backscattered signals, simultaneously detected, from the molecules of H_2O, N_2 and O_2. The main advantage of this Raman system is its essential independence to the wavelength dependent backscatter problems as induced by aerosols, and the fact that the N_2 and O_2 concentrations are well known as well as the Raman cross-sections of interest. Although the Raman cross-sections are two or three orders of magnitude lower than the elastic backscattering cross-sections, they are compensated by the proportionally much higher concentrations of O_2, N_2 and H_2O compared to trace gases like O_3.

The development of the Raman - DIAL method for atmospheric measurements in the PBL presents several challenges. One is the development of highly-sensitive lidar systems, in particular the optical receiver, the spectrometer and the signal acquisition for the Raman part of the Raman-DIAL system. Also the data processing procedure for simultaneous evaluation of the ozone and the water vapor profiles. Both of these challenges present a number of issues, theoretical and practical, that are investigated in the frame of this work.

Chapter 1

Introduction

After a general introduction on air pollution with its effects on both human, vegetal and mineral, we describes the subjects of interest and introduce them to further discussions.

The second paragraph deals with the general characteristics of the atmosphere and definitions of the different atmospheric nomenclatures are proposed. As the tropospheric case is of high interest for us, a further discussion is made.
The ozone and the water vapor components, being at the central part of our discussion, they are presented, and their contributions in the atmospheric processes are discussed.
The origins and development of the lidar technique is exposed as well as the typical physical processes that have been used. It introduces the general description of a lidar system and the main optical interactions that can be used, like the Rayleigh and Mie scattering, the fluorescence process, the Raman scattering or the absorption scheme. Taking advantage of these descriptions, the Raman method used in our work for the ozone concentration retrieve and the water vapor mixing ratio one is exposed.

1.1. Air pollution - Introduction

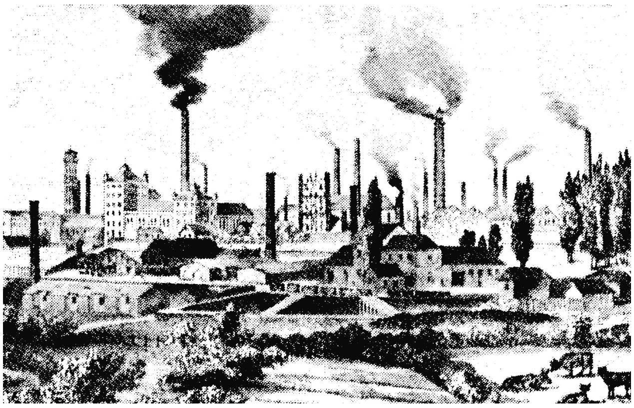

FIGURE 1-1. A lithography showing the industrial pollution in the 30's

Terrestrial atmosphere has been slowly but radically transformed since the formation of our planet, about 4,6 billion years ago. Reductive (strongly or weakly according to the earth accretion theories) at the beginning, the atmosphere is oxidant nowadays knowing that the current oxygen concentration (20,95 % in volume) was reached 400 million years ago.

But, since a few decades, atmosphere composition has been evolving relatively rapidly irrespective to the two major constituent N_2 (78.08 % in volume) and O_2 whose concentrations stay stable, but with the trace components having a mixing ratio less than 100 ppm (N_2O, NO, NO_2, O_3, CO, CH_4, VOC, CFC, …) and the minor component like CO_2. These trace and minor components play an important role in tropospheric (NO_2, VOC,….) and stratospheric chemistry (N_2O, CFC,….), and in the global warming of our planet (CO_2, CFC, O_3, N_2O, CH_4). This change is due in a large part to human activities (fossil gas combustion, farming practices, CFC use, …) that lead to massive, gases or particular, emissions of primary pollutants like SO_2, NO, VOC, CO. Those ones are susceptible to react in the atmosphere to generate secondary pollutants, like photochemical oxidants, which are often more harmful than the initial ones [*Rabinowitz et al.*, 1985].

Air pollution effects are multiple: decrease of the visibibility (especially for particles in suspension which diameter is included between 0,1 and 1 µm), lakes acidification, attack or corrosion of numerous non biological material like historic monuments, injuries to plants, animals and human health (growth of mortality and morbidity).

Dramatic atmospheric pollution episodes (Vallée de la Meuse (France) in 1932, Donora (United States) in 1948 and above all London in 1952) had induced a notable mortality and morbidity increase. For example, in London, the mortality increased by 300 % during a few days. The daily mean concentration on SO_2 and smoke, due to private or/and industrial combustion of coke in conjunction with an atmospheric stagnation (inversion) condition, exceeded each one largely 500 $\mu g/m^3$. Many resolutions has been taken, particularly in developed countries, to improve air quality in order to protect people and their environment against such misdeed.

Despite some real progress has been achieved, those measures are still insufficient and many recent epidemiological studies [*Dockery et al.*, 1993], [*Schwartz*, 1994] still show a significant exceeding of mortality and morbidity (mainly respiratory illness) at short-term (when daily or hourly immission limits are overreached) or at long-term (when annuals limits are overreached). Additionally to the potential effects on health of an increase on earth surface of the sun UV-B radiation, due to the decrease of the stratospheric ozone layer, this radiation increase could also generate higher ozone concentration in the troposphere, created by photolysis, this being the main component of the problematic photochemical smog. In the other hand O_3, N_2O, CFC, CO_2 and CH_4 whose concentrations are also growing (except the water vapor that seems stable) are all greenhouse gases. So they could contribute to a temperature elevation on earth and bring potential effects more dangerous than those that would result from the solely increase of the UV-B radiation.

1.2. Characteristics of the atmosphere

1.2.1. Definition

Derived from the greek ατμοζ (for vapor) and σφαιρα (for sphere), the word *atmosphere* describes the layer, essentially gaseous, that envelopes the earth. The atmosphere can be seen as a fluid in movement, so all the theories related to it will try to explain its behavior and among this its vertical structure, the winds and more generally the meteorology, and the pollution related problems.

1.2.2. The stratified structure

Several classifications can be defined, but the most commonly used is based on the vertical stratification of the temperature as proposed and accepted in 1960, after it had given rise to much controversy, by the Geodesy and Geophysics International Union in Helsinki then in 1962 by the executive committee of the World Meteorological Organization (WMO).
Figure 1-2 gives a schematic view of this "temperature" nomenclature.
- The *troposphere* is the first layer and is of interest for our study. It starts from the ground and is characterized by a negative temperature gradient. This region of the utmost interest for us will be studied more in details in the next section “Focus on the troposphere”, p 9.
- The *stratosphere* starts from the tropopause and is characterized by an increase of the temperature with the altitude. It ends with the *stratopause* at an altitude of approximately 50 km where the temperature reaches a maximum at about 270 K (the highest temperature at the stratopause is reached in the polar regions during their "local" summer, when the insolation is permanent). This temperature increase is the result of the solar UV absorption, mainly due to the ozone which reaches a maximal concentration in the stratosphere. This creates a temperature gradient inversion, with warmer stratospheric air above the colder air of the top of troposphere. Consequently, this restricts considerably the vertical mixing both in the stratosphere itself and between the troposphere and the stratosphere. Due to the low tropopause temperature and this temperature inversion, a water vapor trap is created that explains the low level of water vapor content in the stratosphere.

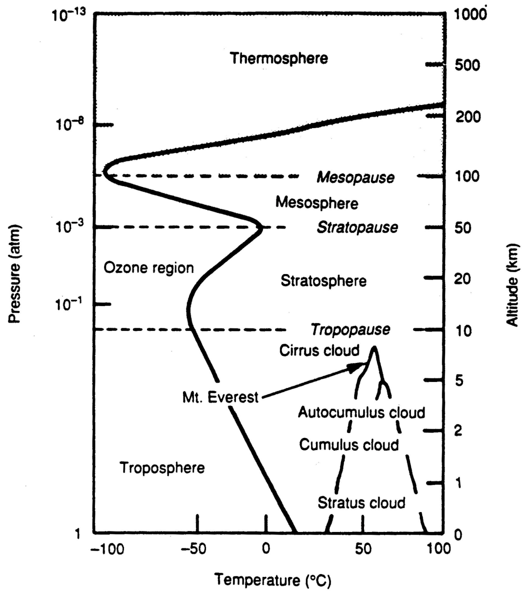

FIGURE 1-2. Temperature vertical profile of the earth atmosphere, expressed versus relative pressure (left scale) and altitude (right scale)

- Beyond the stratopause the infrared emission by CO_2, which is a minor constituent, is sufficient to induce a temperature decrease. This region, named *mesosphere,* extends from 50 km till the *mesopause* at an altitude of about 85 km where the temperature reaches a minimum. Unlike what occurs in the stratopause, the mesopause temperature reaches its highest value (about 210 K) in the polar regions during their "local" winter, and the lowest value (150 K) in the polar regions during their "local" summer. This strange behavior is contradictory with the insolation conditions but can be explained by the existence of a meridian circulation that permits an energy transport from the "summer" polar mesopause to the "winter" polar mesopause.
- The last region is the *thermosphere* which extends after the mesopause, and where the atmosphere is warmed by the UV solar radiation with wavelength lower than 175 nm. The temperature constantly increases (855 K at 200 km, 1000 K at 750 km) till the *thermopause* where the temperature gradient starts to become negligible and gives a quite constant temperature value. The altitude of the thermopause is strongly linked to the solar activity.

We will now briefly expose two other nomenclatures:
- The first one divides the atmosphere in three main regions, on the basis of the chemical composition and the dynamic state. The *homosphere* is the atmospheric region where the mixing phenomenons like winds, convection and turbulence are rapid and important enough to allow a constant volume composition of the main constituents (like O_2, N_2, Ar, but not for minor constituents like O_3 for example) according to the altitude. This homogeneity stops at approximately 80 km, with the *homopause* or *turbopause*, which is a transitional region with the *heterosphere* where turbulence starts to be weak and then does not allow a perfect mixing. In this region the earth gravity induces a molecular diffusion of the main constituents (in the homosphere too, but hidden by the "turbulence-mixing") and then it gives a variable volume

composition of the main constituents. At a certain altitude, depending on the solar activity and the geomagnetism, is the *heteropause* or *exobase* where the particle concentrations start to be very low and where each particle can be approximated to a single one. Beyond in the *exosphere*, rules can be quite different than our usual ones.

- The second one is often used by the radio physicists. It begins with the *neutrosphere*, a region characterized by a very low concentration in free electrons and ending at about 60-70 km with the *neutropause* which makes a separation with the *ionosphere* where the free electron concentration start to be important. Above 750 km the molecular mean free pass starts to be so high that each molecule can be considered as a ballistic particle and then the normal gas physic law is no more valid. This region is called *exosphere* and extends till approximately 2000 km. In the last region the terrestrial magnetism supplants the terrestrial gravity and ions and protons are in majority. It is called *magnetosphere* or *protosphere.*

1.2.3. Focus on the troposphere

The troposphere is characterized by a negative temperature gradient versus altitude of approximately 0.65 °C / 100 m (for dry air the value falls to 1 °C / 100 m). This is due to the absorption, mainly by CO_2 and H_2O, of the infrared radiation reflected from the earth's surface. Unlike the stratosphere that has a positive temperature gradient and then a slow vertical mixing in altitude, the troposphere is characterized by a rapid vertical mixing. This characteristic brings two important phenomenons.

First, the high water vapor content is important for both the general circulation and the weather patterns. The second is linked to the pollution problem. With the pre-mentioned patterns for the troposphere and the stratosphere we can see that those pollutants emitted from the earth surface and having long enough life cycle to reach the tropopause will then spread into the stratosphere and stay there for a long time, due to the slow vertical mixing. This case is well known and famous, like the CFC's for example.

The troposphere can be better illustrated by Figure 1-3.

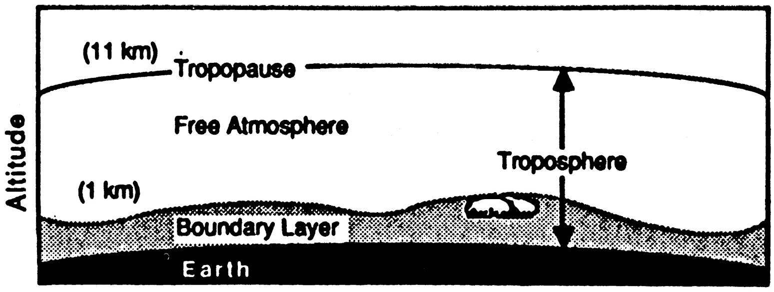

FIGURE 1-3. A focusing altitude view on the different parts of the troposphere showing the PBL, the free troposphere and the tropopause

In this figure the troposphere was divided into two parts. A rapid turbulent mixing region called the *Planetary Boundary Layer* (*PBL*) where reactions of short-life elements occur, and a less turbulent region called the *free troposphere* where the reactions with long-life elements occur.

The troposphere ends at the *tropopause* whose altitude goes from 8 to 18 km depending on the latitude, season and meteorological conditions. For example the polar tropopause is at a lower altitude (approximately 8 km) than the equatorial one (approximately 18 km). Care has to be taken with this definition and we should remember that the tropopause altitude does not consist in a uniform and continuous surface around the earth. There are some "holes", in particular at medium latitudes, that are often associated with jet streams. For this reason, we often use the term of «foliated tropopause». These holes, characterized by a discontinuity in the temperature gradient, allow a matter transport between the troposphere and the stratosphere, and on the other way an intake of stratospheric ozone in the troposphere as we will see in the paragraph “Chemical processes”, p 12.

1.2.4. Physical and chemical properties

Composition

The atmosphere is a mixture of gases containing some liquid and solid particles in suspension. The gaseous part can be divided into two parts: - the first one with the major constituents, which follow a vertical distribution in agreement with the energetic and dynamic state of the global atmosphere, - the second one with the minor constituents which can have a very different behavior depending on the production, destruction and transport mechanisms.

Gases that keep a (quite) constant proportion are forming an ideal gas named "dry air". For the purpose of the meteorology its composition and the molar mass of its constituents has been internationally fixed (the only components that can vary are CO_2, O_3 and Rn) as shown in the Table 1-1.

TABLE 1-1. International values for dry air

Gas	Volume *[%]*	Molecular mass *[g.mol^{-1}]*
N_2	78.084	28.016
O_2	20.948	32.000
Ar	0.934	39.944
CO_2	0.03	44.010
Ne	$1.8.10^{-3}$	20.183
He	$5.24.10^{-4}$	4.003
Kr	$1.14.10^{-4}$	83.07
H_2	$5.0.10^{-5}$	2.016
Xe	$8.7.10^{-6}$	131.3
O_3	$0.4.10^{-6}$	48.000
Rn	$6.0.10^{-18}$	222.000

In the paragraph ("gas law") below we will see that, knowing the total concentration for a given

altitude, we can deduce the partial concentration for a known mixing ratio.
The molecular weight of the dry air is then the sum of these contributions:
$M_{air} = 28.966$ g.mol^{-1}.
From a volume point of view it is worth to say that three gases (N_2, O_2 and Ar) contribute, to about to 99.966 %, on the total volume of the hypothetical dry air.

Gas law
The gases in the troposphere (and the stratosphere), except for H_2O (Van der Walls), are described to a good approximation with the ideal gas law:

$$PV = NRT \qquad \text{(EQ 1.1)}$$

where P *[Pa]* is the pressure, V *[m^3]* is the volume, N *[mole]* is the number of moles, R=8.31 *[m^3.Pa.mol^{-1}.K^{-1}]* is the gas constant, T *[K]* is the absolute temperature.
Among others we can link these quantities with other ones. For example we have:

$$mass\ of\ air\Big|_{volume\,V} = N_{air}.M_{air}\Big|_{volume\,V} = V\rho_{air} \qquad \text{(EQ 1.2)}$$

Where N_{air} *[mole]* is the number of moles of air in the given volume V, M_{air} *[g.mole^{-1}]* is the relative molecular mass of the air, and ρ_{air} *[g.m^{-3}]* is the air volume mass.
The volume mixing ratio, quantity that is independent from temperature and pressure, and thus very important, is a useful quantity for atmospheric calculations.With this notion, the relative molecular mass of the air becomes $M_{air} = \sum_i \xi_i M_i$ where ξ_i *[no unit]* is the volume mixing ratio and M_i *[g.mole^{-1}]* the relative molecular mass of the components i.
We then deduce the equation of interest taking (EQ 1.1) in case of the air:

$$P_{air} = \frac{\rho_{air}}{M_{air}} R\,T_{air} \qquad \text{(EQ 1.3)}$$

A more detailed chapter on this subject, with definitions, can be found in the chapter 9 “Annex”, p 163.

1.3. Introduction to ozone and water vapor

1.3.1. Their importance in the natural environment

Ozone plays an important role in the earth’s radiation budget and is generally considered to be the most important chemically active trace gas in the lower and middle atmosphere. Stratospheric ozone protects the biosphere by absorbing in its Hartley band from 220 to 330 nm the most damaging portion of the sun’s ultraviolet radiation before it reaches the surface of the Earth. The other harmful part of the UV spectrum being absorbed in the upper atmosphere by O_2 (in the Schuman-Runge band from 175 to 200 nm), N_2 and the atomic oxygen (in the Herzberg continuum from 200 to 240 nm). Tropospheric ozone contributes to the greenhouse warming (ozone spectrum has a big absorption peak at about 10 µm, corresponding to the maximum region of radiation emitted from the earth), initiates the formation of photochemical smog, and in high concentrations damages vegetation [*Skarby and Sellden*, 1984] and compromises human health. It is well established that human activities adversely affect the distribution of atmospheric ozone [*W.M.O.*, 1995]. Since the early 1970's, mid-latitude ozone has increased by 10 % per decade in the troposphere because of photochemical reactions involving man-made nitrogen oxides and hydrocarbons, but decreased by 10 % per decade in the lower stratosphere, probably as a result of heterogeneous chemical processes involving anthropogenic chlorine and bromine. Because it is not directly emitted in the atmosphere, tropospheric ozone is a secondary pollutant.

The ultraviolet radiation capable of photo dissociating the oxygen (like in the stratosphere) does not penetrate into the troposphere, so tropospheric ozone must have a different origin. Formerly the ozone in the troposphere was considered [*Junge*, 1962], [*Junge*, 1963] to be the result of stratospheric ozone that enters the troposphere via the tropopause exchange process and then be carried down via turbulent mixing. This theory has stayed till the photochemical smog in big cities made its apparition. A different scheme was then proposed [*Crutzen*, 1973], [*Crutzen*, 1974] in which ozone might be produced even in the unpolluted troposphere by oxidation of methane and other natural hydrocarbons. The main chemical reactions with ozone will be discussed in the following paragraph "Chemical processes", p 12.

Measurement of the water vapor concentration is important to understand the climate and, as it is considered to be the first green-house gas with a global contribution twice the sum of the others, it mainly contributes to the heat budget of the earth's atmosphere. Contrarily to the tropospheric ozone, the photochemistry plays a negligible part in the water vapor cycle and the only sources and sinks come from the precipitation-evaporation cycle. It is then worth to underline that in the atmosphere the three states of water: vapor, liquid and solid are linked and that each one plays an important role in the chemistry or the atmospheric heat budget

1.3.2. Chemical processes

The Chapman process

Firstly it is important to recall this process, even if it occurs in the stratosphere, following the fact that part of the tropospheric ozone comes from this region.

This process is made by four reactions, (REAC 1.1) to (REAC 1.4):

$$O_2 + h\nu \xrightarrow{\lambda < 242.4nm} O(^3P) + O(^3P) \qquad \text{(REAC 1.1)}$$

Slow reaction which occurs in the Herzberg continuum of O_2. $O(^3P)$ denotes the fundamental state of the oxygen atom.

$$O(^3P) + O_2 + M \longrightarrow O_3 + M \qquad \text{(REAC 1.2)}$$

Rapid reaction which is by far the most important reaction producing O_3 in the stratosphere. M stands for O_2 or N_2.

As O_3 is at an equilibrium concentration we must introduce some "O_3 consuming equations":

$$\begin{aligned} O_3 + h\nu &\xrightarrow{\lambda < 310nm} O_2 + O(^1D) \\ &\xrightarrow{310 < \lambda < 1140nm} O_2 + O(^3P) \end{aligned} \qquad \text{(REAC 1.3)}$$

Important reaction which occurs mainly below 800 nm, in the Chappuis band from 450 to 850 nm, in the Huggins complex set of bands from 300 to 450 nm and in the Hartley band from 200 to 300 nm. $O(^1D)$ denotes an exited state of the oxygen atom (created by a more energetic incoming light).

$$O(^3P) + O_3 \longrightarrow 2O_2 \qquad \text{(REAC 1.4)}$$

A variant to the reaction (REAC 1.1) for $\lambda < 175.9$ nm is given below:

$$O_2 + h\nu \xrightarrow{\lambda < 175.9nm} O(^1D) + O(^3P) \qquad \text{(REAC 1.5)}$$

It occurs in the Schumann-Runge continuum of O_2.
$O(^1D)$ can collide with a molecule like O_2 or N_2 to return to its fundamental state $O(^3P)$, or with different components such as H_2O to make various radicals (such as OH).

Tropospheric ozone chemistry
Let us first present two reaction schemes which can occur for the ozone destruction:
- By dry deposition on earth's surface
- By photolysis, following the "first" part of the previous chemical reaction (REAC 1.3)

$$O_3 + h\nu \xrightarrow{\lambda < 310nm} O_2 + O(^1D) \qquad \text{(REAC 1.6)}$$

which gives the following competing reactions for $O(^1D)$:

$$\begin{array}{c} O(^1D) + H_2O \longrightarrow 2OH \quad 15\%\ \textit{rapid} \\ O(^1D) \xrightarrow{M} O(^3P) \quad 85\% \end{array} \qquad \text{(REAC 1.7)}$$

OH is the most reactive component of the atmosphere, reacting with almost all the organic molecules. For this reason it is often called an "atmospheric cleaner".

If we take the case of an "unpolluted" atmosphere, where naturally produced Volatile Organic compounds (VOCs) interact with NO_x (= NO + NO_2), we therefore have a production of O_3. The chemical process is the following and can also be applied to polluted cases:

$$NO_2 + h\upsilon \xrightarrow{295 < \lambda < 430nm} NO + O \qquad \text{(REAC 1.8)}$$

Photo dissociation of NO_2 by near UV solar radiation.

$$O_2 + O + M \longrightarrow O_3 + M \qquad \text{(REAC 1.9)}$$

Reaction of O and O_2 in presence of M (O_2 or N_2) like for (REAC 1.2).

$$NO + O_3 \longrightarrow NO_2 + O_2 \qquad \text{(REAC 1.10)}$$

Rapid reaction of NO with O_3.
As the reaction in (REAC 1.10) is very rapid, urban atmospheres will not see an increase of O_3

until most of the NO (produced by automobiles, industrial or utility sources) has been transformed into NO_2 (which is more harmful than NO). This explains the possible low ozone concentration in urban areas.
But this was an ideal case and we can see that reactions which produces NO_2 without destroying O_3 will disrupt the above equilibrium and result in a net increase of ozone. Oxidation of photochemically reactive VOCs results in the formation of highly reactive chemical species (the free radicals) which are capable of converting NO into NO_2 without destroying O_3.
Two interesting cases for the ozone formation will be presented.
- In the case of an unpolluted area, i.e. with low concentrations of NO_x (some ppb), we will have a chain reaction with the following summary reaction:

$$CO + 2O_2 \xrightarrow[NO:catalysator]{OH\ preserved} CO_2 + O_3 \qquad \text{(REAC 1.11)}$$

- In the case of high NO_X loading, we have the following summary reaction:

$$CH_4 + 4O_2 \xrightarrow[NO:catalysator]{OH\ preserved} CH_2O + H_2O + O_3 \qquad \text{(REAC 1.12)}$$

It is worthy to say that in case of a big excess of NO_x, HNO_3 is formed and then can be transported by wind, photolysed or have a reaction with OH to form NO_2. With this scheme it is understandable that pollution from a town can be exported to a rural place.
But great care has to be taken in this polluted case, as the O_3 production depends not only on the NO_X loading but also on:
- The VOC / NO_x ratio
- The chemical composition of the VOCs

In the Figure 1-4 is shown a typical plot which links the O_3, NO_x and VOC concentrations..

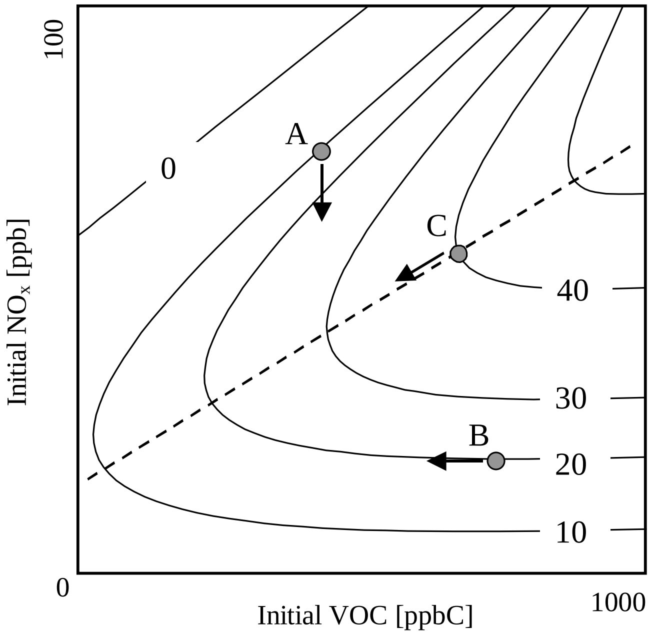

FIGURE 1-4. Secondary ozone formation expressed in [ppb] from the primary emission of NO_X and VOC

This figure represents the relation between the primary VOC and NO_x concentrations that are forming a given O_3 concentration, represented by means of an O_3 isopleth diagram and showing the non linear O_3 production behavior. Such a diagram is a contour plot of maximum O_3 concentrations, with in this case values of 0-10-20-30-40 (ppb) marked on the isopleths, achieved as a function of initial NO_x and VOC concentrations. It shows that the changing of NO_x and VOCs concentrations on the production of O_3 is strongly dependent on the relative but not only the individual concentrations of NO_x and VOCs.
Three typical cases, represented in the graph by points, can be described:

- Point A. The only NO_x concentration decrease implies an even higher O_3 concentration than the initial. The VOC concentration has to be diminished to decrease the O_3 concentration. We are in a region where the VOC concentration is the limiting factor to the O_3 concentration decrease.
- Point B. A decrease of the NO_x concentration imply an O_3 concentration decrease, and a VOC concentration decrease doesn't make a sensible change. In this region the NO_x concentration is the limiting factor to the O_3 concentration decrease.
- Point C. We are at a particular point characterized by a maximum of O_3 production for a simultaneous minimum of primary emissions. A decrease of either NO_x or VOC concentration gives an O_3 concentration decrease.

In summary, above the dot line formed by the series of point C, we are in the VOC controlled part (to decrease O_3, the VOC concentration has to decrease), and below this dot line we are in the NO_x controlled part (to decrease O_3, the NO_x concentration has to decrease). This example is simple and, in general, a numerical simulation is made to retrieve this plot in the particularly used conditions.

Another possible tropospheric ozone incoming is from the stratosphere. Following the work of Junge, Danielson in 1968 found the tropopause folding events where O_3 from the stratosphere is transported down to the troposphere and Crutzen in 1995 showed that 0.1 % of the O_3 produced in the stratosphere leaks inside the troposphere, which makes approximately 20 % of tropospheric ozone production.

The water vapor chemistry

The photochemistry of water vapor is negligible. In conjunction with the ozone the reactions (REAC 1.6) p 13 and (REAC 1.7) p 13 give us (with the radiation in the UV):

$$\begin{aligned} O_3 + h\nu &\rightarrow O_2 + O(^1D) \\ H_2O + O(^1D) &\rightarrow 2OH \end{aligned} \qquad \text{(REAC 1.13)}$$

which furnishes most of the OH radical, considered to be the principal tropospheric oxidant.
The water is present under its three states in the atmosphere: vapor, liquid and solid. Vapor, which is the most common state, can, following local conditions, condense in rain, snow, fog, hale,... . Apart from its important action in the water cycle this condensation phenomenon triggers other processes like:

- it brings to the ground, by wet deposition, other atmospheric components that have an affinity with condensed state. It has a cleaning action.
- it participates to the radiation budget of the earth.
- it plays a prominent role in the atmospheric chemistry, like for the acid rains formation.
- it interacts with aerosols that act like condensation nucleus in the formation of clouds or fog.

Those aerosols, depending on their composition, could dissolve totally, partially or not at all and give birth to complex processes [*Köhler,* 1936], [*Pruppacher and Klett,* 1980].

The spatial and temporal distribution of the ozone concentration and water vapor mixing ratio are variable. Balloon soundings can give the spatial distribution but with a lack in the temporal one. Punctual analyzers give a temporal information but not the spatial one. We therefore see the need of a temporal range resolved technique as the lidar can provide.

1.4. Measurements by the lidar technique

1.4.1. Some history

In 1917 Albert Einstein studied the quantum transitions between two energy levels; he explained the spontaneous emission and predicted the stimulated emission phenomenon. Some decades later, in the 50's, the physicist Alfred Kastler obtained the first inversion of population by optical pumping. In 1954 Townes built the first MASER (Microwave Amplifier by Stimulated Emission of Radiation), based on a transition of the ammoniac molecule and which is the precursor of the laser. After further theoretical investigation, Townes and Schawlow concluded, in 1958, that it was possible to build such a MASER system at higher frequency, i.e. in the visible [*Schawlow and Townes*, 1958] and Maiman was the first in 1960 to build an optical maser with ruby [*Maiman*, 1960]. Then there was an exponential increasing of the research and applications in this field, and the name changed to LASER for Light Amplifier by Stimulated Emission of Radiation.

As the "laser sounding" era did not start because of the unavailability of lasers, some attempts were made by means of searchlight probing technique in 1952 [*Elterman*, 1954], to retrieve temperature, density and pressure in the atmosphere, followed in 1962 by experiments with a similar giant pulse technique [*Mc Clung and Hellworth*, 1962].

First laser soundings on aerosols with a ruby laser were made in the stratosphere [*Fiocco and Smullin*, 1963], to study volcanic compounds. A similar system for the troposphere was made [*Ligda*, 1963]. This so called lidar technique has then expanded and stimulated research into many fields: laser sources, optics, electronics, atmospheric chemistry, and more. The main advantage of this technique is the ability for range resolved probing of the atmosphere at distance in real time. No other systems, even today, can compete with this feature. This system has also some limitations due to the optical concept, the most commonly known are clouds or big aerosol loading.

From the 60’s different techniques were investigated for detecting, with higher resolution, more and more types of molecules, pollutants, clouds or physical process like wind. Among all those tried we can cite:

- Rayleigh lidar which is usually used for determining temperature above 30 km [*Hauchecorne et al.*, 1991]. The feasibility of atmospheric temperature measurement down to 1 km has been also shown [She et al, 1992].
- "Standard" DIAL based on a different absorption, by the molecule studied, of the pump beam. This technology is classic but the emitting system is complicate. It permits the measurement of various constituents [*Uchiumi et al.*, 1994], but the most classical use is for the ozone concentration retrieve [*Browell et al.*, 1985], [*Calpini et al.*, 1997]. The water vapor case is quite diffi-

cult with this method, and numerous problems occur [*Browell et al.*, 1979].
- Shot per shot lidar to retrieve wind and ozone fluxes [*Fiorani et al.*, 1998].
- Raman lidar in vibrational [*Renaut and Capitini*, 1988] (water vapor in the boundary layer), rotational [*Arshinov et al.*, 1983] (temperature under 1 km), or resonant form [*Rosen et al.*, 1975] (SO_2 and NO_2 concentrations under 1 km, with eyes safety considerations), [*Hochenbleicher et al.*, 1976] (conditions of application).
- Fluorescence lidar, used for mesospheric temperature measurement, where quenching is small [*She et al.*, 1992].
- Pump and probe lidar to estimate the OH radical concentration [*Jeanneret et al.*, 2000].

The idea of using the Raman effect for lidar, came in 1967 [*Leonard*, 1967], when the first Raman shifts from the atmospheric oxygen and nitrogen were observed, and the advantage of this novel technique was pointed out. Several pioneering groups then worked in this promising way: Cooney [*Cooney*, 1968] measured atmospheric density profiles from N_2, Inaba [*Inaba and Kobayashi*, 1969] theoretically showed that it was possible to monitor atmospheric gases or pollutants and proposed a diagram for the lidar to be built. First observation of water vapor by this technique was made by Melfi [*Melfi et al.*, 1969].

1.4.2. General principle of the lidar technique

The principle of probing the atmosphere with a laser is a direct transposition of the radar principle to the optical wavelengths. The lidar method is an active method because it uses an artificial source of light to retrieve the atmospheric parameters, in contrast to the passive methods, using the emission from natural light sources (moon, sun) or the thermal emission.
The use of a laser is due to its qualities:
- Spatial properties: the very small divergence and the possibility to have very short pulses (from several fs to some µs) allows a high space resolution (for example 1.5 m for a pulse length of 10 ns).
- A high power density.
- A quasi monochromatic beam which allows an efficient filtering of the backscattered energy. This spectral sharpness allows a high-resolution analysis.

All lidar system is more or less based on the same model, composed of a transmitting and a receiving section as shown in the Figure 1-5.
A pulsed laser beam is emitted in the atmosphere by the transmitter. It interacts with the atmospheric constituents upon propagation by a multitude of phenomena such as Rayleigh, Mie, and Raman scattering, as well as by inducing fluorescence. Part of it is scattered back (by Rayleigh, Mie, Raman, induced fluorescence...) and a small part of this backscattered light is collected by a receiving telescope, spectrally resolved, converted into an electrical signal and recorded by a detection unit. The magnitude of the electrical signal produced is proportional to the backscattered light intensity. Processes like scattering in other directions than the backscatter's one, or absorption, by the molecules and particles encountered, will mainly diminish it. The detection chain is generally formed by an optical part (filters, polychromators,...) and an electronic part (PMT, digitizer,...). This latter makes the temporal signal analysis and will then defined the measurement spatial resolution, if it is not limited by the laser pulsewidth.

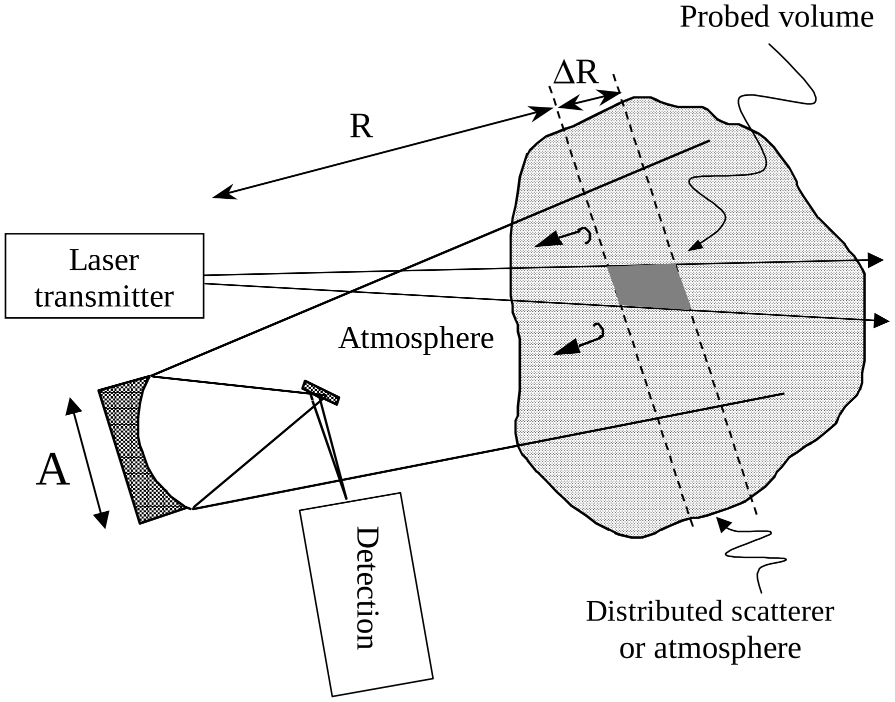

FIGURE 1-5. Lidar principle (biaxial type)

In the elastic or Raman case we can write [*Measures*, 1992] that the received energy backscattered by the media between the distance R and R+ΔR is given by:

$$E(\lambda, R) = E_L(\lambda_L) \cdot C(R) \frac{A}{R^2} \tilde{\Delta} R \cdot \beta \cdot T_1 \cdot T_2 \qquad \text{(EQ 1.4)}$$

Where

- -E(λ,R) represents the received mean energy from the probed volume at a distance R to the scattering volume and at a wavelength λ (for example the Raman process generates a wavelength shift).
- -$E_L(\lambda_L)$ is the emitted laser mean energy at the laser pump wavelength λ_L.
- -C(R) is the instrument constant that take into account the transmitter and receiver efficiencies, and the overlap function (which describe the overlap between the emitted beam and the receiver field of view).
- -A is the effective receiver area.
- - $\tilde{\Delta} R$ is the spatial resolution.
- -β is the backscattered cross-section. It takes into account the used physical process (elastic, Raman...) and then allows to quantify it.
- -T_1 is the atmospheric transmittance from the transmitter to the probed volume and T_2 is the atmospheric transmittance from the probed volume to the receiver. They measure the transmissions through the medias of interest and include all the different losses that could cause a decrease, such as scattering or absorption.

We can also express the lidar equation (EQ 1.4) by mean of the power, knowing that $P(\lambda,R) = \frac{E(\lambda,R)}{\tau_D}$, where P(λ,R) represents the received power from the probed volume at a distance R to the scattering volume and at a wavelength λ.

The laser mean power $P_L(\lambda_L)$ for a pulse duration τ_L is given by $P_L(\lambda_L) = \frac{E_L(\lambda_L)}{\tau_L}$, and the spatial resolution by $\tilde{\Delta} R = \frac{c\tau_D}{2} + \frac{c\tau_L}{2} + \frac{c\tau_P}{2}$, where c *[m.s^{-1}]* the light speed, τ_D *[s]* the detection response time (equal in our case to the digitizer one because of the fast PMT's response), τ_L *[s]* the laser pulsewidth, and τ_P *[s]* the optical interaction process lifetime.

In most of the cases, the detection is the limiting factor and then we have $\tilde{\Delta} R = \frac{c\tau_D}{2}$.

This finally gives the lidar equation by mean of the power:

$$P(\lambda,R) = P_L(\lambda_L) \cdot C(R) \frac{A}{R^2} \Delta R \cdot \beta \cdot T_1 \cdot T_2 \qquad \text{(EQ 1.5)}$$

Where $\Delta R = \frac{c\tau_L}{2}$ is the effective length.

From this equation we deduce two main possibilities:
1. the measurement of β will give the scattering element concentration.
2. the measurement of T_1 and T_2 will give the absorbent concentration.

The first possibility will be feasible only if the scattering element is abundant enough, or if the scattering process is efficient enough.

Method n°1: «Based on the scattering properties of the atmosphere»

Elastic scattering

The atmospheric constituents diffuse the incident beam in an elastic manner, whatever wavelength is used. In this phenomenon the scattered light has the same wavelength than the incident one. The elastic contribution always superposes itself to other effects.

Rayleigh scattering

If the exciting wavelength is much higher than the dimensions of the atoms and of the molecules, it fulfils the Rayleigh scattering condition. The Figure 1-6 illustrates this case where the laser radiation is elastically scattered from atoms or molecules and is observed with no change of frequency: $\nu_0 = \nu_R$. In the resonant case, the radiation matches in frequency to that of a specific atomic transition. For one incoming photon, one photon is re-emitted with the same energy.

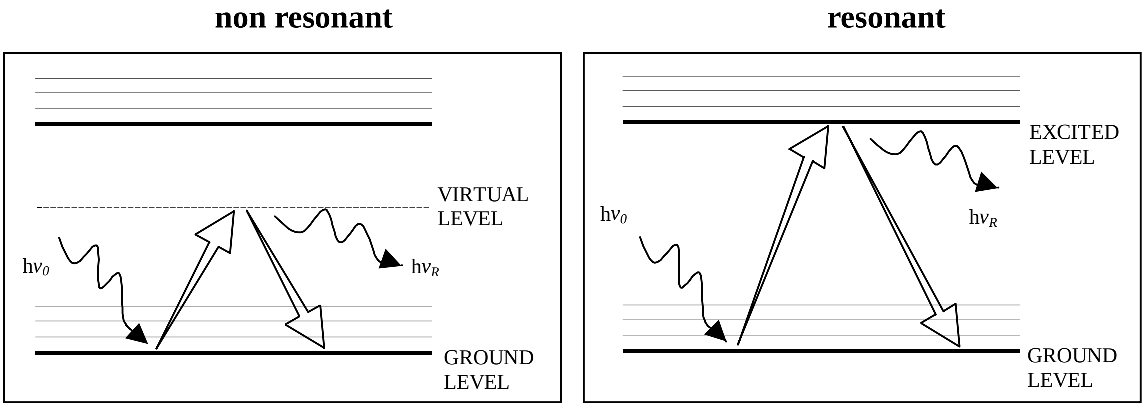

FIGURE 1-6. Rayleigh (or molecular) interaction

This interaction is always present in the "lower" atmosphere, where the air density is important (if the altitude increases this contribution will then decrease). Its cross-section follows a λ^{-4} wavelength dependence, and for this reason the shorter wavelengths are more scattered. This explains the blue sky color. In this case the life time of the process is about 10^{-8}-10^{-9} s, which is lower than the time between two collisions.

In case of off-resonance scattering the cross-section is about $10^{-23} – 10^{-26}$ cm^2.molec^{-1}. As all molecules of the atmosphere are participating (of the order of 10^{19} molec.cm^{-3} in the lower troposphere), this compensates partially the inefficiency of the process. The resulting spectral line has a certain width that is due to the Doppler effect coming from the translation movements of the molecules. With this scattering effect we can measure molecular concentrations or temperatures.

The resonance scattering phenomenon takes place when the laser's emitted wavelength is near or coincides with a transition of atomic or molecular resonance. The cross-sections take higher values, around 10^{-17} - 10^{-13} cm^2.molec^{-1} for the molecules. By tuning the laser frequency we can then be selective for the element studied. Also, in this case, the laser will affect the process efficiency (convolution of the laser linewidth and the transition profile) and by playing with the ratio laser linewidth / absorbent linewidth we can have the following informations:

- If the laser linewidth is slightly superior to the absorbent linewidth we can directly have a measure of the concentration.
- If the laser linewidth is less than some tenths of the absorbent linewidth, we can then measure this linewidth and so deduct the temperature or, with the Doppler shift measurement, we can measure the wind.

Mie scattering

In the presence of particles with a size comparable to the exciting wavelength (> 0.1 µm), the Mie scattering becomes more important. The laser radiation is elastically scattered from small particulates or aerosols (of a size comparable to wavelength of radiation) and is observed with no change in frequency, $\nu_0 = \nu_R$, as shown in Figure 1-7. In this case the "same" photon is re-emitted.

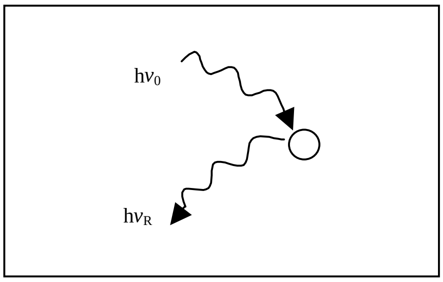

FIGURE 1-7. Mie (or aerosol) interaction

Its efficiency is generally much bigger than the Rayleigh's one, due to cross-sections of the order of magnitude of $10^{-26} – 10^{-8}$ $cm^2.molec^{-1}$ (10^{-10} $cm^2.molec^{-1}$ in the visible spectra for particles with size around 0.1 μm). The interaction life time is of the order of 10^{-8}-10^{-9} s. Sometimes with a single wavelength it is difficult to separate the Rayleigh and Mie contributions. In this case we will be using two wavelengths making a hypothesis on the wavelength dependence of the Mie backscattering coefficient (λ^{-k}). Yet with this method we only obtain the total density or concentration of aerosols, but we are unable to differentiate the different constituents.

In both Rayleigh and Mie cases, neither the linewidth nor its position is critical. It is important, obviously, to avoid coincidences with the absorption wavelengths of the atmosphere components or with resonant molecular transitions.

The inelastic scattering (molecular processes)

Fluorescence

The laser radiation matched to a specific electronic transition of an atom or a molecule suffers absorption and subsequent emission at lower frequency. Broadband emission is observed in case of molecules as shown in Figure 1-8, with photons having a higher wavelength than the exciting wavelength. The re-emitted photons have then less energies than the incoming one.

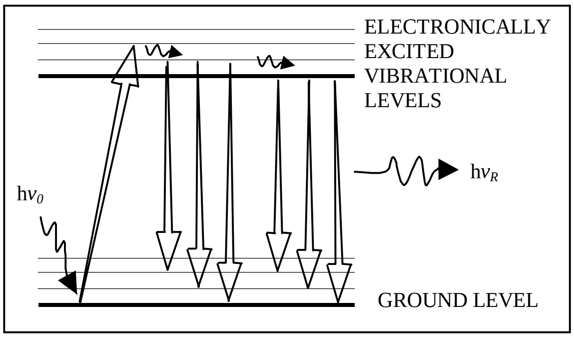

FIGURE 1-8. Fluorescence interaction

This process is efficient, due to cross-sections around 10^{-20} $cm^2.molec^{-1}$, but the life time of the excited levels, from 10^{-6} to 1 s, is in general much longer than the time separating two collisions. It then induces a process of energy loss (or de-energizing) by collisions (quenching), the photon giving its energy to another molecule. As a consequence it implies a reduction of the process efficiency. In practical we will have to choose frequencies and apply a collision de-energizing factor, or remain in the altitudes superior to 30 km so that the time between two collisions is much longer (and then cancel the problems).

The main problems in this case concern the lifetime interaction, and also the resulting shifted wavelengths that can be confounded with Raman ones. The paragraph 2.2.5. “Differences between Raman scattering, fluorescence and IR absorption processes”, p 37 will detail how to differentiate and recognize the two processes.

Raman scattering

When the laser radiation is inelastically scattered from molecules and is observed with a frequency shift characteristic of the molecule (and with a known backscattering cross-section), we are in the Raman case. In Figure 1-9 two types of Raman scattering that occurred simultaneously are shown: the Stokes process which shifts the wavelength to upper ones: $\upsilon_R = \upsilon_0 - \upsilon_{shift} < \upsilon_0 \quad \Rightarrow \quad \lambda_R > \lambda_0$, and the anti Stokes one which shifts the wavelengths to lower values: $\upsilon_R = \upsilon_0 + \upsilon_{shift} > \upsilon_0 \quad \Rightarrow \quad \lambda_R < \lambda_0$. In this scheme one photon is re-emitted with less (Stokes) or more (anti Stokes) energy than the incoming one This scattering results from the interaction between the exciting radiation and the electric dipole moment of the molecule. It induces a change in the rotational or / and vibrational states of the molecule. The interaction life time is very small, quasi instantaneous, and smaller than 10^{-14} s. It is produced whatever the exciting wavelength is and gives a shifted lines spectrum with respect to this wavelength, whose shifting depends on the studied molecule.

The study of such a spectrum allows the simultaneous measure of a wide variety of components and the absolute measurement of their mixing ratio. This process has a very low efficiency (cross-sections about 10^{-32} - 10^{-28} $cm^2.molec^{-1}$), and can be improved by working in the UV, at shorter wavelengths, because the Raman differential cross-section follows a law in λ^{-4}.

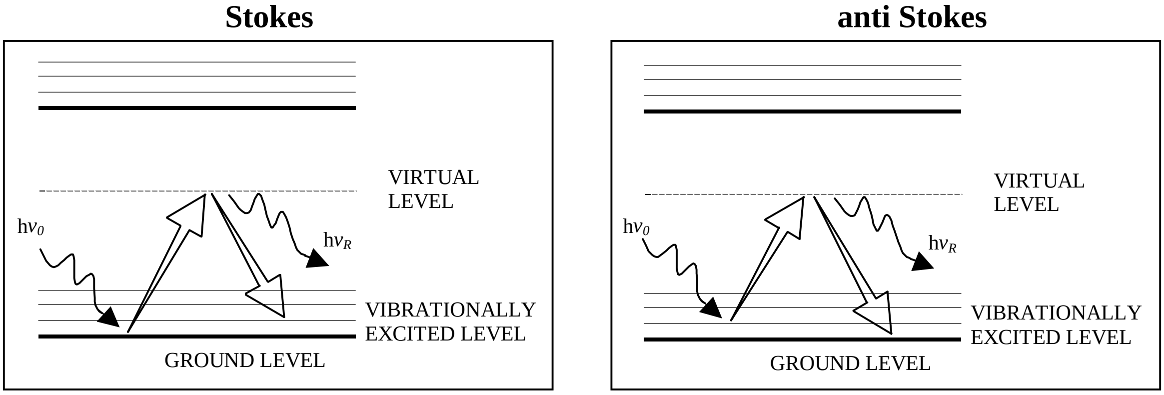

FIGURE 1-9. Raman interaction

In case the exciting wavelength gets close to a resonance line the cross-section becomes around 10^{-26} $cm^2.sr^{-1}.molec^{-1}$ but, then, the method becomes specific to a component. The cross-section is then very sensitive to the wavelength and its value is more difficult to retrieve. Possible interferences with the fluorescence have also to be taken into account.

As this effect is at the basis of this work, a more detailed paragraph will be dedicated to describe this interaction (see paragraph 2.2.2. “The Raman process”, p 30).

Method n°2: «Based on the absorption properties of the atmosphere»

(Probing by differential absorption)

In the method n°1 we have supposed to have enough scattering components that would give a measurable backscattering. Often the component to be measured will not contribute enough to the backscattering, thus we will measure it mainly by its absorption.

At the basis of this method is the absorption effect, where the incoming photon is absorbed, and then "lost", by the molecule allowing its energy level to jump into a higher one. The cross-sections are in the order of magnitude of 10^{-22} - 10^{-18} $cm^2.sr^{-1}.molec^{-1}$). This process gives an attenuation of the laser beam when the frequency matches with the absorption band of a given molecule or atom. The Figure 1-10 gives a schematic description of this phenomenon.

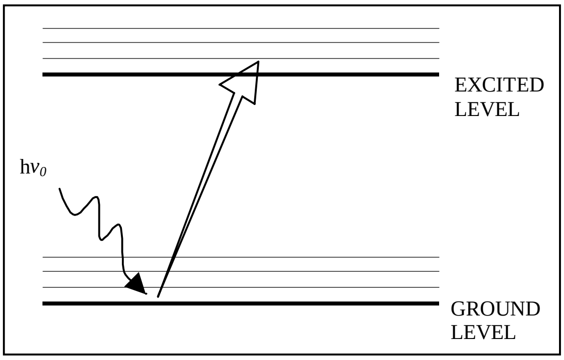

FIGURE 1-10. Absorption interaction (for a molecular process)

In this case, we use two wavelengths very close to each other, so that the scattering effect can be considered as identical for the two wavelengths, but chosen in a way to assure a maximum absorption difference by the component to be measured (the so called "ON" is absorbed, the other so called "OFF" is not absorbed). The advantage of using these two close wavelengths stands in the elimination of the instrument characteristics in the calculations, supposing that they are identical at these two wavelengths. The measure is then automatically calibrated. We can use this method in the spectral areas where the molecules present absorption bands due, either to electronic transitions, either to vibration/rotation transitions.

For example, in the UV, the absorption cross-section variations with respect to the wavelength of components like SO_2 and NO_2 are sufficiently slow to enable the use of relatively large laser linewidth (about 0.1 nm) and a value of 1 nm between the ON and OFF wavelengths. The possibility to use close wavelength pairs (with the largest possible cross-section difference) is to be considered because it avoids an important difference in the Mie scattering contribution. For the ozone, in the Hartley band, due to the absorption cross-section shape, the choice of the wavelengths has to be a compromise between the $\Delta\sigma$ (difference of the absorption cross-sections) and the Δλ (difference of the wavelengths): in other words the ratio $\Delta\sigma / \Delta\lambda$ has to be optimized [*Ancellet and Bösenberg*, 1996].

1.4.3. The Raman lidar

DIAL measurements of the water vapor are generally performed around 720 nm. The biggest problem is the thinness of those bands. As a consequence of that we have to take into account the non monochromaticity of the laser line and to develop lasers working with very narrow spectral linewidth: 0.1 pm. Consequently, this implies also an improvement of the spectral spectroscopic datas. Two very important corrective effects have to be applied: Doppler correction, Lorentz correction (convolution which will give the de Voigt profile). We have again, in this case, a direct relation between the precision of the measure and the relation between the linewidth of the laser and the absorption one:

$$\Delta l_{laser\ line} / \Delta l_{absorbent\ line} \sim 1 \ \rightarrow error \sim 20\%$$
$$\Delta l_{laser\ line} / \Delta l_{absorbent\ line} \sim 0.5 \ \rightarrow error \sim 5\%$$
$$\Delta l_{laser\ line} / \Delta l_{absorbent\ line} \sim 0.1 \ \rightarrow error \sim 0.1\%$$

Furthermore, for a retrieve error of 0.1 % in the troposphere a laser linewidth of about 2 pm has to be used. In the stratosphere, due to the pressure broadening phenomenon (the absorption linewidth is smaller with smaller pressure, like in the stratosphere) a laser linewidth of 0.2 pm has to be used.
For this reasons, the Raman solution for the water vapor mixing ratio retrieve can be a less complicated approach than the traditional DIAL one.

For the O_3 concentration retrieve we use a modified DIAL method, taking advantage of two systems: that of the Raman scattering and the one of the traditional DIAL which will give us the differential absorption. The main advantage of this method is the elimination of the Mie backscattering part in the lidar equation. Above all, to counter balance the Raman backscattering cross-sections, we will consider (because all the molecules of the atmosphere are excited) only the result of the Raman interaction of the O_2 and N_2, the most abundant molecules in the atmosphere and in the most stable and well defined quantities. In this method, by using a single excitation wavelength (instead of two like in classic DIAL), we generate a couple of backscattered wavelengths (by O_2 and N_2) which being absorbed differently by the ozone on their way back, will be at the origin of a DIAL (-like) effect and at the same time allows a possible measure of the O_3 concentration.
The following Figure 1-11 shows the absorption feature of O_3 in the Hartley band, from 200 to 300 nm, at 298 K and with a resolution of 0.01 nm [*Daumont et al.*, 1992]. In this figure are shown the pump wavelengths for the KrF (solid line) and Nd:YAG (short dot line) laser, and their related Raman shifts from the atmospheric O_2, N_2 and H_2O. This spectrum is characterized by a very broad structure (about 50 nm FWHM) with no strongly absorbing narrow spectral lines. The cross-sections related to the KrF case are always higher than the Nd:YAG one, giving a higher O_3 absorption of the pump and Raman wavelength in the KrF configuration.

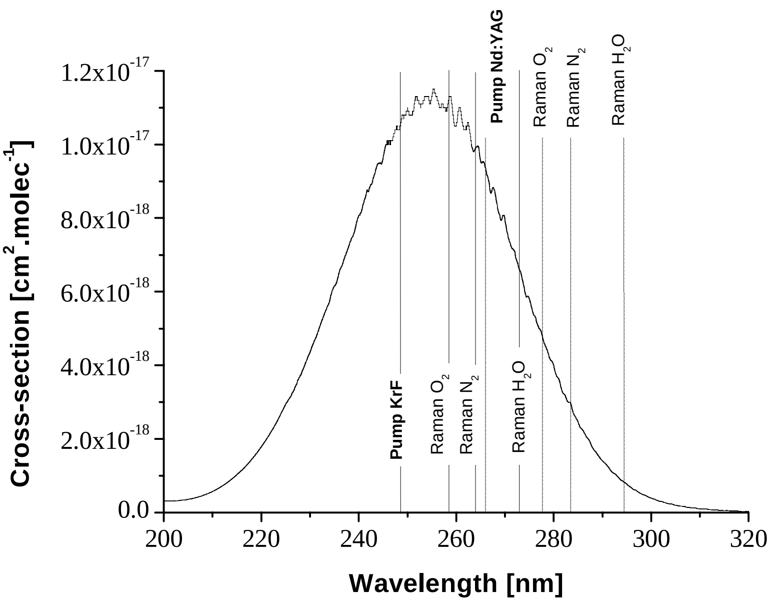

FIGURE 1-11. Ozone absorption spectrum in the Hartley band at 298K

Concerning H_2O mixing ratio, the retrieve is more classical and uses only the Raman scattering method. For this quantity we will calculate the ratio between the H_2O and the N_2 (or O_2) Raman backscattered signals. But, as it will be seen in following chapters (n° 2 “Theory”, p 27 for example), the influence of the ozone on the retrieve is important. We then will have to take into account a third channel (already there for O_3) to quantify this effect.
This gives the following procedure for the H_2O mixing ratio retrieve:
- Use of the H_2O / N_2 (or O_2) Raman backscattered signals, following the Raman scattering method, for the rough retrieve of H_2O (without the «ozone correction»).
- Use of the O_2 / N_2 Raman backscattered signals, following the modified DIAL process like exposed before, for the retrieve of the integrated value of O_3 concentration.

Chapter 2

Theory

The bases to understand what physically occurs in the Raman scheme are presented, as well as the "know how" to retrieve the ozone concentration, the water vapor mixing ratio and the aerosol extinction coefficient.
This chapter is linked to chapter 4 “Corrections and errors analysis”, p 65 giving the possible approximations and the results for the theory exposed here.

After a brief summary on the possible atmospheric interactions, already described in the introduction chapter, basics on the molecular spectroscopy are exposed without too much emphasis. The Raman scattering process, being at the heart of our retrieves, will be more developed and both the theory and the selection rules for the molecules of interest, O_2, N_2 and H_2O, are exposed. Application to our case and principal differences between the Raman scattering and the infrared absorption or the fluorescence are given.
The retrieve of the lidar equation in the Raman case is performed, including all the contributing terms such as the Rayleigh and Mie scattering or the molecular absorption. The retrieve of the ozone concentration is then made with the O_2 and N_2 Raman signals, taking into account the different contributing terms. For the water vapor mixing ratio retrieve, the ozone interference correction is calculated, allowing the retrieve by mean of the O_2, N_2 and H_2O Raman signals. As for the ozone case, all the other contributing terms are taken into account.

2.1. Laser interactions with the atmosphere: introduction

The atmosphere contains a wide range of constituents extending from the atoms (Angström range) and the molecules to the aerosols (up to some tens of micrometers or more). Each of the three physical phases are encountered: the gas, liquid or solid ones. The mixture of such different components explains the atmospheric behavior and the vast and complex interactions that can occur with a laser beam.

Some interactions are always present and not "selectives", like the Rayleigh, Mie or Raman scattering and are more or less important depending on the atmosphere characteristics (for example the aerosols loading in case of the Mie scattering).

Some other interactions depend on specific conditions. The absorption scheme is in this sense a selective process, depending on the absorption spectrum at the laser wavelength. The resonant processes (Rayleigh or Raman) are also selective, the laser wavelength radiation matching a specific electronic transition of the molecule.

The main interactions, as well as the ones of interest for us, were briefly described in the paragraph 1.4.2. “General principle of the lidar technique”, p 17. Descriptions like spontaneous or simultaneous emission, or peculiar processes (near-resonant Raman, resonance fluorescence....) were voluntarily omitted, as being out of the main purpose of this work, and can be found in references such as [*Gouesbet and Grehant*, 1998], [*Chevallier*, 1986], [*Measures*, 1992]. In the following paragraph we will focus on the Raman process after a general recall about the molecular spectroscopy.

2.2. Basics in molecular spectroscopy

2.2.1. Spectra

Molecules can be classified into five families, one for the monoatomic molecules (i.e. atoms) and four for the polyatomic molecules, depending on the symmetry's properties of the molecules. This classification allows a certain simplification for the spectra study of molecules.

As for atoms whose spectra consist of sharp lines, molecules appear to be made up of bands containing a densely packed line structure. Spectra arise from the emission or absorption of definite quanta of radiation when transitions occur between certain energy levels. In an atom the energy levels represent different allowed states for the orbital electrons. For a molecule several cases can occur. It can absorb or emit energy in transitions between different - electronic (associated, for example, with different molecular orbitals), - vibrational (changes in the vibrations of the atoms within the molecule), - rotational, energy levels. The two last cases are suited to molecules and do not exist in the atoms. As for the electronic case, their related energies are quantized, so that only certain distinct levels of vibrational and rotational energy are permissible.

In first approximation, it is usual to consider that the energy of a molecule can be expressed simply as the sum of three contributions

$$E_{tot} = E_{elec} + E_{vib} + E_{rot} \qquad \text{(EQ 2.1)}$$

associated respectively to the electron motion (E_{elec}), to the atomic nuclei vibration around their equilibrium position (E_{vib}), and to the molecule rotation around its mass center (E_{rot}).

This partitioning of the energy into three distinct categories is not strictly correct. For example, the atoms in a rapidly rotating molecule are pushed apart by centrifugal forces, which thereby affect the character of the vibrations themselves. Nevertheless, the approximation is precise enough to explain most of the observed characteristics of molecular spectra.
Figure 2-1 shows the molecule energy levels diagram related to these quantized three terms.

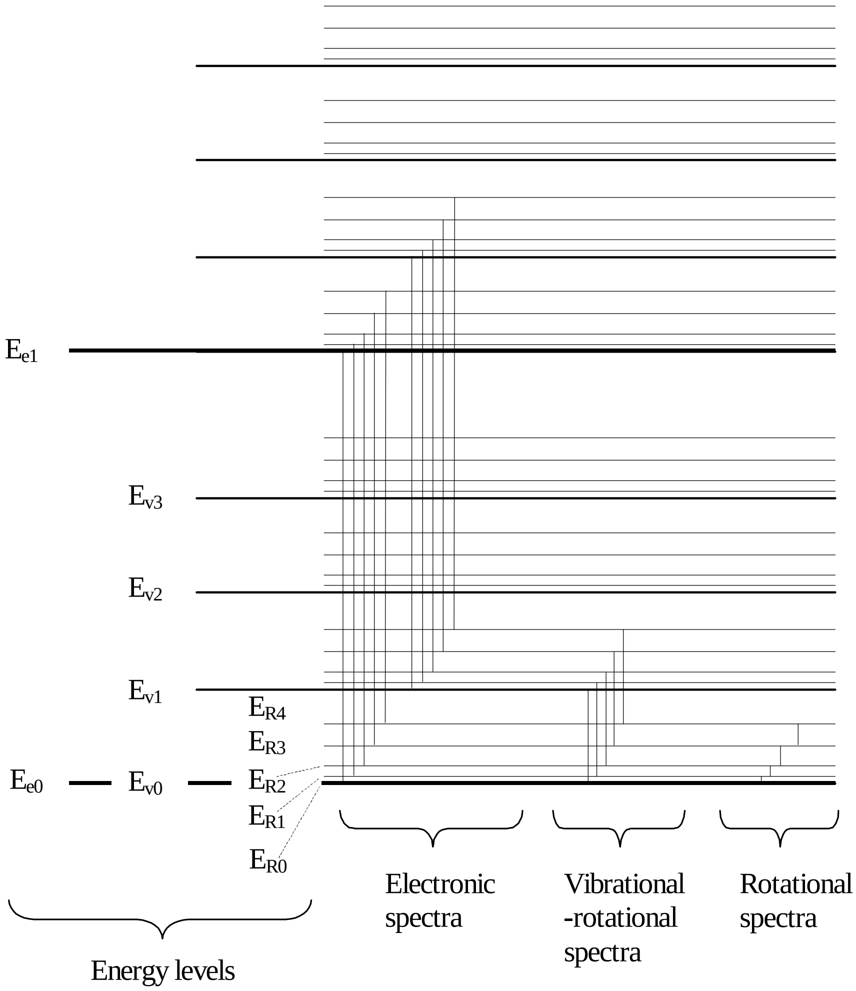

FIGURE 2-1. Grotrian molecule energy levels diagram

The separations between electronic energy levels are usually much larger than those between vibrational energy levels, which in turn are much larger than those between rotational levels [*Herzberg*, 1966]. Associated with each electronic level are a series of vibrational levels, each of which is in turn associated with a series of rotational levels. The close packing of the rotational levels is responsible for the banded structure of molecular spectra.
Transitions between different electronic levels give rise to spectra in the visible or ultraviolet region; these are called electronic spectra. Transitions between vibrational levels within the same electronic state are responsible for spectra in the near infrared, called vibration-rotation spectra. Finally, transitions between rotational levels within the same vibrational state are responsible for the spectra observed in the far infrared.

It can then be seen that the incoming wavelength will be related to the type of interaction. As the photon's energy is given by E = hν, an excitation process induced by a photon wavelength from the far infrared to the ultraviolet will generate respectively a rotational, vibrational or electronic energy level.

2.2.2. The Raman process

Theory

When a light beam passes through a medium, a certain amount is absorbed, another is transmitted, and the remainder (small) scattered in all directions. The scattered light can be studied by observations perpendicular to the direction of the incident beam (Tyndall effect). Most of the light is scattered without change in wavelength (Rayleigh scattering), but there is in addition a small amount of scattered light whose wavelength has been altered. If the incident light is monochromatic, e.g. an isolated atomic spectral line, the scattered spectrum will exhibit a number of lines displaced from the original wavelength. This effect predicted from theory by Smekal was first observed by C. V. Raman and K. S. Krishnan in 1928, and is now commonly called the Raman effect.

The origin of the Raman effect can be briefly explained as follows. Consider that a quantum hν of incident light strikes a molecule. Two solutions are available: - if it is scattered elastically its energy is not changed and the scattered light has the same frequency as the incident light, - if it is scattered inelastically, it can give up energy to the molecule or take up energy from the molecule. This exchanged energy must naturally be in quanta hν', where hν' = E_1 - E_2 is the energy difference between two stationary states E_1 and E_2 of the molecule (for example, two vibrational energy levels). The frequency of the radiation that has undergone Raman scattering will therefore be $\nu'' = \nu \pm \nu'$. The Raman frequency ν' is completely independent of the incident light frequency ν. We can observe pure rotational and vibrational-rotational Raman spectra, which are the counterparts of the absorption spectra in the far and near infrared. The Raman spectra, however, are studied with light sources in the visible or ultraviolet. In many cases the Raman and Infrared (IR) spectra of a molecule complement each other, since vibrations and rotations that are not observable in the IR may be active in the Raman (like the O_2 molecule which has no spectrum in the IR).

From a theoretical point of view, any motion of a molecule system that is connected with a change of its electric dipole moment leads to the absorption or emission of radiation. It is also the case for the electric quadrupole or magnetic dipole moment [*Teller and Jahrb*, 1934], [*Herzberg*, 1950], but their contributions are generally negligible.

The diffusion is linked to the molecular polarizability which traduces the faculty of the molecular system to deform itself and then to acquire an electric dipole moment under the influence of an electric field. The induced dipole moment (the polarization $\vec{P}$) and the electric field $\vec{E}$ are joined by a second order tensor (represented by a symmetric 3x3 matrix), the polarizability $\bar{\bar{\alpha}}$ as following:

$$\vec{P} = \bar{\bar{\alpha}}\vec{E} \qquad \text{(EQ 2.2)}$$

The polarizability term $\bar{\bar{\alpha}}$ is of first importance, and its behavior for the molecule studied can give the Rayleigh effect if it is isotrope (and then the dipolar moment is parallel to the electric field) or the Raman one, as will be shown further, if it varies during a vibration or rotation of the molecule.

To describe this effect the quantum description of the molecule is needed. The quantum state of the molecular system is described by the wave function ψ and takes into account: - the translation of the molecule, - the vibration of the atomic nuclei, - the rotation of the atomic nuclei, - the movement of the electrons around the atomic nuclei, - the electronic and nuclear spin.

The interaction of an electromagnetic wave having an electric field $\vec{E}$ with a molecular system is, in a first approximation, the interaction with the electric dipole moment of the molecule [*Herzberg*, 1950]. If $\hat{P}$ is the hamiltonian of the electric dipole moment $\vec{P}$ of the transition, the matrix elements for a transition between two states *n* and *m* due to this interaction are

$$[P]^{mn} = \int \psi_n^* \hat{P} \psi_m \, d\tau \qquad \text{(EQ 2.3)}$$

The probability of transition can then be deduced as being:

$$\Pi^{mn} \propto \left| [P]^{mn} \right|^2 \qquad \text{(EQ 2.4)}$$

Let us consider first a constant (tensor of) polarizability, e.g. without variation during molecular vibration or rotation. As the wave functions ψ are orthogonals we then can deduce that the integrals of (EQ 2.3) vanish. In this case no molecular change has occurred during the diffusion: the process is an elastic one, often called Rayleigh scattering.

In order for a vibration or rotation to be active in the Raman process, the polarizability must change during the rotation or vibration (the polarizability changes during rotation of any non-spherical molecule). Then depending on which family the molecule belongs to, the selection rules can be given for the Raman case [*Herzberg*, 1950], [*Herzberg*, 1946]. To observe a line in the vibrational-rotational spectra, first condition is that the transition obeys to the vibrational selection rules, in other terms that it belongs to a permitted band. Then the transition has also to obey to the rotational selection rules particular to the considered vibrational band.

By definition, if the molecule is in a lower energy level after the interaction, the transition is of a Stokes type (and the diffused light is shifted to upper wavelengths). On the opposite, the transition is of an anti-Stokes one.

The diatomic linear molecules case $D_{\infty h}$ (like O_2 and N_2):

As shown in Figure 2-2, one vibration mode is possible.

The vibrational allowed transitions follow $\Delta\upsilon = 0, \pm 1, \pm 2, \ldots$, where υ is the vibrational quantum number.

All the transitions are allowed but their intensities decrease as $\Delta\upsilon$ increase. The Stokes bands are much more intenses than the anti-Stokes ones (because the population of the lower energetic level is much more important).

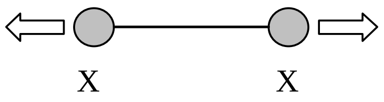

Symmetrical elongation
v_1 mode

FIGURE 2-2. Normal vibrational mode for a diatomic molecule

The rotational allowed transitions follow $\Delta J = 0, \pm 2$ for each vibrational branch, where J represents the rotational quantum number.
ΔJ = -2 corresponds to the O-branch, $\Delta J = 0$ to the Q-branch and $\Delta J = +2$ to the S-branch.

Summary

The transition specified by $\Delta \upsilon = 0$ and $\Delta J = \pm 2$ corresponds to pure rotational Raman scattering. The two correspondent branches are called S-branches.
The transitions specified by $\Delta \upsilon = \pm 1, \pm 2, \ldots$ and $\Delta J = 0, \pm 2$ correspond to vibrational-rotational Raman scattering.
The case $\Delta \upsilon = 0$ and $\Delta J = 0$ naturally corresponds to the Rayleigh case.

The asymmetric rotator family C_{2V} (which include H_2O):
For the vibrational case, as this group has three atoms, 3N-6 = 3 normal vibrational modes are expected. This modes, represented in Figure 2-3 for the H_2O molecule, are in first approximation the symmetrical elongation, the anti-symmetrical elongation and the deformation of the valence angle.

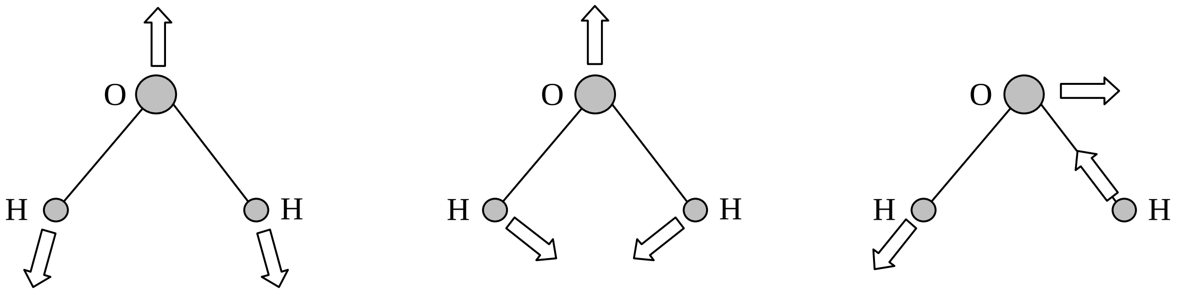

Symmetrical elongation
v_1 mode

Anti-symmetrical elongation
v_2 mode

Deformation
v_3 mode

FIGURE 2-3. Vibrational modes for the H_2O molecule

Each of this vibrational modes follows $\Delta \upsilon_i = 0, \pm 1, \pm 2, \ldots$, but the most probable and important mode is the symmetric elongation one, denoted as the v_1 one.
As for the diatomic case, all the transitions are allowed with decreasing intensities as $\Delta \upsilon_i$ increase. Again the Stokes bands are much more intense than the anti-Stokes ones (because of

the population consideration).
The rotational allowed transitions follows $\Delta J = 0, \pm 1, \pm 2$ for each vibrational branch [*Placzek and Teller*, 1933], [*Herzberg*, 1946].
ΔJ = -1 corresponds to the P-branch and ΔJ = +1 to the R-branch. The other branches (O, Q and S ones) have been defined for the linear molecule case.

Summary
The transition specified by $\Delta \upsilon_i = 0$ and $\Delta J = \pm 1, \pm 2$ corresponds to pure rotational Raman scattering.
The transitions specified by $\Delta \upsilon_i = \pm 1, \pm 2, ...$ and $\Delta J = 0, \pm 1, \pm 2$ correspond to vibrational-rotational Raman scattering.
The case $\Delta \upsilon_i = 0$ and $\Delta J = 0$ naturally corresponds to the Rayleigh case.

Conclusion

Figure 2-4 shows a summary in case of diatomic molecules, and where the term σ denotes the ratio E/hc. For the energy level diagrams only one electronic state (0: the ground state), two vibrational ones (0 and 1) and six rotational ones (0 to 5) are drawn. The Herzberg convention is taken: ‹"› denotes the lower level and ‹'› denotes the upper one. It should also be mentioned that, for clarity, we made the following drawing approximation:

The diagram

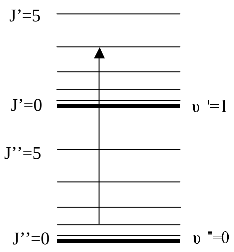

represents

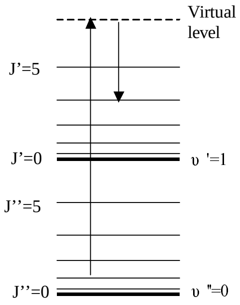

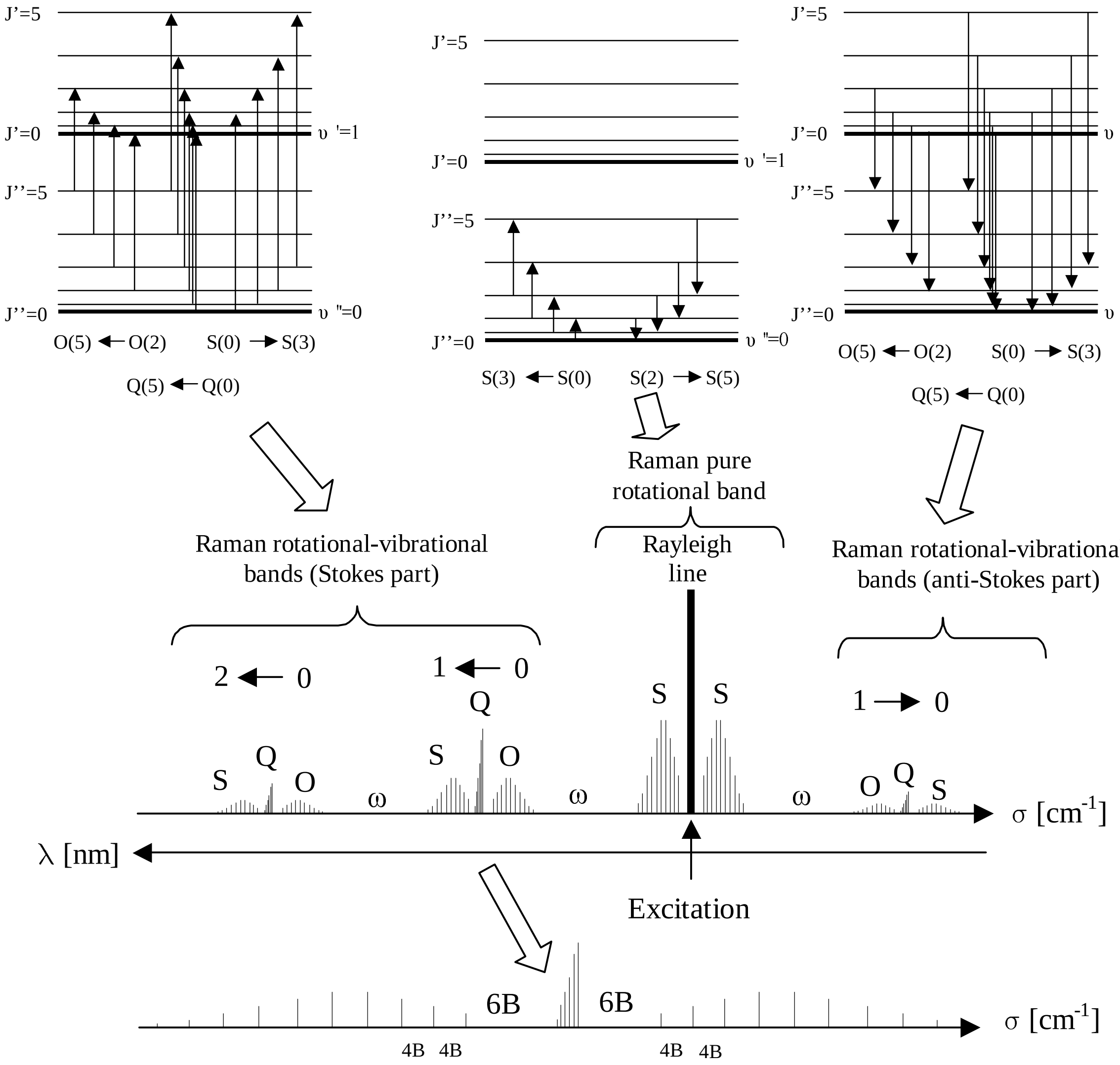

FIGURE 2-4. Summarized scheme for a diatomic molecule in the harmonic case

In this figure the Stokes and anti Stokes branches of the rotational vibrational structure are shown as well as the pure rotational one. Important parameters like the width between lines are put, and an enlargement of the first Stokes band is made to better show the "inside" structure. The structure of the Q-branch is also shown. Often it is considered as a "single" line because the bands are much less spaced than in the O- or S-branches for example. Typically the width of the Q-branch goes from tenths of cm^{-1} to tens of cm^{-1}.

The following Figure 2-5 gives an example of a simulated N_2 Raman spectrum, where the pure rotational part and a vibrational -rotational one are shown. These two graphs are intentionally put with a vertical offset, to allow a continuity in the cross-section axis and to show the relative importance of the different branches.

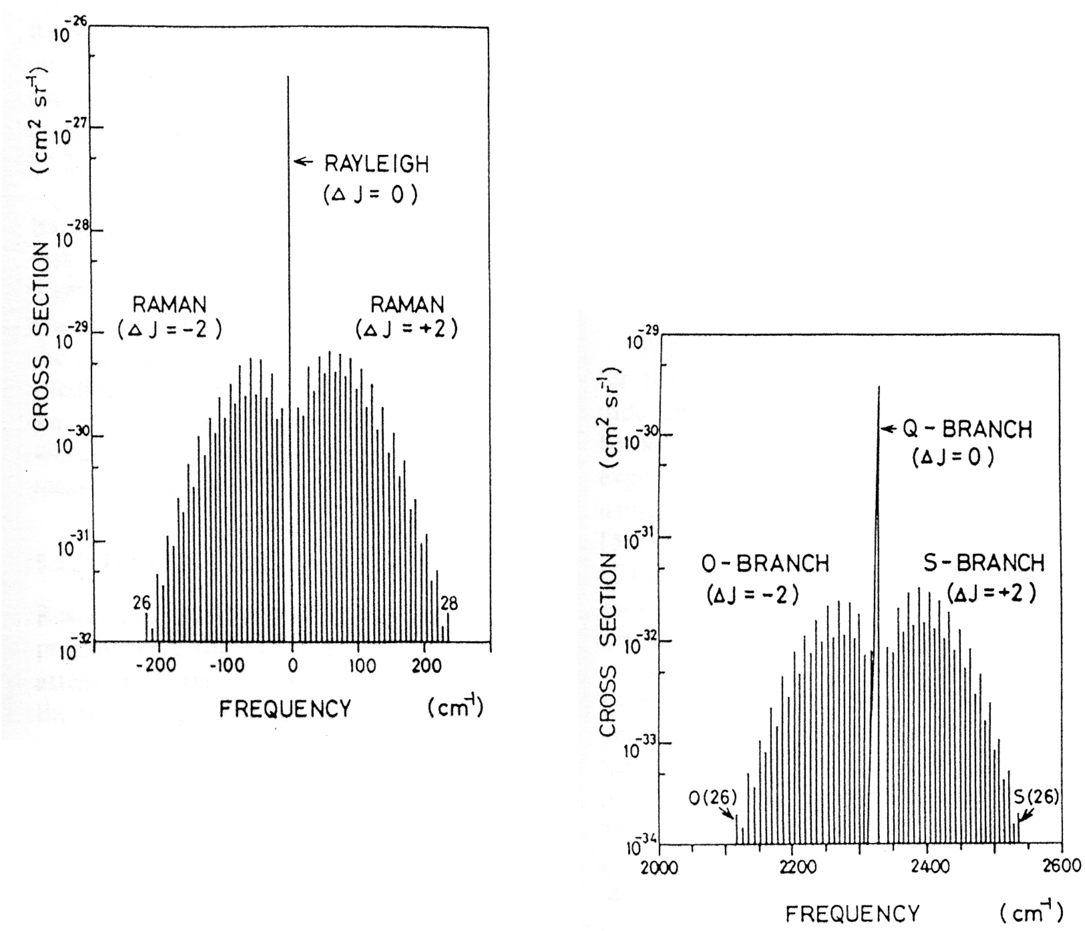

FIGURE 2-5. Calculated distribution of pure rotational Raman spectra (on left) and vibrational-rotational one (on right) in case of a N_2 molecule at 300K, excited at a wavelength of 33.1 nm [*Inaba and Kobayashi,* 1972]

Raman scattering cross-sections

The intensity of a Raman line is determined by the scattering cross-section $\sigma(\ell \rightarrow m)$ of the transition between the energy levels E_ℓ *and* E_m. In case of vibrational-rotational transitions, according to Placzek's polarizability theory [*Placzek,* 1934] the scattering cross-section of a transition $\ell \rightarrow m$ can then be expressed through the matrix elements of the components of the polarizability tensor. The expression for the total vibrational Raman backscattering cross-section of a Stokes shifted vibrational Raman band υ_j (sum of the Q-branch vibrational Raman backscattering cross-section and the O- and S- branches ones) is given by:

$$\frac{d\sigma}{d\Omega}(\upsilon_0) = \frac{(2\pi)^4}{45}\frac{(\upsilon_0 - \upsilon_j)^4 b_j^2}{1-\exp(-hc\upsilon_j / kT)} g_j\left(45a_j^2 + 7\gamma_j^2\right) \qquad \text{(EQ 2.5)}$$

Where υ_j *[cm^{-1}]* is the frequency of the jth vibrational mode of the molecule, $b_j = \left(\frac{h}{8\pi^2 c\upsilon_j}\right)^{\frac{1}{2}}$ is the zero point amplitude of this jth vibrational mode, T *[K]* is the absolute temperature, g_j is the degeneracy of the jth vibrational mode, a_j and γ_j are the isotropic and anisotropic parts of the polarizability tensor derived with respect to the normal coordinates q_j of the normal vibration υ_j .

Usually the N_2 Raman scattering cross-section is taken as a reference and the other Raman cross-sections are then expressed relatively to this one. The unknown parameters of the (EQ 2.5) are experimentaly determined and methods to retrieve the cross-section of a given molecule in a given state are defined by several papers [*Schrötter and Klöckner*, 1979], [*Bischel and Black*, 1983].

2.2.3. Important notes concerning the selection rules and approximations

The selection rules given in the previous paragraph were made under the harmonic hypothesis. In reality molecules do not behave like an ideal harmonic oscillator. The anharmonic effects imply a modification in the vibrational energy levels and also an interaction of the vibration modes in the polyatomic molecules.

By the same way, during the rotation process, the molecule vibration will modify the rotational constants and, as a direct consequence, the vibro-rotational energy levels will be changed. The Coriolis type pertubations, which tend to elongate the molecule, will also give interaction between vibrational modes and then an energy change.

Another important fact that has to be mentioned concerns the transitions between two different electronic energy levels. To illustrate this possibility it will be taken the case of a diatomic molecule with a pure electronic transition, i. e. with the same vibrational and rotational energy levels. Even in this simple case, the vibrational constant ω and the rotational constant B can have very different values in the two different electronic energy levels, and care has to be taken about the calculation of the different line positions.

2.2.4. Application to our case

At atmospheric temperature most molecules are in their vibrational ground state $\upsilon = 0$ (and also the electronic one). The Stokes bands will then be much more important than the anti-Stokes ones. In addition each vibrational line, gives rise to a closely spaced band of lines corresponding to different transitions in the rotational quantum number.

Then, the laser excitation of the O_2, N_2 and H_2O atmospheric molecules due to the laser beam will give essentially the Stokes type transition $\upsilon : 0 \rightarrow 1$.

The Raman displacements from the exciting wavelength, referred to the central frequency of the Q-branch (see paragraph 9.2. “Raman shifted wavelengths calculation”, p 167) are the following: 1555 cm^{-1} for O_2, 2331 cm^{-1} for N_2 and 3652 cm^{-1} for the ν_1 mode of H_2O.

Unlike for the Q-branch, where the temperature has little influence, it has a spreading influence on the O- and S-branches. With a temperature increase the rotational bands will then extend further. For example, the rotational bands relatives to the Q-first Stokes-branch range below 200 cm^{-1} at normal temperature (300 K), and their contribution to the total band intensity is

less than 20 % [*Inaba and Kobayashi*, 1969]. For O_2 this extent is on the range of 150 cm^{-1}. The H_2O case [*Bribes et al.*, 1976] shows a very narrow Q-first Stokes-branch, independent of the temperature and, so, being the only significant contribution to the Raman spectrum.
Following previous developments [*Whiteman et al.*, 1994], [*Bischel and Black,* 1983], the Raman scattering cross-sections relative to the Q-first Stokes-branch are given in the following Table 2-1, for the two pump wavelengths of interest for us.

TABLE 2-1. Raman scattering cross-sections

	Molecular Raman scattering cross-section relatively to the Q branch [$cm^2.sr^{-1}.molec^{-1}$]	
Molecule	KrF laser (248.7 nm)	Nd:YAG laser (266.04 nm)
O_2	$3.99\ 10^{-27}$	$2.33\ 10^{-27}$
N_2	$1.54\ 10^{-27}$	$1.07\ 10^{-27}$
H_2O	$4.79\ 10^{-27}$	$3.33\ 10^{-27}$

These Raman scattering cross-sections are subject to numerous controversies about their experimentally retrieved values [*Faris and Copeland*, 1997], [*Schrötter and Klöckner*, 1979],[*Burris et al.*, 1992], and it will be seen in the following chapters that, "by chance", the exact knowledge of these values is not required. The ozone concentration retrieve does not need at all these values, due to an independence on our temperature ranges giving a null derivative with respect to the altitude. The water vapor mixing ratio retrieve will need them only in the case we choose to calculate the different constants. If the method of an external calibration is used, then there is no need to know these constants.

2.2.5. Differences between Raman scattering, fluorescence and IR absorption processes

We must explain in a few words the difference between Raman scattering and fluorescence. In both cases a light quantum is produced which has a frequency different from that of the incident quantum.
In fluorescence, if the incident light is at an absorption frequency of the system, the quantum *hv* will first be absorbed and then re-emitted as a quantum *hv*", with a shift characteristic to the involved transition. The fluorescence shows an exponential decay which can go to the seconds for the lifetime process.
In Raman scattering, the incident light can be of any frequency, the re-emitted one being shifted from a constant value characteristic to the molecule. The Raman process can be regarded as instantaneous.

Concerning the Raman scattering and the IR absorption, these two processes seem similar in their results, but a little comparison will show the differences [*Brodersen*, 1979]. Talking about the rotational-vibrational spectra, the Raman selection rules are more relaxed than the one for the absorption, giving a significantly larger selection of changes in both rotational and vibrational energy levels. For the intensity distribution in the spectra, even if transitions are allowed in both cases, they can be very different. This is why the two techniques using IR absorption and Raman scattering are so complementary. From a more theoretical point of view differences between the two processes can be easily explained. The fundamental difference lies in the operators: the polarizability used in the Raman's theory is replaced by the permanent dipole moment of the molecule in case of the absorption's one. The intensity parameters are derivative of the polarizability in case of Raman scattering scheme and of the permanent dipole moment in case of the absorption one. Thus, as it cannot be expected that the polarizability and the permanent dipole moment are related in a simple way, these different operators will then imply fundamental differences between the two spectra.

2.3. Raman lidar theory

Here we will present the theory for the ozone concentration and water vapor mixing ratio retrieve, with corrections, by the Raman formalism. Discussion and result presentations will be done in the chapter 4 “Corrections and errors analysis”, p 65, and in the article chapters.

2.3.1. The Raman lidar equation

Atmospheric O_2, N_2 and H_2O molecules induce a specific shift in frequency of the pump laser beam. To each one of the three Raman-shifted wavelengths corresponds a lidar equation [*Measures*, 1992]:

$$P_X(\lambda_L, \lambda_X^{Ram}, R) = P_L(\lambda_L)\, K_X \,\frac{A(R)}{R^2}\, \Delta R\, n_X(R)\, {}^{\pi}\beta_X^{Ram}(\lambda_L, \lambda_X^{Ram}, R)\, T(\lambda_L, R)\, T(\lambda_X^{Ram}, R) \qquad \text{(EQ 2.6)}$$

Where (the index X stands for O_2 , N_2 or H_2O):

$P_X(\lambda_L, \lambda_X^{Ram}, R)$ *[W]* : Raman lidar power backscattered from species X, at Raman-shifted wavelength λ_X^{Ram} and distance R

$P_L(\lambda_L)$ *[W]* : Laser emitted power at wavelength λ_L

K_X *[no unit]* : Instrument constant at Raman-shifted wavelength λ_X^{Ram}

A(R) *[m^2]* : Telescope active surface area

R *[m]* : Range between telescope and atmospheric target

ΔR *[m]* : Range resolution

$n_X(R)$ *[$molec.cm^{-3}$]* : Molecular concentration of the specie X at the distance R

${}^{\pi}\beta_X^{Ram}\left(\lambda_L,\lambda_X^{Ram},R\right)\equiv\dfrac{d\,{}^{\pi}\sigma_X^{Ram}}{d\Omega}$ *[cm^{2}.molec^{-1}sr^{-1}]* : Raman differential backscattering cross-section for species X

$T(\lambda_L,R)\{resp\,T(\lambda_X^{Ram},R)\}$ *[cm^{-1}]* : Atmospheric transmission at the wavelength $\lambda_L\ \{resp\ \lambda_X^{Ram}\}$

The transmission term is described following the Beer-Lambert law. Following what was developed [*Hinkley,* 1976], [*Measures,* 1992] care has to be taken in its limit of application. If the power density is to high, an induced saturation effect appears and the Beer-Lambert law no longer follows an exponential law but a linear one (the absorption decreases which is an effect of the saturation). This effect occurs for a density power in the order of more than 10^7 W.cm^{-2}. If we take the example of the configuration with the Nd:YAG laser we have an energy of 120 mJ in a pulse duration of 6 ns and a beam diameter of 2.4 cm after the three times beam expander. This gives a power density of 0.442x10^7 W.cm^{-2}, a value that is still within the limit of application of the Lambert-Beer law.
In its integrated form we have:

$$T(\lambda_i,R)=\exp\left\{-\int_0^R\alpha^{atmos}(\lambda_i,r)dr\right\}\quad with\ \lambda_i\equiv\lambda_i,\lambda_X^{Raman} \tag{EQ 2.7}$$

Where $\alpha^{atmos}(\lambda_i,r)$ *[cm^{-1}] is the* atmospheric extinction (or attenuation) coefficient at the wavelength λ_i , written by "convention" $\alpha_{attenuation}^{atmos}(\lambda_i,r)\equiv\alpha^{atmos}(\lambda_i,r)$.
We can split the extinction coefficient in the following way:

$$\alpha^{atmos}(\lambda_i,r)=\alpha^{gaz}(\lambda_i,r)+\alpha^{aer}(\lambda_i,r) \tag{EQ 2.8}$$

where $\alpha^{gaz}(\lambda_i,r)$ represents the molecular extinction contribution and $\alpha^{aer}(\lambda_i,r)$ the aerosol extinction contribution to the (total) extinction coefficient.

The molecular contribution
It can be written as follows:

$$\begin{aligned}\alpha^{gaz}(\lambda_i,r)=\alpha^{molecule}(\lambda_i,r)&=\alpha_{inelastic\ scattering}^{molecule}(\lambda_i,r)+\alpha_{elastic\ scattering}^{molecule}(\lambda_i,r)+\alpha_{absorption}^{molecule}(\lambda_i,r)\\&=\alpha_{in\ scatt}^{molec}(\lambda_i,r)+\alpha_{el\ scatt}^{molec}(\lambda_i,r)+\alpha_{abs}^{molec}(\lambda_i,r)\end{aligned} \tag{EQ 2.9}$$

where $\alpha_{el\ scatt}^{molec}(\lambda_i,r)$ {resp. $\alpha_{el\ scatt}^{molec}(\lambda_i,r)$ }represents the extinction contribution due to the molecular elastic scattering {resp. the inelastic scattering}, and $\alpha_{el\ scatt}^{molec}(\lambda_i,r)$ the extinction contribution due to the molecular absorption.
According to Hinkley [*Hinkley,* 1976], the inelastic part is several orders of magnitude lower than the elastic one. This term is then neglected.

Concerning the elastic part, as we are in the condition where the size of the molecule is much smaller than the laser wavelength, the elastic process follows the Rayleigh approximation:

$$\alpha_{el\ scatt}^{molec}(\lambda_i, r) = \alpha_{Rayl}^{molec}(\lambda_i, r) \qquad \text{(EQ 2.10)}$$

The gas absorption term is a sum of contributing terms. Each molecule has its own absorption spectrum which is the result of all the different transitions, electronic, vibrational, rotational..., and is represented by a series of absorption lines. Generally speaking, each line is characterized by three parameters: position, width and intensity. The advantage of the used Raman method stands on the shape of the ozone spectrum in the UV. As this spectrum is large, the line broadening does not have to be considered (Lorentz or Doppler correction). This is valid for the corrections in the ozone and water vapor retrieve due to the absorption of the other gases (see the chapters “The ozone retrieve”, p 42 and “The water vapor retrieve (first formulation)”, p 42).
The molecular absorption coefficient for the group of molecules {Y} $\alpha_{abs}^{molec}(\lambda_i, r)$ *[cm^{-1}]* is defined as follows:

$$\alpha_{abs}^{molec}(\lambda_i, r) = \sum_{\{Y\}} n_Y(r)\sigma_{abs}^{Y}(\lambda_i, r) \qquad \text{(EQ 2.11)}$$

Where $\sigma_{abs}^{Y}(\lambda_i, r)$ *[cm^2.molec^{-1}]* is the molecular absorption cross-section of the molecule Y, and n_Y(r) *[molec.cm^{-3}]* is the volumic concentration of the molecule Y.
The calculation of this term then requires, for each molecule Y, the knowledge of:
- the volumic concentration, which can be deduced from its mixing ratio and the air volumic concentration profile (given by a sounding or a mathematical model like the NOAA one).
- the molecular absorption cross-section for the considered wavelengths. It is given by experiments but not all the atmospheric components were yet studied in the UV. Some molecules are already well known, like O_3 but others like O_2 still cause uncertainties in the UV.

The molecular contribution is then given by:

$$\alpha^{gaz}(\lambda_i, r) = \alpha_{Rayl}^{molec}(\lambda_i, r) + \sum_{\{Y\}} n_Y(r)\sigma_{abs}^{Y}(\lambda_i, r) \qquad \text{(EQ 2.12)}$$

The aerosol contribution
The atmosphere contains also a wide range of particles and aerosols as the simple following experience will show. If we look the atmosphere at a visible wavelength, 550 nm for example, the approximated Rayleigh scattering extinction coefficient given by (EQ 4.27) p 72 in the chapter 4 “Corrections and errors analysis” furnishes a value of α_R = 0.0116 km^{-1} at sea level. A measurement of the atmospheric visibility, the "meteorological range" V_M is given by the Koschmieder relation [*Middleton*, 1952], [*Horvath*, 1971]: $V_M = 3.91 / \alpha$, where α is the total atmospheric extinction coefficient. In a pure Rayleigh atmosphere, where $\alpha = \alpha_R$, the sea level visibility would reach 250 km, which is impossible even in very clear conditions (max. 50 km). This demonstrates that other contributions to the scattering molecular one exist that

are given by the aerosols or the molecular absorption.

The main problem is that aerosol scattering properties become very complex as soon as the particle dimension becomes similar to the wavelength of excitation. A size parameter $\tau = \frac{2\pi a}{\lambda}$ is commonly introduced, with "a" the mean radius of the particle and "λ" the excitation wavelength. As a first approximation the "simple" Rayleigh theory can be still used for $\tau < 0.5$, but as soon as we have $\tau > 0.5$ the complicated Mie theory has to be used.

The aerosol contribution is given by:

$$\alpha^{aer}(\lambda_i, r) = \alpha^{aer}_{scatt}(\lambda_i, r) + \alpha^{aer}_{abs}(\lambda_i, r) \tag{EQ 2.13}$$

The "exact" retrieve of this term is still known nowadays mainly by numerical simulations.

From equations (EQ 2.7) p 39, (EQ 2.8) p 39, (EQ 2.12) follows:

$$T(\lambda_i, R) = \exp\left\{ -\int_0^R \left[\alpha^{aer}(\lambda_i, r) + \alpha^{molec}_{Rayl}(\lambda_i, r) + \sum_Y n_Y(r)\sigma^Y_{abs}(\lambda_i, r) \right] dr \right\} \tag{EQ 2.14}$$

With the Raman backscattered signal equation (EQ 2.6) p 38 and considering the Raman backscattering coefficient as independent of R in the lower troposphere (see chapter 9 “Annex”, p 163) it gives:

$$\begin{aligned} P_X(R) = {} & P_L(\lambda_L)\, K_X\, \frac{A(R)}{R^2} \Delta R\, n_X(R)\, {}^{\pi}\beta^{Ram}_X \\ & \times \exp\left\{ -\int_0^R \left[\begin{aligned} & \alpha^{aer}(\lambda_L, r) + \alpha^{aer}(\lambda^{Ram}_X, r) + \alpha^{molec}_{Rayl}(\lambda_L, r) + \alpha^{molec}_{Rayl}(\lambda^{Ram}_X, r) \\ & + \sum_Y n_Y(r)\left(\sigma^Y_{abs}(\lambda_L, r) + \sigma^Y_{abs}(\lambda^{Ram}_X, r)\right) \end{aligned} \right] dr \right\} \end{aligned} \tag{EQ 2.15}$$

For (future) convenience we group terms to show the $n_{O_3}(r)$ one, taking into account that the ozone absorption cross-section is independent of the distance r (see chapter 9 “Annex”, p 163 for further details):

$$\begin{aligned} P_X(R) = {} & P_L(\lambda_L)\, K_X\, \frac{A(R)}{R^2} \Delta R\, n_X(R)\, {}^{\pi}\beta^{Ram}_X \\ & \times \exp\left\{ -\int_0^R \left[\widetilde{\alpha^{atmos}}(\lambda_L, r) + \widetilde{\alpha^{atmos}}(\lambda^{Ram}_X, r) + n_{O_3}(r)\left(\sigma^{O_3}_{abs}(\lambda_L) + \sigma^{O_3}_{abs}(\lambda^{Ram}_X)\right) \right] dr \right\} \end{aligned} \tag{EQ 2.16}$$

Where

$$\begin{aligned} \widetilde{\alpha^{atmos}}(\lambda_i, r) & \equiv \alpha^{atmos}(\lambda_i, r) - n_{O_3}(r)\sigma^{O_3}_{abs}(\lambda_i) \\ & = \alpha^{molec}_{Rayl}(\lambda_i, r) + \alpha^{aer}(\lambda_i, r) + \sum_{Y' = \{Y - O_3\}} n_{Y'}(r)\sigma^{Y'}_{abs}(\lambda_i, r) \end{aligned} \tag{EQ 2.17}$$

2.3.2. The ozone retrieve

The ozone concentration can be calculated by taking the ratio between the N_2 and O_2 Raman signals with the (EQ 2.16):

$$\frac{P_{N_2}(R)}{P_{O_2}(R)} = \frac{K_{N_2} n_{N_2}(R)\,{}^{\pi}\beta_{N_2}^{Ram}}{K_{O_2} n_{O_2}(R)\,{}^{\pi}\beta_{O_2}^{Ram}} \times \exp\left\{ -\int_0^R \left[\begin{array}{l} \left(\widetilde{\alpha^{atmos}}\left(\lambda_{N_2}^{Ram}, r\right) - \widetilde{\alpha^{atmos}}\left(\lambda_{O_2}^{Ram}, r\right)\right) \\ + n_{O_3}(r)\left(\sigma_{abs}^{O_3}(\lambda_{N_2}^{Ram}) - \sigma_{abs}^{O_3}(\lambda_{O_2}^{Ram})\right) \end{array} \right] dr \right\} \qquad \text{(EQ 2.18)}$$

Then, by taking the derivative of the natural logarithm we finally get, taking into account that the ratio between N_2 and O_2 concentrations is constant in the lower troposphere (giving a null value for its derivative):

$$n_{O_3}(R) = \underbrace{\frac{\dfrac{\partial}{\partial R}\left(\ln \dfrac{P_{N_2}(R)}{P_{O_2}(R)}\right)}{\sigma_{abs}^{O_3}(\lambda_{O_2}^{Ram}) - \sigma_{abs}^{O_3}(\lambda_{N_2}^{Ram})}}_{n_{O_3}^{0\,order}(R)} - \underbrace{\frac{\left(\widetilde{\alpha^{atmos}}\left(\lambda_{O_2}^{Ram}, r\right) - \widetilde{\alpha^{atmos}}\left(\lambda_{N_2}^{Ram}, r\right)\right)}{\sigma_{abs}^{O_3}(\lambda_{O_2}^{Ram}) - \sigma_{abs}^{O_3}(\lambda_{N_2}^{Ram})}}_{\delta_{corr}(O_3)} \qquad \text{(EQ 2.19)}$$

The result is an absolute value, with no need of external reference. We can see that the ozone concentration can mainly be decomposed into two terms.

- The zero-order term, denoted as $n_{O_3}^{0\,order}(R)$, depends on the first derivative of the ratio between two Raman signals (O_2 and N_2). This term, and then the ozone concentration retrieve, is sensitive to the signal to noise ratio.
- The second term, denoted as $\delta_{corr}(O_3)$, is a source of systematic errors. It groups the Rayleigh and Mie scattering as well as the absorption (without O_3) one, for the O_2 and N_2 Raman shifted wavelengths. This term has been taken into account for the data treatment and, as we will see in the paragraph 4.3. “Corrections”, p 81, it can be of importance in certain atmospheric conditions.

2.3.3. The water vapor retrieve (first formulation)

The water vapor mixing ratio, in *[g H_2O / g_dry air]*, is defined by

$$\xi_{H_2O}^{(N_2)}(R) = \left.\frac{\text{Mass of H}_2\text{O}}{\text{Mass of dry air}}\right|_{\text{given volume}} = \frac{M_{H_2O}N_{H_2O}(R)}{M_{dry\,air}N_{dry\,air}(R)} = \frac{n_{H_2O}}{n_{N_2}}(R)\times\frac{M_{H_2O}}{M_{dry\,air}}\times\chi_{N_2} \qquad \text{(EQ 2.20)}$$

where M_X *[g.mol^{-1}]* is the molecular weight, N_X *[mole.cm^{-3}]* is the number of moles per volume, n_X *[molec.cm^{-3}]* is the number of molecules per volume (i.e. concentration). This is entirely related to the species X, including the dry air one. χ_{N_2} *[%]* is the percentage of nitrogen in dry air, which is constant in the lower troposphere.

The term (N_2) in the upper index denotes the fact that we take the calculation relatively to the

nitrogen.
Taking the ratio of the H_2O Raman shifted signal to the Raman N_2 shifted signal with (EQ 2.16) p 41 yields to the following expression:

$$\begin{aligned} \frac{P_{H_2O}(R)}{P_{N_2}(R)} &= \frac{K_{H_2O}\, n_{H_2O}(R)\, {}^{\pi}\beta^{Ram}_{H_2O}}{K_{N_2}\, n_{N_2}(R)\, {}^{\pi}\beta^{Ram}_{N_2}} \\ &\quad \times \exp\left\{ -\int_0^R \left[\begin{array}{l} n_{O_3}(r)\left(\sigma^{O_3}_{abs}(\lambda^{Ram}_{H_2O}) - \sigma^{O_3}_{abs}(\lambda^{Ram}_{N_2})\right) \\ + \left(\widetilde{\alpha^{atmos}}\left(\lambda^{Ram}_{H_2O}, r\right) - \widetilde{\alpha^{atmos}}\left(\lambda^{Ram}_{N_2}, r\right)\right) \end{array} \right] dr \right\} \end{aligned} \tag{EQ 2.21}$$

And, it gives with (EQ 2.20):

$$\begin{aligned} \xi^{(N_2)}_{H_2O}(R) &= \frac{M_{H_2O}}{M_{dry\ air}}\, \chi_{N_2}\, \frac{P_{H_2O}}{P_{N_2}}(R)\, \frac{K_{N_2}}{K_{H_2O}}\, \frac{{}^{\pi}\beta^{Ram}_{N_2}}{{}^{\pi}\beta^{Ram}_{H_2O}} \\ &\quad \times \exp\left\{ \int_0^R \left[\begin{array}{l} \left(\sigma^{O_3}_{abs}(\lambda^{Ram}_{H_2O}) - \sigma^{O_3}_{abs}(\lambda^{Ram}_{N_2})\right) n_{O_3}(r) \\ + \left(\widetilde{\alpha^{atmos}}\left(\lambda^{Ram}_{H_2O}, r\right) - \widetilde{\alpha^{atmos}}\left(\lambda^{Ram}_{N_2}, r\right)\right) \end{array} \right] dr \right\} \end{aligned} \tag{EQ 2.22}$$

In contrast to the ozone concentration retrieve, the water vapor mixing ratio retrieve depends linearly upon the ratio of the Raman H_2O signal to the Raman N_2 signal. It makes this retrieve less sensitive to noise than the ozone one. But this method is not self calibrated and the exact knowledge of K_X or an independent measurement for instrument calibration is needed.
We can write (EQ 2.22) in a more explicit manner to show the different contributions:

$$\begin{aligned} \xi^{(N_2)}_{H_2O}(R) &= \frac{M_{H_2O}}{M_{dry\ air}}\, \chi_{N_2}\, \frac{P_{H_2O}}{P_{N_2}}(R)\, \frac{K_{N_2}}{K_{H_2O}}\, \frac{{}^{\pi}\beta^{Ram}_{N_2}}{{}^{\pi}\beta^{Ram}_{H_2O}} \qquad \leftarrow \text{zero-order} \\ & \left.\begin{array}{ll} \times\exp\left\{ \left(\sigma^{O_3}_{abs}(\lambda^{Ram}_{H_2O}) - \sigma^{O_3}_{abs}(\lambda^{Ram}_{N_2})\right) \int_0^R n_{O_3}(r)\,dr \right\} & \leftarrow O_3 \text{ interference} \\ \times\exp\left\{ \int_0^R \left(\widetilde{\alpha^{atmos}}\left(\lambda^{Ram}_{H_2O}, r\right) - \widetilde{\alpha^{atmos}}\left(\lambda^{Ram}_{N_2}, r\right)\right) dr \right\} & \leftarrow \text{Other interferences} \end{array} \right\} \delta_{corr}(H_2O) \end{aligned} \tag{EQ 2.23}$$

- The zero-order term gives the H_2O mixing ratio retrieve, supposing that no Rayleigh, Mie or absorption contribution is significant. In general this unique term is not sufficient, specially in the UV wavelength region of interest for us, where the ozone absorption is important.
- The corrective term, denoted as $\delta_{corr}(H_2O)$, can be divided into two contributions. The main one comes from the ozone absorption influence on the H_2O and N_2 Raman signals and can affect significantly the final results [*Renaut et al.*, 1980]. This factor can be calculated with another additional Raman signal, as we will see later in this paragraph. The factor denoted as "other interferences" takes into account all the atmospheric influences, without the O_3

absorption one, on the H_2O and N_2 Raman signals, by scattering (Rayleigh or Mie) and absorption. Its influence on two typical schemes (remote and urban area) is studied in the paragraph 4.3. “Corrections”, p 81.

The ozone interference on the water vapor Raman lidar retrieve

Two methods can be used to retrieve the "ozone corrective term" $\left(\sigma_{abs}^{O_3}(\lambda_{H_2O}^{Ram})-\sigma_{abs}^{O_3}(\lambda_{N_2}^{Ram})\right)n_{O_3}(r)$ in (EQ 2.22).

The first one can be done with an independent ozone measurement, such as with a balloon for example, but is not convenient for practical purposes and therefore is more suitable for calibration and verification of the lidar system.

The second one takes advantage of the three Raman backscattered signals (from O_2, N_2 and H_2O) we have. The integrated ozone corrective term is calculated on the same scheme as for the previous ozone concentration retrieve.

Taking the ratio $\dfrac{P_{O_2}(R)}{P_{N_2}(R)}$ of the O_2 and N_2 Raman signals gives us, with (EQ 2.16) p 41:

$$\frac{P_{O_2}(R)}{P_{N_2}(R)}=\frac{K_{O_2}n_{O_2}(R)\,{}^{\pi}\beta_{O_2}^{Ram}}{K_{N_2}n_{N_2}(R)\,{}^{\pi}\beta_{N_2}^{Ram}} \times\exp\left\{-\int_0^R\left[\begin{matrix} n_{O_3}(r)\left(\sigma_{abs}^{O_3}(\lambda_{O_2}^{Ram})-\sigma_{abs}^{O_3}(\lambda_{N_2}^{Ram})\right) \\ +\left(\widetilde{\alpha^{atmos}}\left(\lambda_{O_2}^{Ram},r\right)-\widetilde{\alpha^{atmos}}\left(\lambda_{N_2}^{Ram},r\right)\right)\end{matrix}\right]dr\right\} \qquad \text{(EQ 2.24)}$$

The integrated ozone term of interest can then be deduced:

$$\exp\left\{\int_0^R n_{O_3}(r)dr\right\}=\left(\frac{P_{O_2}}{P_{N_2}}(R)\right)^{\frac{1}{\sigma_{abs}^{O_3}\left(\lambda_{N_2}^{Ram}\right)-\sigma_{abs}^{O_3}(\lambda_{O_2}^{Ram})}}\left(\frac{K_{N_2}}{K_{O_2}}\frac{n_{N_2}}{n_{O_2}}\frac{{}^{\pi}\beta_{N_2}^{Ram}}{{}^{\pi}\beta_{O_2}^{Ram}}\right)^{\frac{1}{\sigma_{abs}^{O_3}\left(\lambda_{N_2}^{Ram}\right)-\sigma_{abs}^{O_3}(\lambda_{O_2}^{Ram})}} \times\exp\left\{-\frac{\int_0^R\left[\widetilde{\alpha^{atmos}}\left(\lambda_{N_2}^{Ram},r\right)-\widetilde{\alpha^{atmos}}\left(\lambda_{O_2}^{Ram},r\right)\right]dr}{\sigma_{abs}^{O_3}\left(\lambda_{N_2}^{Ram}\right)-\sigma_{abs}^{O_3}(\lambda_{O_2}^{Ram})}\right\} \qquad \text{(EQ 2.25)}$$

Further, by combining (EQ 2.22) and (EQ 2.25), the water vapor mixing ratio is given by:

$$\xi_{H_2O}^{(N_2)}(R)=K_{cal}^{N_2}\frac{P_{H_2O}(R)}{P_{N_2}(R)}\left[\frac{P_{O_2}(R)}{P_{N_2}(R)}\right]^{\hat{\Delta}\sigma_{abs}^{O_3}} \times\exp\left\{\int_0^R\left[\left(\widetilde{\alpha^{atmos}}\left(\lambda_{H_2O}^{Ram},r\right)-\widetilde{\alpha^{atmos}}\left(\lambda_{N_2}^{Ram},r\right)\right)-\hat{\Delta}\sigma_{abs}^{O_3}\left(\widetilde{\alpha^{atmos}}\left(\lambda_{N_2}^{Ram},r\right)-\widetilde{\alpha^{atmos}}\left(\lambda_{O_2}^{Ram},r\right)\right)\right]dr\right\} \qquad \text{(EQ 2.26)}$$

with $\widehat{\Delta}\sigma_{abs}^{O_3} = \frac{\sigma_{abs}^{O_3}(\lambda_{H_2O}^{Ram}) - \sigma_{abs}^{O_3}(\lambda_{N_2}^{Ram})}{\sigma_{abs}^{O_3}(\lambda_{N_2}^{Ram}) - \sigma_{abs}^{O_3}(\lambda_{O_2}^{Ram})}$ and where the constant $K_{cal}^{N_2}$ is defined as:

$$K_{cal}^{N_2} = \frac{M_{H_2O}}{M_{dry\ air}} \chi_{N_2} \frac{K_{N_2}}{K_{H_2O}} \frac{{}^{\pi}\beta_{N_2}^{Ram}}{{}^{\pi}\beta_{H_2O}^{Ram}} \left(\frac{K_{N_2}}{K_{O_2}} \frac{n_{N_2}}{n_{O_2}} \frac{{}^{\pi}\beta_{N_2}^{Ram}}{{}^{\pi}\beta_{O_2}^{Ram}} \right)^{\widehat{\Delta}\sigma_{abs}^{O_3}} \qquad \text{(EQ 2.27)}$$

This constant can be determined by calculation if the K_X terms are known, or by an external calibration.

2.3.4. The water vapor retrieve (second formulation)

With the same nomenclature as in (EQ 2.20) p 42, we can also define the water vapor mixing ratio relatively to the air oxygen content:

$$\xi_{H_2O}^{(O_2)}(R) = \left.\frac{\text{Mass of H}_2\text{O}}{\text{Mass of dry air}}\right|_{\text{given volume}}(R) = \frac{M_{H_2O}N_{H_2O}(R)}{M_{dry\ air}N_{dry\ air}(R)} = \frac{n_{H_2O}}{n_{O_2}}(R) \times \frac{M_{H_2O}}{M_{dry\ air}} \times \chi_{O_2} \qquad \text{(EQ 2.28)}$$

where $\chi_{O_2} \simeq 1 - \chi_{N_2}$ *[%]* is the percentage of oxygen in dry air.

Taking the ratio between the two water vapor mixing ratio retrieve given by (EQ 2.20) p 42 and (EQ 2.28) gives:

$$\frac{\xi_{H_2O}^{(N_2)}(R)}{\xi_{H_2O}^{(O_2)}(R)} = \frac{\chi_{N_2}}{\chi_{O_2}} \frac{n_{O_2}}{n_{N_2}} \equiv 1 \qquad \text{(EQ 2.29)}$$

The water vapor mixing ratio can then be retrieved either with the N_2 or O_2 Raman signal, and Figure 2-6 illustrates this behavior. The files are taken from the second intercomparison measurement campaign in the EPFL on April 08th, 2000 with the lidar ran in the Nd:YAG configuration. The averaged file, treated in photon counting mode, corresponds to the 11h30-12h measurements (4 x 4000 shots). The binning is taken equal to 2 and, with the sliding average, the resulting range resolution is 22 m. The first measurement point is at 308 m.

This interesting behavior is possible with three Raman signals, i.e. with the O_3 interference (auto-) correction on the H_2O mixing ratio retrieve calculated by means of the lidar. In this figure we can see the same mixing ratio retrieve for both O_2 and N_2 calculation, and a slightly higher statistical error (see paragraph 4.5. “Statistical errors”, p 89 for definition of the terms) with the O_2 case due to the weaker O_2 Raman backscattered signal.

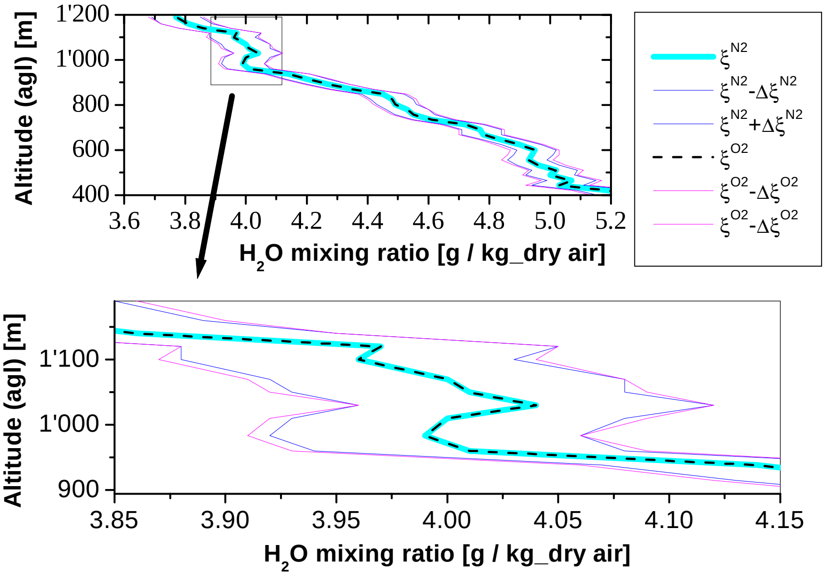

FIGURE 2-6. Comparison between the H_2O mixing ratio retrieved with the N_2 or O_2 Raman signal

Chapter 3

Experimental part

The last version of the Raman lidar system is described, different tests are shown and a characteristics table summarizes the essential properties of the system.

After a general experimental layout, the Raman system is described step by step from the laser sources to the acquisition of the backscattered signals in the PC. Focuses on the bandpass filters, to show their optical behaviors, and also on the special optical configuration used in front of the PMTs to decrease the spatial inhomogeneity are proposed.
The main tests which were performed on the system to assess its reliability are shown. Among these, we will show the polychromator dispersion verification, the relative sensitivity of the PMTs or the crosstalk measurements.
The essential characteristics of the different elements composing the system are summarized at the end of the chapter in a convenient table.

3.1. System description

The Figure 3-1 shows the general layout of the final Raman system. The main technical characteristics are presented in paragraph 3.5. “Raman lidar specifications table”, p 60.

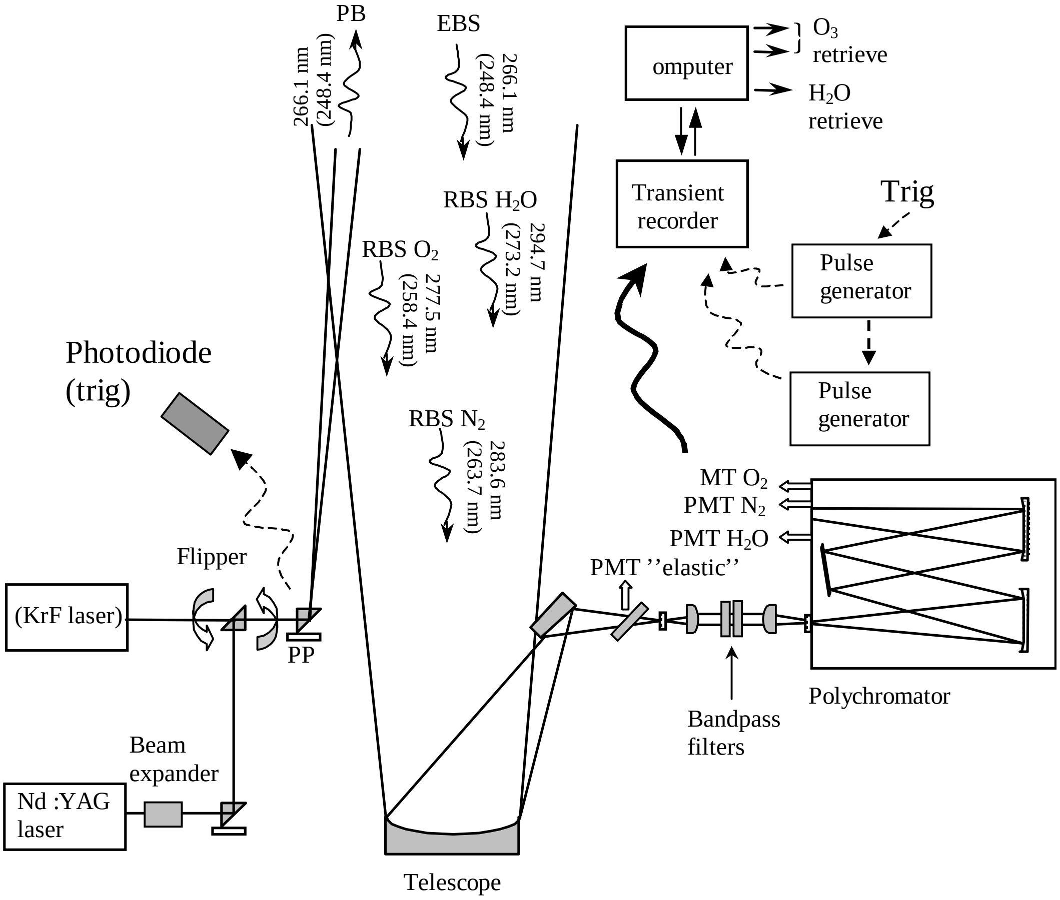

FIGURE 3-1. The experimental layout

The Raman lidar for the O_3 concentration and H_2O mixing ratio measurements was operated with two different laser sources, a 4th harmonic Nd:YAG and a KrF one. The KrF was used with a positive branch unstable resonator for reducing the beam divergence. The Nd:YAG beam was expanded three times before emitting to reduce the initial 0.50 mrad divergence to 0.17 mrad. The laser beam selection is made with a right angle prism mounted on a flipper. The selected beam is then emitted into the atmosphere via a right angle prism mounted on a piezo electric controlled stage. In the KrF configuration, the laser beam goes straight through this final prism, but for the Nd:YAG configuration, another right angle prism mounted on a piezo electric controlled stage was used before the flipper. This ensures an independent alignment of both emitting systems and the ability to move from one to the other more rapidly and without major realignments.

After atmospheric interactions, the backscattered signals are collected by a Newtonian-type telescope based on an off-axis paraboloid primary mirror.

The optical receiver, shown in Figure 3-2, ensures the spectral separation of the elastic backscattered signal and also the O_2, N_2 and H_2O Raman backscattered ones.

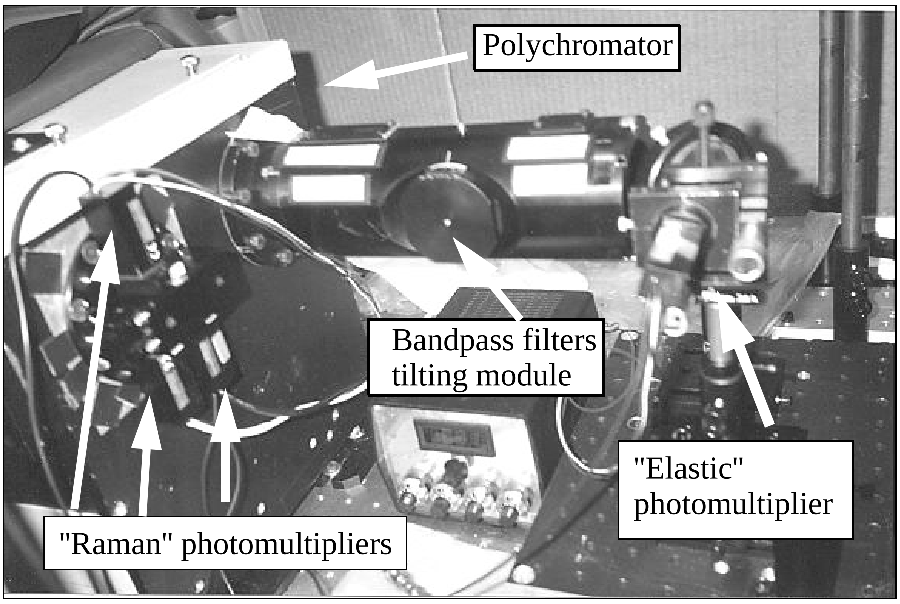

FIGURE 3-2. View of the receiver after the telescope

First separation is made with a 45° oriented fused silica window which allows to inject a fraction of the elastic backscattered signal into a PMT. This elastic signal permits to make a comparison with the Raman signals in case of clouds (test for elastic leakage in the Raman channels) or gives the possibility to retrieve the aerosol extinction coefficient.
To separate the O_2, N_2, H_2O Raman signals, a more complicate system has to be used. The main problems are the very weak Raman signals and the rejection of the strong elastic backscattered signal. A first step is made inside the "bandpass filters tube" shown in Figure 3-3.

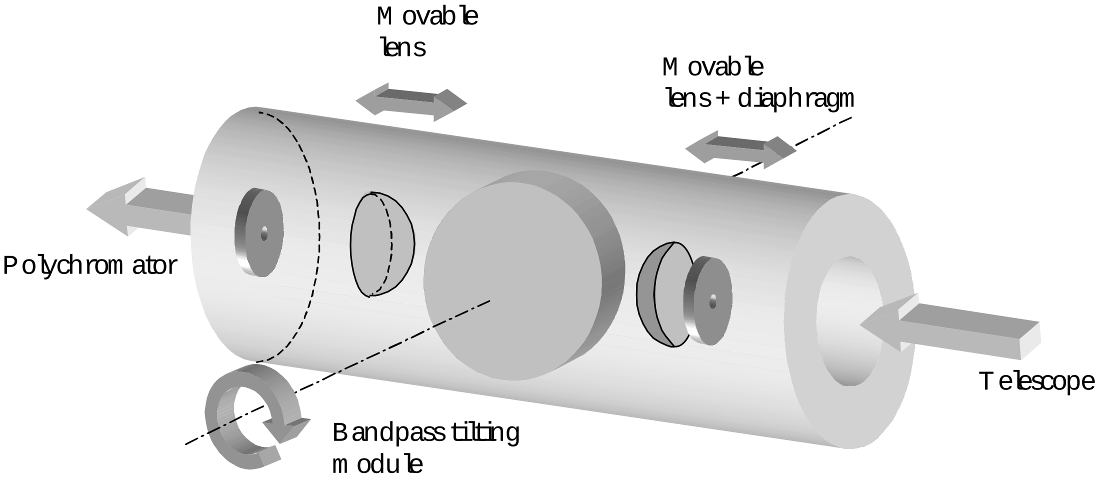

FIGURE 3-3. The bandpass filters tube

The numerical apertures (F numbers) of the receiving telescope and of the polychromator are fitted with a system of two (positive plano convex) lenses. To allow a fine adjustment, the set called "lens + diaphragm" and the second one called "lens" can be translated. A circular diaphragm in front of the entrance lens and near to the focal plane of the telescope defines the field of view of the receiver. A second diaphragm placed at the entrance of the polychromator slit reduces the level of the scattered light leaking into the polychromator. The bandpass filters, mounted inside the "bandpass module", are placed into the parallel beam between the two lenses and, to insure a good rejection of the elastic part, two identical bandpass filters are used together. This module can be tilted, if necessary, to tune the bandpass filter spectral response. For convenience two of these pieces have been made, one for Nd:YAG and one for KrF. Thus going from one to the other configuration just requires to plug in the right bandpass module, which is safer and quicker. After this first filtering, the received signal passes through a solar blind filter for an additional suppression of the daylight background and then enters the polychromator. This latter performs a spectral separation, allowing to detect separately the three Raman backscattered signals. It also acts as a filter to additionally reject the residual elastic signal and daylight. The three Raman signals are detected simultaneously by three Hamamatsu photodetector modules and acquired by three transient recorders. Figure 3-4 shows a detailed view of the photomultipliers reception module.

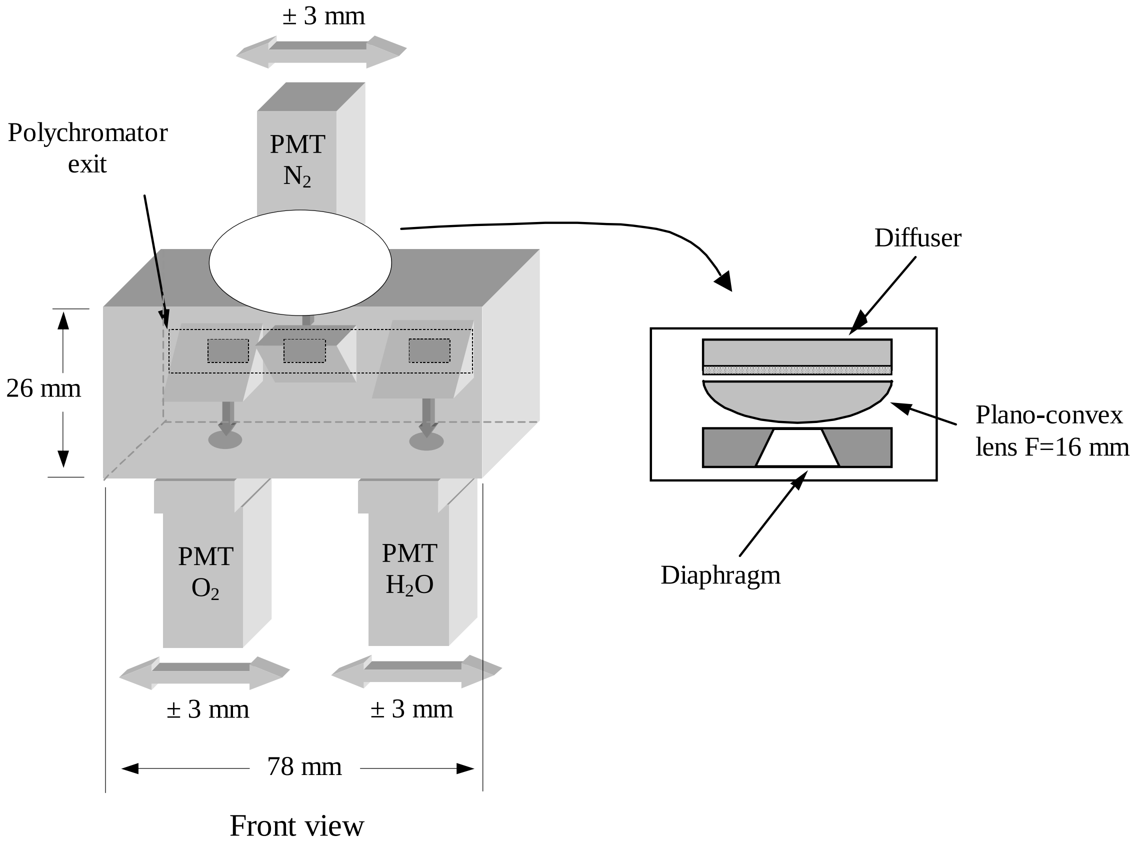

FIGURE 3-4. Detailed sketch of the photomultipliers module part

Each PMT can be displaced linearly of ± 3 mm from a central position, calculated for the

Nd:YAG configuration. This allows the possibility to: - make a fine alignement of the PMTs' positions in order to set the optimum Raman signal intensities,- pass from the Nd:YAG configuration to the KrF one (due to the different pump wavelengths, the resulting Raman signals are not at the same place). Each PMT uses a special optical configuration in front of it, to overcome its spatial uniformity problem (see the paragraph 3.3. “The photosensor modules”, p 53).

The transient recorders are controlled via a NI-DAQ (National Instruments Data Acquisition) card installed in a PC and working under a LabVIEW program. The trig used to monitor the different transient channels is given by a photodiode which takes the scattered light from the last prism before it is emitted in the atmosphere. This initial pulse then goes through two pulse generators (two channels each) which ensure suitable TTL levels for triggering the transient recorders. The advantage of the pulse generator use stands in the possibility to accurately tune the position and width of the transient channel trigs, and then to have identical ones. The program, shown in annex, allows us to visualize in real time the signals, criteria parameters and raw retrieves for the ozone concentration and the water vapor mixing ratio.

3.2. Bandpass and solar blind filters

One of the main problems is the strong elastic backscattered signal that could leak inside the Raman channels. The polychromator rejects this elastic signal by a factor of 10^5. Custom designed bandpass filters were used for each of the two (pump) laser sources, with specifications that are shown in Figure 3-5 for the KrF eximer laser source and in Figure 3-6 for the Nd:YAG 4th harmonic laser source. These bandpass filters enable the three Raman backscattered signals from O_2, N_2 and H_2O to be transmitted, and strongly reject the unwanted elastic contribution (backscattered and residual). In paragraph 3.4.4. “Crosstalk measurements”, p 58 we will describe the method and the measurement results of this elastic crosstalk with the Raman channels.

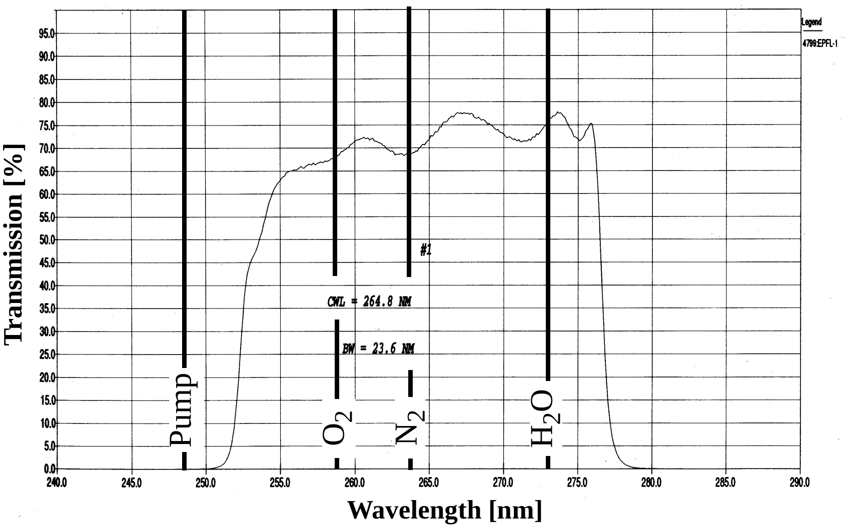

FIGURE 3-5. Wavelength transmission dependence for the KrF bandpass filter

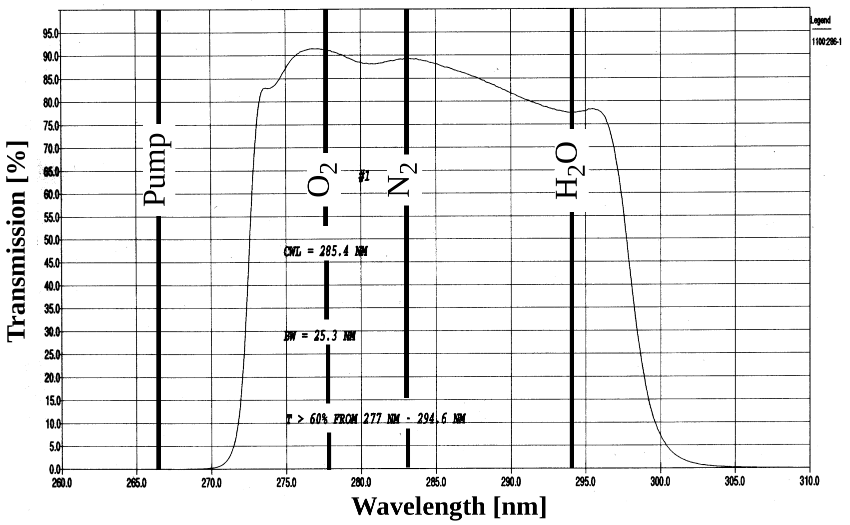

FIGURE 3-6. Wavelength transmission dependence for the Nd:YAG bandpass filter

In these two graphs (Figure 3-5 and Figure 3-6) are drawn the positions of the pump wavelengths and the Raman backscattered ones. For the KrF case, the pump wavelength is at 248.7 nm and the Raman shifted wavelengths for O_2, N_2 and H_2O are respectively at 258.70 nm, 264 nm and 273.54 nm. For the Nd:YAG case, the pump wavelength is at 266.04 nm and the Raman shifted wavelengths for O_2, N_2 and H_2O are respectively at 277.52 nm, 283.63 nm and 294.67 nm. The transmission is always higher than 65 % in the Raman spectral window (the region where the three Raman wavelengths are detected) for the KrF case, and 75 % for the Nd:YAG one. In both cases the Raman spectral window is far enough from the edges of the filter, allowing small variations in the Raman wavelengths, or shifts due to tilting or temperature.

For an additional suppression of the visible part of the daylight spectra, a solar blind filter was used. The experiment shows that using this filter enables a better ozone concentration retrieve.

Concerning the bandpass filters choice, two main possibilities were available:

- First solution was to choose a bandpass filter with a wide cutting region besides the Raman window. The major problem (apart its higher price) was its low efficiency compared to the solution described below.
- Second solution consisted in a "narrow" bandpass filter that just fits the "Raman window". It gives a much higher efficiency than with the first solution and by adding a solar blind filter, the solar background is rejected without too much transmission losses in the Raman window. The second solution was chosen for our experiment.

A useful effect of a bandpass filter is illustrated in the Figure 3-7. It shows the wavelength shift response of a bandpass filter as a function of the angle of incidence. The O° case corresponds at normal angle of incidence, and so on. This shift goes in the direction of shorter wavelengths as soon as the angle of incidence of the beam is tilted out of the normal. An approximation of this angle effect can be calculated as follows [*Spectrogon_manual*, 16th edition]:

$$\lambda_\theta = \lambda_0 \left(n_e^2 - \sin^2\theta\right)^{1/2} n_e^{-1} \qquad \text{(EQ 3.1)}$$

Where λ_θ *[nm]* is the resulting shifted wavelength for a bandpass filter tilting angle θ *[°]* and an initial wavelength λ_0 *[nm]*. n_e *[dimensionless]* is the effective index of the filter.
Nevertheless for angles of incidence over 30°, transmission will decrease greatly and distortion of the bandpass filter response will occur. This "angle-shift" behavior was used with our first set of bandpass filters, in a Nd:YAG configuration, as their bandpass shape didn't fit the Raman window made by the O_2, N_2 and H_2O wavelengths as drawn in Figure 3-7. A suitable angle of 18° was then used (see for example the IJEAC article in chapter 5, p 99).

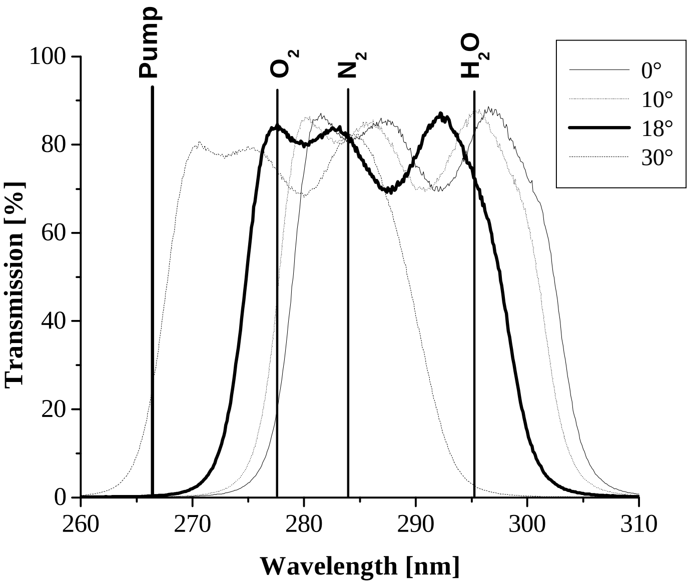

FIGURE 3-7. Wavelength shift as a function of the tilting angle (Omega filter for the first Nd:YAG configuration)

The temperature dependence [*Spectrogon_manual*, 16th edition] is very small and the observed shift, expressed in nm / °C, is in the order of 0,01 nm /°C. This effect can then be neglected in our conditions if we take, as for the cross-section (non) dependence with the distance, a difference on temperature of approximately 40°.

3.3. The photosensor modules

One of the most important error source comes from the PMT [*Measures*, 1992]. In our initial experiments we used Thorn EMI classical type glass-bulb / head on photomultiplier tubes, 9829 QB series. Though they have a high sensitivity (about ten times more than the Hamamatsu metal package PMT, 5783-06 and 6780-06 series we use now), main disadvantages are their relative big size and, worse, the fact they have shown to induce an after pulse effect.

The final design was made with compact photosensor modules from Hamamatsu (22 x 22 x 50 mm) which have a time response about ten times faster (0.78 ns) than the Thorn EMI ones . Due to a new dynode design, the after pulse effect is negligible, but the PMT shows very poor spatial uniformity. This latter characteristic of a PMT is defined as the variation of its sensitivity with the position of an incident light on the photocathode. The use of a PMT with spatial nonuniformity for detecting the lidar signals can cause artifacts, because different areas of the photocathode detect the signal from different distances. The lidar systems that work at short distances, as our lidar, are affected more by this effect. This is due to the bigger dislocations and variations in size, with the distance, of the image of the probed air volume on the photocathode. The extensive experiments made in our laboratory [*Simeonov et al.*, 1999] have shown that the spatial nonuniformity of this photosensor can be significant, as illustrated in Figure 3-8.

This figure shows the measured spatial uniformity of the Hamamatsu H5783-06 photosensor module, alone, used in the detection channel. The twelve important maximums in the sensitivity correspond to the entrances of the most centrally positioned multipliers. The contribution of the four peripherical multipliers is smaller and the maximums caused by them are not as well distinguished as the others. The central minimum that separates the twelve main maximums into two pairs of six is due to the central wire that passes through the focusing electrode and the dynodes. The normalized spatial uniformity of the active area with a diameter of 8 mm (resp. 2 mm) can vary from 0.2 to 2.8 times (resp. 0.7 to 1.4) the average value defined for the central part of the PMT (2 x 2 mm).

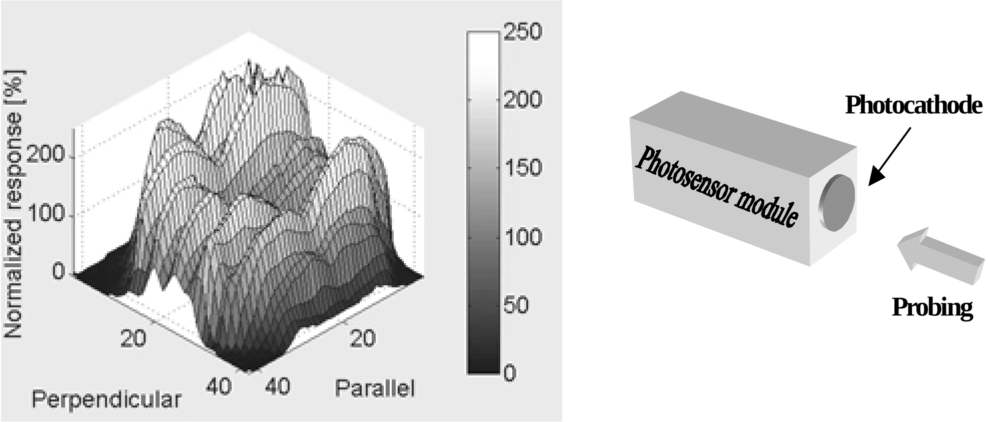

FIGURE 3-8. Anode spatial uniformity of a Hamamatsu H5783-06 photosensor module

As with this «all-sealed-PMT» we cannot play with the different PMT electrode voltages [*dos Santos et al.*, 1996], other solutions were investigated. The first one deals with the influence of the PMT orientation on the retrieved signal. So, by rotating the PMT on its main axis, it will enable a better retrieved signal value. The second, and preferred solution, attempts to improve the spatial uniformity of the PMT itself. Figure 3-9 shows the result obtained with a special optic configuration (a plano-convex lens F = 16mm and a 3 mm thickness diffuser grounded with abrasive mesh 600) set in front of the PMT. In this case the variations of this area uniformity are between 0.9 and 1.45 times the average of the central zone. The 3 mm central part has a uniformity better than 2 % and the one within a 7 mm ring better than 10 %. In this configu-

ration the PMT efficiency is reduced by approximately 45 %.
This optical configuration was utilized in front of each one of the three PMTs used for the three Raman backscattered signals. Additionally, a circular diaphragm was set before this configuration, as shown in the enlargement part of the Figure 3-4, p 50. It ensures a higher background light rejection and its diameter was experimentally determined in order not to cut the Raman backscattered signal

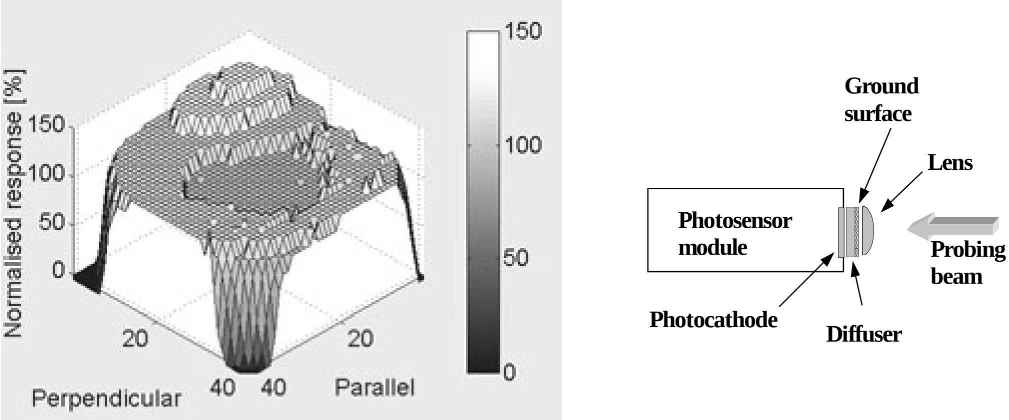

FIGURE 3-9. Anode spatial uniformity of a Hamamatsu H5783-06 photosensor module WITH a diffuser AND a lens

3.4. Tests

Before the real lidar measuraments were made, several laboratory tests of the receiving part were performed to confirm the theoretical investigations and to analyze the different sensitive elements of the system. These tests include the polychromator dispersion and crosstalk, the relative PMT sensitivities, the suppression of the laser line, and the positions of the output channels measurments. In figure Figure 3-10 a view of the experiment is shown, with the Raman cell used for several of these tests.

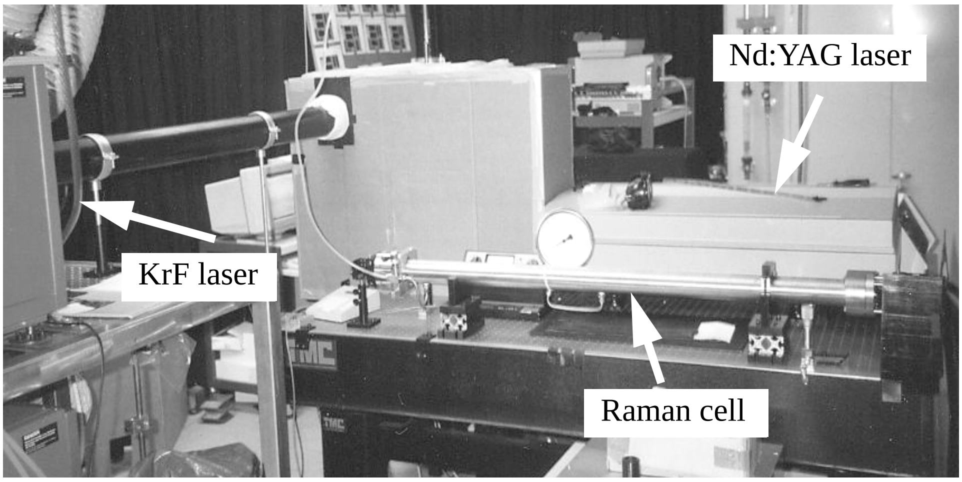

FIGURE 3-10. The Raman cell used for different tests

3.4.1. The polychromator dispersion

Before the "PMT's module part" shown in Figure 3-4, p 50 was designed and set in operation, the polychromator dispersion was calculated using the data supplied by the grating and spectrograph manufacturers and also experimentally measured.
A first test was made with a mercury lamp set into the bandpass filter tube, in place of the rotating part. As the spectra of such lamp is well known and documented [*Lide*, 1992-1993] it is then, in principle, easy to calculate the resulting dispersion of two intense lines. But the resulting lines at the output of the polychromator after the grating dispersion were not luminous enough to clearly distinguish them.
Another experiment was then made, using two laser sources with known wavelengths:- a quadrupled Nd:YAG at 266.04 nm, - an eximer pumped dye tuned at 270.00 nm (the wavelength difference with the quadrupled Nd:YAG laser and a XeCl (308 nm) or KrF (248 nm) one is too important, being out of the polychromator separation capability).
The two beams from the lasers were combined into one beam containing the two wavelengths by a Pellin-Broca prism. A small amount of this resulting beam was delivered to the polychromator entrance by an optical fiber. For higher accuracy, instead of the diaphragm used for the lidar experiments, the original entrance slit of the spectrograph was taken in these measurements. The positions of the images of the entrance slit in the exit plane of the spectrograph at the two laser wavelengths were measured and used to calculate the real dispersion of the spectrograph. The measured dispersion has a value of 0.513 nm / mm.
The error on this value has to be calculated. The distance between the two lines at the output of the spectrograph, marked with a pencil on a sheet of paper, was measured with a sliding caliper. A reasonable error on this position measurement gives 0.1 mm. Concerning the lasers, both have a linewidth of approximately 0.01 nm. If we consider to have a dispersion of 0.513 nm / mm, the extent at the output of the spectrograph due to this linewidth gives 0.02 mm. The error induced by the laser linewidth is smaller by a factor of five compared to the position measurement one, and will be hidden by this latter. The error on the measurement of the dispersion is then 0.1 mm which finally gives for the dispersion value: 0.513 ± 0.05 nm / mm.
The measured dispersion value is in good agreement with the theoretical one and was used to calculate the relative positions of the exit diaphragms for the O_2, N_2 and H_2O Raman backscattered wavelengths.

3.4.2. Settings of the polychromator grating angle and the PMTs' positions

The receiver alignment (polychromator grating angle and PMTs' positions) was performed using the first vibrational Stokes of N_2, produced by stimulated scattering in a high pressure gas cell. The alignment scheme is presented in Figure 3-11. The cell was filled with 35 atm of N_2 and pumped by the 4^{th} harmonic of a Nd:YAG laser. A Pellin Broca prism enabled the spectral separation of the generated Raman spectra, and the N_2 first Stokes was selected. A small amount of it was then injected by an optical fiber into the receiving telescope. The receiver was aligned by tuning the polychromator grating until the image of the telescope field diaphragm was centered into the exit diaphragm of the N_2 channel. The centering was first observed visually on a piece of calking paper placed just behind the exit diaphragm of the N_2 channel. The O_2 and H_2O receivers were set at positions calculated from the dispersion data. The fine alignement of these channels was performed by optimizing real range corrected lidar signals, moving the corresponding photomultipliers.

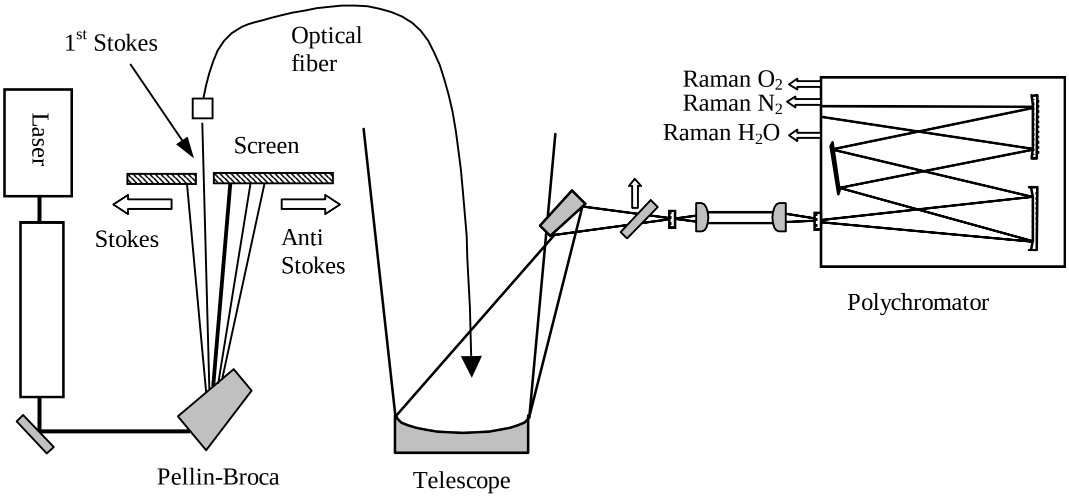

FIGURE 3-11. Optimization of the receiver alignment

Since the conversion efficiency in N_2 is very low when pumped by a KrF laser, we were not able to use the same procedure to align the receiver for operation with a KrF laser. In this case the N_2 receiver was kept at the same position as for the Nd:YAG experiment. The grating position as well as the O_2 and H_2O receiver positions were set at precalculated values. With real backscattered lidar signals the N_2 channel was optimized by tuning the grating and, finally, the O_2 and H_2O receiver positions were optimized by small translational movements of the corresponding receivers.

Conclusion

The central position of each of the three PMTs, for the photomultiplier module part design, was calculated for the Nd:YAG case. As the stimulated Raman conversion in oxygen or water vapor can be hardly achieved directly in the cell, the final places of these PMTs were checked against real Raman backscattered lidar signals.

- For the Nd:YAG case, a very slight adjustment of the PMT's positions was made, confirming the calculated values.
- For the KrF case the central position of the nitrogen PMT was kept and the polychromator grating tilted at the right value. After a coarse alignment for the oxygen and water vapor PMTs made by calculation, final precise value was given like in the Nd:YAG case with real Raman backscattered lidar signals. This procedure, where the nitrogen PMT keeps the same position, permits to jump from the Nd:YAG configuration to the KrF one with a minimum number of realignment steps, and could be achieved within a few minutes.

3.4.3. Relative sensitivity of the PMTs

The relative sensitivity of each PMT has been measured, for different cathode voltage values, in order to estimate the correction factor to be applied for the correct retrieval of the water vapor mixing ratio or for the crosstalks measurements. These measurements were done by tuning the polychromator grating to sequentially illuminate the different PMTs with the same amount of light. The obtained results are as follows:

TABLE 3-1. Relative sensitivity of the PMT used

	PMT O_2 / PMT N_2	PMT O_2 / PMT H_2O	PMT N_2 / PMT H_2O
PMT Voltage = 800 V	0.84	0.66	0.79
PMT Voltage = 900 V	1.20	0.96	0.80
PMT Voltage = 980 V	1.32	1.12	0.85

Due to many factors each PMT is particular, and then has a different sensitivity. Our lidar measurements were made with values around 900 V for the PMT cathode voltages, where the PMT behavior is almost linear. As the Raman backscattered signal level from N_2 is higher than the O_2 one, itself higher than the H_2O one, the more sensitive PMT was set for the H_2O Raman channel, and so on.

3.4.4. Crosstalk measurements

The crosstalks between the different Raman channels and the incomplete rejection of the pump wavelength can be two important sources of systematic errors [*Lazzarotto et al.*, 2000]. Both have been carefully measured in our system for the Nd:YAG configuration. Even though the three signals may affect each other, the influence of the N_2 channel on the two others is stronger because it is the "central" wavelength and it has the highest intensity level. Therefore, we measured the optical crosstalks caused by the N_2 signal on the O_2 and H_2O channels.

Crosstalks between the Raman channels N_2 / O_2 and N_2 / H_2O

The setup for measuring the N_2 / O_2 crosstalk is shown in Figure 3-12.

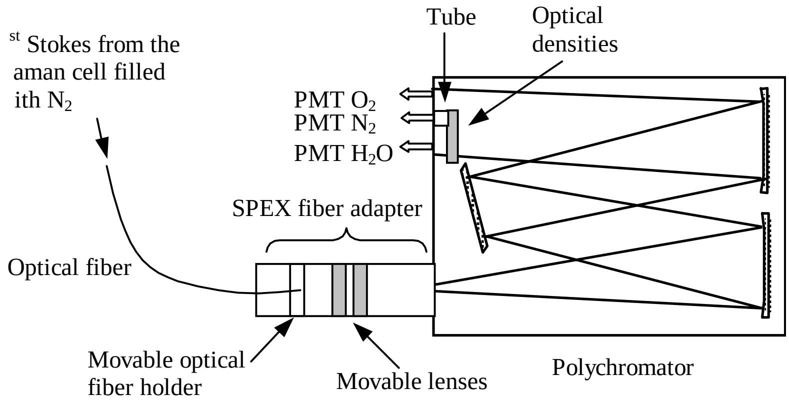

FIGURE 3-12. Experiment for the N_2 / O_2 Raman channel crosstalks

The light source used for these tests is the same as for the tests described in the paragraph 3.4.3. “Relative sensitivity of the PMTs”, p 57 (the 283.6 nm Raman shifted light is generated by injecting the 266 nm laser beam inside a Raman cell filled with 35 atm of N_2 gas). The light was delivered by an optical fiber, which output was fitted to the polychromator entrance by a two lenses fiber adapter (made by SPEX). With this device the desired spot can be achieved at the polychromator output.

The intensity of the injected 283.6 nm light was chosen so that the resulting crosstalks intensities were well above the photo-detectors noise level, but below their saturation level. The grating was set in its normal working position, i.e. to send the resulting beam inside the "N_2 PMT". The light intensity in the N_2 and O_2 channels is measured by the photomultiplier modules used for lidar measurements. At the output of the N_2 channel, we inserted a set of neutral density filters, in front of the PMT. The total attenuation of these filters is chosen so to achieve almost equal signals in both channels. A tube was set between this set of filters and the N_2 output, thus ensuring that no other scattered light leaked in this channel.

For the N_2 / H_2O crosstalk study, the experiment was performed in a similar manner, in this case with a set of optical densities in front of the N_2 and O_2 PMTs.

Results

The crosstalk in the O_2 and H_2O channels was calculated as a ratio between the crosstalk intensity in the respective channel and the intensity in the N_2 one, taking into account the relative photo-detectors sensitivity and the neutral density filters attenuation in the N_2 channel. The measured crosstalk levels were respectively: 2.2×10^{-5} for O_2 / N_2 and 5.2×10^{-5} for H_2O / N_2. A simulation study (see chapter 6 p 107 (Applied Optics article) or [*Lazzarotto et al.*, 2000]) showed that a detectable bias on ozone or water vapor retrieve could be expected only with a crosstalk greater than 10^{-3}. Our experimental crosstalk values were much lower, and low enough to neglect their influence. These values were also in good agreement with the stray light level stated by the polychromator manufacturer.

Crosstalk of the residual pump beam in the three Raman channels:

Care was also taken to "suppress" the residual elastic signal and to measure the degree of this suppression in the Raman channels. Since this degree is very high, its direct measurement was impossible. Instead, the suppression of the elastic signal by the bandpass filters and the polychromator was measured separately.

For the polychromator, the elastic backscatter light suppression was measured in a similar way than the one described above for the crosstalk among the Raman channels, this time injecting directly a fraction of the 266 nm light into the receiving telescope. A first "reference" measurement was done in the nitrogen channel, the grating being tilted for maximum transmission of the 266 nm light in this channel, with a total set of optical densities at the entrance of the polychromator. Then, the grating was tilted back to its working place, and the entrance density was decreased by a factor of five. The suppression degrees for the different Raman channels were then calculated as a ratio between the intensity of the 266 nm light entering the polychromator and the light intensities detected in these channels. The measured level of suppression values were as follows: for N_2 channel = 1.5×10^5; for O_2 channel = 5.9×10^4; for H_2O channel = 3.5×10^4. The band-pass filters were measured separately, with a total attenuation ratio of the elastic signal (ratio before versus after the filters) of 1.58×10^5 times.

Thus the total suppression of the elastic backscatter signal at the receiver was always higher than 5×10^9. This value ensured that the residual pump beam in the three Raman channels was not the source of systematic error, as was also reported by the model results (see chapter 6 p 107 or [*Lazzarotto et al.*, 2000]: Applied Optics article). This high rejection of the elastic signal was further confirmed by the fact that no detectable echo from low altitude dense clouds was observed in the different Raman channels.

3.5. Raman lidar specifications table

Nd:YAG solid state laser

Manufacturer and model:	Continuum Powerlite 8000 series
Wavelength:	266.04 nm (quadrupled)
Repetition rate:	10 Hz
Max. Pulse Energy:	120 mJ @ 266.04 nm
Pulsewidth FWHM:	5-7 ns
Linewidth FWHM:	1 cm^{-1} @ 1064.15 nm (i.e. 30 GHz, i.e. 0.113 nm) 0.014 nm @ 266.04 nm
Beam diameter:	8 mm (exit)
Divergence:	0.50 mrad
Beam pointing stability:	0.1 mrad
Jitter:	± 0.5 ns
Energy stability (shot to shot):	10 % @ 266.04 nm
Power drift (8 hours average):	5 %
Beam spatial profile:	0.95 (for far field, fit to Gaussian profiles. 1 would be the best)

KrF eximer laser

Manufacturer and model:	Lambda Physik LPX 210 i
Modifications:	Unstable home made resonator, to decrease the initial 1 x 3 mrad divergence
Type:	Unstable resonator, telescopic type, positive branch
End mirror:	Concave, 40 mm diameter, F = 2000 mm
Exit mirror:	Convex, 4 mm diameter, F = -386 mm
Wavelength:	248.7 nm (tunable from 248.4 to 249.1 nm if a special configuration is set)
Gas mixture:	Mixture for eximer 5% F_2 / 95 % He 4.6: 80 mbar Kr 4.0:120 mbar Ne 4.0: 2300 mbar
Repetition rate:	1 - 100 Hz
Max. Pulse Energy:	150 mJ
Pulsewidth FWHM:	28 ns
Linewidth FWHM:	0.32 nm
Beam dimension:	10 x 20 mm (exit)
Divergence:	0.5 x 0.5 mrad
Jitter:	± 2 ns
Energy stability (shot to shot):	± 3 %

Bandpass filter (for Nd:YAG configuration)

Manufacturer and batch:	Barr Associates Inc, n°1100:286-1
Diameter:	2" (50.8 mm)
Center wavelength:	285.4 nm
Bandwidth FWHM:	25.3 nm
Transmission:	75 % < T < 92 % for 273 nm < λ < 296 nm
Cutting:	OD > 4 @ 266 nm

Bandpass filter (for KrF configuration)

Manufacturer and batch:	Barr Associates Inc, n°4799:EPFL-1
Diameter:	2" (50.8 mm)
Center wavelength:	264.8 nm
Bandwidth FWHM:	23.6 nm
Transmission:	65 % < T < 77 % for 256 nm < λ < 276 nm
Cutting:	OD > 4.5 @ 248.7 nm

Solar Blind filter

Manufacturer and reference:	Corion SB-300-A
Diameter:	12.74 mm
Minimum active area:	7.6 mm
Center wavelength:	300 nm
Bandwidth FWHM:	85 nm
Transmission:	50 % < T < 56 7% for 272 nm < λ < 320 nm
Cutting:	OD > 3 for λ > 360 nm

Beam Expander

Manufacturer and reference:	CVI, BXUV-10.0-3X
Material:	UV grade fused silica. Coated
Max input beam:	10 mm diameter
Expansion:	3 x
Type:	Galilean, negative lens + positive lens
Transmission:	> 97 %
Damage threshold:	500 mJ / cm^2

Telescope

Type:	Newtonian / off axis
Focal length:	1100.75 mm
Primary mirror:	See after
Secondary mirror:	See after

Primary mirror

Manufacturer and reference:	Optical Surfaces LTD
Type:	Off axis paraboloid
Material:	Duran 50, Al + MgF_2 coating 258-295 nm
Diameter:	225 mm
Aperture:	200 mm
Thickness:	42 mm ± 1 mm
Off-axis distance:	223 mm
Focal length:	1110.75 mm

Secondary mirror

Manufacturer and reference:	Optical Surfaces LTD
Type:	Elliptical flat mirror
Material:	Duran 50, Al + MgF_2 coating
Dimensions:	140 - 100 mm

Thickness: 16 mm

Right angle prism (emission)

Manufacturer and reference: Comar, 40 RS 00
Material: UV grade fused silica
Dimensions: 40 x 40 mm
Special: Anti reflection coating broadband

Right angle prism (reception)

Manufacturer and reference: Comar, 40 RS 00
Material: UV grade fused silica
Dimensions: 16 x 16 mm

Polychromator

Manufacturer and reference: Jobin Yvon, SPEX 500 M
Type: Czerny-Turner configuration, one stage
Focal length: 500 mm
Aperture: f / 4 with 100 x 100 mm grating
Spectral range: 220 - 500 nm
Resolution: 6.67×10^{-3} nm
Repeatability: ± 1.67×10^{-3} nm
Accuracy: ± 1.67×10^{-2} nm
Driver Step Size: 8.33×10^{-5} nm
Dispersion: 0.513 nm / mm (for the grating described after)

Grating

Manufacturer and reference: Jobin Yvon
Type: Holographic
Dimensions: 100 x 100 mm
Density of grooves: 3600 gr / mm
Wavelength range: 225 - 500 nm
Efficiency: Approximately 40 %

Photomultiplier

Manufacturer and reference: Hamamatsu photosensor module, model 5783-06 & 6780-06 (-06 denotes a higher UV sensibility)
Type: Photomultiplier with built-in high voltage power supply
Dimensions: 22 x 22 x 50 mm
Effective area: 8 mm diameter
Spectral response range: 185 to 650 nm
Time response: 0.78 ns @ 0.8 V on control voltage (max 0.9 V)
Radiant sensitivity: 43 µA / nW @ 0.8 V on control voltage (max 0.9 V)
Dark current: 0.2 nA typically @ 0.8 V on control voltage (max 0.9 V)
10 nA maximum @ 0.8 V on control voltage (max 0.9 V)

Transient recorder

Manufacturer and model: Licel

General description:	Built in analog and photon counting acquisition device
Analog acquisition:	
Signal input range:	0-20, 0-100, 0-500 mV @ 50 Ω load
A/D resolution:	12 bit
Sampling rate:	20 MHz, giving a lidar spatial resolution of 7.5 m
Summation memory:	4094 acquisitions for the two channels together
SNR single shot:	66 dB @ 100 mV
Memory depth:	8192 or 16384 bins (i.e. 61440 m or 122880 m)
Max repetition rate:	150 Hz @ 400 µs signals, 75 Hz @ 800 µs signals
Trigger delay and jitter:	50 ± 12.5 ns
Photon counting acquisition:	
Signal input range:	0-20, 0-100 mV @ 50 Ω load
Discriminator:	64 levels software controlled
Bandwidth:	10 - 250 MHz
Summation memory:	4094 acquisitions for the two channels together
Memory depth:	8192 or 16384 bins (i.e. 61440 m or 122880 m)
Trigger:	
Generalities:	Two trigger inputs to acquire signals in two separate memories Threshold and slope 2.5 V, positive, 50 Ω load
Delay and jitter:	50 ± 12.5 ns

Pulse generator

Manufacturer and model:	Stanford Research Systems, DG 535
Loadings:	50 Ω or high impedance
Delay resolution:	5 ps
Delay accuracy:	< 1.5 ns + time base error x delay
Jitter:	60 ps + 10^{-8}x delay

Motorized optical mount

Manufacturer and model:	New Focus, model # 8852
Style:	Corner
Optic diameter:	2"
Motorized axes:	3
Angular resolution:	0.7 µrad
Driver:	New Focus economical multi-axis driver model # 8801

Flipper

Manufacturer and model:	New Focus, model # 9892
Optic diameter:	2"
Repeatability:	< 0.2 mrad
Resolution / 5° turn:	0.26 mrad

Photodiode

Manufacturer and model:	Thorlabs, SI PIN FDS 010
Active area:	1 mm^2
Spectral response:	220 - 1100 nm

Dark current:	2.5 nA
Time response:	1 ns

Acquisition software and hardware

Program:	Made under LabVIEW 5.1
Card:	National instruments NI-DAQ card

Chapter 4

Corrections and errors analysis

Here is applied and completed the formalism developed in the chapter 2 “Theory”, p 27 to calculate the different atmospheric contributions, and to retrieve the quantities of interest. The statistical errors are calculated.

The second paragraph tends to know what is the required precision in the correction terms and then which approximations can be made in the conditions of our measurements. The corrections, due to the Rayleigh and Mie scattering and to the molecular absorption, on the ozone concentration retrieve and on the water vapor mixing ratio one are calculated and discussed for two typical conditions, remote and urban. This discussion is done for two laser sources, a quadrupled Nd:YAG and a KrF one. The aerosol extinction coefficient is derived from the Raman lidar equation and compared with theoretical retrieves.
The Signal to Noise Ratio (SNR) of the Raman signals are compared and analyzed for different conditions. Statistical errors on the ozone concentration retrieve and on the water vapor mixing ratio one are calculated and comparisons with a Nd:YAG or a KrF laser sources is made.
As the ozone concentration retrieve suffers from the KrF configuration, experiments were made to overcome this and a solution is proposed.
The last chapter deals with the retrieve of the water vapor mixing ratio correction value, although the water vapor calibration is not difficult. This calculations are made in case of an ozone correction by an external measurement and in case of an auto (ozone) correction by the lidar.

4.1. The NOAA 76 atmospheric profile

In the following corrections we have to consider a model to retrieve a concentration at a given altitude. To retrieve the temperature and pressure at the distance R the NOAA 76 model, tropospheric part, was chosen [*NOAA et al.*, 1976], with a modification to use the pressure and temperature at the lidar altitude as calibrating ones:

$$P_{atmos}(R) = P_D \left(\frac{T_D}{T_{atmos}(R)} \right)^{-5.255877} \qquad \text{(EQ 4.1)}$$

$$T_{atmos} = T_D - 0.0065 \cdot R \qquad \text{(EQ 4.2)}$$

Where P_D *[Pa]* is the air pressure and T_D *[K]* is the absolute temperature at the lidar site. R *[m]* is the distance from the lidar site to the probed region.
So it gives for the atmospheric concentration $n_{atmos}(R)$ *[molec.cm^{-3}]* at a range R, with the ideal gas law:

$$n_{atmos}(R) = \frac{P_{atmos}(R)}{k_B T_{atmos}(R)} = \frac{P_D T_D^{-5.255877}}{k_B} \left(T_D - 0.0065 \cdot R \right)^{4.255877} \qquad \text{(EQ 4.3)}$$

Where $k_B = 1.381 \times 10^{-23}$ *[J.K^{-1}]* denotes the Boltzmann constant.
If a difference in altitude of 2000 m is taken, a temperature difference of approximately 13 K, and a pressure difference of approximately 220 mbar can be deduced from this NOAA model. Concerning the temperature, taking also into account the seasonal change which is in the order of 30 K, the possible temperature difference will be approximately 40 K.

4.2. Precision in the correction terms

4.2.1. The extinction term due to molecular scattering

The molecular scattering extinction term $\alpha_{Rayl}^{molec}(\lambda_i, r)$ is linked to the total Rayleigh molecular scattering cross-section ${}^{tot}\sigma_{Rayl}^{molec}(\lambda_i, r)$ by:

$$\alpha_{Rayl}^{molec}(\lambda_i, r) = n_{atmos}(r) \times {}^{tot}\sigma_{Rayl}^{molec}(\lambda_i, r) \qquad \text{(EQ 4.4)}$$

Where $n_{atmos}(r)$ *[molec.cm^{-3}]* is the air concentration.
Let us assume an electromagnetic wave hitting a molecule as it is shown in the following Figure 4-1, which illustrates some of the parameters used in the formula for calculating the Rayleigh cross-section.

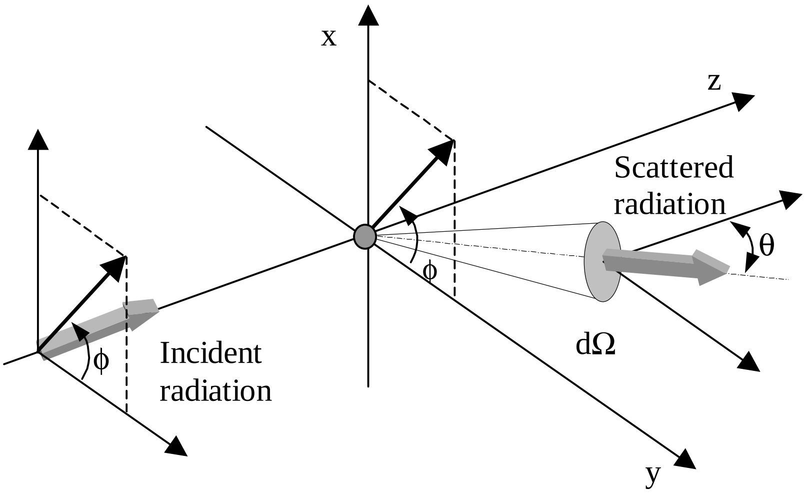

FIGURE 4-1. Schematic diagram for the incident and scattered beam

ϕ is the polarization angle of the linearly polarized incident electromagnetic wave propagating according to the z-axis. The resulting scattered radiation makes an angle θ with the z-axis (in the yz plane) and emits in a solid angle dΩ.
The molecular Rayleigh scattering cross-section is then given by [*Penndorf*, 1957]:

$$\frac{d\sigma^{molec}_{Rayl}(\phi,\theta,\lambda_i,r)}{d\Omega} = \frac{9\pi^2(\widetilde{n_s}^2-1)^2}{\lambda_i^4\, n^2_{atmos}(r)\,(\widetilde{n_s}^2+2)^2}\left(\frac{6+3\rho}{6-7\rho}\right)\left\{\cos^2\phi\cos^2\theta+\sin^2\phi\right\} \qquad \text{(EQ 4.5)}$$

Where:

$\frac{d\sigma^{molec}_{Rayl}(\phi,\theta,\lambda_i,r)}{d\Omega}$ *[cm^2.sr^{-1}.molec^{-1}]* : Differential molecular Rayleigh scattering cross-section

λ_i *[cm]* : Wavelength of interest

$\widetilde{n_s}$ *[dimensionless]* : Refractive index of the air

$n_{atmos}(r)$ *[molec.cm^{-3}]* : Air molecular concentration

$\left(\frac{6+3\rho}{6-7\rho}\right) \equiv F(air)$ *[dimensionless]* : Depolarization term or King factor, with ρ *[dimensionless]* the depolarization ratio

ϕ *[rad]* : Polarization angle

θ *[rad]* : Scattering angle

Notice that in this equation it is important to express $\widetilde{n_s}$ and $n_{atmos}(r)$ at the same temperature and pressure.
By definition, we have for the total Rayleigh molecular scattering cross-section ${}^{tot}\sigma^{molec}_{Rayl}(\lambda_i,r)$ *[cm^2.molec^{-1}]* (integration over 4π steradians):

$$ {}^{tot}\sigma^{molec}_{Rayl}(\lambda_i,r)=\iint_{\phi,\theta}\frac{d\sigma^{molec}_{Rayl}(\phi,\theta,\lambda_i,r)}{d\Omega}=\frac{24\pi^3(\widetilde{n_s}^2-1)^2}{\lambda_i^4 n^2_{atmos}(r)(\widetilde{n_s}^2+2)^2}\left(\frac{6+3\rho}{6-7\rho}\right) \qquad \text{(EQ 4.6)} $$

Its main behavior concerns the λ^{-4} wavelength dependence which is a first (good) approximation. The air refractive index and the depolarization ratio also exhibit a wavelength dependence which will induce a slight change in this λ^{-4} wavelength dependence. For example, the air refractive index wavelength dependence is of the order of 3 % [*Elterman*, 1968].

It should also be pointed out that the depolarization term F(air) does not depend on temperature and pressure but on gas mixture, and that n_{atmos} has the opposite behavior: dependent on temperature and pressure but independent on gas mixture. The result for the total molecular Rayleigh scattering cross-section is a dependence on the gas composition but not on the temperature and pressure [*Mc Cartney*, 1976], [*Bucholtz*, 1995].

The calculations for the depolarization term and the air refractive index term, without the usual approximation $\widetilde{n_s}^2+2\simeq 3$ [*Measures*, 1992] is presented in the following part.

The molecular scattering extinction term $\alpha^{molec}_{Rayl}(\lambda_i,r)$ is then linked to the total Rayleigh molecular scattering cross-section ${}^{tot}\sigma^{molec}_{Rayl}(\lambda_i,r)$ by:

$$ \alpha^{molec}_{Rayl}(\lambda_i,r)=n_{atmos}(r)\times{}^{tot}\sigma^{molec}_{Rayl}(\lambda_i,r)=\frac{24\pi^3(\widetilde{n_s}^2-1)^2}{\lambda_i^4 n_{atmos}(r)\,(\widetilde{n_s}^2+2)^2}\underbrace{\left(\frac{6+3\rho}{6-7\rho}\right)}_{F(air)} \qquad \text{(EQ 4.7)} $$

We need to consider if the different terms in (EQ 4.7) are known with sufficient accuracy, and also if ${}^{tot}\sigma^{molec}_{Rayl}(\lambda_i,r)$ needs to be defined with more accuracy.

Depolarization term

The depolarization ratio ρ, which is part of the depolarization factor, calculation is one of the main reasons why published Rayleigh optical depth are not always in agreement. A value of $\rho = 0.035$ [*Elterman*, 1968], [*Penndorf*, 1957] (and then F(air) = 1.0608) was commonly used since, based on more recent depolarization data for dry air, Young [*Young*, 1980], [*Young*, 1981] recommended the value $\rho = 0.0279$ (giving F(air) = 1.0481). This correction has been accepted for modern Rayleigh scattering calculations in the atmosphere and it reduces the Rayleigh scattering values by 1.3 %.

As the depolarization factor F(air) is wavelength and air composition dependent, several works [*Bates*, 1984], [*Bucholtz*, 1995] were published to discuss in detail the depolarization term. It appears that today’s best estimate is given by Bates who recommended to calculate it by using the following procedure.

The calculation of the air depolarization term F(air) is a weighting of the depolarization terms for N_2, O_2, Ar and CO_2, ignoring the other gases, and with recognizable concentration values of the major constituents of the air as listed in the table“. International values for dry air”, p 10:

$$F(air) = \frac{78.084F(N_2) + 20.946F(O_2) + 0.934F(Ar) + \xi_{CO_2}F(CO_2)}{78.084 + 20.946 + 0.934 + \xi_{CO_2}} \qquad \text{(EQ 4.8)}$$

The depolarization terms for N_2, O_2, Ar and CO_2 are described by the following equations, with λ_i in *[nm]*:

$$F(N_2) = 1.034 + 3.17\times10^{-4}\times\frac{1}{\lambda_i^2} \qquad \text{(EQ 4.9)}$$

$$F(O_2) = 1.096 + 1.385\times10^{-3}\times\frac{1}{\lambda_i^2} + 1.448\times10^{-4}\times\frac{1}{\lambda_i^4} \qquad \text{(EQ 4.10)}$$

$$F(Ar) = 1.00 \qquad \text{(EQ 4.11)}$$

$$F(CO_2) = 1.15 \qquad \text{(EQ 4.12)}$$

The resulting value for the depolarization term is then:

$$F(air) = \frac{104.6297 + 1.15\times\xi_{CO_2} + 5.37628\times10^{-2}\times\lambda_i^{-2} + 3.033\times10^{-3}\times\lambda_i^{-4}}{99.964 + \xi_{CO_2}} \qquad \text{(EQ 4.13)}$$

With ξ_{CO_2} expressed in parts per volume by percent (i.e. 0.036 for 360 ppm) and λ_i in *[nm]*.

First calculation is made with the wavelength-independent part of (EQ 4.13), taking a common value of 360 ppm for CO_2. F(air) = 1.046711 and then ρ = 0.027139. This reduces the Rayleigh scattering values by 0.1 % with respect to the Young value.
Second one will be made to check the wavelength dependence. We assume, as before, 360 ppm for the CO_2 concentration. The (EQ 4.13) then becomes:

$$F(air) = 1.046711 + 5.37628\times10^{-4}\times\lambda_i^{-2} + 3.033\times10^{-6}\times\lambda_i^{-4} \qquad \text{(EQ 4.14)}$$

In our case, as our wavelength range goes from 248.7 nm for the KrF pump to 294.67 nm for the water vapor Raman return (pump with the Nd:YAG), the depolarization term will then go respectively from 1.0467110087 to 1.0467110062. It gives an additional value for the Rayleigh scattering of less than $6\text{x}10^{-7}$ %.
In our case we can then cancel the wavelength dependence and take either the Young's value or the one given by (EQ 4.13) with only the CO_2 concentration.
To go further, the more we go in the UV direction the more the correction will be "important". As a conclusion, out of our range in the X-ray region, this corrective term starts to be important: at 0.02 nm the depolarization term has a value of 191.95 and at 0.01 nm a value of 3039.42.

Air refractive index

The formalism recommended by Bodhaine [*Bodhaine*, 1999] was chosen, followed by Edlén's one for the different corrections [*Edlén*, 1966]. As the Owens's proposed formalism for the cor-

rections falls out of our conditions for the water vapor [*Owens*, 1967], it will not be used.
The method is iterative, with a starting refractive index value taken for dry air with 300 ppm CO_2 [*Peck and Reeder,* 1972]:

$$(\tilde{n}_{300}-1)\times10^{8}=8060.51+\frac{2480990}{132.274-\lambda_i^{-2}}+\frac{17455.7}{39.32957-\lambda_i^{-2}} \qquad \text{(EQ 4.15)}$$

with λ_i in µm, for a temperature of 288.15 K and a pressure of 1013.25 mb.
To get the refractive index for the CO_2 concentration value of interest the following formula is used [*Edlén*, 1966]:

$$\frac{\tilde{n}_{n_{CO_2}}-1}{\tilde{n}_{300}-1}=1+0.54(n_{CO_2}-3\times10^{-4}) \qquad \text{(EQ 4.16)}$$

with n_{CO_2} as parts per volume (i.e. 0.00036 for 360 ppm). (EQ 4.15) and (EQ 4.16) then gives:

$$(\tilde{n}_{n_{CO_2}}-1)\times10^{8}=\left\{1+0.54(n_{CO_2}-3\times10^{-4})\right\}\times\left\{8060.51+\frac{2480990}{132.274-\lambda_i^{-2}}+\frac{17455.7}{39.32957-\lambda_i^{-2}}\right\} \qquad \text{(EQ 4.17)}$$

Furthermore, correction on temperature and pressure was proposed by Edlén [*Edlén*, 1966] as an improvement of previous measurements [*Barrell and Sears*, 1939] and is the following:

$$(\tilde{n}_{T,P}-1)=(\tilde{n}_{n_{CO_2}}-1)\frac{P}{720.775}\frac{1+P(0.817-0.0133\times T)}{1+0.003661\times T} \qquad \text{(EQ 4.18)}$$

In a temperature range of 5 °C to 30 °C, and with the temperature T in °C and the pressure P in Torr.
Edlén [*Edlén*, 1953], [*Edlén*, 1966] pointed out that the effects induced by high concentrations of water vapor on the refractive index of the air may be of the same order as CO_2. Nevertheless, in most common conditions, the total water vapor in vertical column is small and does not significantly affect the previous calculations. We may therefore neglect this effect.

From (EQ 4.7) p 68 it can be seen that the air refractive index contribution to the molecular scattering term is given by $\frac{(\widetilde{n_s^2}-1)^2}{(\widetilde{n_s^2}+2)^2}$, which will be named $\Upsilon(\widetilde{n_s})$.
First of all, we will check the wavelength dependence of this term $\Upsilon(\widetilde{n_s})$, with several formulas given as follows. The wavelength range is taken from 247.8 nm to 294.67 nm.
The Edlen's 1953 one:

$$\tilde{n}_{Edlen53}=1+\left\{6432.8+\frac{2949810}{146-\lambda_i^{-2}}+\frac{25540}{41-\lambda_i^{-2}}\right\}\times10^{-8} \qquad \text{(EQ 4.19)}$$

The Edlen's 1966 one:

$$\tilde{n}_{Edlen66} = 1 + \left\{ 8342.13 + \frac{2406030}{130 - \lambda_i^{-2}} + \frac{15997}{38.9 - \lambda_i^{-2}} \right\} \times 10^{-8} \qquad \text{(EQ 4.20)}$$

The Peck and Reeder's 1972 one, which is at the basis of the development made in our case:

$$\tilde{n}_{Peck72} = 1 + \left\{ 8060.51 + \frac{2480990}{132.274 - \lambda_i^{-2}} + \frac{17455.7}{39.32957 - \lambda_i^{-2}} \right\} \times 10^{-8} \qquad \text{(EQ 4.21)}$$

We may see that, contrarily to the depolarization term, the wavelength dependent terms are of essential importance. The wavelength dependence behaviour gives more contribution in the UV direction, then the lowest wavelength value of 248.7 nm will be taken for comparison. Taking the Edlen's 53 formula, it gives $\Upsilon(\widetilde{n_s}) = 4.048 \times 10^{-8}$ with all terms taken. This value will be used as the "reference" for this paragraph. In case that only the first term is taken into account we have $\Upsilon(\widetilde{n_s}) = 0.184 \times 10^{-8}$, which make a relative error of 95 %. If the first and second terms are taken into account, this coefficient becomes $\Upsilon(\widetilde{n_s}) = 3.777 \times 10^{-8}$, giving 6.7 % of relative error.

We can now compare the different formulas, all terms kept, at a wavelength of 247.8 nm. The Peck and Reeder's one will be taken as the reference value, because it has been recognized to give accurate values for a wide range of wavelengths. It gives a value of $\Upsilon(\widetilde{n_s}) = 4.048384 \times 10^{-8}$. Compared with Edlen's 66 formula, where $\Upsilon(\widetilde{n_s}) = 4.048397 \times 10^{-8}$, the relative error is about -3.2×10^{-4} %, and with the Edlen's 53 one, where $\Upsilon(\widetilde{n_s}) = 4.048127 \times 10^{-8}$, the relative error is about 6.4x10^{-3} %.

In our conditions no big difference can be seen between these three possibilities. Nevertheless, the Peck and Reeder's formalism will be chosen.

The (EQ 4.17) p 70 gives the refractive index of the air corrected for a CO_2 concentration:

$$\tilde{n}_{\xi_{CO_2}} - 1 = \left\{ 1 + 0.54(\xi_{CO_2} - 3 \times 10^{-4}) \right\} \times \left\{ 8060.51 + \frac{2480990}{132.274 - \lambda_i^{-2}} + \frac{17455.7}{39.32957 - \lambda_i^{-2}} \right\} \times 10^{-8} \qquad \text{(EQ 4.22)}$$

and (EQ 4.18) p 70 gives the additional temperature and pressure dependence, with the temperature T in °C, in a range of 5 °C to 30 °C, and the pressure P in Torr.

$$(\tilde{n}_{T,P} - 1) = (\tilde{n}_{n_{CO_2}} - 1) \frac{P}{720.775} \frac{1 + P(0.817 - 0.0133 \times T)}{1 + 0.003661 \times T} \qquad \text{(EQ 4.23)}$$

For the CO_2 correction a concentration of 360 ppm is used. It gives a value of $\Upsilon(\widetilde{n_s}) = 4.205970 \times 10^{-8}$, for a wavelength of 248.7 nm. Compared with the value without the CO_2 concentration correction, i. e. the Peck and Reeder formula, the relative error is about 3.75 %.

To finish, it will be investigated the temperature and pressure dependence of the (EQ 4.23). Concerning the temperature it will be taken from 5 °C to 30 °C, and the pressure from 960 mbar to 740 mbar (see paragraph 4.1. “The NOAA 76 atmospheric profile”, p 66). The calculations are performed with 248.7 nm.

The couple (30 °C, 960 mbar) gives a value of $\Upsilon(\widetilde{n_s}) = 3.409452 \times 10^{-8}$, and then a relative error compared with the (EQ 4.22) of -18.9 %. At higher altitudes, the couple (5 °C, 740 mbar) gives a value of $\Upsilon(\widetilde{n_s}) = 2.406964 \times 10^{-8}$. The resulting relative error will be of -42.8 %.
So, we can conclude in the need of using such temperature and pressure correction in our case. In the sets of data collected from our various measurements the temperature ranges within approximately 5 °C to 30 °C , allowing such correction.

Approximated formula for the molecular extinction due to the Rayleigh scattering
For atmospheric gas mixture below an altitude range of 100km, Collis and Russell [Collis, 1976 #196] have shown that the (differential) Rayleigh (molecular) backscattering cross-section ${}^{\pi}\sigma_{Rayl}^{molec}(\lambda_i)$ *[cm^2.molec^{-1}.sr^{-1}]* is given by:

$$ {}^{\pi}\sigma_{Rayl}^{molec}(\lambda_i) = 5.45\left(\frac{550}{\lambda_i(nm)}\right)^4 \times 10^{-28} \qquad \text{(EQ 4.24)}$$

Elterman [Elterman, 1968 #197] showed that this expression is valid if we neglect the very slight wavelength dependence due to dispersion of the refractive index of the air (app. 3 %). In the other case the exponent has to take the value 4.09.
By definition the (differential) Rayleigh (molecular) backscattering cross-section is linked to the molecular Rayleigh scattering cross-section,(EQ 4.5) p 67, by:

$$ {}^{\pi}\sigma_{Rayl}^{molec}(\lambda_i, R) = \frac{d\sigma_{Rayl}^{molec}(\phi, \theta = \pi, \lambda_i, R)}{d\Omega} = \frac{9\pi^2(\widetilde{n_s}^2 - 1)^2}{\lambda_i^4 n_{atmos}^2(R)\,(\widetilde{n_s}^2 + 2)^2}\left(\frac{6+3\rho}{6-7\rho}\right) \qquad \text{(EQ 4.25)}$$

It gives the following simple relation between the total Rayleigh (molecular) scattering cross-section defined in the (EQ 4.6) p 68 and the (differential) Rayleigh (molecular) backscattering cross-section given by the (EQ 4.25):

$$ {}^{tot}\sigma_{Rayl}^{molec}(\lambda_i, R) = \frac{8\pi}{3} \times {}^{\pi}\sigma_{Rayl}^{molec}(\lambda_i, R) \qquad \text{(EQ 4.26)}$$

Combining (EQ 4.4) p 66, (EQ 4.24) and (EQ 4.26) we finally get the molecular extinction term $\alpha_{Rayl}^{molec}(\lambda_i, R)$ *[cm^{-1}]*due to the Rayleigh scattering:

$$ \alpha_{Rayl}^{molec}(\lambda_i, R) = n_{atmos}(R) \times 4.57\left(\frac{550}{\lambda_i(nm)}\right)^4 \times 10^{-27} \qquad \text{(EQ 4.27)}$$

The comparison with the complete corrected formula (EQ 4.7) p 68 gives, as it could be expected, some substantial differences. Just to illustrate this, we may compare results obtained at two different altitudes. The ground level conditions are taken at 20 °C and 970 mbar, and the CO_2 concentration is 360 ppm. Under these conditions the relative error between the empiric retrieve and the complete one is of the order of 17.2 % at ground level, and 43.8 % at

2000 m AGL.
So, under these conditions, it is justified to use the complete formula.

4.2.2. The molecular absorption coefficient

The molecular absorption coefficient $\alpha_{abs}^{molec}(\lambda_i, r)$ *[cm^{-1}]* for the group of molecules {Y} is defined as follows:

$$\alpha_{abs}^{molec}(\lambda_i, r) = \sum_{\{Y\}} n_Y(r)\sigma_{abs}^{Y}(\lambda_i, r) \tag{EQ 4.28}$$

Where $\sigma_{abs}^{Y}(\lambda_i, r)$ *[cm^2.molec^{-1}]* is the molecular absorption cross-section for the molecule Y. An extensive search was made to retrieve this contributive term in the UV. Both reactive and slowly reactive species were showed, and we choose to show some terms even if their contribution is weak (but not all, as for example the CFC's). The absolute absorption cross-sections for SO_2 [*Vandaele et al.*, 1994], O_3 [*Daumont et al.*, 1992], NO_2 [*Schneider et al.*, 1986], N_2O [*Nicolet and Peetermans*, 1972], HNO_3 [*Burkholder et al.*, 1993], CO_2 [*Shemansky*, 1972], HNO_2 [*Cox and Derwent*, 1976], CH_2O [*Meller*, 1992], C_6H_6 [*Trost*, 1994], C_7H_8 [*Trost*, 1994], O_2 [*Mérienne et al.*, 2000], [*Bernath et al.*, 1998] were taken at 298K.
As the atmospheric water vapor content is one of the most important trace gas with respect to the other tropospheric constituents, particular attention has to be taken to search for a possible absorption band in our wavelength range. Some authors [*Karmazin et al.*, 1990], [*Klimkin and Fedorishchev*, 1989] claimed the discovery of an intense water vapor absorption band in the UV, where our Raman system is active. This was not confirmed and to cancel this ambiguity a recent result [*Fiorani*, 1996] is taken. In this work they made an inter-comparison with an ozone DIAL corrected for the "water vapor new band effect", the non corrected result, and punctual analyzers. It immediately follows that, if the corrected scheme is applied, the ozone concentration retrieve shows very different values from the reference ones (this effect applies a negative offset of 40 ppb in their case). This confirms the idea that no important water vapor absorption bands are present in our wavelength region of interest, and that we shall neglect this contribution to the total atmospheric absorption.

In this section the absorption extinction term due to the molecular absorption, which is the product of the absorption cross-section times the concentration, is shown instead of the sole absorption cross-section. In this case the typical concentrations of each species in the atmosphere is considered and comparison of the real optical contribution in the atmosphere is possible with the Rayleigh and Mie case. Two typical cases, remote and urban conditions, will be discussed.
This values are mainly taken from [*Finlayson-Pitts and Pitts*, 1986], [*Yung and DeMore*, 1999], [*Warneck*, 1988], [*Seinfeld and Pandis*, 1998].

TABLE 4-1. Concentrations for two typical cases

Molecule	Concentration [ppb]	
	Remote	Urban
SO_2	1	200
O_3	50	20
NO_2	1	200
N_2O	320	320
HNO_3	0.1	10
CO_2	360000	360000
HNO_2	0.03	2
CH_2O	2	20
C_6H_6	0.5	20
C_7H_8	0.5	20
O_2	$2.09476x10^8$	$2.09476x10^8$

The absorption extinction coefficient for those molecules as well as the Rayleigh and Mie scattering coefficients can be graphically represented to show the wavelength dependence. In Figure 4-2 the assumption of a temperature of 20 °C and a pressure of 970 mbar is used (corresponding to the ground level atmospheric conditions of the lidar during a day of March). The visibility is taken equal to 6 km for the remote case and equal to 2 km for the urban one.

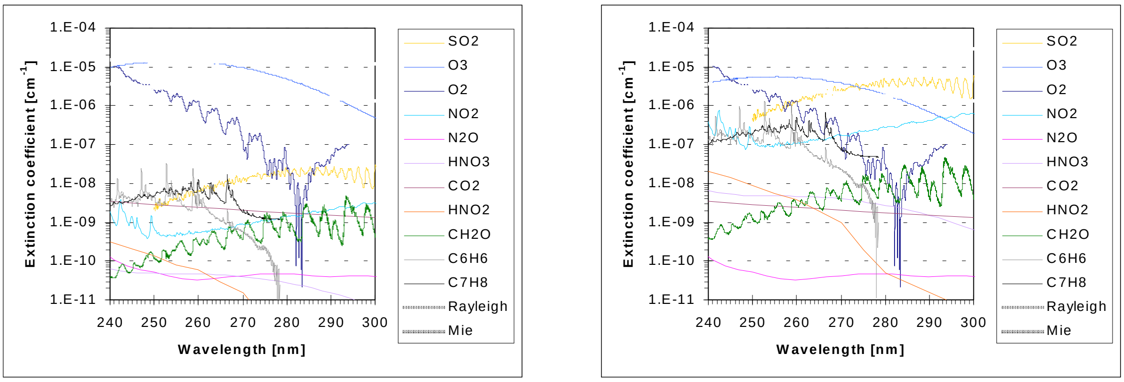

remote (a) **urban (b)**

FIGURE 4-2. Extinction coefficients in the UV for gas concentrations stated in Table 4-1 and with the Rayleigh and Mie contributions

The extinction coefficients are calculated for molecular absorption, molecular and aerosol scattering under the two typical cases of the Table 4-1, at the zero altitude. Figure 4-2 (a) stands for the “remote” case and Figure 4-2 (b) for the “urban” one. Both cases are computed from 240 to 300 nm.

The “remote” case shows a main extinction contribution due to the Mie and Rayleigh scattering and to the O_3 and O_2 (which is important for the KrF case) absorption. All the other molecular extinctions are at least 10^3 lower. The “urban”case keeps a similar behavior to the “remote” one. The Rayleigh scattering extinction as well as the O_2 absorption extinction stays the same, due to similar conditions and a constant O_2 concentration. A small decrease in the O_3 absorption extinction arises but the major change comes from the SO_2 absorption extinction contribution. This latter is important for both KrF and Nd:YAG case and an important corrective effect can be expected. In this case, apart the NO_2, C_6H_6 and C_7H_8 absorption contributions which are lower by a factor of 10^2, all the other molecular contributions are at least 10^3 lower.

This plot is made for the 0-altitude above ground level (agl) and, to retrieve a similar one at a different altitude, vertical concentration profiles have to be known. Concentrations of stable molecules like O_2 are well defined, but for molecules like SO_2, a vertical concentration profile is needed to describe the changes.

As SO_2 is one of the biggest contributions a special care was taken in the “urban” case described in Table1. This pollutant is emitted from the ground and its vertical mixing ratio distribution will then decrease with the altitude. Typical SO_2 altitude distributions were taken [*Warneck*, 1988], [*Kuebler*, 2000] and, in a urban condition, we approximate this decreasing distribution by a line with a slope of $\frac{-n_{SO_2}^0}{2500}$, where $n_{SO_2}^0$ is the (initial) ground level SO_2 concentration, for altitudes under 2500 m and by a vertical (zero) line for altitudes above 2500 m where the SO_2 concentrations are negligible.

This distribution is used in the following sections for the different correction calculations.

4.2.3. The aerosol term

Like for the molecular case we have several possibilities to retrieve this aerosol extinction term.

The Raman lidar retrieve

We give here an experimental approach, taking advantage of having Raman signals. With the Raman lidar equation (EQ 2.16) p 41 we have:

$$P_X(R) = P_L(\lambda_L)\, K_X\, \frac{A(R)}{R^2} \Delta R\, n_X(R)\, {}^{\pi}\beta_X^{Ram} \times \exp\left\{ -\int_0^R \left[\alpha^{aer}(\lambda_L, r) + \alpha^{aer}(\lambda_X^{Ram}, r) + \alpha^{molec}(\lambda_L, r) + \alpha^{molec}(\lambda_X^{Ram}, r) \right] dr \right\} \qquad \text{(EQ 4.29)}$$

Following previous work [*Ansmann et al.*, 1990], the derivative of the logarithm of the Raman lidar equation (EQ 4.29) is taken. With $\Delta R = const \rightarrow \frac{\partial}{\partial R}\ln(\Delta R) = 0$ and considering to be at full overlap $A(R) = 1 \rightarrow \frac{\partial}{\partial R}\ln\left(A(R)\right) = 0$, we obtain:

$$\frac{\partial}{\partial R}\ln\left(\frac{n_X(R)}{R^2P_X(R)}\right)=\alpha^{aer}(\lambda_L,R)+\alpha^{aer}(\lambda_X^{Ram},R)+\alpha^{molec}(\lambda_L,R)+\alpha^{molec}(\lambda_X^{Ram},R) \qquad \text{(EQ 4.30)}$$

When the Raman scheme is used, the Angström empirical formula [*Angström*, 1929] (which is similar to the one derived if the particles follow the Junge model [Junge, 1963 #198]) is often used

$$\alpha^{aer}(\lambda_i,R) = \text{constant}\times\lambda_{\mathrm{i}}^{\text{-k}} \qquad \text{(EQ 4.31)}$$

The parameter k is a constant depending on the size and composition of the aerosols. Several values for k can be found in the literature with a value between 0 and 2 [*Ansmann et al.*, 1992], [*van de Hulst*, 1981]. A value of less than 1 is encountered for aerosols larger than the laser wavelength. Notice that negative values have been found [*Valero and Pilewski*, 1992]. To give an idea about the error, if we take k = ±2 the error on the aerosol extinction will be approximately 8 % at 300 nm [*Gathen*, 1995]. We will choose for the numerical application the value k=1 which is the "recognized" value for normal atmosphere condition. The term k will however be kept in the calculation to have a more general result.
The following ratio can be formed:

$$\frac{\alpha^{aer}(\lambda_X^{Ram},R)}{\alpha^{aer}(\lambda_L,R)}=\left(\frac{\lambda_X^{Ram}}{\lambda_L}\right)^{-k} \qquad \text{(EQ 4.32)}$$

and using the term $\alpha^{aer}(\lambda_X^{Ram},R)$ in the equation (EQ 4.30) gives:

$$\frac{\partial}{\partial R}\ln\left(\frac{n_X(R)}{R^2P_X(R)}\right)=\left(1+\left(\frac{\lambda_X^{Ram}}{\lambda_L}\right)^{-k}\right)\alpha^{aer}(\lambda_L,R)+\alpha^{molec}(\lambda_L,R)+\alpha^{molec}(\lambda_X^{Ram},R) \qquad \text{(EQ 4.33)}$$

and finally:

$$\alpha^{aer}(\lambda_L,R)=\frac{\frac{\partial}{\partial R}\ln\left(\frac{n_X(R)}{R^2P_X(R)}\right)-\left(\alpha^{molec}(\lambda_L,R)+\alpha^{molec}(\lambda_X^{Ram},R)\right)}{1+\left(\frac{\lambda_X^{Ram}}{\lambda_L}\right)^{-k}} \qquad \text{(EQ 4.34)}$$

This expression is valid for the three Raman wavelengths but, as $n_{H_2O}(R)$ is not constant, the retrieve of $\alpha^{aer}(\lambda_L,R)$ from the water vapor Raman signal is more difficult than the one with oxygen and nitrogen.

We can also retrieve the aerosol extinction for the three Raman shifted wavelengths relative to O_2, N_2 and H_2O by combining this (EQ 4.34) with (EQ 4.32):

$$\alpha^{aer}(\lambda_X^{Ram},R)=\left(\frac{\lambda_X^{Ram}}{\lambda_L}\right)^{-k}\frac{\frac{\partial}{\partial R}\ln\left(\frac{n_X(R)}{R^2P_X(R)}\right)-\left(\alpha^{molec}(\lambda_L,R)+\alpha^{molec}(\lambda_X^{Ram},R)\right)}{1+\left(\frac{\lambda_X^{Ram}}{\lambda_L}\right)^{-k}} \qquad \text{(EQ 4.35)}$$

The empirical retrieve

The most used one [Kruse, 1963 #195] is given by the following formula for visual clear air:

$$\alpha^{aer}(\lambda_i,R)\simeq\alpha_{scatt}^{aer}(\lambda_i,R)=\frac{3.91}{\mathrm{V_M}}\left(\frac{550}{\lambda_i\,[nm]}\right)^{q} \qquad \text{(EQ 4.36)}$$

With $q=0.585\left(V_M\,[km]\right)^{\frac{1}{3}}$ for $V_M\le 6\,km$, where $\mathrm{V_M}$ is the atmospheric visibility.

q = 1.3 in average seeing conditions.

A more accurate discussion on the different cases and values of q was proposed by Woodman [Woodman, 1974 #199].

The "lidar ratio" approach

Another possible approach was given as a result in the chapter 6 p 107 (Applied Optics article) and, in order to develop this approach, two parameters must first be defined.

- The total lidar ratio e is defined as the ratio between the total scattering coefficient and the total backscattering coefficient, at the pump wavelength λ_L:

$$e=\frac{\alpha_{scatt}^{atmos}(\lambda_L,R)}{{}^{\pi}\beta_{scatt}^{atmos}(\lambda_L,R)}=\frac{\alpha_{Rayl}^{molec}(\lambda_L,R)+\alpha_{Mie}^{aer}(\lambda_L,R)}{{}^{\pi}\beta_{Rayl}^{molec}(\lambda_L,R)+{}^{\pi}\beta_{Mie}^{aer}(\lambda_L,R)} \qquad \text{(EQ 4.37)}$$

where the molecular backscattering coefficient ${}^{\pi}\beta_{Rayl}^{molec}(\lambda_L,R)$ is defined as:

$${}^{\pi}\beta_{Rayl}^{molec}(\lambda_L,R)=n_{atmos}(R)\,{}^{\pi}\sigma_{Rayl}^{molec}(\lambda_L,R) \qquad \text{(EQ 4.38)}$$

- The backscattering ratio is defined as the ratio between the total backscattering coefficient and the molecular backscattering one, again at the pump wavelength λ_L:

$$b=\frac{{}^{\pi}\beta_{scatt}^{atmos}(\lambda_L,R)}{{}^{\pi}\beta_{scatt}^{molec}(\lambda_L,R)}=\frac{{}^{\pi}\beta_{Rayl}^{molec}(\lambda_L,R)+{}^{\pi}\beta_{Mie}^{aer}(\lambda_L,R)}{{}^{\pi}\beta_{Rayl}^{molec}(\lambda_L,R)} \qquad \text{(EQ 4.39)}$$

We can deduce, by combining (EQ 4.37) and (EQ 4.39):

$$\alpha_{Rayl}^{molec}(\lambda_L,R)+\alpha_{Mie}^{aer}(\lambda_L,R)=e\cdot b\;{}^{\pi}\beta_{Rayl}^{molec}(\lambda_L,R) \qquad \text{(EQ 4.40)}$$

With (EQ 4.26), (EQ 4.38)and (EQ 4.4) p 66 we can retrieve the molecular backscattering coefficient:

$$^{\pi}\beta_{Rayl}^{molec}(\lambda_L, R) = \frac{3}{8\pi}\alpha_{Rayl}^{molec}(\lambda_L, R) \qquad \text{(EQ 4.41)}$$

Then by combining (EQ 4.41) with (EQ 4.40) we have:

$$\alpha_{Mie}^{aer}(\lambda_L, R) = \left(\frac{3}{8\pi}e \cdot b - 1\right)\alpha_{Rayl}^{molec}(\lambda_L, R) \qquad \text{(EQ 4.42)}$$

We now have to derive this aerosol scattering coefficient in case of another wavelength λ_i. In the molecular case (EQ 4.24) or (EQ 4.25) p 72 gives us, on a first approximation, a $\frac{1}{\lambda_i^4}$ dependence for the molecular scattering extinction coefficient. We then can write:

$$\alpha_{Rayl}^{molec}(\lambda_i, R) = \left(\frac{\lambda_L}{\lambda_i}\right)^4 \alpha_{Rayl}^{molec}(\lambda_L, R) \qquad \text{(EQ 4.43)}$$

For the aerosol case, the (EQ 4.32) p 76 gives us a $\frac{1}{\lambda_i^k}$ dependence for the aerosol scattering extinction term:

$$\alpha_{Mie}^{aer}(\lambda_i, R) = \left(\frac{\lambda_L}{\lambda_i}\right)^k \alpha_{Mie}^{aer}(\lambda_L, R) \qquad \text{(EQ 4.44)}$$

Taking these two last (EQ 4.43) and (EQ 4.44) inside (EQ 4.42) gives the relation of interest:

$$\alpha_{Mie}^{aer}(\lambda_i, R) = \left(\frac{3}{8\pi}e \cdot b - 1\right)\left(\frac{\lambda_L}{\lambda_i}\right)^{k-4} \alpha_{Rayl}^{molec}(\lambda_i, R) \qquad \text{(EQ 4.45)}$$

We can also write the difference of the aerosol contribution for the N_2 / O_2 wavelength pair as it appears in the ozone retrieve, and N_2 / O_2 plus N_2 / H_2O in the water vapor retrieve:

$$\frac{\alpha_{Mie}^{aer}(\lambda_{O_2}^{Ram}, R) - \alpha_{Mie}^{aer}(\lambda_{N_2}^{Ram}, R)}{\alpha_{Rayl}^{molec}(\lambda_{O_2}^{Ram}, R) - \alpha_{Rayl}^{molec}(\lambda_{N_2}^{Ram}, R)} = \left(\frac{3}{8\pi}e \cdot b - 1\right)\lambda_L^{k-4}\frac{\left(\lambda_{O_2}^{Ram}\right)^{-k} - \left(\lambda_{N_2}^{Ram}\right)^{-k}}{\left(\lambda_{O_2}^{Ram}\right)^{-4} - \left(\lambda_{N_2}^{Ram}\right)^{-4}} \qquad \text{(EQ 4.46)}$$

and:

$$\frac{\alpha_{Mie}^{aer}(\lambda_{H_2O}^{Ram}, R) - \alpha_{Mie}^{aer}(\lambda_{N_2}^{Ram}, R)}{\alpha_{Rayl}^{molec}(\lambda_{H_2O}^{Ram}, R) - \alpha_{Rayl}^{molec}(\lambda_{N_2}^{Ram}, R)} = \left(\frac{3}{8\pi}e \cdot b - 1\right)\lambda_L^{k-4}\frac{\left(\lambda_{H_2O}^{Ram}\right)^{-k} - \left(\lambda_{N_2}^{Ram}\right)^{-k}}{\left(\lambda_{H_2O}^{Ram}\right)^{-4} - \left(\lambda_{N_2}^{Ram}\right)^{-4}} \qquad \text{(EQ 4.47)}$$

As said before, the value k = 1 is the generally accepted value for normal atmospheric conditions.

Comparisons

This aerosol parameter is one of the most complicated to be discussed. One should remember that a good theoretical approach to this problem can only be made by a numerical simulation. The value given by mean of the lidar retrieve should be the best one, based on "in situ" measurements. Nevertheless a range of magnitude can be given by these different aerosol retrieves. In the Figure 4-3 a comparison is made between the Kruse empirical retrieve and the "lidar ratio" approach one. The influence of the visibility parameter V_M, as well as the total lidar ratio e, the backscattering ratio b and exponent term k are considered. As the equation (EQ 4.45) contains the terms e.b, we may consider the dependence on e or b. Here we choose to vary the value of e. The Rayleigh term in the Mie extinction equation (EQ 4.45) is calculated following the (EQ 4.7) p 68, and parameters are set to 20 °C for the temperature, P = 970 mbar for the pressure and a mixing ratio of 360 ppm for CO_2.

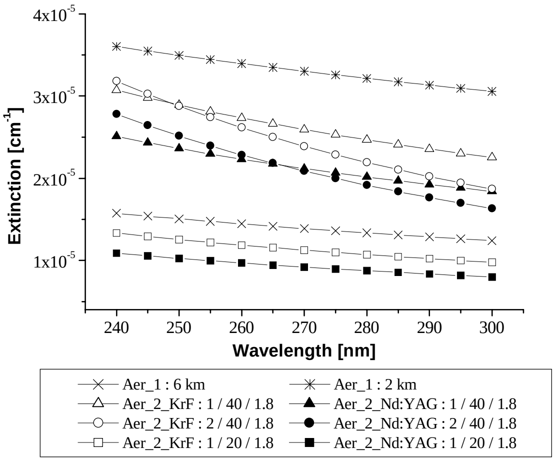

FIGURE 4-3. Comparison of two methods to retrieve the aerosol extinction coefficient

In this graph the two curves related to "Aer_1 : V_M" are calculated under the Kruse model (see (EQ 4.36) p 77), and the four curves related to "Aer_2_X : k / e / b" are calculated under the "lidar ratio" approach (see (EQ 4.45) p 78) and individualized for the Nd:YAG or KrF configuration (the letter X). "Normal" atmospheric conditions correspond to a visibility of 6 km and to the set of values 1 / 20 / 1.8. It gives the three lower curves and an extinction coefficient of approximately $1x10^{-5}$ cm^{-1}. As soon as we decrease the visibility, or increase the lidar ratio, the effect is an atmosphere with a higher aerosol density. The result can be seen in the graph with curves shifted to the upper values. In the "lidar ratio" approach the two extinction curves corresponding to the KrF or Nd:YAG laser are well separated and denote that:

$$\frac{\lambda_{KrF}^{pump}}{\lambda_{N_2}^{Raman}(with\ KrF)} = \frac{248.40}{264.00} = 0.941 > \frac{\lambda_{Nd:YAG}^{pump}}{\lambda_{N_2}^{Raman}(with\ Nd:YAG)} = \frac{266.04}{283.63} = 0.938$$

The parameter k has an influence on the slope, and negative values will invert it. The related curve to the KrF case (resp Nd:YAG) rotates around the point corresponding to the pump wavelength. This behavior implies no change in the extinction coefficient at the pump wavelength, and bigger changes around this wavelength.

Taking advantage of KrF or Nd:YAG measurements, we retrieve the vertical profiles of the aerosol extinction coefficient. The Nd:YAG "averaged file" is taken from the second intercomparison measurement campaign in the EPFL area on April 08th, 2000, and corresponds to the 11h30-12h measurements. For the KrF case, with 10 Hz repetition rate, the "averaged file" corresponds to the 16h30-17h measurements made on September 15th, 2000. The data treatment was performed with two different binnings. A binning of 2 plus the sliding average, which gives a vertical range resolution of 22 m and a first retrieved point at 370 m, and a binning of 6 plus the sliding average, which gives a vertical range resolution of 67 m and a first retrieved point at 465 m. As the N_2 Raman signal has the highest level and SNR (see the following paragraph), this signal was chosen for the aerosol retrieve procedure. The result is shown in Figure 4-4.

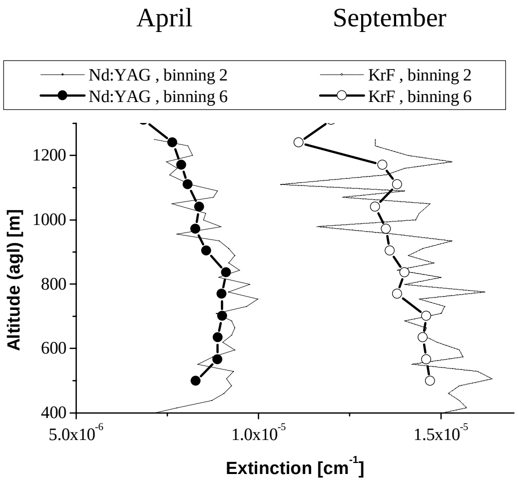

FIGURE 4-4. Two typical examples of lidar aerosol extinction coefficients for the Nd:YAG and the KrF configuration

Compared with the theoretical results presented before in Figure 4-3 it shows similar values to the "normal" case, for $V_M = 6$ km or k = 1 / e = 20 / b = 1.8, between $1x10^{-5}$ and $1.5x10^{-5}$. Also the shift between the KrF and Nd:YAG retrieves can be seen in both figures, with the "lidar ratio" approach in the theoretical case.

Nevertheless this results and comparisons are indicatives, and big differences can occur depending on the set parameters. The lidar retrieve takes also into account the aerosol absorption, which is not the case in the theoretical retrieve. Figure 4-4 should be regarded as a good first approximation of the aerosol contribution based on this Raman lidar approach.

4.3. Corrections

4.3.1. The ozone

Following the theoretical development we have, from (EQ 2.19) p 42, for the O_3 concentration retrieve:

$$n_{O_3}(R)=\frac{\frac{\partial}{\partial R}\left(\ln\frac{P_{N_2}(R)}{P_{O_2}(R)}\right)}{\sigma^{O_3}_{abs}(\lambda^{Ram}_{O_2},R)-\sigma^{O_3}_{abs}(\lambda^{Ram}_{N_2},R)}-\underbrace{\frac{\left(\widetilde{\alpha^{atmos}}\left(\lambda^{Ram}_{O_2},r\right)-\widetilde{\alpha^{atmos}}\left(\lambda^{Ram}_{N_2},r\right)\right)}{\sigma^{O_3}_{abs}(\lambda^{Ram}_{O_2},R)-\sigma^{O_3}_{abs}(\lambda^{Ram}_{N_2},R)}}_{\delta_{corr}(O_3)} \qquad \text{(EQ 4.48)}$$

With the terms explained in the paragraph 2.3.2. “The ozone retrieve”, p 42, and the ozone correction term defined as:

$$\delta_{corr}(O_3)=\frac{\left(\begin{array}{l}\alpha^{molec}_{Rayl}(\lambda^{Ram}_{O_2},R)-\alpha^{molec}_{Rayl}(\lambda^{Ram}_{N_2},R)\\+\alpha^{aer}(\lambda^{Ram}_{O_2},R)-\alpha^{aer}(\lambda^{Ram}_{N_2},R)\\+\sum\limits_{\{Y'\}=\{Y-O_3\}}n_{Y'}(R)\left(\sigma^{Y'}_{abs}(\lambda^{Ram}_{O_2},R)-\sigma^{Y'}_{abs}(\lambda^{Ram}_{N_2},R)\right)\end{array}\right)}{\sigma^{O_3}_{abs}(\lambda^{Ram}_{O_2},R)-\sigma^{O_3}_{abs}(\lambda^{Ram}_{N_2},R)} \qquad \text{(EQ 4.49)}$$

Under the conditions of the Table 4-1 this ozone corrective term is represented, for the KrF laser tuned at 248.4 nm and the Nd:YAG one, versus the altitude in the Figure 4-5..

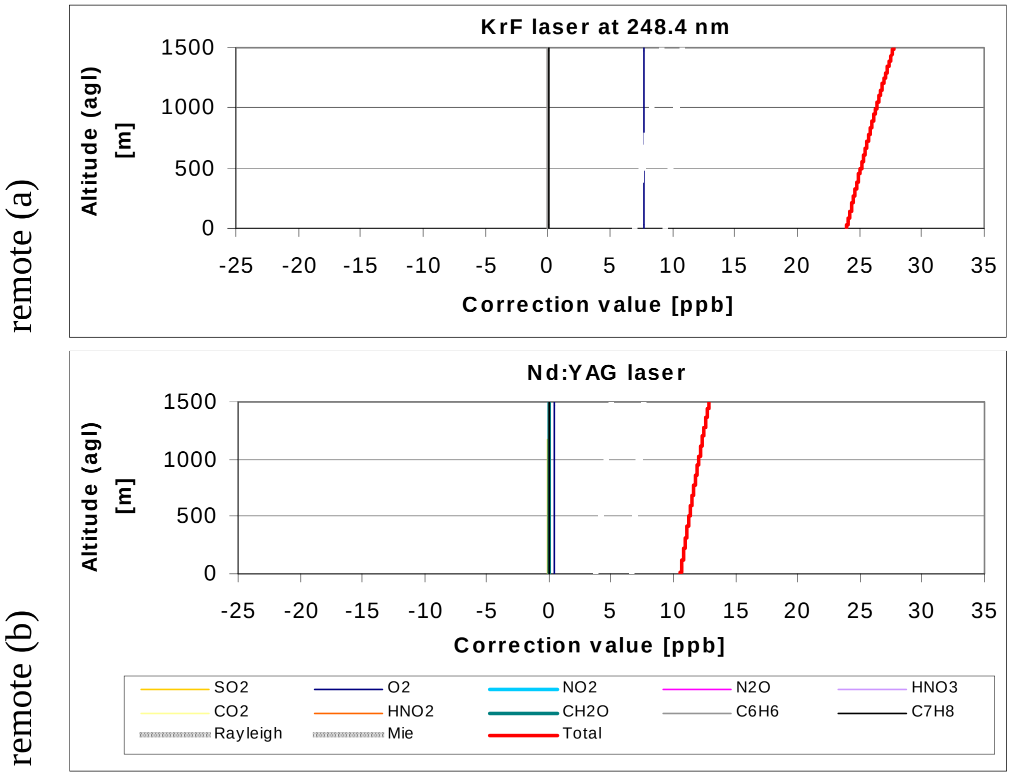

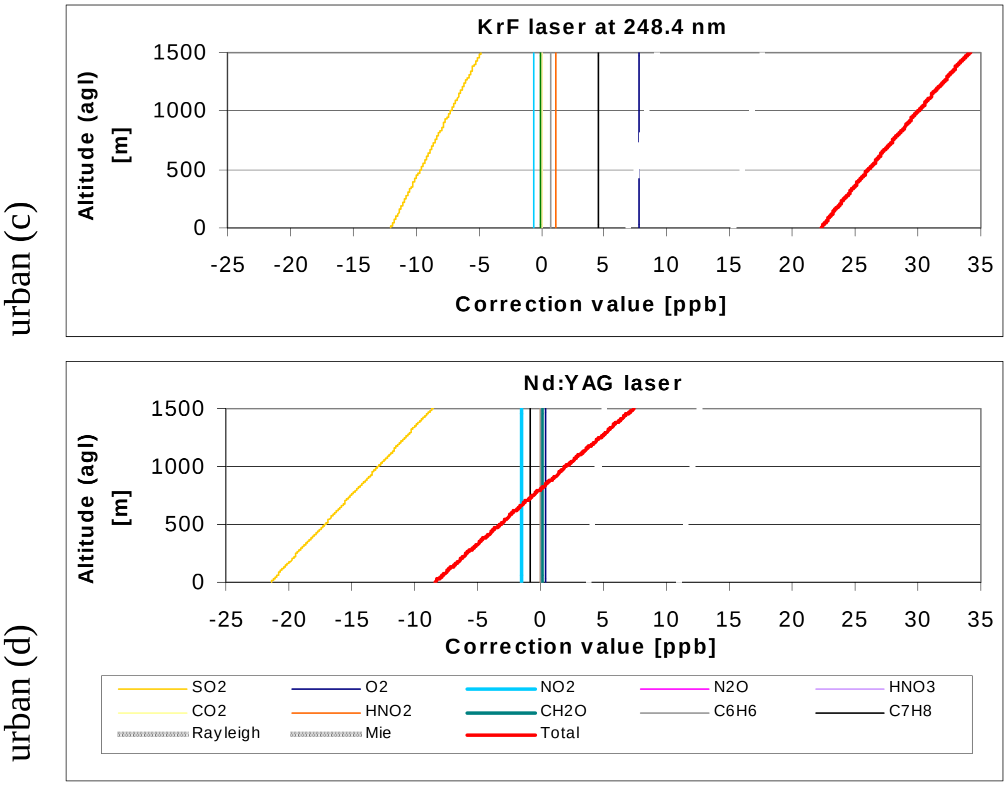

FIGURE 4-5. Corrections to the O_3 concentration retrieve

In these graphs the SO_2 profile described at the end of the paragraph 4.2. “Precision in the correction terms”, p 66 is used.

As a general remark from Figure 4-5 we may conclude that, looking to the total corrective term, smaller corrections in the Nd:YAG configuration than in the KrF one are needed. The term $\Delta\sigma = \sigma_{abs}^{O_3}(\lambda_{O_2}^{Ram}) - \sigma_{abs}^{O_3}(\lambda_{N_2}^{Ram})$ in the denominator of the ozone corrective term $\delta_{corr}(O_3)$ given by the (EQ 4.49) can explain this behavior. It takes into account the difference of the ozone absorption cross-section at the O_2 Raman shifted wavelength and at the N_2 one. In the KrF case we have $\Delta\sigma(\text{KrF @248.4 nm}) = 1.39 \cdot 10^{-18}\ \text{cm}^2.\text{molec}^{-1}$ and in the Nd :YAG one this term becomes $\Delta\sigma(\text{Nd:AG}) = 1.97 \cdot 10^{-18}\ \text{cm}^2.\text{molec}^{-1}$. So, going from the Nd:YAG configuration to the KrF one, the corrective factor has to be multiplied by a factor of 1.4 as a first approximation. But other contributions in the numerator can change this behavior, due to the wavelength dependence of its different components. As soon as the concentrations become higher, like in the Figure 4-5 (c) and (d), care as to be taken. We can see that a bigger individual correction, like the SO_2 one in Figure 4-5 (d) for the Nd:YAG case, can help to minimize the total correction.

4.3.2. The water vapor

The H_2O mixing ratio, with respect to N_2, is given by (EQ 2.23) p 43.

$$\begin{aligned}
\xi_{H_2O}^{(N_2)}(R) = & \frac{M_{H_2O}}{M_{dry\ air}} \chi_{N_2} \frac{P_{H_2O}}{P_{N_2}}(R) \frac{K_{N_2}}{K_{H_2O}} \frac{{}^{\pi}\beta_{N_2}^{Ram}}{{}^{\pi}\beta_{H_2O}^{Ram}} && \leftarrow \text{zero-order} \\
& \left.\begin{aligned}
& \times \exp\left\{ \left(\sigma_{abs}^{O_3}(\lambda_{H_2O}^{Ram}) - \sigma_{abs}^{O_3}(\lambda_{N_2}^{Ram}) \right) \int_0^R n_{O_3}(r)\,dr \right\} && \leftarrow \mathrm{O_3}\ \text{interference} \\
& \times \exp\left\{ \int_0^R \left(\widetilde{\alpha^{atmos}}\left(\lambda_{H_2O}^{Ram}, r\right) - \widetilde{\alpha^{atmos}}\left(\lambda_{N_2}^{Ram}, r\right) \right) dr \right\} && \leftarrow \text{Other interferences}
\end{aligned}\right\} \delta_{corr}(H_2O)
\end{aligned} \qquad \text{(EQ 4.50)}$$

The terms are defined in related pages of the paragraph 2.3.3. “The water vapor retrieve (first formulation)”, p 42.

If the "O_3 interference term" is retrieved with the lidar, it then gives the final expression for the water vapor mixing ratio:

$$\begin{aligned}
\xi_{H_2O}^{(N_2)}(R) = & K_{cal}^{N_2} \frac{P_{H_2O}(R)}{P_{N_2}(R)} \left[\frac{P_{O_2}(R)}{P_{N_2}(R)} \right]^{\widehat{\Delta}\sigma_{abs}^{O_3}} \\
& \times \exp\left\{ \int_0^R \left[\left(\widetilde{\alpha^{atmos}}\left(\lambda_{H_2O}^{Ram}, r\right) - \widetilde{\alpha^{atmos}}\left(\lambda_{N_2}^{Ram}, r\right) \right) - \widehat{\Delta}\sigma_{abs}^{O_3} \left(\widetilde{\alpha^{atmos}}\left(\lambda_{N_2}^{Ram}, r\right) - \widetilde{\alpha^{atmos}}\left(\lambda_{O_2}^{Ram}, r\right) \right) \right] dr \right\}
\end{aligned} \qquad \text{(EQ 4.51)}$$

with $\widehat{\Delta}\sigma_{abs}^{O_3} = \dfrac{\sigma_{abs}^{O_3}(\lambda_{H_2O}^{Ram}) - \sigma_{abs}^{O_3}(\lambda_{N_2}^{Ram})}{\sigma_{abs}^{O_3}(\lambda_{N_2}^{Ram}) - \sigma_{abs}^{O_3}(\lambda_{O_2}^{Ram})}$ and where $K_{cal}^{N_2}$ is a constant.

The same conditions as for the previous ozone corrective term discussion are taken here. The H_2O corrective terms are represented versus the altitude in the following Figure 4-6.

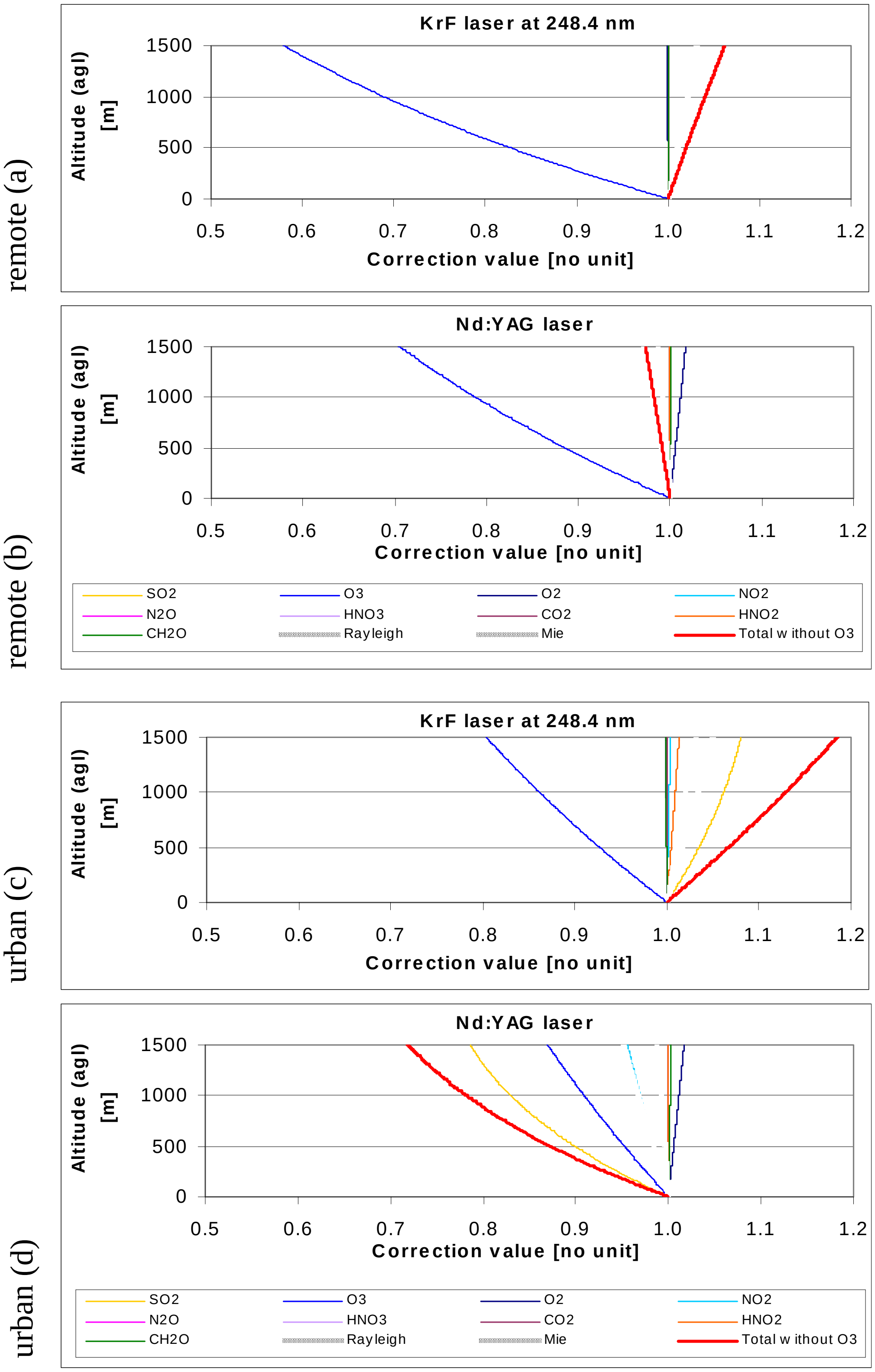

FIGURE 4-6. Corrections to the H_2O mixing ratio retrieve

In these figures the total correction term doesn't take into account the O_3 correction one. This is due to the fact that with our - three Raman backscattered signals - lidar, we can perform an auto-correction for the ozone. As the ozone correction term is the most important contribution for all the situations exposed in Figure 4-6, the auto-correction by mean of the lidar will be the best choice to calculate this contribution.
Speaking now about the total correction term (without O_3), for the "remote" case, a smaller correction is required in the Nd:YAG configuration than in the KrF one. There is essentially no need for any correction, apart from the O_3 auto-correction (by the lidar), in the Nd:YAG configuration and the KrF one requires a small correction. For the "urban" case, the SO_2 contribution is the main one, under the concentration given in Table 4-1, and the total correction to be applied is bigger for the Nd:YAG case than for the KrF one.

Both of these exposed corrections, for the O_3 and H_2O concentration retrieves, can be exported in an Excel file to the LabVIEW data treatment program. It provides the scattering and absorption corrections for these retrieves and can be used for the data treatment of lidar signals.

4.3.3. The aerosol correction

To conclude this "correction" analysis paragraph we will give an example of intercomparison on the aerosol correction (for the O_3 concentration retrieve).

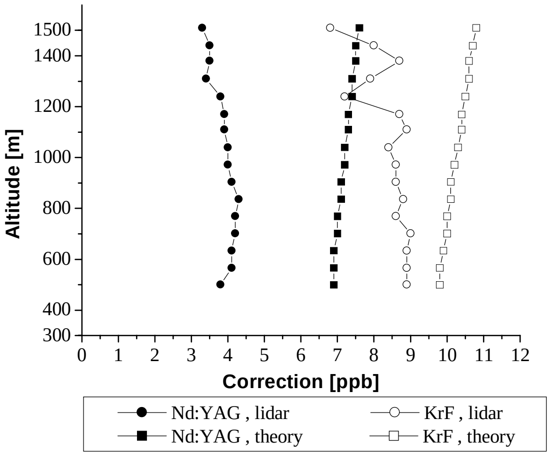

FIGURE 4-7. Comparison of theoretical and experimental aerosol corrections

In Figure 4-7, the theoretical curves for the correction due to the aerosol are taken from Figure 4-5, p 82. Concerning the lidar retrieved values, although the curves seem to be similar to the ones in Figure 4-4, p 80 (aerosol extinctions), the correction value was calculated, in both KrF and Nd:YAG cases, with:

$$\frac{\alpha^{aer}(\lambda_{O_2}^{Ram}, R) - \alpha^{aer}(\lambda_{N_2}^{Ram}, R)}{\sigma_{abs}^{O_3}(\lambda_{O_2}^{Ram}, R) - \sigma_{abs}^{O_3}(\lambda_{N_2}^{Ram}, R)} \qquad \text{(EQ 4.52)}$$

The comparison between the theory and the experiment shows results of the same order of magnitude, and the need of a higher aerosol correction for the KrF configuration compared to the Nd:YAG one. This fact can be a limiting factor in case of high aerosol loading if the lidar is set in the KrF configuration. Concerning the validity of the results, the theoretical results were derived from the Kruse's model, which is a simple model to give a rough approximation for the aerosol extinction. The presented theoretical results give then an order of magnitude for this effect. Concerning the experimental results, they should normally give better results, more relevant to what occurs in the atmosphere. This is due to the theory used to treat the experimental datas. Apart problems on the signals similar to the ones for the O_3 concentration retrieve (SNR, crosstalks...), one major assumption is made with the value of the constant k. All the other terms in the calculation retrieve, like the Rayleigh contribution, are well known.

4.4. SNR on the Raman signals

The conversion of the weak backscattered light intensity into an electrical signal is made by a very sensitive device, the photomultiplier. The measured light intensity is then affected by the photons to electrons aleatory processes, and by the internal amplification of the emitted electrons.

If we assume that the received number of photons is small enough to approximate the detected signal by a Poisson distribution, the signal-to-noise ratio (SNR), for a given lidar signal, can be approximated by the following equation [*Bösenberg et al.*, 1997]:

$$SNR_P(R) = \frac{\sqrt{N} \cdot P(R)}{\sqrt{P(R) + P_b}} \qquad \text{(EQ 4.53)}$$

Where N is the number of shots, P(R) the lidar received signal, including all noises, and P_b the measured signal due to the background skylight. This value P_b is related to the detection channel of interest (for example, due to the wavelength difference of the N_2 Raman shifted wavelength and the O_2 one, P_b will not have the same value for the N_2 Raman channel than for the O_2 Raman one).

For P_b we take the mean value of the residual signal on the last bins of the lidar signal P(R). This method gives in fact a bigger value to P_b. It includes the background skylight, but also others contributions like the signal induced by the electronic noises (like the shot noise of the PMT) or by the residual light in the laboratory. The resulting SNR will then be smaller than with the sole value of the background skylight. Nevertheless, it gives a minimum value to the SNR measurements and it is applied here.

If we strictly want to apply (EQ 4.53) the following procedure has to be completed. Two measurements of 4000 shots each have to be made in two special cases.

First measurement is made with all the lidar system running, but with the emitted beam blocked. It gives a signal, called P_{tot}, which is the sum of the signal P_b due to the background skylight and all other noise signals induced by the electronic, the residual laboratory light (peak of the emitted laser pulse and all other sources). These latter contributions are represented by $P_{elec+res}$.

Second measurement is made with the same conditions as in the first measurement but, additionaly, the reception mirror is also covered to prevent light detection. The resulting signal is given by the electric noise and the residual laboratory light, called $P_{elec+res}$.

From these two measurements the measured signal due to the background skylight P_b can be deduced by: $P_b = P_{tot} - P_{elec+res}$. But this method depends on the different intensity values of the solar background for specific conditions: day, night, clouds. It implies to have a series of specific values for P_b.

To illustrate this, typical series and intercomparisons will be shown. All series are treated in photon counting mode. For the Nd:YAG case, the files are taken from the second intercomparison measurement campaign in the EPFL on April 08th, 2000. The single file corresponds to the 11h34 one (1 x 4000 shots) and the averaged file corresponds to the 11h30-12h measurements (4 x 4000 shots). For the KrF case, with 10 Hz repetition rate, the averaged file corresponds to the 16h30-17h measurements made on September 15th, 2000.
For the O_3 concentration retrieve, with a binning of 6 and the sliding average, the resulting range resolution is 67 m. The first SNR measurement point is at 465 m. For the H_2O mixing ratio retrieve, the binning is taken equal to 2. With the sliding average, the resulting range resolution is 22 m. The first measurement point is at 308 m.

The Figure 4-8 shows the comparison between a "single" 4000 shots file and a "summed" 4 x 4000 shots file.

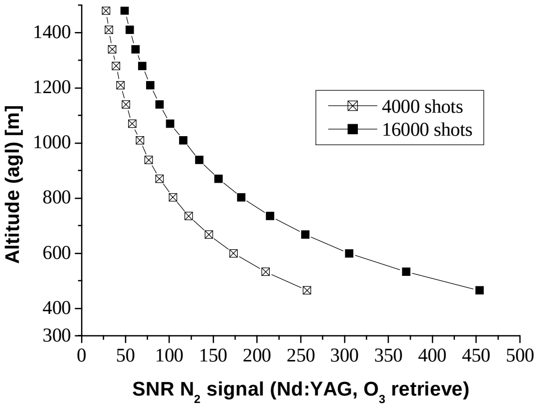

FIGURE 4-8. SNR comparison for two numbers of laser shots

For this case the lidar was run in the Nd:YAG configuration, and the SNR calculation, on the N_2 Raman signal, is based on the parameters (like the binning) defined for the O_3 retrieve. The SNR for the "averaged file" case is multiplied by nearly a factor of 2 with respect to the one for a "single file". This behavior is due to the factor $\sqrt{N}$ in (EQ 4.53), and a perfect system, with the same experimental conditions during the measurement, would give a factor equal to 2.

Figure 4-9 illustrates the Raman signal levels difference. Here the Nd:YAG configuration was taken and the SNR calculations made for the O_3 retrieve parameters and a "averaged file". Due to physical parameters (like the Raman backscattering coefficients, the O_3 absorption cross-section or the O_2, N_2 and H_2O concentrations) the received N_2 Raman backscattered signal is bigger than the O_2, this latter being bigger than the H_2O one. "Artificial" parameters like, for example, the relative sensitivity of the PMTs are not taken into account.

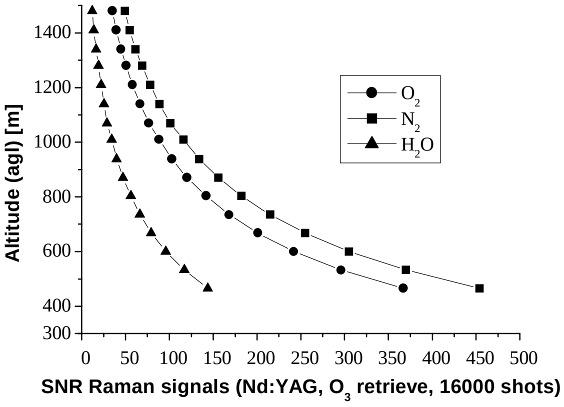

FIGURE 4-9. SNR of the Raman signals

The SNR of the N_2 Raman signal is about 1.2 times bigger than the O_2 one, and about 3 times bigger than the H_2O one and these values slowly increase with the altitude, probably due to the higher N_2 Raman signal level compared with the others. To overcome this, the O_2 and N_2 PMTs were chosen with similar sensitivities, and the H_2O one with the best sensitivity.

As the O_3 concentration and the H_2O mixing ratio are retrieved with different parameters, like the binning, different SNR are expected for a same Raman signal. Figure 4-10 takes the example of the N_2 Raman "averaged file" acquired with the Nd:YAG configuration.

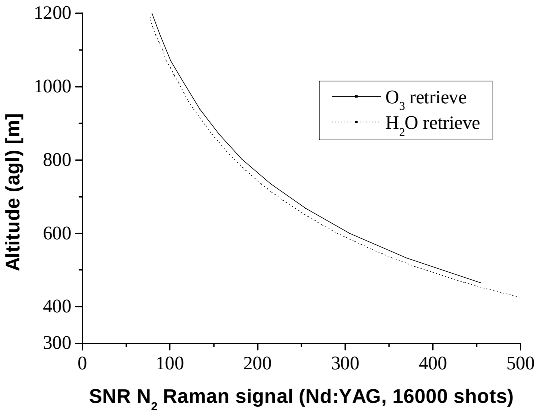

FIGURE 4-10. SNR comparison between the O_3 retrieve with a binning of 6 and the H_2O retrieve with a binning of 2

The difference between the two situations is small. The O_3 retrieve case has a SNR 4 % higher than the H_2O one, which is due to a higher binning value for the O_3 retrieve.

Taking now advantage of the two laser sources used to perform measurements, a Nd:YAG and a KrF, we naturally compare the SNR of both systems. The SNR in the Nd:YAG configuration is higher by a factor of approximately 1.6 compared with the KrF one.

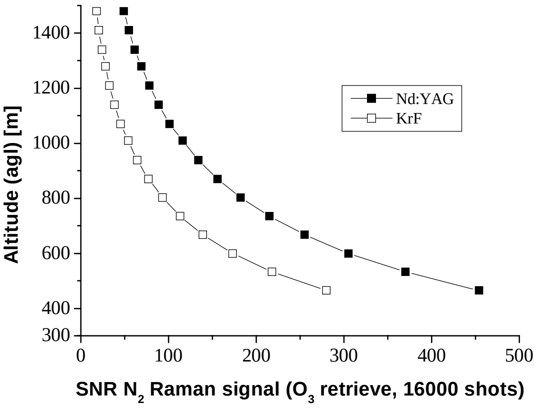

FIGURE 4-11. SNR comparison between the Nd:YAG and KrF configurations

The main reason is due to the O_3 absorption in the atmosphere. Referring to its spectrum in the UV [*Daumont et al.*, 1992], we can see that, due to higher absorption cross-sections, the pump beam and the related Raman backscattered signals are more absorbed for the KrF case than for the Nd:YAG one. The result is lower Raman signals for the KrF case. The same phenomenon occurs for the O_2 absorption in the atmosphere [*Mérienne et al.*, 2000], [*Bernath et al.*, 1998] showing a bigger absorption in the KrF case than in the Nd:YAG one. The Rayleigh scattering, with its law in $1 / \lambda^4$ (in a first approximation), is also a reason for a bigger attenuation of the KrF related wavelengths in comparison to the Nd:YAG ones.

We have then to look the energy per pulse of the two different lasers used, to see if the worse atmospheric situation (related to the KrF configuration) is compensated with a higher energy per pulse value.The KrF laser uses a special unstable resonator to decrease its divergence, and it causes a decrease in the output energy from the initial configuration. In the best situations, with a new fill of gases and thyratron high voltage at its maximum, an energy of 150 mJ per pulse can be expected. But, due to gases lifetime, the energy falls depending on the time of use, and we also never use the laser with the high voltage at its maximum. In most cases we use energy / pulse values for the KrF laser similar or lower than those of the Nd:YAG laser at 120 mJ per pulse.

4.5. Statistical errors

4.5.1. The ozone concentration

Taking the ozone retrieve formula given by (EQ 2.19) p 42, which is a "standard" DIAL equation modified in case of Raman signal, we can deduce the statistical error on the ozone concentration, assuming that the Raman backscattered signals are not correlated [*Bösenberg et al.*, 1997]:

$$\varepsilon_{O_3}^{stat}(R) = \frac{1}{n_{O_3}\left(\sigma_{abs}^{O_3}(\lambda_{O_2}^{Ram}) - \sigma_{abs}^{O_3}(\lambda_{N_2}^{Ram})\right)\Delta R}\sqrt{\frac{1}{N}\left(\frac{2}{SNR_{P_{O_2}}^2(R)} + \frac{2}{SNR_{P_{N_2}}^2(R)}\right)} \qquad \text{(EQ 4.54)}$$

Where n_{O_3} is the ozone concentration, $\sigma_{abs}^{O_3}(\lambda_{O_2}^{Ram})$ $\left\{resp\ \sigma_{abs}^{O_3}(\lambda_{N_2}^{Ram})\right\}$ is the ozone absorption cross-section at the wavelength $\lambda_{O_2}^{Ram}$ $\left\{resp\ \lambda_{N_2}^{Ram}\right\}$, ΔR the range resolution, N the number of shots and $SNR_{P_{O_2}}(R)$ $\left\{resp\ SNR_{P_{N_2}}(R)\right\}$ the SNR for the lidar signal P_{O_2} $\left\{resp\ P_{N_2}\right\}$.

Note that for the "standard" elastic DIAL case (EQ 4.54) would have included in its denominator an additional factor of 2. This denotes the fundamental difference between the "standard" DIAL and our Raman DIAL method: a probing length twice longer in the first case (probing there and back) than in the second one (probing back).

If Δσ is defined as the difference of the O_3 absorption cross-sections $\sigma_{abs}^{O_3}(\lambda_{O_2}^{Ram}) - \sigma_{abs}^{O_3}(\lambda_{N_2}^{Ram})$, we have for the KrF case $\Delta\sigma(\text{KrF @248.4 nm}) = 1.39 \cdot 10^{-18}\ \text{cm}^2.\text{molec}^{-1}$ and for the Nd :YAG $\Delta\sigma(\text{Nd:AG}) = 1.97 \cdot 10^{-18}\ \text{cm}^2.\text{molec}^{-1}$. This term Δσ is then multiplied by a factor of 1.4, and the resulting statistical error will then be multiplied by a factor of 0.7 if we go from the KrF configuration to the Nd:YAG one.

To have an order of magnitude we take also the result of the SNR comparison between the Nd:YAG configuration and the KrF one for the Raman N_2 channel (see explainations related to Figure 4-10, p 88). It gives a SNR 1.6 times higher in the Nd:YAG case compared to the KrF one. The statistical error is then multiplied by a factor of 0.6 between the KrF and Nd:YAG cases.The resulting statistical error, taking into account these two contributions and supposing that the SNR between the N_2 and O_2 Raman signals are quite similar (see explainations related to Figure 4-8, p 87), will then be divided by approximately a factor of 2 if we go from the KrF configuration to the Nd:YAG one.

The following Figure 4-12 illustrates the difference in the statistical errors for the Nd:YAG and KrF configurations.

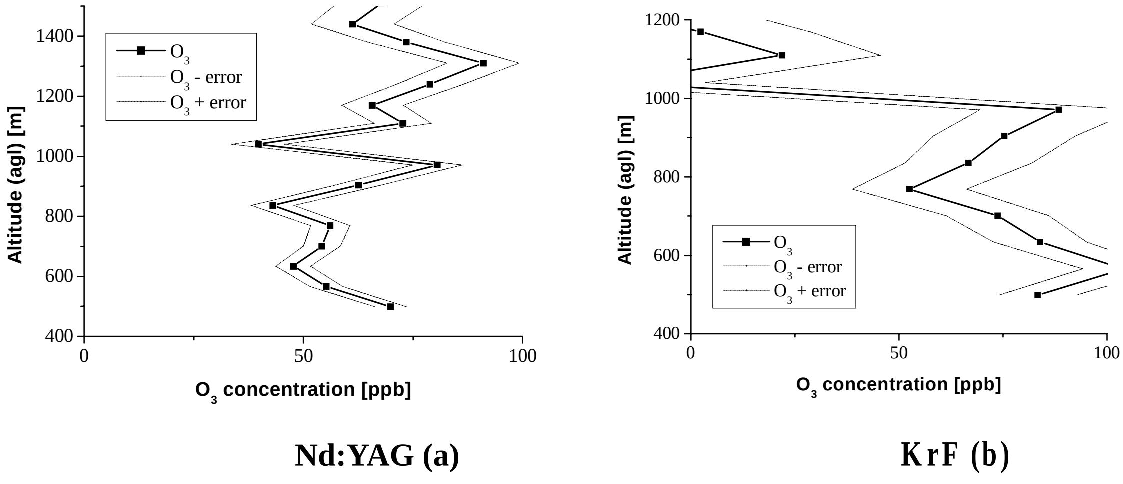

Nd:YAG (a) **KrF (b)**

FIGURE 4-12. Statistical error for an O_3 concentration retrieve

Figure 4-12 (a) shows the Nd:YAG 11h30-12h photon counting averaged file taken from the second intercomparison measurement campaign in the EPFL area, 08th of April 2000. Figure 4-12 (b) shows the 16h30-17h photon counting averaged file for the KrF case, with 10 Hz repetition rate, resulting from measurements made the 15th of September 2000. Both averaged files were treated with the same conditions, giving for the O_3 retrieve a range resolution of 67 m.
In this comparison we can see the expected bigger statistical error and the less "smoothed" retrieve for the KrF configuration. A trial to solve these problems will be exposed in the paragraph 4.6. “The KrF "repetition rate" experiment”, p 92.

4.5.2. The water vapor mixing ratio

The relative error on the H_2O mixing ratio have been derived by Renaut [*Renaut and Capitini*, 1988], if the PMT dark current and the skylight background are neglected:

$$\varepsilon_{H_2O}^{rel}(R) = \frac{c}{2\,\Delta R}\sqrt{\frac{1}{N}\left(\frac{1}{P_{H_2O}(R)} + \frac{1+\widehat{\Delta\sigma}_{abs}^{O_3}}{P_{N_2}(R)} + \frac{\widehat{\Delta\sigma}_{abs}^{O_3}}{P_{O_2}(R)}\right)} \qquad \text{(EQ 4.55)}$$

Where c is the speed of the light, ΔR the range resolution, N the number of shots, $P_{H_2O}\ \{resp\ P_{N_2}, P_{O_2}\}$ the H_2O backscattered Raman signal {resp N_2, O_2}, and $\widehat{\Delta\sigma}_{abs}^{O_3} = \frac{\sigma_{abs}^{O_3}(\lambda_{H_2O}^{Ram}) - \sigma_{abs}^{O_3}(\lambda_{N_2}^{Ram})}{\sigma_{abs}^{O_3}(\lambda_{N_2}^{Ram}) - \sigma_{abs}^{O_3}(\lambda_{O_2}^{Ram})}$ with $\sigma_{abs}^{O_3}(\lambda_X^{Ram})$ is the ozone absorption cross-section at the wavelength λ_X^{Ram} (X : O_2, N_2 or H_2O).
The statistical error can then be deduced by:

$$\varepsilon_{H_2O}^{stat}(R) = n_{H_2O}\,\frac{\varepsilon_{H_2O}^{rel}(R)}{100} \qquad \text{(EQ 4.56)}$$

For the KrF case we have $\widehat{\Delta\sigma}_{abs}^{O_3}(KrF\ @\ 248.4\ nm) = 2.35$ and for the Nd:YAG one this term becomes $\widehat{\Delta\sigma}_{abs}^{O_3}(Nd:YAG) = 1.06$. Again the statistical error will be bigger in the KrF case than in the Nd:YAG one.

Figure 4-13 shows the retrieved H_2O mixing ratio for the Nd:YAG 11h30-12h photon counting averaged file taken from the 08th of April 2000 measurement campaign. With the data treatment parameters the resulting range resolution is 22 m. The H_2O mixing ratio retrieve shows a more smoothed curve compared to the O_3 concentration one, even if the H_2O mixing ratio retrieve is made under a lower binning value. This is explained by the derivative method to retrieve the O_3 concentration with respect to the linear one for the H_2O mixing ratio retrieve.

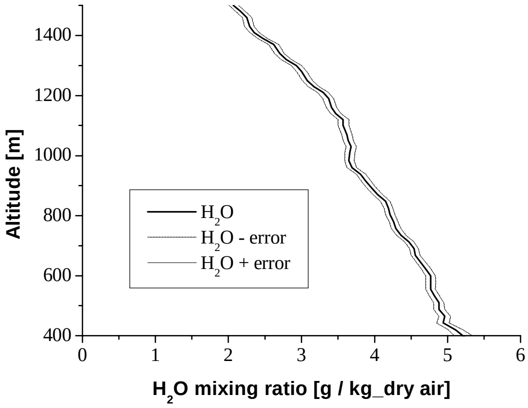

FIGURE 4-13. Statistical error for an H_2O concentration retrieve

4.6. The KrF "repetition rate" experiment

The results from the various campaigns (see the related articles) show a good H_2O mixing ratio comparison with external measurements. For the O_3 concentration the retrieve is more delicate due to the differential form of the retrieve equation (EQ 2.19) p 42, and the results give worse comparisons.

Several attempts were made with the Nd:YAG configuration, changing the position of the lenses inside the bandpass filters tube, the PMTs' voltage, the size of the diaphragms, the telescope type, the licel channels, etc. but without big improvements to the O_3 concentration retrieve.

We took advantage of experiments with a KrF laser to try to overcome this problem in case of the O_3 retrieve. The most convincing result, exposed here, was obtained by changing the repetition rate of the laser. The averaged files shown in Figure 4-14 are related to the 16h30-17h measurements (a) made on September 15th, 2000 for the 10 Hz case, to 17h30-18h (b) for the 20 Hz case, to 18h30-19h (c) for the 40 Hz case, and 19h30-20h (d) for the 80 Hz case. The punctual analyzer (Horiba O_3 analyzer) mounted on the roof of the building where the lidar was installed indicated values of 76 ppb O_3 at 16h falling down to 50 ppb at 20h. This analyzer's values taken at a different altitude than the lidar retrieved ones can just give an indication, but not a comparison even if the mean values of the lidar profiles are similar to the ones given by the punctual analyzer.

The Figure 4-14 shows an expected smoothing of the profiles when the repetition rate increases, and a statistical error which decreases. Although the O_3 concentration retrieve is better with a higher repetition rate, results still have to be improved with the other parameters of the lidar with, perhaps, no significant improvement.

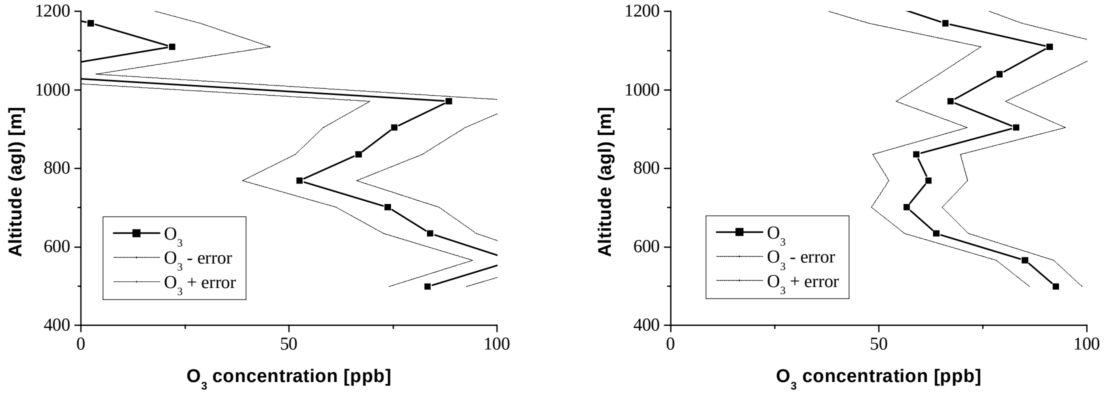

10 Hz (a)

20 Hz (b)

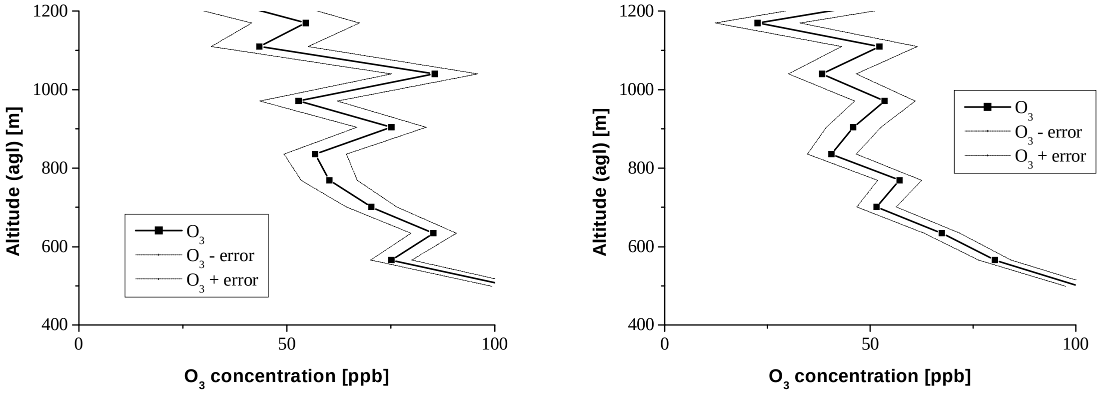

40 Hz (c)

80 Hz (d)

FIGURE 4-14. O_3 retrieve for the KrF laser run at four different repetition rates

4.7. A calibration method to retrieve the influence of O_3 on the H_2O mixing ratio

The calibrating of the H_2O mixing ratio is not difficult in itself, but to retrieve the value of the H_2O mixing ratio correction due to O_3, i.e. $\Delta\xi_{H_2O}^{(N_2)}(R) \equiv \xi_{H_2O}^{(N_2)}(R)\Big|_{O_3\ corr} - \xi_{H_2O}^{(N_2)}(R)\Big|_{O_3\ uncorr}$, is more difficult.

In fact here we take the (EQ 2.22) p 43:

$$\xi_{H_2O}^{(N_2)}(R)=K\frac{P_{H_2O}}{P_{N_2}}(R)\times\exp\left\{\int_0^R\left[\left(\sigma_{abs}^{O_3}(\lambda_{H_2O}^{Ram})-\sigma_{abs}^{O_3}(\lambda_{N_2}^{Ram})\right)n_{O_3}(r)\right]dr\right\}\underbrace{\times\exp\left\{\int_0^R\left[\left(\widetilde{\alpha^{atmos}}\left(\lambda_{H_2O}^{Ram},r\right)-\widetilde{\alpha^{atmos}}\left(\lambda_{N_2}^{Ram},r\right)\right)\right]dr\right\}}_{\Theta(R)} \quad \text{(EQ 4.57)}$$

Then

$$\xi_{H_2O}^{(N_2)}(R)\Big|_{O_3\,corr}=\underbrace{K\frac{P_{H_2O}}{P_{N_2}}(R)\times\Theta(R)}_{\xi_{H_2O}^{(N_2)}(R)\big|_{O_3\,uncorr}}\times\underbrace{\exp\left\{\int_0^R\left[\left(\sigma_{abs}^{O_3}(\lambda_{H_2O}^{Ram})-\sigma_{abs}^{O_3}(\lambda_{N_2}^{Ram})\right)n_{O_3}(r)\right]dr\right\}}_{O_3\ correction\ value} \quad \text{(EQ 4.58)}$$

To calibrate the water vapor mixing ratio several methods are available [*Ferrare et al.*, 1998] like with: - a balloon sonde, - an analyzer mounted on a tower, - making the integral of the mixing ratio to have the precipitable water amount, knowing that it is also possible to retrieve this integrated value with a microwave radiometer or GPS instrument.

We propose here to calibrate with two methods, depending on the chosen "ozone correction" method:

- if this correction is made with a balloon sonde
- if we are in an auto correction mode

Solution n°1: Ozone correction by an external measurement like a balloon sonde

For the uncorrected case we have:

$$\xi_{H_2O}^{(N_2)}(R)\Big|_{O_3\ uncorr}=K\frac{P_{H_2O}}{P_{N_2}}(R)\times\Theta(R) \quad \text{(EQ 4.59)}$$

For the corrected case the calibration procedure takes into account the effect of the ozone from 0 m (AGL) to R_0, first retrieved altitude point by mean of the lidar.

Then rewriting (EQ 4.58):

$$\xi_{H_2O}^{(N_2)}(R)\Big|_{O_3\,corr}=K\underbrace{\frac{P_{H_2O}}{P_{N_2}}}_{lidar}(R)\times\Theta(R)\times\exp\left\{\int_0^R\left[\left(\sigma_{abs}^{O_3}(\lambda_{H_2O}^{Ram})-\sigma_{abs}^{O_3}(\lambda_{N_2}^{Ram})\right)\underbrace{n_{O_3}(r)}_{balloon}\right]dr\right\} \quad \text{(EQ 4.60)}$$

Here the ozone values for correcting the water vapor mixing ratio will be taken from the balloon sonde measurement.

All the other terms can be calculated so that the factor K is determined with this (EQ 4.60) (the corrected case for the water vapor better fits to the sonde values). We take one point on the balloon sonde water vapor mixing ratio profile to calibrate the lidar, and have K identical as in the uncorrected case.

With this we can then calculate the correction value $\Delta\xi_{H_2O}^{(N_2)}(R)$.

Solution n°2: Auto correction by the lidar

Another way to correct the water vapor profile of the lidar is to take the ozone profile from the lidar and make a "self correction" as it is proposed with (EQ 2.24) p 44 to (EQ 2.26) p 44. The major problem, as we will see, is the need of an external reference to retrieve the unknown constants.

We have already made the calculation for this ozone correction value, with the (EQ 2.26) p 44 and the constant value $K_{cal}^{N_2}$:

$$\xi_{H_2O}^{(N_2)}(R)\Big|_{O_3\,corr} = \frac{P_{H_2O}}{P_{N_2}}(R)\,\Theta(R)\underbrace{\underbrace{\frac{M_{H_2O}}{M_{dry\,air}}\chi_{N_2}\frac{K_{N_2}}{K_{H_2O}}\frac{{}^{\pi}\beta_{N_2}^{Ram}}{{}^{\pi}\beta_{H_2O}^{Ram}}}_{K}\underbrace{\left(\frac{K_{N_2}}{K_{O_2}}\frac{n_{N_2}}{n_{O_2}}\frac{{}^{\pi}\beta_{N_2}^{Ram}}{{}^{\pi}\beta_{O_2}^{Ram}}\right)^{\hat{\Delta}\sigma_{abs}^{O_3}}}_{K_1}}_{K\cdot K_1 = K_{cal}^{(N_2)}}\left(\frac{P_{O_2}}{P_{N_2}}(R)\right)^{\hat{\Delta}\sigma_{abs}^{O_3}}\times\tilde{\Theta}(R) \qquad \text{(EQ 4.61)}$$

with $\tilde{\Theta}(R) = \exp\left\{\int_0^R\left[-\hat{\Delta}\sigma_{abs}^{O_3}\left(\widetilde{\alpha^{atmos}}\left(\lambda_{N_2}^{Ram}, r\right) - \widetilde{\alpha^{atmos}}\left(\lambda_{O_2}^{Ram}, r\right)\right)\right]dr\right\}$

It gives us the simple equation that we will use now:

$$\xi_{H_2O}^{(N_2)}(R)\Big|_{O_3\,corr} = \frac{P_{H_2O}}{P_{N_2}}(R)\,\Theta(R)\,KK_1\left(\frac{P_{O_2}}{P_{N_2}}(R)\right)^{\hat{\Delta}\sigma_{abs}^{O_3}}\tilde{\Theta}(R) \qquad \text{(EQ 4.62)}$$

First step: *calibration of the constant K_1*

With a development in Taylor's series of $n_{O_3}(r)$ with $r \in [0, R]$, we have by taking only the zero order term:

$$\int_0^R\left(\sigma_{abs}^{O_3}(\lambda_{H_2O}^{Ram}) - \sigma_{abs}^{O_3}(\lambda_{N_2}^{Ram})\right)n_{O_3}(r)dr \simeq (R-0)\left(\sigma_{abs}^{O_3}(\lambda_{H_2O}^{Ram}) - \sigma_{abs}^{O_3}(\lambda_{N_2}^{Ram})\right)n_{O_3}(R) \qquad \text{(EQ 4.63)}$$

In fact this assumption (to not consider the other terms of the series) supposes to have a constant O_3 profile versus the altitude. This solution can only be taken if the sonde balloon shows constant O_3 profile versus the altitude. In a general case, where this O_3 profile is not constant, the integral has to be kept and calculated as for the solution n°1.

$$O_3 \text{ correction value in } R_0 = \exp\left\{\int_0^{R_0}\left(\sigma_{abs}^{O_3}(\lambda_{H_2O}^{Ram}) - \sigma_{abs}^{O_3}(\lambda_{N_2}^{Ram})\right)\underbrace{n_{O_3}(r)}_{balloon}\,dr\right\}$$

$$= \underbrace{K_1\left(\frac{P_{O_2}}{P_{N_2}}(R_0)\right)^{\hat{\Delta}\sigma_{abs}^{O_3}}}_{lidar}\tilde{\Theta}(R_0) \qquad \text{(EQ 4.64)}$$

Giving the value for K_1:

$$K_1 = \frac{\exp\left\{\left(\sigma_{abs}^{O_3}(\lambda_{H_2O}^{Ram}) - \sigma_{abs}^{O_3}(\lambda_{N_2}^{Ram})\right)\int_0^{R_0} \underbrace{n_{O_3}(r)}_{balloon}\, dr\right\}}{\left(\frac{P_{O_2}}{P_{N_2}}(R_0)\right)^{\hat{\Delta}\sigma_{abs}^{O_3}} \tilde{\Theta}(R_0)} \qquad \text{(EQ 4.65)}$$

The case with a constant O_3 profile till the altitude R_0 gives:

$$K_1 \simeq \frac{\exp\left\{R_0\left(\sigma_{abs}^{O_3}(\lambda_{H_2O}^{Ram}) - \sigma_{abs}^{O_3}(\lambda_{N_2}^{Ram})\right)\underbrace{n_{O_3}(R_0)}_{balloon}\right\}}{\left(\frac{P_{O_2}}{P_{N_2}}(R_0)\right)^{\hat{\Delta}\sigma_{abs}^{O_3}} \tilde{\Theta}(R_0)} \qquad \text{(EQ 4.66)}$$

Second step: *Calibration of the constant K*

Here the assessment is to say that $\xi_{H_2O}^{(N_2)}(R_0)\Big|_{O_3\ corr}$, retrieved by the lidar, is the value which best fits with the one given by the other method (sonde measurements for example), at the distance R_0:

$$\xi_{H_2O}^{(N_2)}(R_0)\Big|_{O_3\ corr} = \xi_{H_2O}^{balloon}(R_0) \qquad \text{(EQ 4.67)}$$

Which gives us with (EQ 4.63):

$$\frac{P_{H_2O}}{P_{N_2}}(R_0)\ \Theta(R_0)\ KK_1\left(\frac{P_{O_2}}{P_{N_2}}(R_0)\right)^{\hat{\Delta}\sigma_{abs}^{O_3}} \tilde{\Theta}(R_0) = \xi_{H_2O}^{balloon}(R_0) \qquad \text{(EQ 4.68)}$$

And as we already have calculated K_1 ((EQ 4.65)) we then can give K:

$$K = \frac{\xi_{H_2O}^{balloon}(R_0)}{\exp\left\{\left(\sigma_{abs}^{O_3}(\lambda_{H_2O}^{Ram}) - \sigma_{abs}^{O_3}(\lambda_{N_2}^{Ram})\right)\int_0^{R_0} \underbrace{n_{O_3}(r)}_{balloon}\, dr\right\}\frac{P_{H_2O}}{P_{N_2}}(R_0)} \qquad \text{(EQ 4.69)}$$

And for the constant O_3 profile case:

$$K \simeq \frac{\xi_{H_2O}^{balloon}(R_0)}{\exp\left\{R_0\left(\sigma_{abs}^{O_3}(\lambda_{H_2O}^{Ram}) - \sigma_{abs}^{O_3}(\lambda_{N_2}^{Ram})\right)n_{O_3}(R_0)\right\}\frac{P_{H_2O}}{P_{N_2}}(R_0)} \qquad \text{(EQ 4.70)}$$

The main results will be summarized here under. As we have K and K_1 we then can retrieve:

$$\xi_{H_2O}^{(N_2)}(R)\Big|_{O_3\,corr} = \frac{P_{H_2O}}{P_{N_2}}(R)\,\Theta(R)\,KK_1\left(\frac{P_{O_2}}{P_{N_2}}(R)\right)^{\hat{\Delta}\sigma_{abs}^{O_3}}\tilde{\Theta}(R) \tag{EQ 4.71}$$

$$\xi_{H_2O}^{(N_2)}(R)\Big|_{O_3\,uncorr} = K\,\frac{P_{H_2O}}{P_{N_2}}(R)\times\Theta(R) \tag{EQ 4.72}$$

Which finally gives for the correction value:

$$\Delta\xi_{H_2O}(R) = \frac{P_{H_2O}}{P_{N_2}}(R)\;\Theta(R)\,K\left(K_1\left(\frac{P_{O_2}}{P_{N_2}}(R)\right)^{\hat{\Delta}\sigma_{abs}^{O_3}}\tilde{\Theta}(R)-1\right) \tag{EQ 4.73}$$

In Figure 4-15 the method exposed above is applied. Datas are taken from a measurement campaign which occurred in the EPFL area from the 31^{th} of April to the 1^{st} of March 1999.

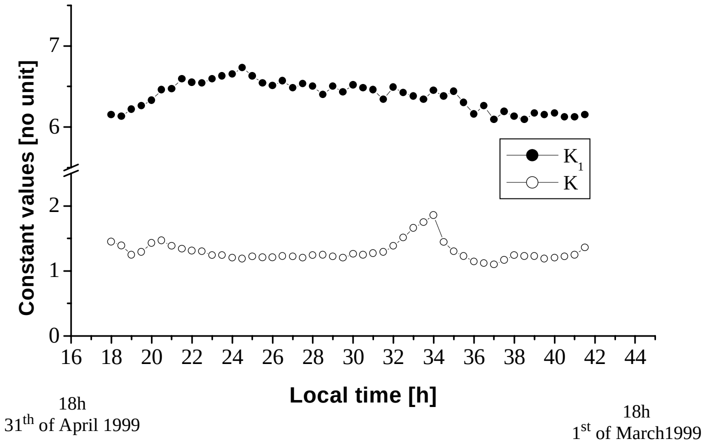

FIGURE 4-15. H_2O calibration constants

A perfect system would have given straight lines, denoting the constant type of K and K_1. The calculated mean values for the real system give K = 1.30 with a standard deviation of 0.15 and K_1 = 6.38 with a standard deviation of 0.18. The major peak seen at 34 h local time (10 h a.m) for the constant K corresponds to a "realignment" period. It seems to show the biggest sensitivity of the K constant with respect to the other one, perhaps due to the fact that K_1 is calculated with the N_2 and O_2 Raman signals and K with the N_2 and weaker H_2O ones.
Another example can be seen in the Figure 9 of the chapter 6 p 107 (Applied Optics article). This method was applied in this case to one profile taken from measurements made during the Crete PAUR2 campaign, and shows the H_2O correction values versus the altitude.

Chapter 5

A Raman differential absorption lidar for ozone and water vapor measurement in the lower troposphere

This article was submitted to the *International Journal of Analytical Chemistry* (IJEAC) on April 20th, 1998 and accepted for publication with minor changes. It was in final form on July 24th, 1998 and published in vol. 74, pp. 255-261, 1999.

It followed the first set of results from march 1998 and, at that time, the Raman lidar was developed and ran in the LPAS movable lidar truck, based at the EPFL site for improvements. The Raman lidar was run under a Nd:YAG configuration.

The system was in its first developments and only the bandpass filters tube was done. As the experiments with the big Thorn Emi glass bulb PMTs didn't give good results, the small Hamamatsu H5783 PMTs were tried, with success. The first design exposed here allowed the simultaneous detection of two channels, O_2 and N_2, and permitted the O_3 concentration retrieve. The theory was exposed for the O_3 concentration retrieve, but also for the H_2O mixing ratio one. The data treatment took the simplest form of the O_3 concentration retrieve (the 0-order) and didn't take into account the contributions from the Rayleigh and Mie scattering or the molecular absorption. A 15 h comparison between an ozone point monitor situated 12 m above the ground and the 262 m lidar values showed a similar behavior.

255

Intern. J. Environ. Anal. Chem., Vol. 74, pp.255-261
Reprints available directly from the publisher
Photocopying permitted by license only

1999 OPA (Overseas Publishers Association)
Amsterdam N. V. Published under license by
the Gordon and Breach Science Publishers inprint.
Printed in Singapore

A RAMAN DIFFERENTIAL ABSORPTION LIDAR FOR OZONE AND WATER VAPOR MEASUREMENT IN THE LOWER TROPOSPHERE

BENOÎT LAZZAROTTO, PHILIPPE QUAGLIA, VALENTIN SIMEONOV,
GILLES LARCHEVÊQUE, HUBERT VAN DEN BERGH and
BERTRAND CALPINI*[1]

Laboratory for air pollution / Lidar group. EPFL, Swiss Federal Institute of Technology.
1015 LAUSANNE. SWITZERLAND

(Received 20 April, 1998; In final form 24 July 1998)

A new way of measuring ozone and water vapor in the Planetary Boundary Layer (PBL) is proposed. The method is based on the simultaneous measurement of the Raman backscattering in the UV by O_2 , N_2 and H_2O, using a single pump beam at 266 nm. The ozone concentration is retrieved from the differential absorption of the N_2 and O_2 Raman backscattered signals, while the water vapor is measured using the classical Raman scheme. We present some preliminary results showing daytime ozone measurements in good correlation with a point monitor.

Keywords: Raman, LIDAR, ozone, water vapor, UV.

INTRODUCTION

The UV **d**ifferential **a**bsorption **l**idar (DIAL) technique is a well known technique successfully applied both to tropospheric and stratospheric studies [1,2,3]. However, strong uncertainties are caused by aerosols, mainly due to the unknown wavelength dependence of the aerosols backscattering coefficient [4]. In order to perform daytime boundary layer measurements of ozone and water vapor even in cases of high aerosol load, we are developing a new way to measure ozone concentration.
By using a single excitation wavelength, namely the 4th harmonic of a Nd:YAG laser, vibra-

---

[1] * Corresponding author : Fax: +41 21-693 61 85. E-mail: bertrand.calpini@epfl.ch

tional Raman shifted wavelengths from atmospheric O_2 and N_2 are obtained. The two gases have well known Raman cross sections and constant mixing ratio. Such Raman shifted wavelengths are well suited for differential ozone measurements in the Hartley band. The two Raman backscattered signals are essentially independent of the uncertainties in the aerosol Mie scattering cross sections. Moreover, they are situated in the solar blind region, making daytime measurements possible. Furthermore the water vapor mixing ratio can be retrieved using the classical Raman method (i.e. using the relative intensity of the H_2O Raman backscattered line) [5].

This method, called Raman DIAL, has already been used successfully in the stratosphere under night time conditions for ozone measurements [6]. We have adapted this technique for daytime monitoring of the ozone in the PBL and the lower troposphere.

EXPERIMENTAL SET-UP

The optical layout is shown in Figure 1. The system is based on a quadrupled Nd:YAG laser which emits 266.1 nm radiation pulses of 120 mJ at 10 Hz, with a beam divergence of 0.5 mrad in a non coaxial configuration. In order to reduce the minimum altitude of the measurement (actually 250 m), some tests have been made with a coaxial configuration, but with no significant improvement. By using of a beam expander, we plan to reduce this value to around 100 m. The three backscattered Raman signals of interest are collected by a Newtonian telescope with a 20 cm diameter primary mirror, 60 cm focal length and 5 mrad field of view. The Raman signals are spectrally separated by a monochromator (500 mm optical path) with a background noise rejection of 10^5. The monochromator has a 1.1 nm / mm resolution using a 1´800 gr / mm grating. Additional rejection of the LIDAR backscattered signal at the pump wavelength is performed by two custom designed holographic bandpass filters, with an optical density 2.6 at 266 nm for each filter and up to 80% transmission for the three Raman wavelengths when tilted at 18 degrees. The bandpass filter transmission curves for a tilt of 0 and 20 degrees are shown in Figure 2.

With the combination of the monochromator and the two bandpass filters, we obtain over 10^{10} rejection at 266 nm. The f number of the monochromator and telescope are matched using two plano - convex lenses, a 40 mm focal length lens to collimate the light in the bandpass filters and a 60 mm focal length lens at the entrance of the monochromator.

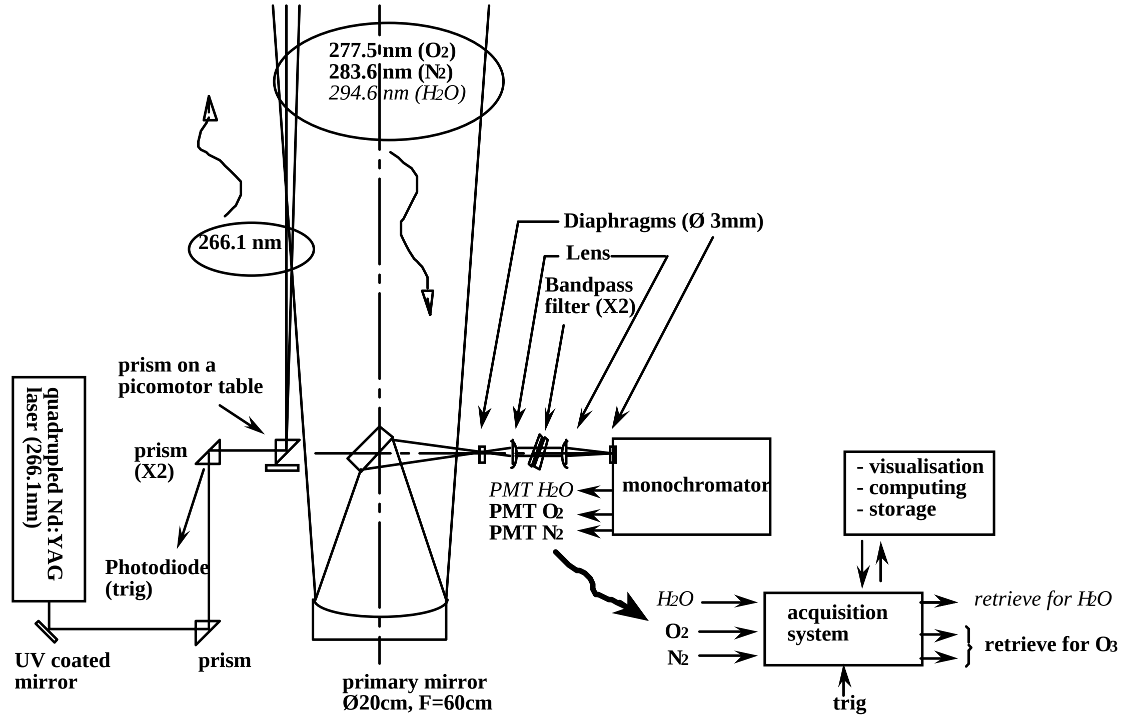

FIGURE 1. Experimental setup

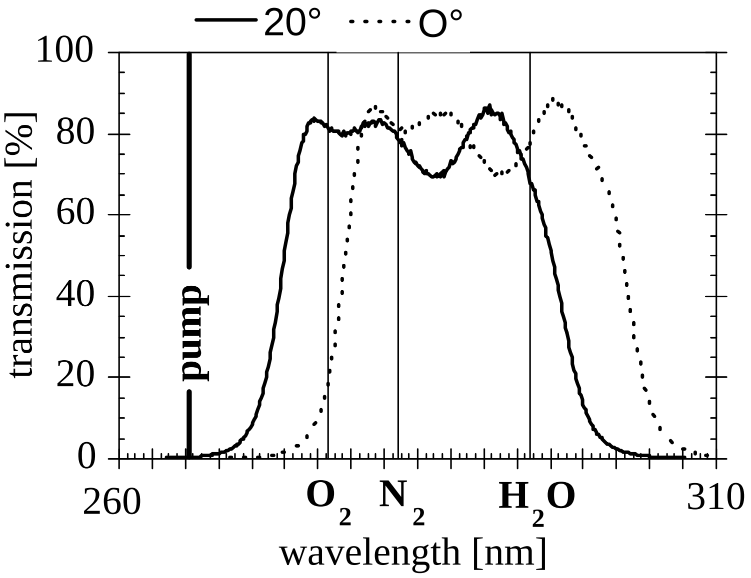

FIGURE 2. Bandpass filter transmission curves between 260 - 310 nm, at 2 different angles of the incident light.

The two main Raman shifted wavelengths (by N_2 and O_2) at the output of the monochromator are simultaneously detected by two Hamamatsu H5783-06 photodetection modules, and the signals are recorded with a 12 bit - 20 MHz transient ADC recorder, with the control of the acquisition and treatment of the data performed by a PC. An additional photomultiplier tube (PMT) and acquisition channel is added for the water vapor retrieval.

DATA ANALYSIS

The Lidar equation for a vibrational Raman signal is the following [7] :

$$P_X(\lambda_X^{Raman}, R) = P_0 K_X(\lambda)\frac{1}{R^2}\beta_X^R(R)n_X(R)O(R)$$
$$\exp\left\{-\int_0^R \left[\alpha_1(r) + \alpha_X(r) + n_{O_3}(r)\sigma_1(r) + n_{O_3}(r)\sigma_X(r)\right]dr\right\}$$

Where X stands for O_2 , N_2 or H_2O.

$R = ct/2$: distance LIDAR - probed volume (t is the time for the backscattered signal to come from this volume to come and c is the velocity of the light).

$P_X(R)$ [W]: received energy for the component X.

P_0[W]: emitted energy of the laser.

$K_X(\lambda)$ [no dimension]: constant which takes into account the optical efficiency of the transmission and detection part for the lidar (telescope surface, quantum efficiency of the detector, optical transmission coefficients,...).

$\beta_X^R(R)$ [cm^2/mol]: Raman cross section for the vibrational transition of the corresponding element X.

$n_X(R)$ [#mol/cm^3]: density of the molecules X.

O(R): optical overlap recovery function.

$\alpha_X(r)$ (resp. $\alpha_1(r)$) [cm^{-1}]: extinction coefficient for the Raman shifted wavelength of the element X (resp. for the laser emitted wavelength).

$\sigma_X(r)$ (resp. $\sigma_1(r)$) [cm^2/mol]: ozone absorption cross section for the Raman shifted wavelength of the element X (resp. for the laser emitted wavelength).

Raman shifts are 1555 cm^{-1} for O_2 , 2331 cm^{-1} for N_2 and 3651 cm^{-1} for H_2O. With the 266.1 nm pump beam, the vibrational Raman wavelengths are correspondingly 277.5 nm for O_2 , 283.6 nm for N_2 and 294.6 nm for H_2O [8]. The corresponding ozone cross section for the Raman shifted wavelengths are 490.6×10^{-20} cm^2/mol for O_2 and 296.3×10^{-20} cm^2/mol for N_2 [9].

Taking $S_X = \ln(R^2 P_X(R))$, with $S_{N_2}(R)$ and $S_{O_2}(R)$ we can retrieve the ozone concentration:

$$n_{O_3}(R) = \frac{\frac{d}{dR}\left(S_{N_2}(R)\right) - \frac{d}{dR}\left(S_{O_2}(R)\right) - \left(\alpha_{O_2}(R) - \alpha_{N_2}(R)\right)}{\sigma_{O_2}(R) - \sigma_{N_2}(R)}$$

By detecting the H_2O Raman signal at 294.6 nm, the water vapor profile can be calculated by applying the method proposed in [4]: with a normalization of P_{H_2O} and in taking into account P_{N_2}, the water vapor density is calculated as:

$$n_{H_2O}(R) = n_{N_2}(R) \frac{P_{H_2O}}{P_{N_2}}(R) \frac{\beta^R_{N_2}}{\beta^R_{H_2O}} \frac{K_{N_2}}{K_{H_2O}} \exp\left\{ \int_0^R \left\{ \alpha_{H_2O}(r) - \alpha_{N_2}(r) + n_{O_3}(r)\left(\sigma_{H_2O}(r) - \sigma_{N_2}(r)\right) \right\} dr \right\}$$

RESULTS AND DISCUSSIONS

With the presented configuration, Raman signals have been acquired in the analog detection mode for altitudes up to 1000 m. The high rejection ratio of 266 nm was confirmed by the absence of the elastic lidar echo in O_2 and N_2 Raman channels caused by low level clouds. Two typical range corrected signals obtained with the system are shown in Figure 3, for the O_2 and N_2 Raman shifted wavelengths, based on a 4000 shots average. The graph shows the difference in the slopes of the curves due to different ozone absorption cross-sections. The O_2 shifted signal corresponds to the *on* wavelength (i.e. the more absorbed beam) and the N_2 shifted signal to the *off* wavelength. No degradation of the signal due to background daylight has been observed.

In figure 4 we show a comparison between the ozone concentration measured by a point monitor 12 m above the ground and by the Raman DIAL values started at 262 m above the ground. The calibrated ozone point monitor was started at 08:01pm on the 20th of March and gave values every 1'26", with a 2ppb resolution, until 02:38pm the 21st of March. The LIDAR was operated from 11:12pm on the 20th of March till 08:16pm on the 21st of March, with a 4000 shots average implying that each ozone versus height profile took 06'40". The DIAL data points are obtained with a binning of 150 meters (20x7.5 m) and we show here the first layer of the profile at 262 m above the ground level. Error bars indicate the 67% confidence intervals of the measurements. The comparison shows the same behavior for both measurements (reduction of ozone content during the night and increase during the morning) and no reduction of the ozone measurement quality during daytime. The different altitudes of the two measurements do not allow to conclude quantitatively on the accuracy of the Raman DIAL measurement.

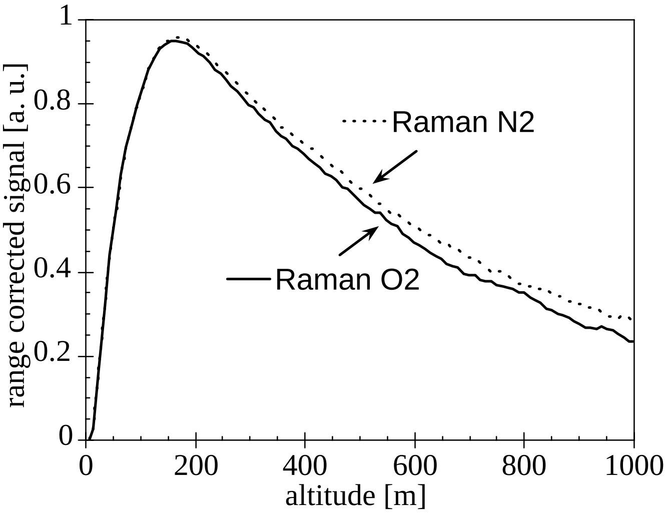

FIGURE 3. Typical range corrected Raman signal for N_2 and O_2 signals.

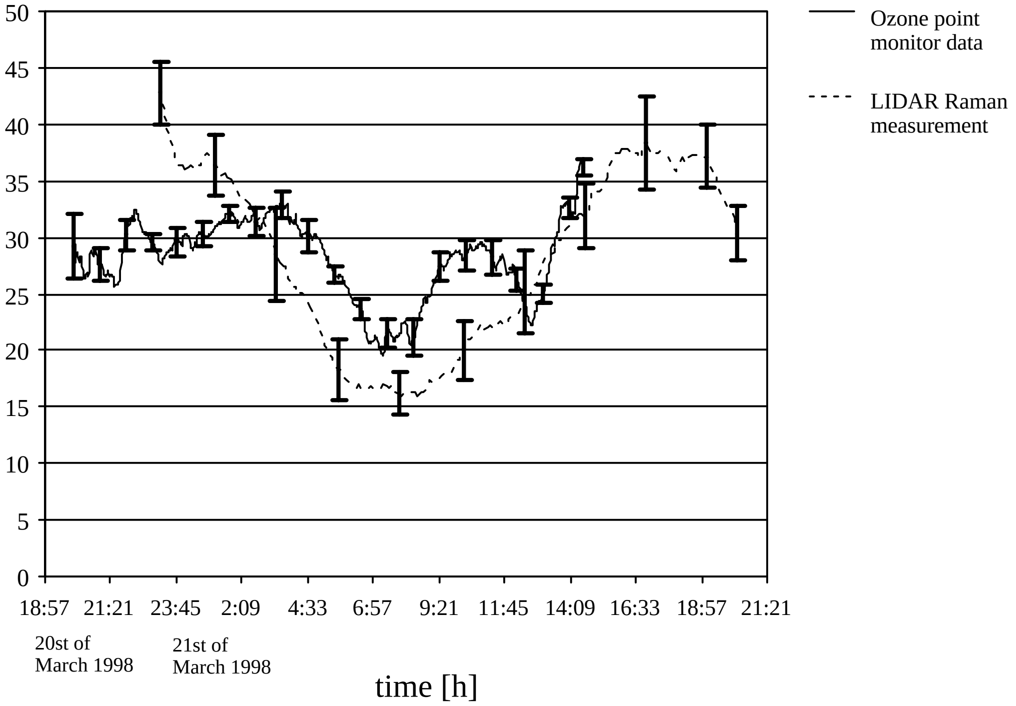

FIGURE 4. Comparison between a calibrated ozone point monitor at 12 meters above the ground level (AGL) and a LIDAR profile measured around 262m AGL on the 20 - 21 of March 1998.

In order to asses the effect of some possible differences in the sensitivity (and the spatial uniformity [10] of the two PMTs, we have done some measurement using a single PMT configuration [9] in which we acquire one channel after the other, thus yielding an ozone profile every 13 minutes. The retrieved ozone values were not realistic, mainly due to fluctuation of the atmosphere on such time scale. This check will be done in the near future using a fast switch (chopper) between the channels.

CONCLUSIONS

The principle and design of a new single wavelength excitation Raman-DIAL for daytime ozone measurement in the boundary layer has been proposed. The relatively simple and cheap combination of a commercial spectrometer and holographic band pass filters in the receiving part has proved to efficiently reject background daylight and elastic scattering from the emitted laser wavelength. Comparison with an ozone point monitor shows a good correlation for the ozone retrieval, even during daytime with a short averaging time (6'40"). By using a third photomultiplier tube, we will be able to retrieve the water vapor mixing ratio simultaneously. Using the photon counting technique instead of the analog mode, we hope to extend the measurement range up to the free troposphere.

References

[1]. B. Calpini, V. Simeonov, F. Jeanneret, J. Kuebler, V. Sathya, and H. van den Bergh, Chimia, 51, n°10, 700-704 (1997).

[2]. J. Pelon, S. Godin, and G. Mégie, J. Geophys. Res., 91:8667-8671 (1986).

[3]. L. Schoulepnikoff, H. van den Bergh, B. Calpini, V. Mitev, Encyclopedia of Environmental Analysis and Remediation, 8, 4873-4909 (1998).

[4]. E. V. Browell, S. Ismail, and S. T. Shipley, Applied Optics, 24, n°17, 2827-2836 (1985).

[5]. S.H. Melfi, J.D. Lawrence Jr, and M.P. Mc Cormick, Appl. Phys. Lett. , 15, 295-297 (1969).

[6]. T.J. Mc Gee, M. Gross, R. Ferrare, W. Heaps, and U. Singh, Geophysical Research Letter, 20, 955-958 (1983).

[7]. Laser remote chemical analysis (edited by R. M. Measures, John Wiley & sons, 1988).

[8]. W.K. Bishel and G. Black, Wavelength dependence of Raman scattering cross-sections from 200 - 600 nm, in eximer lasers (edited by C.K. Rhodes, H. Egger and H. Pummer, American Institute of Physics, New York, 1983, pp. 181-194).

[9]. Laser monitoring of the atmosphere (Ed. E. David Hinkley, Springer, 1976).

[10]. V. Simeonov, G. Larchevêque, P. Quaglia, H. van den Bergh, and B. Calpini, submitted to Applied Optics (1998).

[11]. B. Lazzarotto, V. Simeonov, P. Quaglia, G. Larchevêque, H. van den Bergh, B. Calpini, M Frioud, and V. Mitev, 19th ILRC (1998).

Chapter 6

Ozone and water vapor measurements by Raman lidar in the planetary boundary layer: error sources and field measurements

This article, submitted to *Applied Optics* on June 6th, 2000, was accepted for publication after minor revisions on December 4th, 2000.

It shows measurements made at the EPFL (April 1999) and in Crete during the international PAUR 2 campaign (May 1999). An extensive comparison with numerical simulations is presented.
The lidar was run in the Nd:YAG configuration, and the photomultipliers module part was designed and incorporated in the optical reception part. It enabled the use of three small Hamamatsu PMTs, series H5783, and the simultaneous retrieve of the O_3 concentration and H_2O mixing ratio. The lidar theory was exposed and the O_3 contribution correction was incorporated in the H_2O mixing ratio retrieve. The error source contributions to the Raman lidar retrieves, like the ozone interference on the water vapor retrieve, the influence of the statistical noise, the optical cross-talk or the after pulse effect, were calculated for several situations by mean of numerical simulations. An additional discussion on systematic errors induced by the absorbing species NO_2 and SO_2 was proposed. Confrontation with the experiment was made for the optical cross-talks and the after pulse effect concluding that, with the measured values, the resulting errors would not be significant with the developped Raman lidar system. Taking the developed formalism, temporal series were calculated with the 0-order term for the O_3 concentration and incorporating the O_3 correction by mean of the lidar for H_2O mixing ratio. This O_3 correction on the retrieved H_2O mixing ratio was presented and discussed. Comparison with an O_3 punctual analyzer was proposed. The correction, by mean of an external source (sonde balloon), of the H_2O mixing ratio for the O_3 contribution was calculated. The resulting vertical H_2O mixing ratio lidar profile was then compared with the one of the sonde balloon.

Ozone and water vapor measurements by Raman lidar in the planetary boundary layer: error sources and field measurements

Benoît Lazzarotto[a], Max Frioud[b], Gilles Larchevêque[a], Valentin Mitev[b], Philippe Quaglia[a], Valentin Simeonov[a], Anne Thompson[c], Hubert Van den Bergh[a] and Bertrand Calpini[a]

[a] Laboratory for air pollution / Lidar group. EPFL, Swiss Federal Institute of Technology
CH-1015. LAUSANNE. SWITZERLAND

[b] Observatory of Neuchatel,
CH-2000. NEUCHATEL. SWITZERLAND

[c] NASA / GSFC
Code 916, Grennbelt MD 20771. USA

Corresponding author: e-mail bertrand.calpini@epfl.ch , tel : (++41) (021) 693 61 85

Abstract

For the purpose of tropospheric ozone and water vapor measurements at low altitude, a new lidar instrument is developed. The lidar uses Raman scattering of a UV beam from atmospheric nitrogen, oxygen and water vapor to retrieve ozone and water vapor vertical profiles. In this work, we investigate the sensitivity of the method to both atmospheric and device perturbations by numerical simulation. The aerosol optical effect in the planetary boundary layer (PBL), ozone interference on water vapor retrieval, statistical error, optical cross-talk between Raman-shifted channels, optical cross-talk between elastically backscattered signal in the Raman-shifted signals and after pulse effect are studied in detail. Supporting the main conclusions of this model study, different time series of ozone and water vapor obtained at EPFL and during a field campaign in Crete, Greece, are presented. They are compared with point monitor and balloon sounding measurements for day and night time conditions.

OCIS codes: 280.0280, 280.1910, 010.1120, 010.3640, 010.7030

Keywords: Remote sensing, DIAL, air pollution monitoring, lidar, simulation, troposphere, ozone, water vapor.

1. Rationale

Why do we need time series of ozone and water vapor profile at low altitude?

The degradation of air quality is a very serious environmental problem that affects urban and industrial areas worldwide. Air pollution injures human health and ecosystems, diminishes crop yield, and spoils patrimony and materials. The phenomena involved in air pollution are very complex. Once emitted into the atmosphere, (primary) pollutants are transported, dispersed, transformed by gas/solid phase change and chemical reaction, and finally removed by dry and wet deposition.

Most challenging is the fact that the health and environmental impacts of secondary pollutants (formed in the atmosphere) are frequently more severe than those of their precursors (primary pollutants). This is the case of ozone and other photochemical pollutants, such as peroxyacetil nitrate (PAN) and secondary particles, produced in the atmosphere by the photo-oxidation of volatile organic compounds (VOC) catalyzed by nitrogen oxides (NO_X). Photochemical air pollution is a complex science because of the non-linearity of its response to changes in primary emission (see for example Finlayson-Pitts, 1999).[1]

Three Dimensional air quality models are used as the most powerful tool for identifying effective strategies to improve air quality. With the meso-scale Eulerian chemical transport model developed at EPFL we may simulate pollutant dynamics over region like Athens, Milan, or regions with high traffic loads in Switzerland and provide technical guidance to air quality management agencies.[2-4] The model resolution is of the order of 1km on the horizontal scale, with a vertical resolution of some tens of meters for the lowest layer of the model, up to 500 m for the top layer, and a total height of 5 km above ground level. The domain size is typically 100 x 100 km. Before the model results can be used with confidence, they must be validated against field measurements with similar spatial and time resolution.

Most of the time, an air quality network in densely urbanized region is built upon a set of ground based stations equipped with point detectors. Trace gas measurements are often influenced by local sources and thus are not representative of the averaged concentrations over the typical grid size of the model. On the contrary, tropospheric lidar measurements are based on an integrated optical path of typically 50 to 500 m depending upon the trace gas species. This spatial resolution is in ideal agreement with the model resolution and may help retrieving essential information for the model validation among which the ozone or water vapor vertical profile.

Ozone as a secondary pollutant is an ideal species to compare with its predicted values obtained by the model. Because ozone is "produced" in the model by photochemical reactions and transport effects, a good agreement between field measurements and model values is an indicator of the model performance. On the other hand, the water vapor content in the atmosphere plays a major role in the dynamics and climatology of the atmosphere and is also a clear tracer of the daily evolution of the top of the PBL. Thus its continuous remote detection over a period of time of some days, the typical duration of an air pollution event, may also contribute significantly to improve the model predictions.

This paper presents the design and development of a Raman lidar system with optimized resolution in comparison with model results. This ozone / water vapor Raman lidar development is a follow up of our recent work in the field of elastic ozone DIAL technique.[5-7] The latter is a method with higher sensitivity than the Raman lidar and with well-established ozone results in atmospheric conditions where the aerosol density is low enough, or homogeneous, as for example in the free troposphere. In the PBL where highly variable aerosol concentrations are frequently observed, elastic DIAL may fail or even not be used anymore due to strong and unpredictable aerosol optical interference on the ozone retrieve.[8,9] In particular the aerosol backscatter and its high but poorly known wavelength dependence were pointed out by Volger.[10]

On the other hand, the PBL is also the atmospheric layer described with the highest vertical resolution in the model. This brought us to the idea of developing an alternative instrument with respect to the elastic DIAL, an instrument much less perturbed by the non-homogeneous aerosol load condition in the PBL, and able to perform simultaneous ozone and water vapor measurements with high resolution at very low altitude. This instrument is based on the measurement of the Raman shifted backscattered light induced by the most abundant molecular species in the atmosphere, i.e. nitrogen, oxygen and water vapor, from a UV laser pulse emitted in the atmosphere. The water vapor content is obtained by the classical Raman analysis. Ozone is calculated by a differential absorption method using oxygen and nitrogen Raman backscatter as ON and OFF signals. The different Raman return signals are generated simultaneously from a single laser source, thus probing the "same" volume of air at a given time and essentially avoiding the problems related with pulse to pulse laser stability or atmospheric turbulence that is the case for most of the elastic DIAL instruments where two successive pulses are emitted.[11] The disadvantage caused by the weaker Raman signals compared with the elastic signals is compensated by the high molecular densities and the well-known values of the Raman cross sections. This idea refers to the pioneering work by Melfi and Mc Cormick,[12] and by Renault and Capitini[13] where these authors published a first measurement of the vertical water vapor distribution in the PBL, and later propose to correct the water vapor Raman return for tropospheric ozone attenuation.[14] The same principle was also successfully applied in the stratosphere.[15]

Here we apply these earlier concepts to the development of an operational lidar instrument, for day and night-time measurements, and for time series of some days to follow the vertical dynamics and time evolution of an air pollution episode. Section 2 of this paper presents a model estimate of the determination of the critical system parameters. Section 3 defines the experimental setup and Section 4 gives some typical results obtained for different time series of ozone and water vapor concentration and comparison with other instruments.

2. Raman lidar: principle and predicted error sources

Figure 1 shows a schematic of the Raman lidar system. The ozone retrieve is based only on the N_2 and O_2 Raman backscattered signals. For the water vapor retrieval, we may use either N_2 & H_2O or O_2 & H_2O pairs of signals.

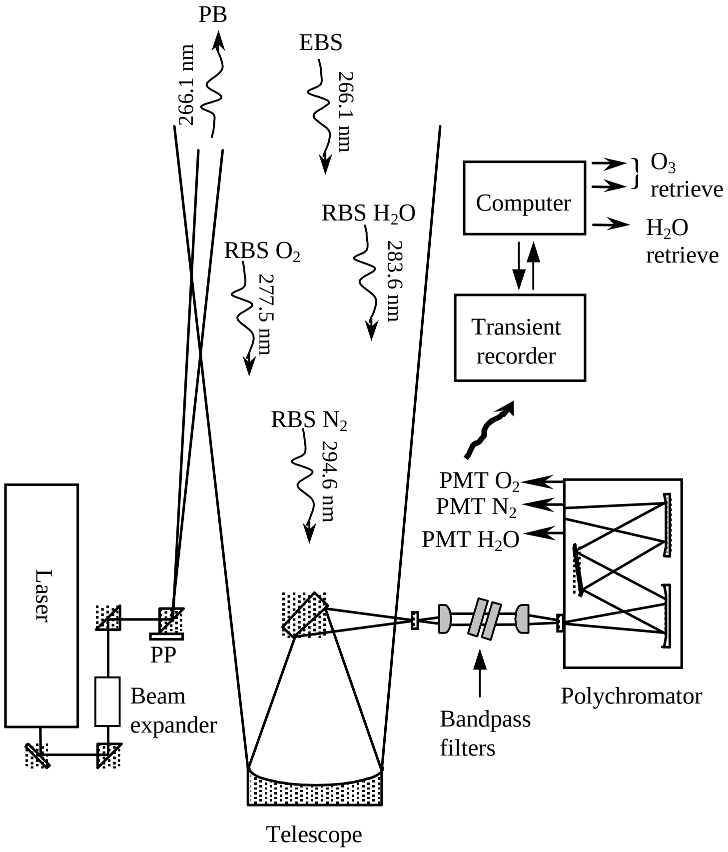

Figure 1. Raman Lidar Scheme: A pulsed laser beam (PB) is emitted into the atmosphere via a beam expander (x3) and a set of right angle prisms. The elastically backscattered signal (EBS) and the Raman shifted backscattered signal (RBS) are collected by a 200 mm newtonian telescope, filtered at the entrance of a polychromator where they are spectrally resolved and detected by three photomultiplier tubes (PMT). The different PMT signals are stored in a transient recorder (ADC 20 MHz / 12 bit and photon-counting) and a PC based computer unit allows for real time ozone and water vapor retrieval (raw data).

To each of the three Raman-shifted wavelengths corresponds a lidar equation:

$$P_X(\lambda_X^{Raman},R)=P_L(\lambda_L)K_X\frac{A(R)}{R^2}n_X(R)\beta_X^{Raman}(R)\Delta R\exp\left\{-\int_0^R\left[\alpha_L(r)+\alpha_X(r)+n_{O_3}(r)\left(\sigma_L(r)+\sigma_X(r)\right)\right]dr\right\}\quad(1)$$

Where the index X stands for O_2, N_2 or H_2O, $P_X(\lambda_X^{Raman},R)$ the Raman lidar power backscattered from species X at Raman-shifted wavelength λ_X^{Raman} and distance R, $P_L(\lambda_L)$ the laser emitted power at wavelength λ_L, K_X the instrument constant at Raman-shifted wavelength λ_X^{Raman}, $A(R)$ the telescope active surface area, $n_X(R)$ the molecular density of species X at distance R, $\beta^{Raman}(R)$ the Raman differential backscattering cross-section for species X, $\alpha_X(r)$ and $\alpha_L(r)$ the atmospheric extinction coefficient at Raman-shifted wavelength λ_X^{Raman} and respectively at the pump laser wavelength λ_L, $\sigma_X(r)$ and $\sigma_L(r)$ the ozone absorption cross section at Raman-shifted wavelength λ_X^{Raman} and respectively at the pump laser wavelength λ_L. The ozone concentration $n_{O_3}(R)$ can be calculated from the N_2 and O_2 Raman signals using a modified DIAL equation in the following form:

$$n_{O_3}(R) = \frac{1}{\sigma_{O_2} - \sigma_{N_2}} \frac{d}{dR} \left(\ln \frac{P_{N_2}(R)}{P_{O_2}(R)} \right) - \frac{\left(\alpha_{O_2}(R) - \alpha_{N_2}(R) \right)}{\sigma_{O_2} - \sigma_{N_2}} \tag{2}$$

The water vapor mixing ratio in [g H_2O / kg_dry air] is obtained from the ratio of the water vapor Raman shifted signal to either the Raman N_2 or Raman O_2 shifted signal. Using the N_2 channel, this yields the following expression,

$$\frac{n_{H_2O}}{n_{N_2}}(R) = \frac{P_{H_2O}}{P_{N_2}}(R) \frac{K_{N_2}}{K_{H_2O}} \frac{\beta^{Raman}_{N_2}}{\beta^{Raman}_{H_2O}} \exp\left\{ \left[\int_0^R \left[\left\{ \underbrace{\left(\sigma_{H_2O} - \sigma_{N_2}\right) n_{O_3}(r)}_{"ozone"\ correction} + \left(\alpha_{H_2O}(r) - \alpha_{N_2}(r) \right) \right\} dr \right] \right] \right\} \tag{3}$$

The possibility of using either the Raman N_2 or the Raman O_2 in Eq. (3) gives an additional test of the consistency of the water vapor result. Note that in Eq. (3) the water vapor concentration retrieval depends linearly upon the ratio of the Raman H_2O signal to the Raman N_2 signal, while on the contrary in Eq. (2) the ozone concentration depends upon the first derivative of the two Raman lidar signals (N_2 versus O_2). We shall see later that the different predicted error sources on ozone and respectively water vapor will strongly depend on this point, and that in any case the ozone *differential* retrieval will be much more affected than the water vapor *linear* retrieval.

As the ozone retrieval does not depend on the instrument constant K_X the method can be regarded as self-calibrated. In contrast for absolute water vapor measurements the exact knowledge of K_X or independent parallel measurements for instrument calibration is needed. The term $\left(\sigma_{H_2O} - \sigma_{N_2}\right) n_{O_3}(r)$ denoted as "ozone correction" in the exponential part of Eq. (3) reflects the ozone influence on the H_2O and N_2 Raman signals and can affect significantly the final results,[13] as it will be underlined below.

2.1. Aerosol dependence of the Raman lidar

From Eq. (2) the ozone retrieval does not depend on the backscattering properties of the atmosphere. This is the major advantage of the Raman-DIAL method versus the conventional (elastic) DIAL and may be of crucial importance particularly in case of strong and inhomogeneous aerosol load.[10] The influence of the atmospheric extinction on the ozone retrieval is expressed by the second term of Eq. (2). This term also appears in the elastic DIAL formalism, and can be splitted into its molecular and its aerosol contribution.

First, the molecular atmosphere contribution is estimated using the Rayleigh wavelength–dependence for the extinction. One obtains the following (negative) correction to the ozone relative content:

$$\Delta^{mol} = \frac{\alpha^{mol}_{O_2} - \alpha^{mol}_{N_2}}{n^{mol}_{air} (\sigma_{O_2} - \sigma_{N_2})} \tag{4}$$

where n_{SP} is the air molecular density. As the numerator in Eq. (4) is also directly depending upon the air density, the result Δ^{mol} is given as an altitude independent value in this formalism.

It corresponds to a correction of about -3 ppbv.

Let us now add an homogeneous aerosol layer characterized by two variables in the model: the total lidar ratio e defined as the total extinction α_{total} divided by the total backscattering β_{total}, and the backscattering ratio b defined as the total backscattering β_{total} divided by the molecular backscattering β_g. With the assumption of atmospheric molecular species with mean diameter much smaller than the laser wavelength, the molecular backscattering β_g is defined according to Collis and Russell [16] by:

$$\beta_{\mathrm{g}} = n_{air}^{mol} \frac{d\sigma^{Rayleigh}(\pi)}{d\Omega} = n_{air}^{mol} \left(\frac{550}{\lambda_L} \right)^4 5.45\mathrm{x}10^{-32} \tag{5}$$

Where the molecular backscattering β_g is in [m^{-1}sr^{-1}], the laser wavelength λ_L in [nm] and the air density n_{SP} in [m^{-3}]. One may also assume a power-law for the wavelength-dependency of the extinction due to Mie particles ($\alpha^{aer} \sim \lambda^{\gamma}$) following previous work [17] where γ was shown to range from $\gamma \in [\ -1, -0.5\ ]$. With $\gamma = -1$ the following estimation of the aerosol correction Δ^{aer} to the ozone concentration is obtained:

$$\frac{\Delta^{aer}}{\Delta^{mol}} = \left(\lambda_L\right)^{-3} \frac{\left(\lambda_{O_2}^{Raman}\right)^{-1} - \left(\lambda_{N_2}^{Raman}\right)^{-1}}{\left(\lambda_{O_2}^{Raman}\right)^{-4} - \left(\lambda_{N_2}^{Raman}\right)^{-4}} \cdot \left(\frac{e \cdot b}{c^{rayl}} - 1 \right) \tag{6}$$

where $c^{Rayl} = \frac{8\pi}{3}$ is the molecular lidar ratio (Rayleigh contribution). With the parameters stated in Table 1, this yields the following aerosol contribution to the ozone correction:

$$\Delta^{aer} \cong (0.035 \cdot e \cdot b - 0.3) \cdot \Delta^{mol} \tag{7}$$

Here we used for the molecular density and the water vapor content a model atmosphere defined in (AFGL-TR-86-0110, model n°3)[18] with "midlatitude winter" conditions. The water vapor vertical profile was directly taken from this model atmosphere but multiplied by a factor of three to compare with experimental results presented below. The total extinction and backscattering coefficients were defined for the 4th Harmonic of a Nd:YAG laser source at 266 nm taking into account the effect of a constant aerosol vertical profile. In order to simulate the most severe aerosol conditions, the aerosol optical properties were "tuned" to their maximum acceptable (or worse) values for e and b of respectively 40 and 1.8. With these extreme aerosol conditions, the ozone shift Δ^{aer} due to the aerosol for this Raman DIAL reaches a value of 6.7 ppbv (from Eq. (7) for $\gamma = -1$), while for $\gamma = -0.5$ the ozone shift is $\Delta^{aer} = 3.4$ ppbv. In similar conditions the systematic relative error due to differential aerosol backscatter influencing the elastic DIAL (and not the Raman DIAL) would have exceeded 100 %.[16] This error is negative and leads to non-physical negative ozone concentrations. This difficulty in the case of elastic DIAL measurements is impossible to overcome without additional information about the backscatter properties of the aerosol or without making additional assumptions about the aerosol properties.[8]

Molecule	O_2	N_2	H_2O
Vibrational Raman shift $[cm^{-1}]$	1555	2331	3651
Corresponding Raman wavelength [nm]	277.5	283.6	294.6
Raman differential scattering cross-section.[28] $[10^{-30}\ cm^2\ /\ strad]$	23.3	10.7	33.3
Ozone absorption cross-section[29] at λ_X^{Raman} $[10^{-20}cm^2/molecule]$	490.6	296.3	81.93
SO_2 absorption cross-section[30] at λ_X^{Raman} $[10^{-20}cm^2/molecule]$	64.4	84.5	90.8
NO_2 absorption cross-section[31] at λ_X^{Raman} $[10^{-20}cm^2/molecule]$	4.82	6.30	9.98

Table 1. Spectroscopic data used in the article for a 266 nm pump laser source

2.2. Ozone interference on water vapor Raman lidar retrieval

Ozone absorbs in the Hartley and Huggins bands between 220 and 350 nm and thus affects the signal at each of the Raman O_2, N_2, and H_2O wavelengths. The effect of the ozone absorption on the water vapor retrieval defined in Eq. (3) was simulated using a model atmosphere with different constant values of the ozone concentration, an homogeneous aerosol load ($e = 40$; $b = 1.8$) and the lidar parameters stated in Table 2.

The ozone corrections ΔH_2O on the water vapor retrieval are shown in Fig. 2 as the difference between the water vapor retrieval profile without ozone interference with respect to the same retrieval corrected for the ozone absorption effect. The correction values are set to 0 [g H_2O / kg_dry air] at 200 m where a full overlap between the laser beam and the telescope field of view is assumed. The model shows that even for moderate ozone concentrations of 40 ppbv the correction can exceed 1 [g H_2O / kg_dry air] at 600 m and more than 2.5 [g H_2O / kg_dry air] at 1'200 m, that is around 20 % of the water vapor content in the standard atmosphere.

Laser pulse energy	120 mJ
Transmission efficiency	90 %
Receiver efficiency	20 %
Quantum efficiency	10 %
Telescope diameter	20 cm
PMT gain	10^5
Impedance	50 Ohm
Number of shots	5x4'000
Sampling rate	20 MHz
Full overlap range	200 m

Table 2. Experimental inputs for the Raman lidar simulations

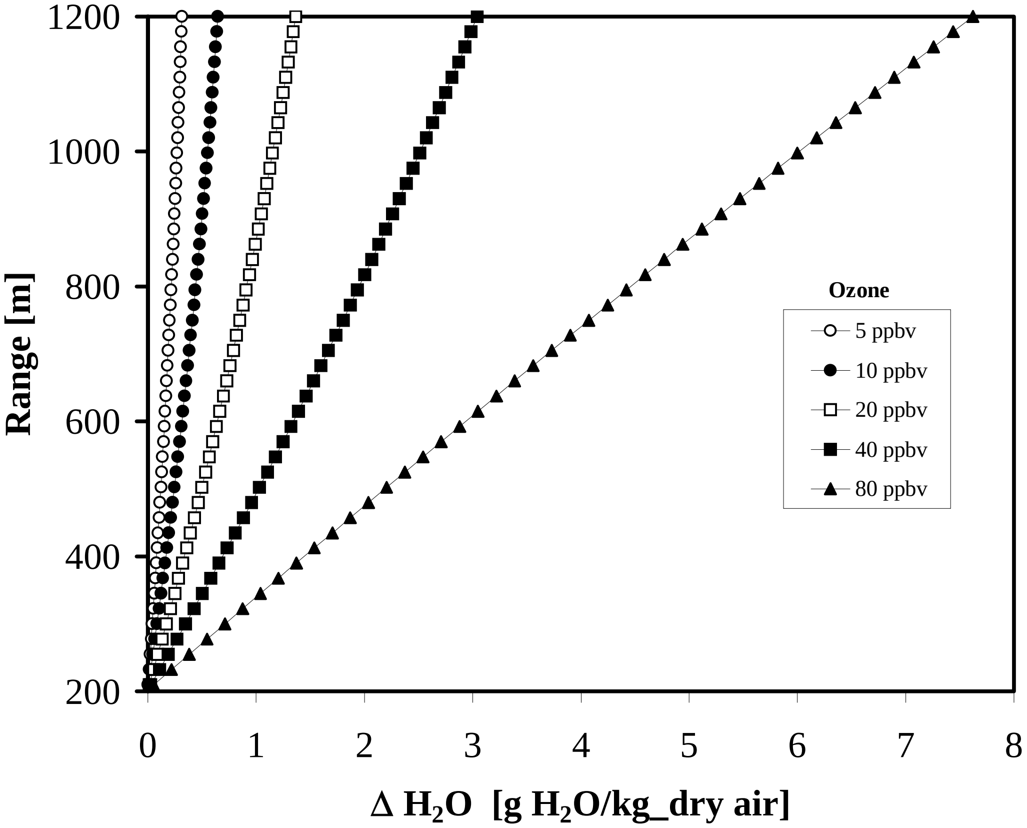

Figure 2. Ozone effect on water vapor retrieval: Predicted error on the water vapor mixing ratio retrieved by Raman lidar due to different ozone constant vertical profile and an homogeneous aerosol load. The horizontal scale is the difference between the water vapor retrieval without taking into account the ozone absorption and the same retrieval with ozone absorption.

The integrated ozone content needed to take into account the ozone correction can be obtained either by independent ozone (for e.g. balloon) measurements or by using additionally the ratio

of the O_2 and N_2 Raman signals. The first method requires additional "absolute" ozone concentrations, but is not convenient for practical purposes and therefore is more suitable for calibration and verification of the lidar system. The second method has the advantage of a "self-corrected" water vapor measurement with the risk of additional uncertainty due to the contribution of each of the three Raman backscattered lidar signals. Both methods were applied in our experiments.
In the second method, the integrated ozone content can be calculated from O_2 and N_2 Raman signals as:

$$\exp\left\{\int_0^R n_{O_3}(r)dr\right\} = \left(\frac{P_{O_2}}{P_{N_2}}(R)\right)^{\frac{1}{\sigma_{N_2}-\sigma_{O_2}}} \left(\frac{K_{N_2}}{K_{O_2}}\frac{n_{N_2}}{n_{O_2}}(R)\frac{\beta_{N_2}^{Raman}}{\beta_{O_2}^{Raman}}\right)^{\frac{1}{\sigma_{N_2}-\sigma_{O_2}}} \tag{8}$$

Further by combining Eq. (3) with Eq. (8) the water vapor mixing ratio can be determined as:

$$\frac{n_{H_2O}}{n_{N_2}}(R) = \frac{P_{H_2O}}{P_{N_2}}(R)\frac{K_{N_2}}{K_{H_2O}}\frac{\beta_{N_2}^{Raman}}{\beta_{H_2O}^{Raman}}\left(\frac{K_{N_2}}{K_{O_2}}\frac{n_{N_2}}{n_{O_2}}(R)\frac{\beta_{N_2}^{Raman}}{\beta_{O_2}^{Raman}}\right)^{\frac{\sigma_{H_2O}-\sigma_{N_2}}{\sigma_{N_2}-\sigma_{O_2}}}\left(\frac{P_{O_2}}{P_{N_2}}(R)\right)^{\frac{\sigma_{H_2O}-\sigma_{N_2}}{\sigma_{N_2}-\sigma_{O_2}}} \tag{9}$$

or as:

$$\frac{n_{H_2O}}{n_{N_2}} = K_{cal}\frac{P_{H_2O}(R)}{P_{N_2}(R)}\left[\frac{P_{O_2}(R)}{P_{N_2}(R)}\right]^{\frac{\sigma_{H_2O}-\sigma_{N_2}}{\sigma_{N_2}-\sigma_{O_2}}} \tag{10}$$

where the factor K_{cal} is the overall instrument constant value and will be established by calibrating the lidar. According to Ref. (13) the Rayleigh and Mie scattering processes are neglected in this formalism as they do not produce any significant error in H_2O determination.

2.3. Statistical (quantum) noise

The statistical noise is a major perturbation in Raman lidar measurements[17] due to the low Raman cross-section, typically four orders of magnitude lower than the elastic cross-section, and therefore due to the low Raman signal level. The statistical noise has been modeled following the Poisson statistics with the parameters defined in Table 2. In this case the model study was performed in a purely molecular atmosphere (no aerosol load). Based on typical experimental values we estimate a number of photo-electrons per pulse at the photo-cathode, from a distance of 200 m and for one ADC channel of 7.5 m resolution, of some hundreds for both N_2 and O_2 Raman lidar signals and some counts for H_2O. This model simulation of the statistical noise is based on series of 100 runs for each similar initial condition. From these series of runs the standard deviation with respect to the mean value is obtained and reported in Fig. 3 versus the range.

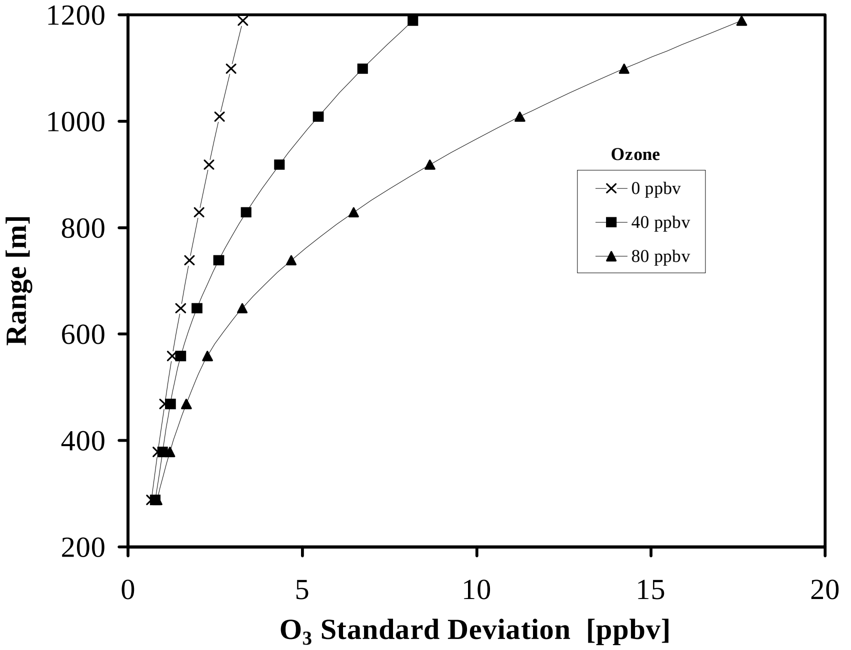

Figure 3(a)

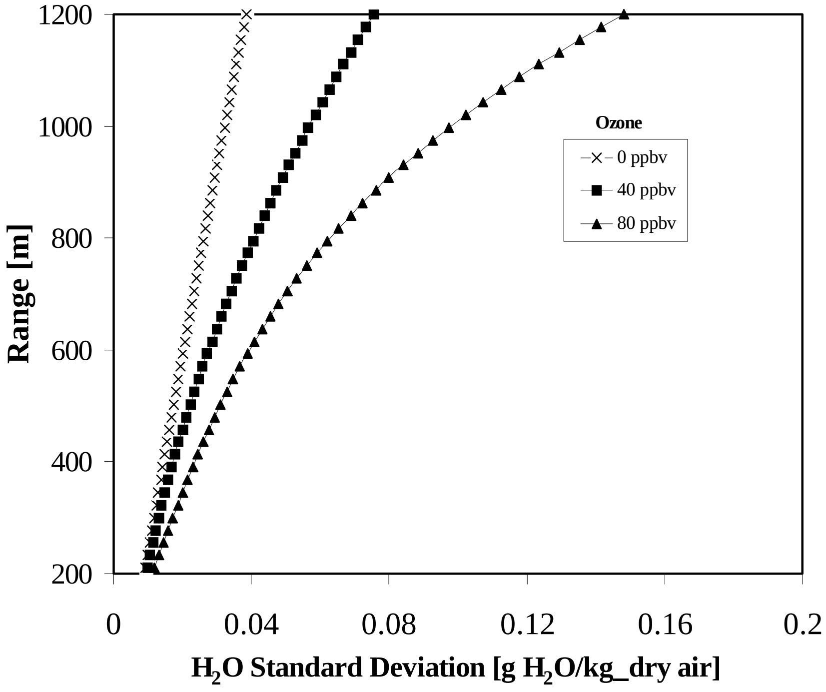

Figure 3(b)

Figure 3. Statistical Noise: Predicted standard deviation for ozone (a) and water vapor (b) Raman lidar retrieval due to the statistical noise (Poisson statistics) with the experimental parameters defined in Table 2.

Figure 3(a) shows the ozone standard deviation due to the effect of the statistical noise on the retrieved ozone concentration for three profiles with constant ozone concentrations of respectively 0, 40 and 80 ppbv. These results are achieved averaging over 5 files of 4'000 laser shots as defined in Table 2. With a sampling rate of 20 MHz the ultimate range resolution is 7.5 m. Such short optical integration path would nevertheless result in too large uncertainty on the ozone retrieval. Thus we used an effective range resolution of 90 m or an equivalent bin resolution of 12 ADC channels. Since the presence of ozone itself lowers significantly the Raman signals through extinction, higher ozone values directly induce greater statistical error. The results in Fig. 3(a) indicate that on one hand an average over at least 20'000 shots is needed for a suitable ozone Raman DIAL retrieval. This means that for a laser source with 10 Hz repetition rate the averaging time will be about half an hour. On the other hand above an altitude range of typically 700 m agl the error source due to the statistical noise is reaching a value higher than 5 % of the measured ozone concentration in the case of a constant profile with 80 ppbv. This uncertainty is considered as an upper acceptable limit. Note that even at O_3 = 0 ppbv the statistical noise affecting the O_2 and N_2 Raman signals already induces an ozone standard deviation. From this simulation of the statistical noise only, one may conclude that the maximum achievable range for ozone with this Raman DIAL system will be on the order of 700 m above the lidar site with a spatial resolution of 90 meters, a time resolution of half an hour, and a precision due to the statistics of ± 5 % for a typical ozone concentration of 80 ppbv in the atmosphere.

A similar statistical analysis is performed for the Raman water mixing ratio retrieval in Fig. 3(b) where again the three constant ozone profiles are considered (0, 40, and 80 ppbv). In this case the range resolution is set at 22.5 m (3 ADC channels) and reasonable water vapor estimates are predicted for an altitude range of up to 1'200 m agl. Note that the standard deviation is calculated for a water vapor mixing ratio with referenced value given at 200 m agl (above ground level), which is the full overlap condition, by the water content model atmosphere. In comparison with the results obtained for ozone, at 700 m agl the water vapor standard deviation in an atmosphere containing 80 ppbv of ozone is less than 1% of the mean water vapor mixing ratio. This better result is directly due to the linear dependence of Eq. (3) in the water vapor retrieval that is less sensitive to the statistical error than in the case of the ozone Raman differential analysis. Here one may conclude that the Raman lidar instrument will give an estimate of the water vapor content in the atmosphere with an accuracy of better than 2 % (statistical noise only) for an altitude range of 1'200 m above the lidar site, a spatial resolution of 22.5 m and a time resolution of half an hour.

2.4. Optical cross-talk in the detection box

The spectral separation of the three Raman signals and rejection of the elastic wavelength are performed by a grating polychromator. In such a device we may consider mutual optical cross-talk among the Raman channels and a leak of not totally suppressed elastic signal into the Raman channels. These two types of optical cross talk are simulated, one due to the elastically backscattered light added to each of the different Raman channels, and the other one due to the cross-talk between adjacent Raman shifted channels.

Let us consider first the cross-talk between N_2 & O_2 Raman signals biasing the ozone retrieve and the cross-talk between H_2O and O_2 Raman signals biasing the water vapor retrieve. Different model runs were performed for cross-talks ranging from 10^{-6} to 10^{-3} with a model atmosphere with constant ozone vertical profile (80 ppbv) and an aerosol layer with b = 1.8 and e = 40. The model results show very small effect due to this optical effect. The associated errors on ozone were always lower than 0.3 ppbv while they remained below 0.01 [g H_2O / kg_dry air] for the water vapor in the worst case. As an example of these simulation runs Fig. 4 shows the cross-talk effect due to the Raman shifted O_2 signal on H_2O versus the altitude range. Since the H_2O Raman signal has by far the weakest signal intensity as compared with the two other Raman signals mainly because of its comparatively much lower concentration one may expect the strongest (or worst) effect of the cross-talk in this case. The predicted shift in the water vapor mixing ratio retrieval ΔH_2O presented in Fig. 4 is the difference between the water vapor retrieval without any cross-talk effect versus the same retrieval biased by the cross-talk of the O_2 signal on H_2O.

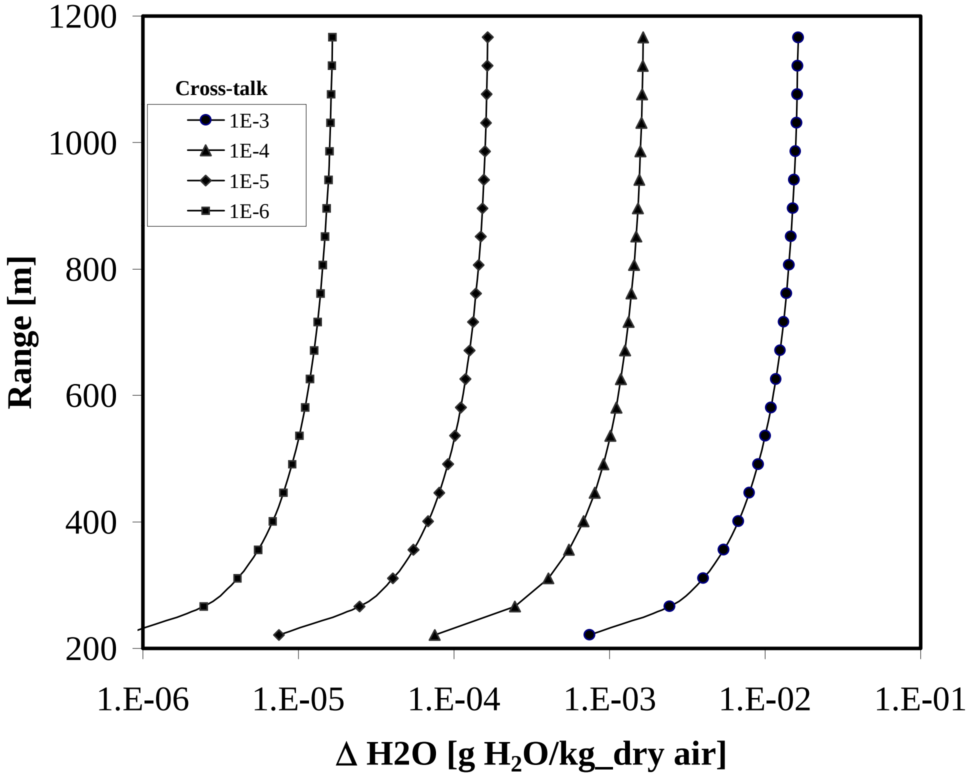

Figure 4. Optical Cross-talk: Predicted error on water vapor Raman lidar retrieval due to the optical cross-talk between H_2O and O_2 Raman signals. The horizontal scale is the difference between the water vapor mixing ratio retrieval without cross-talk effect and the same retrieval bias by the cross-talk effect.

As these runs are performed in an atmosphere with very high aerosol load and a constant 80 ppbv of ozone the simulation shows that the largest cross talk effect are expected at long range where the signal to noise ratio is the weakest. For a cross-talk of 10^{-3} at a range of 200 m the expected shift is about -10^{-3} [g H_2O / kg_dry air] (negative correction) and it reaches a value of -10^{-2} at 1'200 m or an effect higher by typically one order of magnitude. This simulation is performed with a constant detection efficiency versus the range. In this sense the effect of an incomplete detection of the Raman signal at short distance where the probed air volume image in the grating polychromator is the largest is not taken into account.

For the cross-talk between the elastic backscattered light and the Raman channels, one may expect a stronger effect since the elastic backscattered cross section is up to four orders of

magnitude higher than the Raman cross section. This aspect is addressed in detail in the experimental layout presented in Section 3. In order to prevent such strong optical interference, additional filters were set at the entrance of the polychromator with a rejection ratio between the 266 nm light and the other Raman channels of more than five orders of magnitude. Model runs were performed with cross-talk values ranging from 10^{-9} to 10^{-6} between the elastic backscattered light and any of the different Raman channels. The associated errors due to the elastic cross talk on ozone remained always below -0.15 ppbv and for the water vapor below -0.1 [g H_2O / kg_dry air] in the worse case.
In summary, the two types of optical cross-talk have negligible effect if the wavelength separation unit allows achieving a cross-talk level lower than 10^{-3} for two adjacent Raman channels, and lower than 10^{-6} between the elastic backscattered signal at 266 nm and the closest Raman backscattered signal namely O_2 at 277.5 nm.

2.5. After pulse effect

Another instrumental effect that may strongly alter the real lidar return signal is the after pulse effect (APE) of the receiving photomultiplier.[17] The after pulses caused by internal processes within the PMT appear as secondary pulses that follow the genuine pulse. In modern PMTs most after pulses are supposed to be primarily due to positive ions (either residual from manufacture, or helium which diffuses through the glass envelope) that strike the photocathode to release secondary electrons. The APE occurs mostly within 1-2 µs after the main pulse.[19, 20]
The time delay, the duration and the shape of the after pulse depend on the ions involved and the PMT configuration.[21] The influence of the APE on the lidar signal can be estimated as a convolution of the after pulse produced by a short light pulse and the lidar signal. The result is a bias that is superimposed over the original lidar signal. Since the after pulse is shorter compared with the lidar signal duration, the influence of the APE can be presented as a delayed echo of the lidar signal with an integrated value proportional to the lidar signal itself. Let us define the APE relative intensity as the ratio between the APE signal and the Raman lidar signal. In our simulation we choose a time delay for the after pulse of 2 µs or an equivalent range of 300 m after the lidar maximum intensity defined at 200 m far from the lidar experiment. The model atmosphere is chosen with 80 ppbv ozone and the homogeneous aerosol layer (e=40; b=1.8). The simulated APE error is defined as the difference between the ozone respectively the water vapor mixing ratio profile with APE compared to their respective profile without the APE.

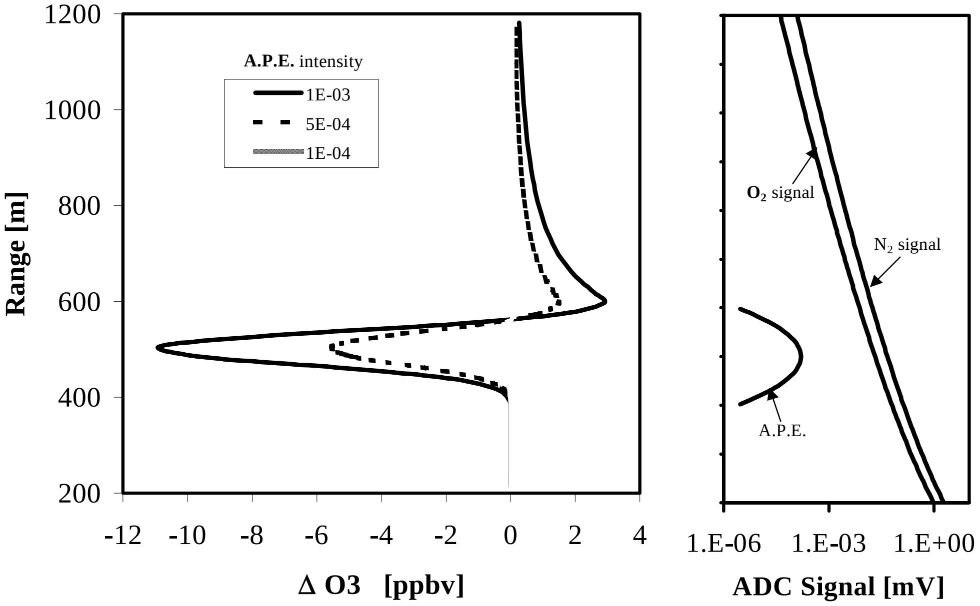

Figure 5(a)

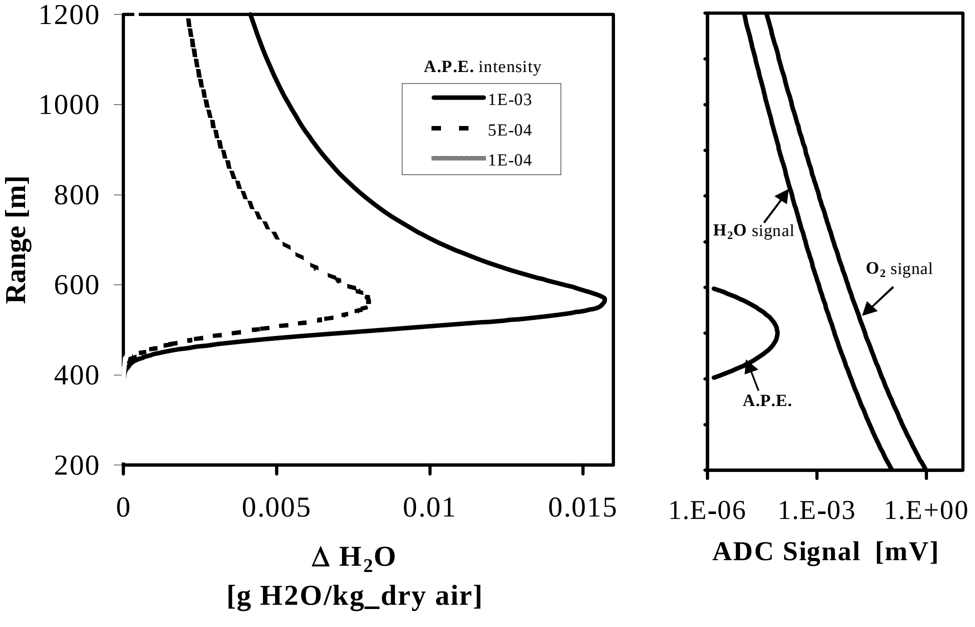

Figure 5(b)

Figure 5. After Pulse Effect (APE): Predicted error on ozone (a) and water vapor (b) Raman lidar retrieval due to the APE. The horizontal scale is the difference between the ozone and the water vapor mixing ratio retrieval with APE compared with their respective retrieval without the APE. The model lidar signals are also shown versus their typical ADC voltage intensities (log scale) with the Raman O_2 & N_2 signals in the case of ozone and the Raman H_2O and O_2 signals for the water vapor mixing ratio.

The APE on ozone retrieval is shown in Fig. 5(a) for three different values of the APE ratio. With an APE of 10^{-3} the maximum predicted ozone error is -11 ppbv (approx. 14 %) while for an APE below 10^{-4} this effect remains within the acceptable limit of precision of the method. The same effect is studied in Fig. 5(b) for the water vapor mixing ratio retrieval. The APE error induced on the water vapor mixing ratio is less than 1 % for an APE intensity of 10^{-3}. The difference in the magnitude and shape of the errors in ozone concentration and water vapor mixing ratio is again explained by the fact that the ozone calculations in Eq. (2) include taking a derivative, which operation reveals a characteristic perturbation in the signal. In conclusion if the photomultiplier units used to acquire the different Raman signals are tested with an APE lower than 10^{-4} this simulation predicts essentially no remaining effect on the signal analysis.

2.6. Additional systematic error sources on Raman lidar

Systematic errors such as interference with other trace gas species in the atmosphere or the spectral stability of the laser source must also be considered.

In Eq. (2) ozone was the only absorbing species taken into account. The DIAL technique is sensitive to the influence of any other absorbing trace-gas species in the wavelength region used. The main interference in the UV for tropospheric measurements is SO_2 and NO_2. Table 1 gives their respective absorption cross-section as compared with ozone for the three Raman wavelengths considered in this study. The systematic error ΔO_3 induced in the ozone retrieval by any interfering gas *(IG)* can be presented as:

$$\Delta O_3 = -\frac{(\sigma_{IG}(\lambda_{N_2}) - \sigma_{IG}(\lambda_{O_2}))N_{IG}}{(\sigma_{O3}(\lambda_{N_2}) - \sigma_{O3}(\lambda_{O_2}))} \tag{11}$$

where N_{IG} is the interfering gas concentration. The ratio of the differential absorption cross-section for IG = NO_2 versus O_3 is $-7.61\text{x}10^{-3}$ while it reaches a value of -10^{-1} for SO_2. In other words the systematic error ΔO_3 in the ozone concentration caused by 100 ppbv of NO_2 is less than -1 ppbv, while 100 ppbv of SO_2 will induce a systematic error of -10 ppbv. One should point out that such error sources affect not only the Raman DIAL but also any elastic DIAL measurements while on the other hand they remain relatively small in most case studies.

The systematic error induced by *IG* in water vapor measurements can be calculated using the same formalism as the one used for ozone correction. The magnitude of this error will be proportional to the differential cross section of the *IG* at N_2 and H_2O Raman wavelengths (see Table 1). The differential cross sections of NO_2 and SO_2 are correspondingly $-2.9\text{x}10^{-2}$ and $-1.17\text{x}10^{-2}$ of the ozone differential cross-section. Since the expected NO_2 and SO_2 systematic errors represent a proportionally small part of the ozone correction, the latter can be neglected. One should nevertheless point out that this correction term appears in the integral term in Eq. (3) and will play a more significant role for a longer range of measurements.

The spectral stability of the laser source may as well be a source of systematic error since a shift in the emitted wavelength will induce a displacement of the lidar signal image at the output of the polychromator. Hence the specified spectral stability of the laser source by the manufacturer is 1 cm^{-1} or a wavelength shift of less than 0.015 nm at 266 nm. With a grating spectral resolution of 0.51 nm / mm the wavelength shift due to the spectral stability of the laser source will be 30 µm. This effect can be neglected.

In summary we will see that the systematic uncertainty induced by effects such as the after pulse in the PMT or the different cross-talks in the detection box may be avoided taking special care in the design of the experiment and the choice of the PMT. The interference with other trace gas species may also be ruled out in most atmospheric conditions. The remaining (and by far the largest) uncertainty in this experiment will be the signal statistics. A 5 % accuracy for an altitude range of up to 700 m, a spatial resolution of 90 m and a temporal resolution of 30 min is expected for the ozone retrieval in typical atmospheric conditions with 80 ppbv ozone, while it is 2 % for an altitude range up to 1'200 m and a spatial resolution of 22.5 m for the water vapor retrieval.

3. Raman lidar experimental setup

The Raman lidar system presented in Fig. 1 is based on a frequency quadrupled Nd:YAG laser (Continuum Inc. Model Powerlite-8000) used in the transmitter.[22] The laser output energy at 266 nm is 120 mJ at 10 Hz repetition rate with 7 ns FWHM pulse duration. The initial laser beam divergence of 0.5 mrad is reduced to 0.17 mrad by a three-time beam expander. The beam is emitted into the atmosphere by a right angle prism mounted on a piezoelectric controlled stage that simplifies the final alignment. The separation between the transmitting and receiving axes of the lidar is 30 cm, which makes possible the full overlap between the laser beam and the telescope field of view at an altitude of 150 m agl typically.

The backscattered light is collected by a 20 cm in diameter, 60 cm focal length Newtonian telescope. A diaphragm is used to adapt the telescope field of view set at 5 mrad. Two custom designed band-pass filters at the entrance of the polychromator achieve an initial suppression of the strong elastic backscattered signal at 266 nm. They are tilted at 18° for an optimum transmission of the three Raman backscattered signals and a maximum rejection of the elastic backscattered light. At this angle each filter has up to 80 % transmission for the three Raman wavelengths and an optical density of 2.6 at 266 nm. This specification was measured directly after the filters were delivered. One year later they show a loss of about 10 % in transmission. The filters were placed in the parallel beam between two lenses that fit the F-numbers of the telescope and polychromator. The wavelength separation of the Raman signals is performed by a 500 mm Cherny-Terner polychromator used as well to reject the daylight background and the elastically backscattered light. The polychromator resolution with a 3’600 gr /mm UV enhanced holographic grating is 0.51 nm / mm. For additional suppression of the daylight background a solar blind filter is placed at the polychromator entrance.

The Raman signals from O_2, N_2, and H_2O are detected simultaneously by three Hamamatsu H-5780-06 photosensor modules. Each of them is equipped with an optical diffuser and a short focal length lens to improve the spatial uniformity of the photosensor module.[23] Thanks to a pulse duration of less than 0.65 ns achieved by such photodetectors, both analog and photon-counting detection modes are possible. The acquisition of the signals is performed using a Licel transient recorder that combines photon counting with a 12 bit 20 MHz analog-to-digital converter. Raw data are averaged over 4'000 shots and stored with the ultimate range resolution of 7.5 m.

3.1. Experimental determination of the optical cross-talk

A careful analysis of the cross-talk measured in our experimental set-up was performed. Even though the three signals may affect each other, the influence of the N_2 channel on the two others is stronger because it is the "central" wavelength and has the highest intensity level. Therefore, we measured the optical cross-talk caused by the N_2 signal in the O_2 and H_2O channels. For the measurements we used light produced by stimulated Raman scattering of a 266 nm laser beam in 35 bar of nitrogen. A small fraction of its first Stokes at 283.6 nm was injected by an optical fiber into the lidar receiving telescope and the resulting crosstalk intensities in the oxygen and water vapor channels were measured by the respective PMTs. The intensity of the injected 283.6 nm light was chosen so that the resulting cross-talk intensities were well above the photo-detectors noise level. The light intensity in the nitrogen channel was measured using neutral density filters that attenuate the signal below the saturation level of the photo-detector. The cross-talk in the O_2 and H_2O channels was calculated as a ratio between the cross-talk intensity in the respective channel and the intensity in the N_2 one, taking into account the relative photo-detectors sensitivity and the neutral density filters attenuation in the N_2 channel. The measured cross-talk levels were respectively : 2.2×10^{-5} for O_2 / N_2 and 5.2×10^{-5} for H_2O / N_2. The previous simulation study showed that it is only with a cross-talk greater than 10^{-3} that a detectable bias on ozone or water vapor retrieve was expected. Our experimental cross-talk values were much lower, and low enough to neglect their influence. These values were also in good agreement with the stray light level stated by the polychromator manufacturer.

Care was also taken to "suppress" the residual elastic signal and to measure the degree of this suppression in the Raman channels. Since this degree is very high its direct measurement was impossible. Instead, the suppression of the elastic signal by the bandpass filters and the polychromator was measured separately. For the polychromator, the elastic backscatter light suppression was measured in a similar way than the one described above for the cross-talk among the Raman channels, this time injecting directly a fraction of the 266 nm light into the receiving telescope. The suppression degrees for the different Raman channels were calculated as a ratio between the intensity of the 266 nm light entering the polychromator and the light intensities detected in these channels. The measured values were as follows: for N_2 channel = 1.5×10^5; for O_2 channel = 5.9×10^4; for H_2O channel = 3.5×10^4. The band-pass filters were measured separately, with a total attenuation ratio of the elastic signal (ratio before versus after the filters) of 1.58×10^5 times. Thus the total suppression of the elastic backscatter signal at the receiver was always higher than 5×10^9. This value ensured that the residual pump beam in the three Raman channels was not the source of systematic error, as was also reported by the model results. This high rejection of the elastic signal was further confirmed by the fact that no detectable echo from low altitude dense clouds was observed in the different Raman channel.

3.2. Experimental determination of the APE

During the initial tests of the Raman lidar setup, classical type glass-bulb / head-on photomultiplier tubes were used that showed APE. An upgrade of the system was made using new type of metal package photomultipliers.[23,24] With these new PMTs, no APE was detectable even when illuminating directly the photocathode with 7 ns laser pulses with very high intensity. Such laser pulses induced PMT output pulse amplitude up to 1 V on 50 Ω load without APE. A possible explanation of this fact is the very short time delay of the after pulses due to the very small (less than 1 mm) distance between the cathode and the first dynode, which makes the after pulses difficult to distinguish from the main pulse. Another possibility is the new metal package that is less permeable than glass-bulb for atmospheric helium that is known to be one of the main reasons for after pulses.

4. Results and discussion

Raman lidar measurements were performed both from the EPFL site in Lausanne, in March-April 1999 and during a field campaign in Crete, Greece, in May 1999. Different results are discussed here and will help to underline the advantage and the limitation of our current instrument.

The first results were obtained with the idea of achieving a time series of Raman lidar measurements at day and night-time conditions for both ozone and water vapor vertical profiles simultaneously. During this time series, additional measurements at 8 m above ground level of the ozone concentration, relative humidity, temperature and pressure were performed. The ozone concentration was monitored by a UV absorption analyzer (Dasibi 1008 AH) with a precision of ± 2 ppbv.

The Raman shifted N_2 and O_2 backscattered signals were acquired in the analog mode using the 12 bit 20 MHz A-D converter, while the photon counting method of detection was used for the H_2O signal. The acquisition of the different signals was performed using a Labview based software with a real-time display of the preliminary results and post-treatment performed using Matlab.

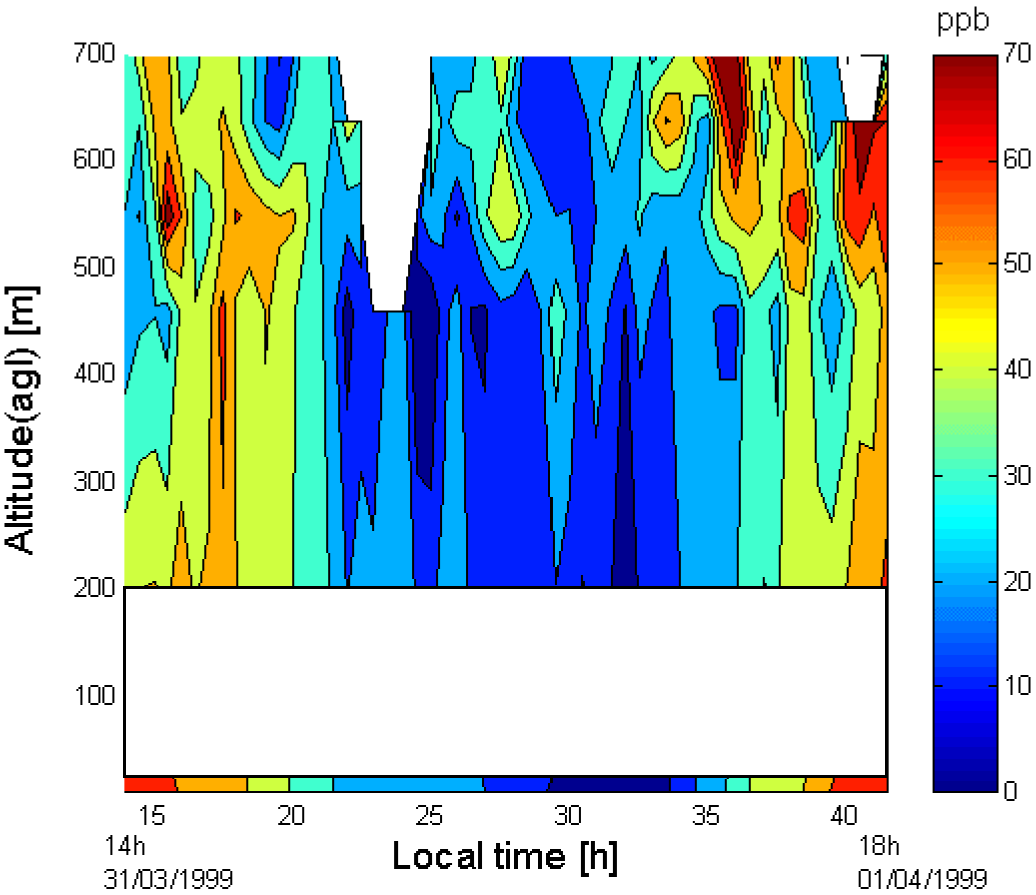

Figure 6. Ozone Raman DIAL obtained in March 1999 for a time series of 28 hours. The ozone concentration measured at the ground are given by an UV absorption detector. They are measured by Raman DIAL from an altitude of 200 m agl and up to 700 m agl. The spatial resolution is 90 m and the time resolution 30 minutes.

The time series in Fig. 6 shows the ozone vertical profile measured continuously over a period of time of 28 hours. Based on the statistical noise analysis presented in Section 2 of this paper, the lidar vertical resolution was set at 90 m and the time resolution at 30 min. A gliding average was applied both on the altitude range and on the time scale. The white rectangle on Fig. 6

indicates the spatial range where ozone cannot be retrieved by lidar due to the uncompleted overlap between the laser beam and the telescope field of view. The ground level ozone concentrations measured by the point monitor are also shown on the figure, below the white rectangle, to compare with the lidar data.

In this time series, the ozone diurnal cycle was well seen, with higher values during the period of high solar radiation, and lower values at nighttime. One should also note that this time series was taken in very humid conditions associated with formation of thin water cloud layers at night. But even so, essentially no data rejection in the ozone retrieval was needed, with the exception of some data between 22 and 24 hours local time at an altitude range higher than 500 m agl. Furthermore during this period of observation of more than one day, a strong variation of the height of the inversion layer was observed. The combined optical interference of cloud layers and the change in aerosol gradient due to the change in height of the top of the planetary boundary layer would have certainly affected or even made impossible any elastic DIAL ozone measurements in similar conditions. Such effects have been often reported [9,10] but did not affect this ozone time series.

The water vapor time series following the data treatment in Eq. (10) with the three N_2, O_2, and H_2O Raman signals is presented in Fig. 7.

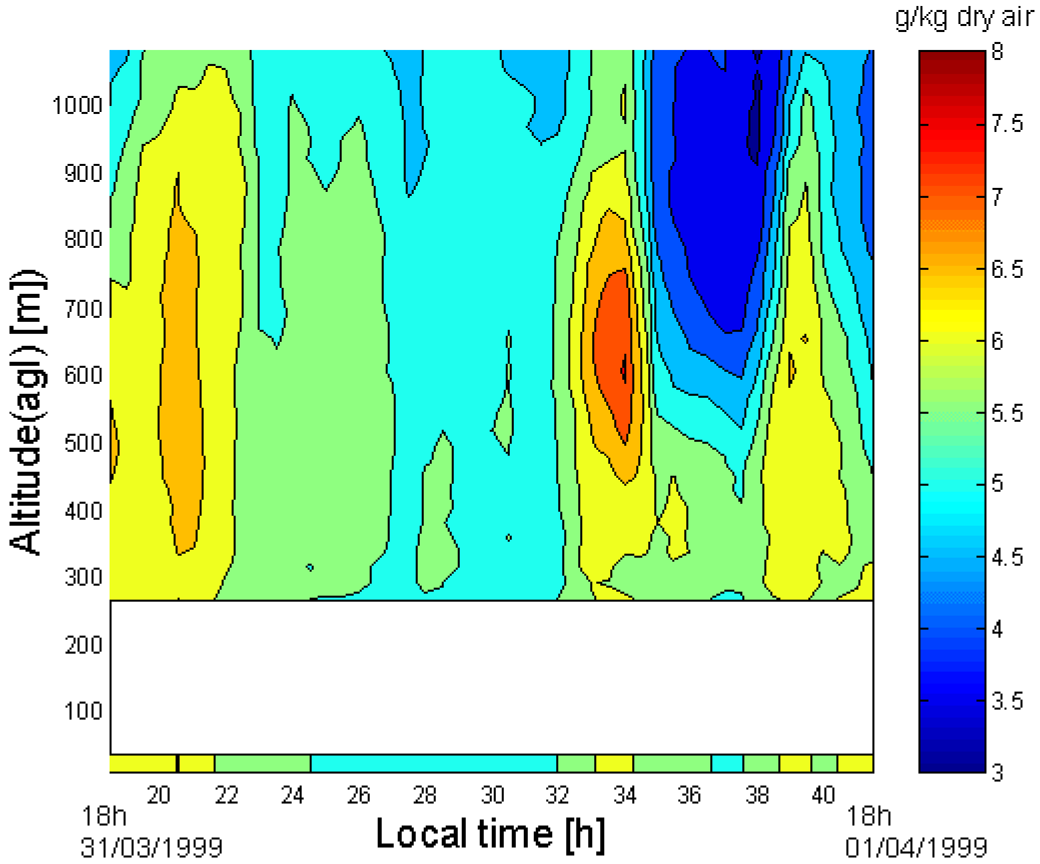

Figure 7. Water vapor mixing ratio retrieved by Raman lidar: obtained in March 1999 for a time series of 24 hours with relative humidity measured at the ground. The latter values are also used at 270 m agl as reference values for the first altitude range of the Raman lidar profile. The spatial resolution is 22.5 m and the time resolution is 30 minutes.

These measurements were taken simultaneously with the ozone measurements. As indicated previously the instrument constant K_{cal} being unknown an absolute profile of the water vapor mixing ratio in the air may only be obtained if an absolute reference is available at a given altitude. Since this is not the case here we used the absolute water vapor mixing ratio measured at the ground level as the reference value of the first altitude achieved by lidar, namely around 270 m agl. In a similar manner to the ozone time series in Fig. 6, the white rectangle in Fig. 7 covers the spatial range where the water vapor mixing ratio cannot be retrieved by lidar. But in this case the values measured close to the ground are equivalent to the reference values at 270 m agl. This means that the present water vapor mixing ratio time series must rather be regarded as a time series with relative numbers, while the example of an absolute water vapor mixing ratio vertical profile compared with balloon measurement will be discussed below.

The measurements are presented with a vertical resolution of 22.5 m and a time resolution of 30 minutes. It is important to note that even under daytime condition, with H_2O Raman shifted wavelength at 294.6 nm close to the "solar-blind border", the solar background did essentially not perturb the photon counting signal detection. This indicates a very good rejection of the solar background achieved by the combination of the polychromator, the band-pass and solar blind filters. This water vapor time series shows the characteristic day / night time behavior of the water vapor content in the atmosphere, with convection at daytime lifting upward air masses with higher water vapor content.

The result in Fig. 7 is obtained accounting for the ozone differential absorption effect described in Eq. (10). In this formalism we used the three Raman backscattered signals and were able to correct the water vapor mixing ratio retrieval for the ozone effect without having to retrieve explicitly the vertical ozone profile. While ozone was explicitly retrieved up to 700 m agl as seen in Fig. 6, the water vapor mixing ratio corrected for the ozone absorption can be retrieved up to 1'200 agl. Based on this formalism it is furthermore possible to express the systematic shift on the water vapor time series due to the ozone differential absorption. Figure 8 illustrates the difference ΔH_2O between the water vapor mixing ratio retrieval uncorrected for the ozone differential absorption effect and the same time series but corrected.

As already shown as a model result in Fig. 2, higher ozone content leads to larger water vapour corrections with an additive effect due to the integral term in Eq. (3). In this sense Fig. 8 gives additional information about the ozone content in the air since low ΔH_2O values will directly be associated with low ozone concentration. This correlation is nicely confirmed if we compare Fig. 6 and Fig 8 for an altitude range up to 700 m agl while it is now possible to gain a first estimate up to an altitude of 1'200 m agl of the ozone contribution. See for example the ΔH_2O vertical profile at 6 am (30 h "local time" in Fig. 8) with values that are essentially around zero. They are confirmed by very low ozone concentration in Fig. 6 up to 700 m agl measured at the same time. They also are indicative of low ozone concentration for the rest of the altitude range up to 1'200 m agl where ozone was not retrieved anymore by Raman DIAL. This information is gained since in this case the ozone contribution is integrated along the profile and not range-resolved. Values of ΔH_2O up to 1.2 [g H_2O / kg_dry air] are indicative of higher ozone content as is the case in the afternoon of the second day of continuous measurement at 6 pm (42 h "local time"). This shift in the water vapor retrieval corresponds to an effect of about 15 % for ozone values typically below 60 ppbv as partially seen in Fig. 6 and would be even worsen in case of atmospheric conditions with higher ozone concentration. Finally one should note that some negative values for ΔH_2O were obtained with magnitude down to -0.1 [g H_2O / kg_dry air] in the worst cases. These negative values corresponds to less than 2 % of the effective water vapor mixing ratio. They are directly associated with the limit of precision of our determination of the water vapor mixing ratio retrieval and are slightly higher than the predicted statistical error defined by the model study.

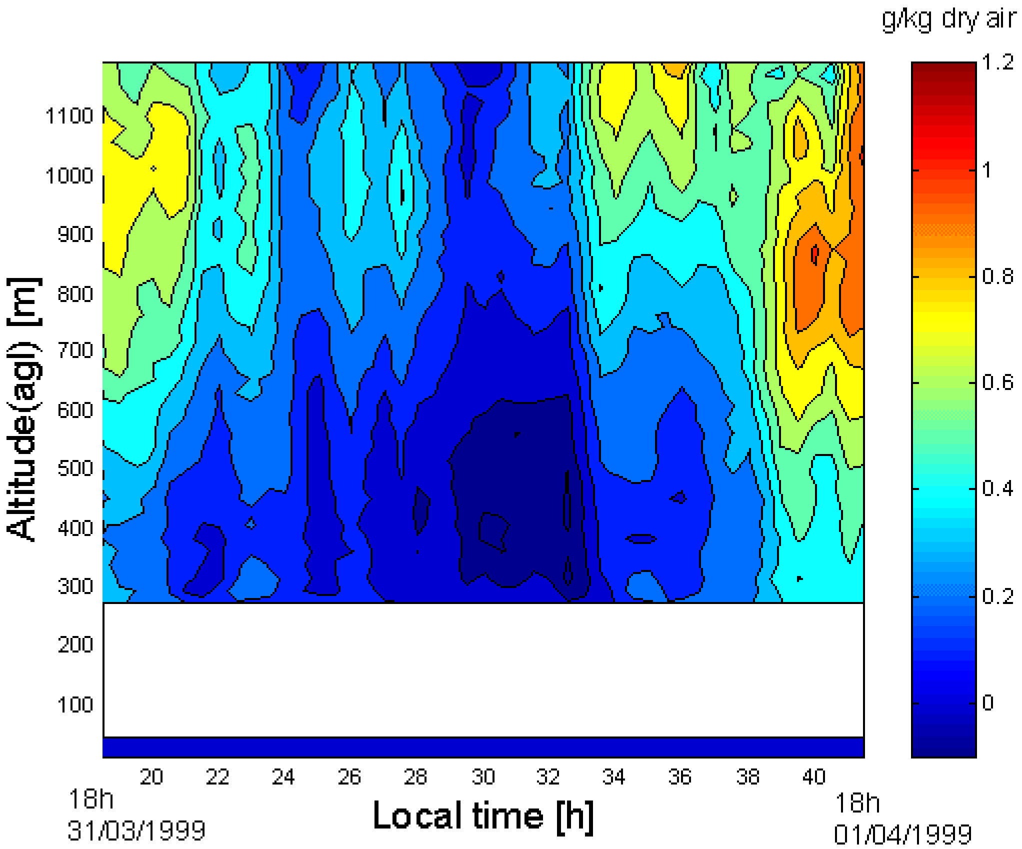

Figure 8. Difference in the water vapor mixing ratio retrieval ΔH_2O uncorrected for the ozone differential absorption effect as compared to the corrected time series. Small values of ΔH_2O along the entire vertical range are associated with low ozone content in the atmosphere. Note that negative ΔH_2O values (>-0.1 [g H_2O / kg_dry air]) are also indicative of the limit of precision of the method (ca. ± 2 %).

Later in the year, the same lidar instrument was equipped on a movable platform and transported to Crete, Greece, to participate to the PAUR II program (Photochemical Activity and Ultraviolet Radiation Modulation Factors).[25] While the system was most of the time operated in the ozone elastic DIAL mode, the chance for additional Raman water vapor measurements was offered for a short period of time with direct comparison with absolute water vapor profile measured by balloon. The balloon ozone and temperature profiles were determined with an electrochemical concentration cell ozone-sonde in combination using the Vaisala RS-80 radiosonde, H-type Humicap sensor. This widely used sensor measures water vapor mixing ratios with an accuracy of ± 5 % in the lower troposphere. Procedures for sonde preparation and data acquisition are similar to those developed by NOAA / Climate Diagnostics and Monitoring Laboratories.[26] One-second data were recorded and processed as described in Thompson et al..[27] The balloon was launched from essentially the same place as the EPFL lidar trailer.

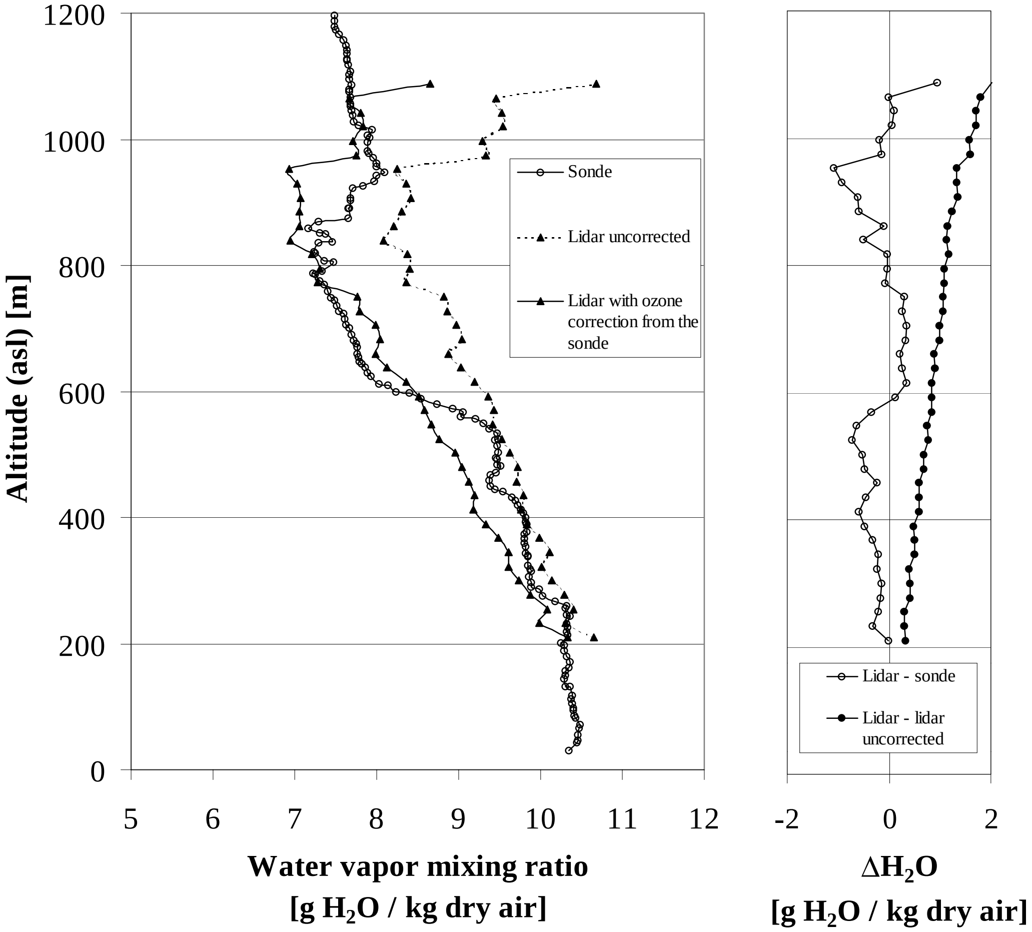

Figure 9. Raman lidar water vapor measurements compared with balloon soundings: The lidar data are shown with a spatial resolution of 22.5 m and a time resolution of 30 minutes. They are compared with one-second balloon data recorded at an ascent speed of ca. 5 m/s. The water vapor balloon measurement at 210 m asl is used as an absolute calibration for the lidar signal. The water vapor mixing ratio vertical profile retrieved by Raman lidar is shown taking into account the ozone differential absorption effect considering the ozone concentration profile measured simultaneously by balloon ("Lidar with ozone correction"). The same lidar profile is also shown without this correction ("uncorrected"). The corresponding difference "Lidar –lidar uncorrected" may be compared with results presented in Fig. 8. The difference ("Lidar-sonde") indicates values below 1 [g H_2O / kg_dry air] over the entire range of measurement or a difference of less than 15 % between the two methods. This comparison was performed in May 1999 in Crete during the PAUR II experiment with the Raman lidar on board of the EPFL lidar trailer.

Figure 9 shows a comparison of the vertical water vapor profile obtained by Raman lidar and the balloon measurements. During this experiment the lidar system was only measuring the

Raman N_2 and H_2O channels. Thus, we used directly the ozone data from the balloon to correct for the ozone interference effect on water vapor according to Eq. (3). The water vapor mixing ratio measured by balloon was used to determine the lidar calibration constant K_{cal} at 210m asl where a full overlap between the laser beam and the telescope field of view was achieved. This absolute water vapor mixing ratio vertical profile retrieved by Raman lidar was obtained from averaging over 5 files of 4'000 laser shots (total integration time of 30 minutes between 8 and 8.30 am) with a vertical resolution of 22.5 m, and appeared to be in good agreement with the balloon data. The difference ΔH_2O reported in Fig. 9 between the water vapor obtained by lidar and by balloon was typically below 1 [g H_2O / kg_dry air] over the entire range, with the highest discrepancy observed at the height of the inversion layer. This transition layer was observed between 850-950 m asl in the balloon data, while in the case of the lidar data it was defined above 950 m asl. This difference may well be explained by the difference in time and air volume sampled by the two methods. In particular averaged values obtained by lidar over a period of 30 minutes were compared with instantaneous values measured by balloon that may in turn be influenced by very local air masses. In this example the balloon was launched at 8.11 am with a vertical speed of about 5 m/s and one data point every second.

In Fig. 9 the water vapor content obtained without considering the ozone correction (called "Lidar uncorrected") is also shown. This profile is calculated with the instrument constant determined as previously without considering the integral factor in Eq. (3). In this case the error estimate $\Delta H_2O_{\text{Lidar-lidar uncorrected}}$ reaches differences as high as 15% for ozone concentrations around 70 ppbv. This is an integrative effect and therefore the highest discrepancy is reached at long range. This difference is higher than the largest discrepancy between balloon and water vapor lidar measurements corrected for the ozone effect. Note that at the calibration height at 210 m asl $\Delta H_2O_{\text{Lidar-lidar uncorrected}}$ is not zero since the water vapor "shift" due to the ozone absorption between the ground and this height is already taken into account.

5. Conclusion

The principle and design of a single wavelength excitation Raman-DIAL instrument for day and night-time ozone and water vapor measurement in the planetary boundary layer was demonstrated. The objective was to perform measurements at low altitude in the PBL, an atmospheric layer characterized by high and inhomogeneous aerosol load, where elastic DIAL observations may in some cases not be used due to unpredictable Mie interference.

Error analysis based on the influence of the instrumental and atmospheric effects that may decrease the Raman lidar performance was made. It concerned the influence of the aerosol content on the ozone retrieval and the ozone concentration on the water vapor retrieval, the statistical noise, the after pulse effect, the cross-talk between Raman channels or the influence of the residual laser light on Raman signals. This study was confirmed by Raman lidar results obtained for the measurements of ozone and water vapor vertical profile in the PBL. The error induced on the water vapor mixing ratio retrieval by the ozone differential absorption effect revealed that if three Raman signals are measured simultaneously (namely O_2, N_2, and H_2O) it is possible to extend the water vapor retrieval range corrected for the ozone effect.

This lidar development is important, since ozone and water vapor measurements are key criteria for the control and quality test of the predictive results obtained by atmospheric transport chemical model. These Raman lidar measurements were furthermore obtained with a resolution that fit both the time and space model resolution. A future combination of the powerful elastic DIAL technique applied at higher altitude or in more homogeneous aerosol conditions with the Raman DIAL method at low altitude will essentially help to cover an altitude range in full agreement with the vertical grid resolution of the model.

6. Acknowledgements

This work was supported by the Swiss National Science Foundation under contract n° 21-50861.97 and the Federal Office for Science and Education under contract n° 97.0377. The balloon sounding was provided by NASA's TOMS project. The authors wish to thank the organizers of the PAUR II project for logistical support in Crete.

7. References

1. B. J. Finlayson-Pitts and J. N. Pitts Jr, "Chemistry of the Upper and Lower Atmosphere: Theory, Experiments, and Applications," Academic Press, San Diego, (1999).
2. A. Clappier, A. Martilli, P. Gross, P. Thunis, F. Pasi, B.C. Krueger, B. Calpini, G. Graziani, and H. van den Bergh, "Effect of sea breeze on air pollution in the Greater Athens Area. Part I: Numerical simulations and field observations," J. Appl. Meteor, **39**, 563-575, (1999).
3. P. Grossi, P. Thunis, A. Martilli, and A. Clappier, "Effect of sea breeze on air pollution in the Greater Athens Area. Part II: Analysis of different emission scenarios," J. Appl. Meteor, **39**, 546-562, (1999).
4. S. Perego, "A numerical mesoscale model for simulation of regional photosmog in complex terrain: model description and application during POLLUMET 1993 (Switzerland)", Meteor. Atmos. Phys., **70**, 43-69, (1999).
5. B. Calpini, V. Simeonov, F. Jeanneret, J. Kuebler, V. Sathya, and H. van den Bergh, "Ozone LIDAR as an Analytical Tool in Effective Air Pollution Management: The Geneva 96 Campaign," Chimia **51**, 700-704, (1997).
6. L. Fiorani, B. Calpini, L. Jaquet, H. van den Bergh, and E. Durieux, "A combined determination of wind velocities and ozone concentrations for a first measurement of ozone fluxes with a DIAL instrument during the Medcaphot Trace campaign," Atm. Env. **32**, 2151-2159, (1998).
7. L. Schoulepnikoff, H. van den Bergh, B. Calpini, and V. Mitev, "Tropospheric air pollution monitoring Lidar," in Encyclopedia of Environmental Analysis and Remediation, R.A. Meyers, ed., (Wiley, New York), 4873-4909, (1998).
8. E. V. Browell, S. Ismail, and T. Shipley, "UV DIAL measurements of O_3 profiles in regions of spatially inhomogeneous aerosols," App. Opt., **24**, 2827-2836, (1985).
9. P. Quaglia, G. Larcheveque, R. Jimenez, V. Simeonov, G. Ancellet, H. van den Bergh, and B. Calpini, "Planetary Boundary Layer ozone fluxes from combined airborne, ground based lidars and wind profiler measurements," Eur. J. Anal. Chem., Analusis, **27**, 305-313, (1999).
10. P. Völger, "Scattering Properties of Selected Model Aerosol Calculated at UV-Wavelengths: Implications for DIAL Measurements of Tropospheric Ozone," Beitr. Phys. Atmosph., 177-187, (1996).
11. A. J. Sedlacek and Mark D. Ray, "Raman DIAL: Application to areas characterized by varying aerosol burden," 19th ILRC, (1998).
12. S. H. Melfi, J.D. Lawrence Jr, and M.P. Mc Cormick, "Observation of Raman scattering by water vapor in the atmosphere," Appl. Phys. Lett., **15** , 295-297, (1969).
13. D. Renault, J.C. Pourny, and R. Capitini, "Daytime Raman-lidar measurements of water

vapor," Optics Letter, **5** (6), 233 - 235, (1980).

14. D. Renault, and R. Capitini, "Boundary-Layer water vapor probing with a solar-blind Raman lidar: validation, meteorological observation and prospects," J. Atmos. Ocean. Tech., **5** (5), 585-601, (1988).
15. T. J. Mc Gee, M. Gross, R. Ferrare, W. Heaps, and U. Singh, "Raman DIAL measurements of stratospheric ozone in the presence of volcanic aerosols," J. Geophys. Res. Let., **20**, 955-958, (1983).
16. R. T. H. Collis, and P. B. Russell, "Lidar measurement of particles and gases by elastic backscattering and differential absorption," Laser monitoring of the atmosphere, E. D. Hinkley ed. , Springer-Verlag, 71-151, (1976).
17. J.A. Sunesson, "Differential absorption lidar system, for routine measurement of tropospheric ozone," Applied Optics, **33**, 7045-7058, (1994).
18. G. P. Anderson, S. A. Clough, F. X. Kneizys, J. H. Chetwynd, and E. P. Shettle, "AFGL atmospheric constituent profiles (0 - 120 km)," Tech. Rep. AFGL-TR-86-0110, Air Force Geophys. Lab., Hascom Air Force Base, Mass., (1986).
19. P. B. Coates, "A theory of afterpulse formation in photomultipliers and the prepulse height distribution," J.Phys.D: Appl.Phys., **6**, 1862-1869, (1973).
20. T. Antonioly, and P. Benetti, "Study of afterpulse effects in photomultipliers," Rev. Sci. Instrum., **54**, 1777-1780, (1983).
21. P. B. Coates, "The origins of afterpulses in photomultipliers," J.Phys.D: Appl.Phys., **6**, 1159-1166, (1973).
22. B. Lazzarotto, V. Simeonov, P. Quaglia G. Larchevêque, H. van den Bergh, and B. Calpini, "A Raman Differential Absorption Lidar for Ozone and Water Vapor Measurement in the Lower Troposphere," Int. J. Env. Analytical Chem., **74**, 255-261, (1999).
23. V. Simeonov, G. Larchevêque, P. Quaglia, H. van den Bergh, and B. Calpini, "The influence of the photomultiplier tube spatial uniformity on lidar signals," Applied Optics, **38**, 5186-5190, (1999).
24. H.Kyushima, Y.Hasegawa, A.Atsumi, K.Nagura, H.Yokota, M.Ito, J.Takeuchi, K.Oba, H.Matsuura, and S.Suzuki, "Photomultiplier tube of new dynode configuration," IEEE Trans.Nucl.Sci, Vol.41, No.4, pp.725- 729, (1994)
25. A. Kylling, A. F. Bais, M. Blumenthaler, J. Schreder, C. Zerefos, and E. Kosmidis, "The effect of aerosols on solar UV irradiances during PAUR campaign," J. Geophys. Res., **103**, 26151-26060, (1998).
26. W.D. Komhyr, S. J. Oltmans, P. R. Franchois, W.F.J. Evans, and W. A. Matthews, "The latitudinal distribution of ozone to 35 Km altitude from ECC ozonesonde observations, 1985-1987, Ozone in the Atmosphere," ed. R.D.Bojkov and P.Fabian, Proc. of Quadrennial Ozone Symposium 1988 and Tropospheric Ozone Workshop, 147-150, (1989).
27. A. M. Thompson, B. G. Doddridge, J. C. Witte, R. D. Hudson, W. T. Luke, J. E. Johnson, B. J. Johnson, S. J. Oltmans, and R. Weller, "Shipboard and Satellite views of a tropical Atlantic Tropospheric ozone maximum and wave-one in January-February 1999," J. Geophys. Res., submitted, (2000).
28. W.K. Bishel, and G. Black, "Wavelength dependence of Raman scattering cross-sections from 200 - 600 nm, in excimer lasers," C.K. Rhodes, H. Egger and H. Pummer, ed., American Institute of Physics, New York, 181-194, (1983).
29. L.T. Molina, and M.J. Molina, "Absolute absorption cross sections of ozone in the 185 to 350 nm wavelength range," J. Geophys. Res., **91**, 14501-14508, (1986).
30. A. C. Vandaele, P. C. Simon, J. M. Guilmot, M. Carleer, and R. Colin, "SO_2 absorption

cross-section in the UV using a Fourier transform spectrometer," J. Geophys. Res., **99**, 25599-25605, (1994)

31. W. Schneider, G. K. Moortgat, G. S. Tyndall, and J. P. Burrows, "Absorption cross-sections of NO_2 in the UV and visible region (200 - 700nm) at 298 K," J. of Photochemistry and photobiology, A: chemistry, **40**, 195-217, (1987).

Chapter 7

Vertical profiles of O_3 and H_2O by Raman lidar, compared with tethered balloon and numerical simulation

This article presented in its draft version, will be submitted.

The lidar measurements were performed on 08th and 09th of April 2000 in the EPFL area during the second intercomparison measurement campaign with a thetered balloon. Comparisons of the H_2O mixing ratio with two numerical models were performed for temporal series and individual profiles.
During these measurements the lidar was run in the Nd:YAG configuration and was transferred from the lidar movable truck to the lidar laboratory at the 5th floor of the chemistry building. The lidar system was mainly the same than in the truck, apart an optical receiver based on an off-axis primary mirror, new bandpass filters with higher performances, and the uncomparable facilities of working in a laboratory. The lidar theory is exposed in an extensive way for a Nd:YAG or a KrF laser source, with explicit details on the calculation of the corrective terms such as the Rayleigh and Mie scattering and the molecular absorption. Graphical representation of these corrective terms, for two specific cases, are exposed and discussed. The possibility of tuning the KrF pump wavelength in order to minimize the absorption by a specific component like SO_2 is presented and the optimum wavelength is given. After the description of the comparison systems, the tethered balloon and the two numerical simulation approaches, individual and mutual comparisons of the different systems available are performed and discussed in order to find the linkings.

Vertical profiles of O_3 and H_2O by Raman lidar, compared with tethered balloon and numerical simulation

Benoît Lazzarotto[a], Stefan Brönnimann[b], René Cattin[b], Olivier Couach[c], Werner Eugster[b], Natalia Hasler[d], Gilles Larchevêque[a], Glen E. Liston[e], Valentin Simeonov[a], Hubert van den Bergh[a], and Bertrand Calpini[a*]

[a]Laboratory for air pollution / Lidar group. EPFL, Swiss Federal Institute of Technology
CH-1015. LAUSANNE. SWITZERLAND

[b]KLIMET. Geographical Institute. University of Bern
CH-3012. BERN. SWITZERLAND

[c]Laboratory for air pollution / Numerical group. EPFL, Swiss Federal Institute of Technology
CH-1015. LAUSANNE. SWITZERLAND

[d]Ecosystems management group. EPFL, Swiss Federal Institute of Technology
CH-1015. LAUSANNE. SWITZERLAND

[e]Atmospheric Science Department, Colorado State University
FORT COLLINS. COLORADO. 80523. USA

*Corresponding author: e-mail: bertrand.calpini@epfl.ch , tel : (++41)(021) 693.61.85

Abstract

UV Raman backscattered signals from atmospheric O_2, N_2, and H_2O can help to retrieve, with a lidar, vertical profiles of ozone concentration and water vapor mixing ratio in the lower troposphere. The theory and the errors due to molecular absorption and scattering by molecules or aerosols are discussed and incorporated in the lidar data treatment. The advantages and inconveniences of the laser source choice, Nd:YAG or KrF, are also discussed. This theoretical background was applied to measurements made during field campaigns in the EPFL area, in parallel to tethered balloon measurements and numerical simulation.

Keywords: Raman lidar, Ozone, Water vapor, Nd:YAG, KrF, Tethered balloon, Numerical simulation.

1. Introduction

The temporal and spatial retrieve of ozone concentrations and water vapor mixing ratio in the troposphere is of essential interest. Contrary to the stratospheric case, the tropospheric ozone can have a harmful impact, with its toxic effect, on humans and vegetation, accelerating the degradation of the minerals and participating in the green-house problem. Concerning the water vapor, knowledge of its highly variable concentration is essential to both the chemistry of the troposphere ($O(^1D) + H_2O \rightarrow 2\,OH$) where it participates in the generation of almost all the important OH radical and to the meteorology. Water vapor is the dominant green-house gas, it plays an important role in the atmospheric chemistry. The conversion and transport of liquid water is the essential point in the earth's heat budget.

Due to the complexity and the non-linearity of the air pollution system including emissions, chemistry, thermal radiation, transport and deposition, pollution abatement strategies can be taken by the use of a three-dimensional mesoscale eulerian photochemical transport model. To check such models, measurement campaigns are undertaken, in which many physical (wind, temperature, H_2O, etc.) and chemical parameters (emissions and imissions) are measured at different parts of the atmosphere.

LIDAR (Light Detection And Ranging), which is a range resolved method for measuring air pollutants in situ, is one of the best tools to make 3-D measurements of gases concentrations like O_3, H_2O and others. Contrary to the ground based measurements that are highly sensitive to the very local conditions, lidar sensitivity and resolution in space and time is optimal to obtain measurements and to compare or give some input data for the model calculations. During the last 30 years, (elastic backscatter) Differential Absorption Lidar (DIAL) has been established as a convenient tool for the monitoring of the three dimensional real time concentrations of air pollutants [*Measures*, 1992], [*Schoulepnikoff et al.*, 1998]. But the DIAL apparatus has shown limitations: - the operation in layers with high aerosol loading like in the Planetary Boundary Layer (PBL) where they are highly variable - the simultaneous detection of several atmospheric components or pollutants is impossible [*Bösenberg*, 1996] - the detection at short range is difficult due to the high dynamics. Furthermore, due to its spectrum and the strong influence from other elements, the water vapor can not be easily measured in the UV with classical DIAL systems.

We developed a method to simultaneously measure the ozone absolute concentration and the water vapor mixing ratio in the PBL. Experiments with Nd:YAG and KrF lasers were made using both analog and photon counting techniques, increasing the dynamic range, were investigated. To retrieve the ozone concentration profile, we use the simultaneous spontaneous Raman backscattering of N_2 and O_2 that have different ozone absorption cross sections. Thus with a modified DIAL technique, the ozone concentration can be measured without most of the interference from poorly known backscatter by particles. Water vapor mixing ratio profiles can also be obtained with a set of three Raman backscattered signals, simultaneously detected, from H_2O, N_2 and O_2. The main advantage of this Raman system is its essential independence to the wavelength dependent backscatter problems induced by aerosols, and the fact that the N_2 and O_2 concentrations are well known as well as the Raman cross sections of interest. The small Raman cross sections are compensated by the high concentrations of O_2, N_2 and H_2O.

Section 2 of this paper presents the needed theoretical background to retrieve the ozone concentration and the water vapor mixing ratio by lidar. The influences of the molecular absorption as well as the Rayleigh and Mie scattering are presented, discussed and applied to

calculate the different corrections to the retrieved quantities. A discussion on the KrF laser pump wavelength, so to optimize the correction due to the SO_2 absorption, is presented.
Section 3 describes the Raman lidar experimental setup, the tethered balloon system and the two numerical models used for intercomparison. Section 4 gives comparisons between the different instruments and models.30-minutes profiles as well as time series of ozone and water vapor concentration are presented. The last section, n°5, deals with the comparison between a Raman lidar system based on a KrF or Nd:YAG laser.

2. Lidar theory

The needed theoretical background to analyze and compare lidar signals from Nd:YAG and KrF emitting configuration is exposed here under. In this formalism, due to the different correction term calculations and the influence study on O_2 and SO_2, terms are written in a more explicit manner than usual. In order to ease the understanding of the formulas, we choose to place some explicit abbreviations besides the symbol letters It permits an easier reading without to many shortened abbreviations.

2.1. Ozone and water vapor retrieve

To each of the three Raman-shifted wavelengths from O_2 , N_2 , and H_2O corresponds a lidar equation [*Measures*, 1992]:

$$P_X(\lambda_L,\lambda_X^{Ram},R) = P_L(\lambda_L)\,K_X\,\frac{A(R)}{R^2}\Delta R\,n_X(R)\,{}^{\pi}\beta_X^{Raman}\left(\lambda_L,\lambda_X^{Ram},R\right)$$

$$\underbrace{\times\exp\left\{-\int_0^R\left[\alpha^{atmos}(\lambda_L,r)+\alpha^{atmos}(\lambda_X^{Ram},r)\right]dr\right\}}_{\Phi(\lambda_L,\lambda_X^{Ram},R)} \qquad \text{EQ 1}$$

Where (the index X stands for O_2, N_2 or H_2O):
$P_X(\lambda_L,\lambda_X^{Ram},R)$ *[W]* is the Raman lidar power backscattered from species X at the laser wavelength λ_L , the Raman-shifted wavelength λ_X^{Ram} and distance *R*, $P_L(\lambda_L)$ *[W]* the laser emitted power at wavelength λ_L , K_X *[no unit]* the instrument constant at Raman-shifted wavelength λ_X^{Ram}, *A(R)* *[m²]* the telescope active surface area, *R [m]* the range between the telescope and the atmospheric target, ΔR *[m]* the range resolution, $n_X(R)$ *[molec.cm^{-3}]* the molecular density of species X at distance *R*, ${}^{\pi}\beta_X^{Raman}\left(\lambda_L,\lambda_X^{Ram},R\right)$ *[cm^2.sr^{-1}]* the Raman differential backscattering cross-section for species X for the emitted wavelength λ_L and Raman-shifted wavelength λ_X^{Ram} and $\alpha^{atmos}(\lambda_L,r)$ {resp. $\alpha^{atmos}(\lambda_X^{Ram},r)$} *[cm^{-1}]*, is the atmospheric attenuation (or extinction) coefficient at the wavelength λ_L {resp. λ_X^{Ram}} defined as the sum of the aerosol, molecular and absorption components of the probed atmosphere:

$$\alpha^{atmos}(\lambda_i,r) = \alpha^{aer}(\lambda_i,r) + \alpha_{Rayl}^{molec}(\lambda_i,r) + \sum_Y n_Y(r)\sigma_{abs}^{Y}(\lambda_i,r) \ \text{ with } \lambda_i = \lambda_L\,,\lambda_X^{Ram} \qquad \text{EQ 2}$$

and where $\alpha^{aer}(\lambda_L,r)$ {resp. $\alpha^{aer}(\lambda_X^{Ram},r)$} *[cm^{-1}]* is the aerosol attenuation coefficient at the wavelength λ_L {resp. λ_X^{Ram}}, $\alpha_{Rayl}^{molec}(\lambda_L,r)$ {resp. $\alpha_{Rayl}^{molec}(\lambda_X^{Ram},r)$}*[cm^{-1}]* the molecular attenuation coefficient at the wavelength λ_L {resp. λ_X^{Ram}}, $\sigma_{abs}^{Y}(\lambda_L,r)$ {resp $\sigma_{abs}^{Y}(\lambda_X^{Ram},r)$}*[cm^2.molec^{-1}]* the molecular absorption cross section for the molecule Y at the wavelength λ_L {resp. λ_X^{Ram}}.

For the ozone concentration retrieve and for the ozone correction term in the water vapor mixing ratio retrieve, the ozone concentration term $n_{O_3}(r)$ will be needed and we then put it in evidence:

$$\alpha^{atmos}(\lambda_i,r)=\widetilde{\alpha^{atmos}}(\lambda_i,r)+n_{O_3}(r)\sigma_{abs}^{O_3}(\lambda_i,r) \quad with \quad \lambda_i=\lambda_L\,,\lambda_X^{Ram} \qquad \text{EQ 3}$$

The term $\widetilde{\alpha^{atmos}}(\lambda_i,r)$ takes into account the Rayleigh (molecules), Mie (aerosols) and absorption contributions, without the O_3 absorption one.

The exponential term $\Phi(\lambda_L,\lambda_X^{Ram},R)$ in Eq. (1) is then given by:

$$\Phi(\lambda_L,\lambda_X^{Ram},R)=\exp\left\{-\int_0^R\left[\begin{matrix}\left(\widetilde{\alpha^{atmos}}(\lambda_L,r)+\widetilde{\alpha^{atmos}}(\lambda_X^{Ram},r)\right)\\ +n_{O_3}(r)\left(\sigma_{abs}^{O_3}(\lambda_L,r)+\sigma_{abs}^{O_3}(\lambda_X^{Ram},r)\right)\end{matrix}\right]dr\right\} \qquad \text{EQ 4}$$

The ozone absorption cross section, as well as the Raman backscattering coefficients for O_2, N_2 and H_2O, are essentially independent of the temperature in the measurements' temperature range (40 K) [*Lazzarotto*, 2000]. As the altitude, and so the measurement range is linked to the temperature [*NOAA et al.*, 1976], the dependence to altitude for ozone absorption cross section and the Raman backscattering coefficients will be cancelled.

The ozone concentration $n_{O_3}(R)$ can then be calculated, with the Eq. (1), from the derivative of the natural logarithm of the ratio between N_2 and O_2 Raman backscattered signals:

$$n_{O_3}(R)=\frac{\dfrac{\partial}{\partial R}\left(\ln\dfrac{P_{N_2}(R)}{P_{O_2}(R)}\right)}{\sigma_{abs}^{O_3}(\lambda_{O_2}^{Ram})-\sigma_{abs}^{O_3}(\lambda_{N_2}^{Ram})}-\underbrace{\frac{\left(\widetilde{\alpha^{atmos}}(\lambda_{O_2}^{Ram},R)-\widetilde{\alpha^{atmos}}(\lambda_{N_2}^{Ram},R)\right)}{\sigma_{abs}^{O_3}(\lambda_{O_2}^{Ram})-\sigma_{abs}^{O_3}(\lambda_{N_2}^{Ram})}}_{\delta_{corr}(O_3)} \qquad \text{EQ 5}$$

The first term of this equation gives the "zero-order" ozone concentration retrieve. It depends on the first derivative of the ratio between the O_2 and N_2 Raman signals.

The last term, denoted as $\delta_{corr}(O_3)$, is a corrective term. It groups the Rayleigh and Mie scattering as well as the absorption (without O_3) one, for the O_2 and N_2 Raman shifted wavelengths. Its influence on the ozone concentration retrieve will be discussed in section 2.2.4.

The water vapor (mass) mixing ratio in [g H_2O / kg dry air] defined as:

$$\xi_{H_2O}(R) = \left.\frac{\text{Mass of H}_2\text{O}}{\text{Mass of dry air}}\right|_{\text{given volume}}(R) = \frac{n_{H_2O}}{n_{N_2}}(R)\times\frac{M_{H_2O}}{M_{dry\ air}}\times\chi_{N_2} \qquad \text{EQ 6}$$

where M$_X$ *[g.mol^{-1}]* is the molecular weight of the species X and χ_{N_2} *[%]* is the content of nitrogen in dry air, which is constant in the lower troposphere.

The water vapor mixing ratio can be calculated from the H_2O and N_2 Raman backscattered signals taking into account Eq. (6) that leads to:

$$\xi_{H_2O}(R) = \frac{M_{H_2O}}{M_{dry\ air}}\chi_{N_2}\frac{P_{H_2O}(R)}{P_{N_2}(R)}\frac{K_{N_2}}{K_{H_2O}}\frac{{}^{\pi}\beta^{Ram}_{N_2}}{{}^{\pi}\beta^{Raman}_{H_2O}}$$

$$\times\underbrace{\exp\left\{\int_0^R\left[\left(\alpha^{atmos}(\lambda^{Ram}_{H_2O},r)-\alpha^{atmos}(\lambda^{Ram}_{N_2},r)\right)\right]dr\right\}}_{\delta_{corr}(H_2O)} \qquad \text{EQ 7}$$

The zero-order term gives the H_2O mixing ratio retrieve, supposing that no Rayleigh, Mie or absorption contribution is significant. In general this unique term is not sufficient, specially in our UV wavelength region where the ozone absorption is important.

The exponential term denoted as $\delta_{corr}(H_2O)$ in Eq. (7) takes into account the differences in the atmospheric extinction at the H_2O and N_2 Raman shifted wavelengths. The main contribution comes from the ozone absorption influence on the H_2O and N_2 Raman signals and can affect significantly the final results [*Renaut et al.*, 1980]. This factor can be calculated with another additional Raman signal. The other contribution takes into account all the atmospheric influences, without the O_3 absorption one, on the H_2O and N_2 Raman signals, by scattering (Rayleigh or Mie) and absorption.

In contrast with the ozone concentration retrieve, the water vapor mixing ratio retrieve depends linearly upon the ratio of the Raman H_2O signal to the Raman N_2 signal. It makes this retrieve less sensitive to noise than the ozone one. But this method is not self calibrated and the exact knowledge of K_X or an independent parallel measurement for instrument calibration is needed.

2.2. Interferences with Raman lidar measurements

The contributions to the atmospheric extinction induced by the molecular absorption as well as the Rayleigh and Mie scattering will be discussed in order to calculate the errors in the ozone and water vapor retrieve. Systematic errors like after pulse effect or optical cross talk were discussed in our previous paper [*Lazzarotto et al.*, 2000].

2.2.1. Contribution terms

Rayleigh scattering

The (Rayleigh) molecular scattering coefficient $\alpha^{molec}_{Rayl}(\lambda_i,R)$ *[cm^{-1}]* is defined by:

$$\alpha^{molec}_{Rayl}(\lambda_i,R) = n_{atmos}(R)\times{}^{tot}\sigma^{molec}_{Rayl}(\lambda_i,R) \qquad \text{EQ 8}$$

Where n$_{atmos}$ (R) *[molec.cm^{-3}]* is the atmospheric volumic concentration at a distance R, and ${}^{tot}\sigma_{Rayl}^{molec}(\lambda_i, R)$ *[cm^2.molec^{-1}]* is the total Rayleigh molecular scattering cross section at the wavelength λ_i [cm] and the range R defined as follows [*Penndorf*, 1957]:

$$ {}^{tot}\sigma_{Rayl}^{molec}(\lambda_i, R) = \frac{24\pi^3 (n_s^2 - 1)^2}{\lambda_i^4 n_{atmos}^2 (R)(n_s^2 + 2)^2} \left(\frac{6 + 3\rho}{6 - 7\rho}\right) \qquad \text{EQ 9} $$

where n$_s$ *[dimensionless]* is the refractive index of the air, retrieved following the Edlén's formula [*Edlén*, 1966] and $F(air) = (\frac{6+3\rho}{6-7\rho})$ *[dimensionless]* is the depolarization term (or King factor) related to ρ *[dimensionless]* the depolarization ratio. For the depolarization term, the development made by Bates [*Bates*, 1984] is chosen.

Aerosol scattering

This term is much more complicated to retrieve than the Rayleigh one and satisfactory results can be found by complex computer simulations. As the aerosol loading can vary a lot, an order of magnitude for the correspondent correction term is given. We take the formula from Kruse et al [Kruse, 1963 #195] who derived the following empirical formula in case of visual clear air for the aerosol attenuation coefficient $\alpha^{aer}(\lambda_i, R)$ *[cm^{-1}]*:

$$ \alpha^{aer}(\lambda_i, R) \simeq \alpha_{scatt}^{aer}(\lambda_i, R) = \frac{3.91}{\mathrm{V_M}} \left(\frac{550}{\lambda_i [nm]} \right)^q \qquad \text{EQ 10} $$

with $q = 0.585 (V_M [km])^{\frac{1}{3}}$ for $V_M \le 6\, km$ where V$_M$ is the atmospheric visibility.

In average seeing conditions it is common to take q=1.3. A more accurate discussion on the different cases and values of q has been discussed by Woodman [Woodman, 1974 #199].

Molecular absorption

Each molecule has its own absorption spectrum which is the result of all the different transitions, electronic, vibrational, rotational..., and is represented by a series of absorption lines. Generally speaking, each line is characterized by three parameters: position, width and intensity. The advantage of the used Raman method is on the UV ozone spectrum use. As this spectrum is large, the line broadening does not have to be considered (Lorentz or Doppler correction). This is valid for the corrections in the ozone and water vapor retrieve due to the absorption of the other gases.

The molecular absorption coefficient for the group of molecules {Y} $\alpha_{abs}^{molec}(\lambda_i, r)$ *[cm^{-1}]* is defined as follows:

$$ \alpha_{abs}^{molec}(\lambda_i, r) = \sum_{\{Y\}} n_Y(r) \sigma_{abs}^{Y}(\lambda_i, r) \qquad \text{EQ 11} $$

Where $\sigma_{abs}^{Y}(\lambda_i, r)$ *[cm^2.molec^{-1}]* is the molecular absorption cross section of the molecule Y, and n$_Y$(r) *[molec.cm^{-3}]* is the volumic concentration of the molecule Y.

The calculation of this term then requires, for each molecule Y, the knowledge of:

- the volumic concentration, which can be deduced from its mixing ratio and the air volumic concentration profile (given by a sounding or a mathematical model like the NOAA one).
- the molecular absorption cross section for the considered wavelengths. It is given by experiments but not all the atmospheric components were yet studied in the UV. Some molecules are already well known, like O_3 but others like O_2 still cause uncertainties in the UV.

An extensive search was made to retrieve this contribution term in the UV. Both reactive and non or slowly reactive species were shown, even if their contribution is small. The absolute absorption cross sections for SO_2 [*Vandaele et al.*, 1994], O_3 [*Daumont et al.*, 1992], NO_2 [*Schneider et al.*, 1986], N_2O [*Nicolet and Peetermans*, 1972], HNO_3 [*Burkholder et al.*, 1993], CO_2 [*Shemansky*, 1972], HNO_2 [*Cox and Derwent*, 1976], CH_2O [*Meller*, 1992], SO_2 [*Vandaele et al.*, 1994], O_3 [*Daumont et al.*, 1992], NO_2 [*Schneider et al.*, 1986], N_2O [*Nicolet and Peetermans*, 1972], HNO_3 [*Burkholder et al.*, 1993], CO_2 [*Shemansky*, 1972], HNO_2 [*Cox and Derwent*, 1976], CH_2O [*Meller*, 1992], C_6H_6 [*Trost*, 1994], C_7H_8 [*Trost*, 1994], O_2 [*Mérienne et al.*, 2000], [*Bernath et al.*, 1998] were taken at 298K.

2.2.2.Results

In this section the absorption extinction term is shown instead of the absolute absorption cross section coefficient for a simple reason: it takes into account the concentrations of each species in the atmosphere and comparison is possible with the Rayleigh and Mie case.

Two typical cases, remote and urban conditions, will be discussed. The corresponding values for these two cases are taken from the literature [*Finlayson-Pitts and Pitts*, 1986], [*Yung and DeMore*, 1999], [*Warneck*, 1988], [*Seinfeld and Pandis*, 1998] and summarized in the following Table 1.

Molecule {Y}	Concentration n_Y [ppb]	
	Remote	Urban
SO_2	1	200
O_3	50	20
NO_2	1	200
N_2O	320	320
HNO_3	0.1	10
CO_2	360000	360000
HNO_2	0.03	2
CH_2O	2	20
C_6H_6	0.5	20
C_7H_8	0.5	20
O_2	$2.09476x10^8$	$2.09476x10^8$
Visibility	6 km	2 km

Table 1 : Concentrations for two typical cases

The absorption extinction coefficient for those molecules as well as the Rayleigh and Mie scattering coefficients can be graphically represented to show the wavelength dependence. Figure 1 is made under a temperature of 20 °C and a pressure of 970 mbar, corresponding to the ground level atmospheric conditions of the lidar during a day of march.

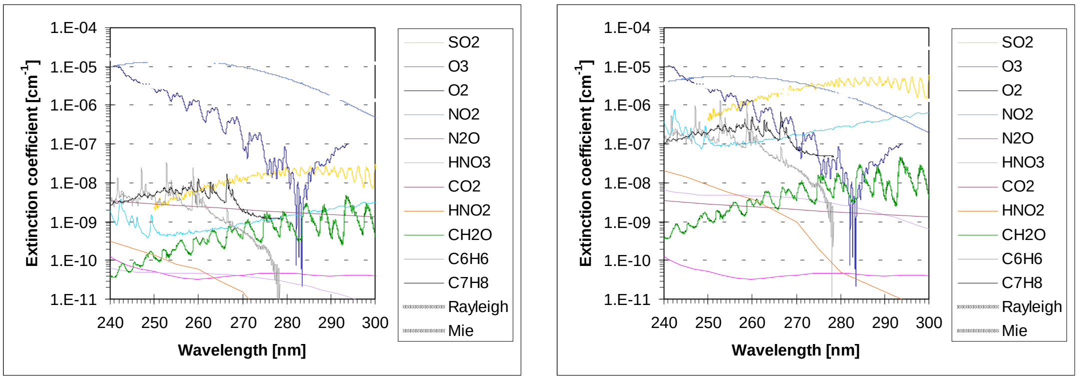

Figure 1(a) **Figure 1(b)**

Figure 1. Extinction coefficients. Coefficients are calculated for molecular absorption, molecular and aerosol scattering under the two typical cases of the table 1, at the zero altitude. Figure 1(a) stands for the "remote" case and Figure 1(b) for the "urban" one. Both case are computed from 240 to 300 nm.

The "remote" case shows a main extinction contribution due to the Mie and Rayleigh scattering and to the O_3 and O_2 (which is important for the KrF case) absorption. All the other molecular extinctions are at least 10^3 lower. The "urban"case keeps a similar behavior to the "remote" one. The Rayleigh scattering extinction as well as the O_2 absorption extinction stays the same, due to similar conditions and a constant O_2 concentration. A small decrease in the O_3 absorption extinction arises but the major change comes from the SO_2 absorption extinction contribution. This latter is important for both KrF and Nd:YAG case and an important corrective effect can be expected. In this case, apart the NO_2, C_6H_6 and C_7H_8 absorption contributions which are lower by a factor of 10^2, all the other molecular contributions are at least 10^3 times lower.

This plot is made for the 0-altitude above ground level (agl) and, to retrieve a similar one at a different altitude, vertical concentration profiles have to be known. Concentrations of stable molecules like O_2 are well defined, but for molecules like SO_2, a vertical concentration profile is needed to describe the changes.

As SO_2 is one of the biggest contributions a special care was taken in the "urban" case. This pollutant is emitted from the ground and its vertical mixing ratio distribution will then decrease with the altitude. Typical SO_2 altitude distributions were taken [*Warneck*, 1988], [*Kuebler*, 2000] and , in an urban condition, we approximate this decreasing distribution by a line with a slope of $\frac{-n^0_{SO_2}}{2500}$, where $n^0_{SO_2}$ is the (initial) ground level SO_2 concentration, for altitudes under 2500 m and by a vertical (zero) line for altitudes above 2500 m where the SO_2 concentrations are negligible.

This distribution correction is very important and will be used in the following sections for the different correction calculations.

2.2.3.Optimisation of the KrF laser wavelength

We propose to find the optimal wavelength of the KrF laser so to minimize the absorption influence of SO_2.on the O_3 concentration and H_2O water vapor mixing ratio retrieve.

Influence on the ozone concentration retrieve

A KrF laser can be tuned from 248.40 nm to 249.10 nm so, assuming Raman displacements of 1555 cm^{-1} for O_2 and 2331 cm^{-1} for N_2 [*Schrötter and Klöckner*, 1979], [*Bischel and Black*, 1983], the corresponding Raman wavelengths go from 258.38 nm to 259.14 nm in case of O_2 and 263.67 nm to 264.46 nm in case of N_2.

The SO_2 absorption cross section wavelength behavior in the O_2 and N_2 Raman shifted wavelength region is shown in Figure 2. It shows that, depending on the KrF pump wavelength, it is possible to minimize the SO_2 contribution.

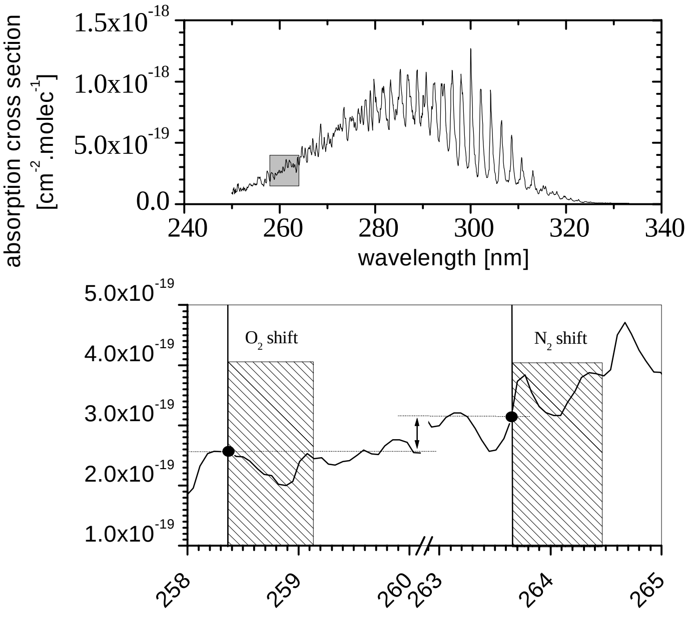

Figure 2. Absorption cross section of SO_2 in the UV. The upper view shows the spectrum from 250 to 330 nm, and the lower view shows an enlargement of the two regions of interest: 258 – 260 nm and 263 – 265 nm.

Going back to the Eq. (5), the aim is to minimize the term $\delta_{corr}(O_3)$ for the SO_2 absorption contribution, thus yielding in a minimization of $\delta_{corr}^{SO_2}(O_3) = \dfrac{\sigma_{abs}^{SO_2}(\lambda_{O_2}^{Ram}, R) - \sigma_{abs}^{SO_2}(\lambda_{N_2}^{Ram}, R)}{\sigma_{abs}^{O_3}(\lambda_{O_2}^{Ram}) - \sigma_{abs}^{O_3}(\lambda_{N_2}^{Ram})}$. By plotting this ratio versus the KrF pump wavelength, it gives the following Figure 3.

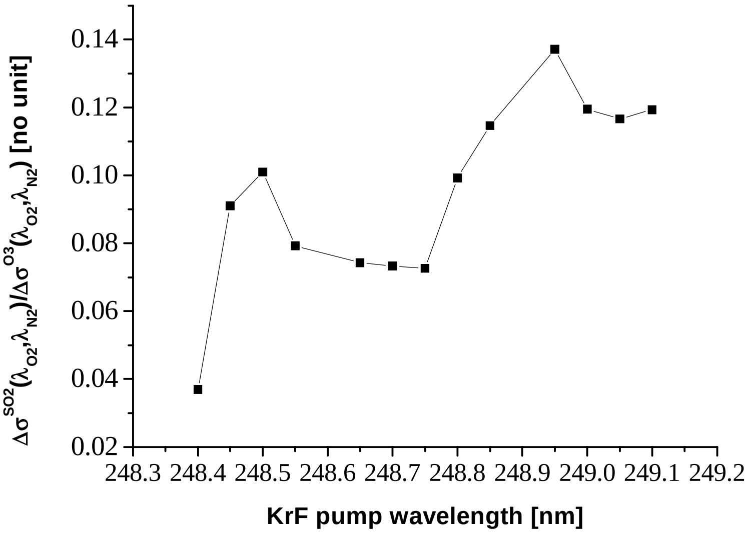

Figure 3. Optimization of the KrF pump wavelength to minimize the SO_2 absorption influence in the O_3 retrieve.

An optimum wavelength to minimize the SO_2 absorption influence on the O_3 concentration retrieve is given for a 248.4 nm KrF pump wavelength. Taking the worst case, around 248.95 nm, will increase this SO_2 absorption influence by almost a factor of 3.7. To illustrate this fact we take the two cases for the SO_2 concentration given in Table 1, and for the first retrieved point at 303.75 m.

The "remote" case gives a SO_2 concentration of 1 ppb. This implies a correction value of $\delta_{corr}^{SO_2}(O_3) = -0.0528$ ppb to the ozone concentration retrieve with the KrF pump wavelength at 248.40 nm. Taking the worst wavelength tuned case, i.e. for 248.95 nm, the correction value to the ozone concentration retrieve will be multiplied by 3.7 and becomes –0.19 ppb.

In the "urban" case the SO_2 concentration is 200 ppb. The correction value on the O_3 concentration retrieve goes then from –10.6 ppb for the 248.40 nm KrF pump wavelength case to –39.2 ppb for the 248.95 nm one.

The wavelength choice can then be of importance for the O_3 correction term, in case of a high SO_2 concentration.

Influence on the water vapor mixing ratio retrieve

Similarly to the O_3 case, we propose to look at the influence of the SO_2 absorption on the H_2O mixing ratio retrieve, depending on the KrF pump wavelength. The correction term relative to SO_2 in Eq. (7) is given by the integral following term:

$$\delta_{corr}^{SO_2}(H_2O) = \exp\left\{\left(\sigma_{abs}^{SO_2}(\lambda_{H_2O}^{Ram}) - \sigma_{abs}^{SO_2}(\lambda_{N_2}^{Ram})\right)\int_0^R n_{SO_2}(r)dr\right\} \qquad \text{EQ 12}$$

Due to the positivity of the integral term, the correction term $\delta_{corr}^{SO_2}(H_2O)$ will have the same behaviour as the term $\Delta\sigma^{SO_2}(\lambda_{H_2O}^{Ram}, \lambda_{N_2}^{Ram}) = \sigma_{abs}^{SO_2}(\lambda_{H_2O}^{Ram}) - \sigma_{abs}^{SO_2}(\lambda_{N_2}^{Ram})$.

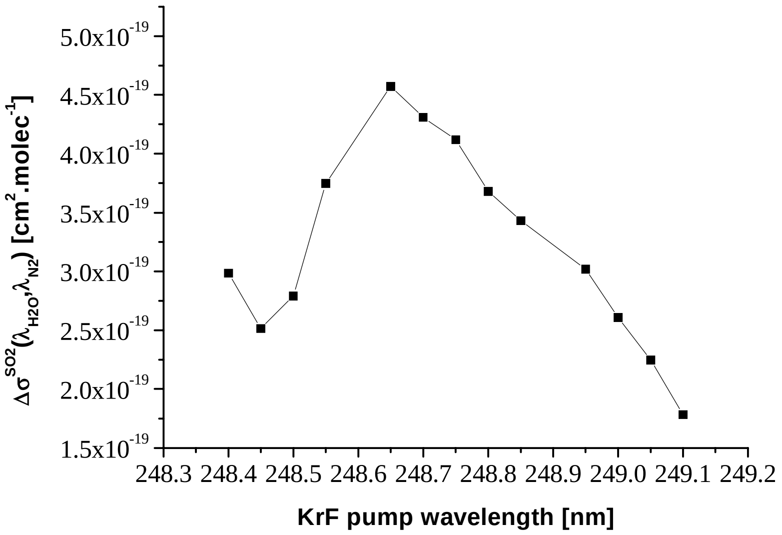

Figure 4. Optimization of the KrF pump wavelength to minimize the SO_2 absorption influence in the H_2O retrieve.

The minimum is reached for 249.1 nm KrF pump wavelength with $\Delta\sigma^{SO_2}(\lambda_{H_2O}^{Ram},\lambda_{N_2}^{Ram}) = 1.78\cdot10^{-19}\ cm^2.molec^{-1}$, and the maximum for 248.65 nm, with $\Delta\sigma^{SO_2}(\lambda_{H_2O}^{Ram},\lambda_{N_2}^{Ram}) = 4.57\cdot10^{-19}\ cm^2.molec^{-1}$. To give an order of magnitude, calculations were made for an hypothetical first retrieved point at 303.75 m.

For the “remote case” $\delta_{corr}^{SO_2}(H_2O) = 1.0001$ for the KrF pump wavelength at 248.40 nm, and $\delta_{corr}^{SO_2}(H_2O) = (1.0001)^{3.4} = 1.0002$ in the 248.95 nm worse case. The H_2O mixing ratio will be increased by a factor of 1.0002, which is negligible.

For the “urban case” $\delta_{corr}^{SO_2}(H_2O) = 1.0230$ for the KrF pump wavelength at 248.40 nm, and $\delta_{corr}^{SO_2}(H_2O) = 1.0804$ in the 248.95 nm case. The H_2O mixing ratio will be increased by a factor of 1.056. So, with a retrieved H_2O mixing ratio of 5 g H_2O / kg dry air (for 200 ppb SO_2) for the best KrF wavelength, it gives 5.28 g H_2O / kg dry air for the worst one. The relative error is approximately 5 % if this correction is not taken into account.

Conclusion

The method exposed above for the SO_2 contribution can be applied to any other molecule, and can be helpful for minimizing the correction in a deeply polluted atmosphere by a given component. If two or more components are in great excess, care has to be taken with this method, and it should be ascertained if a better result with one component will not make the contrary on the others.

The case of gases like O_2 or CO_2 is interesting. The method can be applied but, in fact, we have to wonder why. The mixing ratio of O_2 is constant with the altitude, unlike for most of the pollutants. It implies a well known corrective term for the O_2 case and no need is required to try to minimize its contribution.

The following Figure 5 shows the absorption feature of O_3 in the Hartley band, from 200 to 300 nm, at 298 K and with a resolution of 0.01 nm [Daumont, 1992 #290]. In this figure are shown the pump wavelengths for the KrF (solid line) and Nd:YAG (short dot line) laser, and their related Raman shifts from the atmospheric O_2, N_2 and H_2O. This spectrum is characterized by a very broad structure (about 50 nm FWHM) with no strongly absorbing narrow spectral lines. The cross-sections related to the KrF case are always higher than the Nd:YAG one, giving a higher O_3 absorption of the pump and Raman wavelength in the KrF configuration.

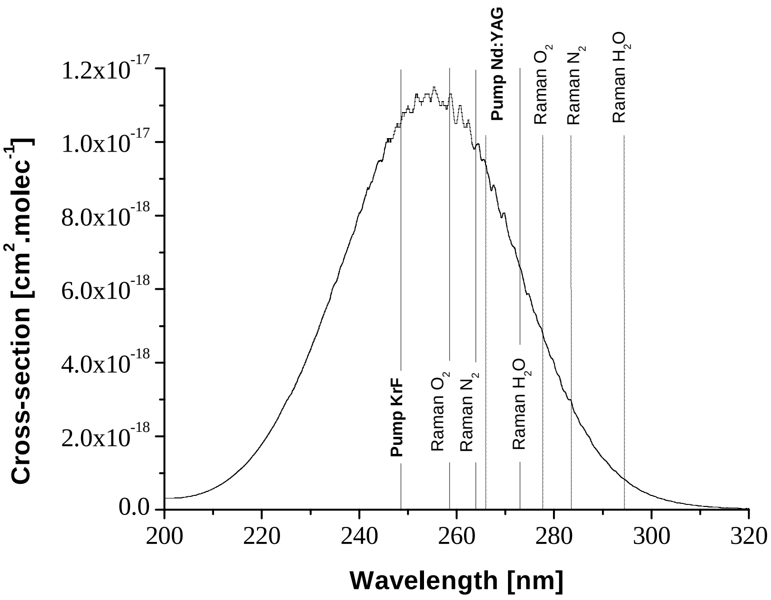

Figure 5 . Ozone absorption spectrum in the Hartley band at 298K

2.2.4.Practical correction scheme

Ozone

We have seen that the corrective term in case of the ozone retrieve presented in the Eq. (5) is, with Eq. (2) and Eq. (3):

$$\delta_{corr}(O_3)=\frac{\begin{pmatrix} \alpha_{Rayl}^{molec}(\lambda_{O_2}^{Ram},R)-\alpha_{Rayl}^{molec}(\lambda_{N_2}^{Ram},R) \\ +\alpha^{aer}(\lambda_{O_2}^{Ram},R)-\alpha^{aer}(\lambda_{N_2}^{Ram},R) \\ +\sum\limits_{\{Y'\}=\{Y-O_3\}} n_{Y'}(R)\left(\sigma_{abs}^{Y'}(\lambda_{O_2}^{Ram},R)-\sigma_{abs}^{Y'}(\lambda_{N_2}^{Ram},R)\right) \end{pmatrix}}{\sigma_{abs}^{O_3}(\lambda_{O_2}^{Ram})-\sigma_{abs}^{O_3}(\lambda_{N_2}^{Ram})} \qquad \text{EQ 13}$$

Under the conditions of the Table 1 and for a KrF laser tuned at 248.4 nm and a Nd:YAG one, this ozone corrective term was represented versus the altitude in the Figures 6 (a), (b), (c), (d). In these graphs the SO_2 profile described in section 2.2.2 is used.

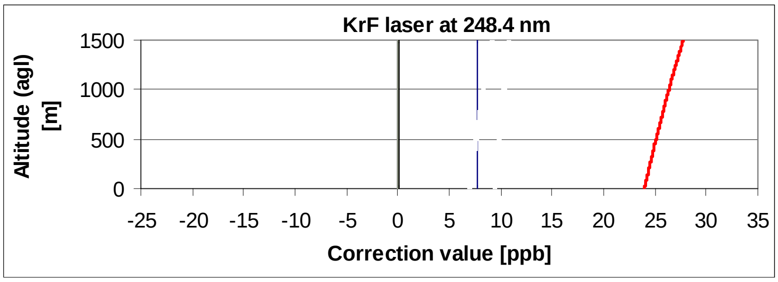

Figure 6(a)

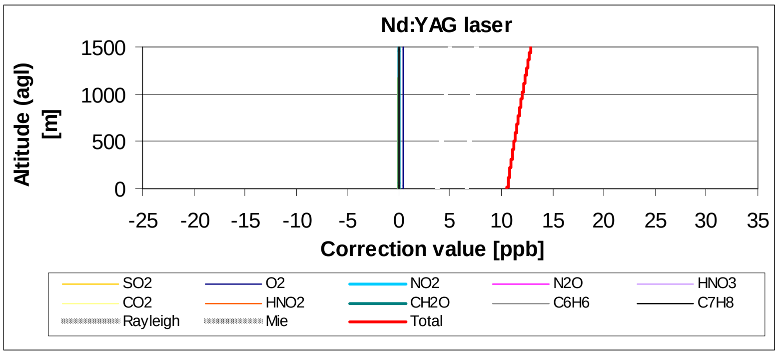

Figure 6(b)

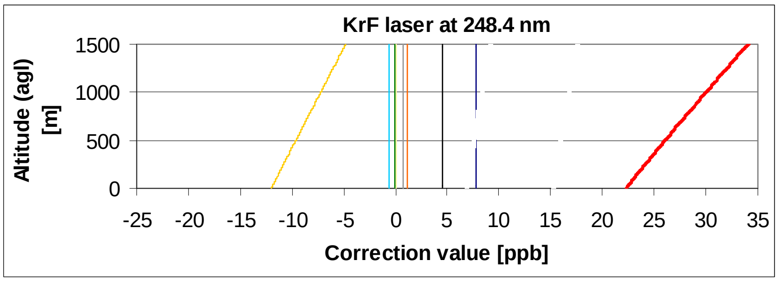

Figure 6(c)

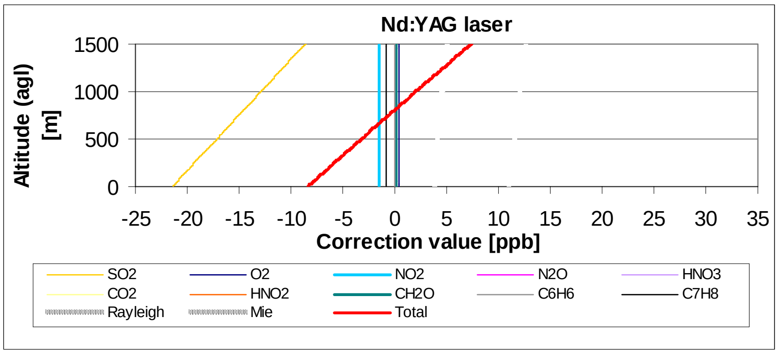

Figure 6(d)

Figure 6. Corrections to the O_3 concentration retrieve. Figure 6(a), for the KrF laser and Figure 6(b), for the Nd:YAG one, illustrates the “remote” case of the Table 1. The “urban” case is shown in Figure 6(c) and Figure 6(d) for the KrF and Nd:YAG lasers.

Looking to the total corrective term, first ascertainment is the need for less corrections in the Nd:YAG configuration than in the KrF one. The term $\Delta\sigma = \sigma_{abs}^{O_3}(\lambda_{O_2}^{Ram}) - \sigma_{abs}^{O_3}(\lambda_{N_2}^{Ram})$ in the denominator of the ozone corrective term $\delta_{corr}(O_3)$ given by the Eq. (13) can explain this behavior. It takes into account the difference of the ozone absorption cross section at the O_2 Raman shifted wavelength and at the N_2 one. In the KrF case we have $\Delta\sigma(\text{KrF @248.4 nm}) = 1.39 \cdot 10^{-18}\ \text{cm}^2.\text{molec}^{-1}$ and in the Nd:YAG one this term becomes $\Delta\sigma(\text{Nd:AG}) = 1.97 \cdot 10^{-18}\ \text{cm}^2.\text{molec}^{-1}$. So, going from the Nd:YAG configuration to the KrF one, the corrective factor has to be multiplied by a factor of 1.4 as a first approximation. But other contributions in the numerator can change this behavior, due to the wavelength dependence of its different components. As soon as the concentrations become higher, like in the Figures 6(c) and 6(d), care as to be taken. We can see that a bigger individual correction, like the SO_2 one in Figure 6(d) for the Nd:YAG case, can help to minimize the total correction.

Water vapor

The three Raman channels O_2 , N_2 and H_2O allow to treat one internal term (the one related to the ozone) in the exponent part of Eq. (7) with a better accuracy [*Renaut et al.,* 1980]. With Eq. (3) the water vapor correction term $\delta_{corr}(H_2O)$ becomes:

$$\delta_{corr}(H_2O) = \exp\left\{ \left(\sigma_{abs}^{O_3}(\lambda_{H_2O}^{Ram}) - \sigma_{abs}^{O_3}(\lambda_{N_2}^{Ram}) \right) \int_0^R \left[n_{O_3}(r) \right] dr \right\} \quad \leftarrow \text{O}_3\text{interference}$$

$$\times \exp\left\{ \int_0^R \left[\widetilde{\alpha^{atmos}}(\lambda_{H_2O}^{Ram}, R) - \widetilde{\alpha^{atmos}}(\lambda_{N_2}^{Ram}, R) \right] dr \right\} \quad \leftarrow \text{others interferences} \qquad \text{EQ 14}$$

The integrated ozone term can be calculated from the ratio of the O_2 and N_2 Raman backscattered signals, with a similar procedure than for the O_3 concentration retrieve:

$$\xi_{H_2O}(R) = K_{cal} \frac{P_{H_2O}(R)}{P_{N_2}(R)} \left[\frac{P_{O_2}(R)}{P_{N_2}(R)} \right]^{\widetilde{\Delta\sigma}_{abs}^{O_3}}$$

$$\times \exp\left\{ \int_0^R \left[\left(\widetilde{\alpha^{atmos}}(\lambda_{H_2O}^{Ram}, r) - \widetilde{\alpha^{atmos}}(\lambda_{N_2}^{Ram}, r) \right) - \widetilde{\Delta\sigma}_{abs}^{O_3} \left(\widetilde{\alpha^{atmos}}(\lambda_{N_2}^{Ram}, r) - \widetilde{\alpha^{atmos}}(\lambda_{O_2}^{Ram}, r) \right) \right] dr \right\} \qquad \text{EQ 15}$$

With $\widetilde{\Delta\sigma}_{abs}^{O_3} = \dfrac{\sigma_{abs}^{O_3}(\lambda_{H_2O}^{Ram}) - \sigma_{abs}^{O_3}(\lambda_{N_2}^{Ram})}{\sigma_{abs}^{O_3}(\lambda_{N_2}^{Ram}) - \sigma_{abs}^{O_3}(\lambda_{O_2}^{Ram})}$

and where the factor K_{cal} is a constant value that can be established by calibrating the lidar. The same conditions as for the previous ozone corrective term discussion are taken here. The water vapor corrective term was represented versus the altitude in the following Figures 7 (a), (b), (c), (d).

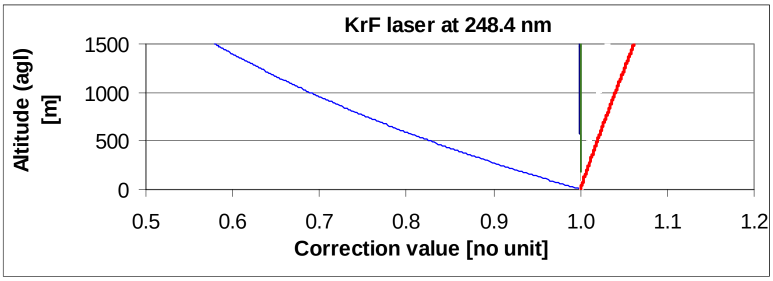

Figure 7(a)

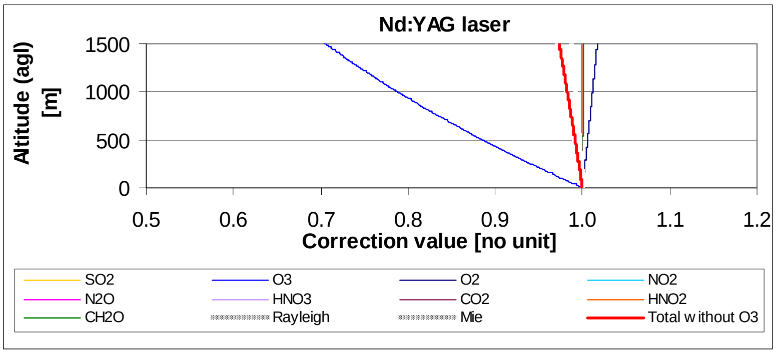

Figure 7(b)

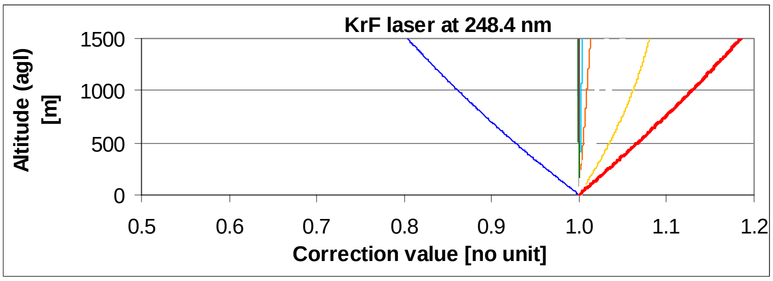

Figure 7(c)

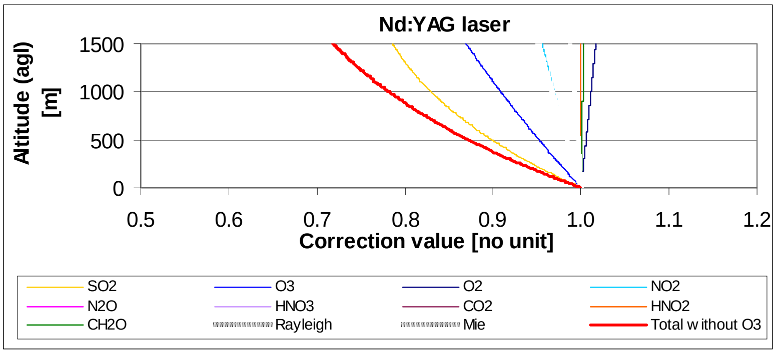

Figure 7(d)

Figure 7. Corrections to the H_2O mixing ratio retrieve (multiplicative factor). Figure 7(a), for the KrF laser and Figure 7(b), for the Nd:YAG one, illustrate the "remote" case of the Table 1. The "urban" case is shown in Figure 7(c) and Figure 7(d) for the KrF and Nd:YAG lasers.

In these figures the total correction term doesn’t take into account the O_3 correction one. This is due to the fact that with the three Raman backscattered signals, we can perform an auto-correction for the ozone. As the ozone correction term is the most important contribution for all the situations exposed in the Figures 7, the auto-correction by mean of the lidar will be the best choice to calculate this contribution.
Speaking now about the total correction term (without O_3), for the “remote” case, a smaller correction is required in the Nd:YAG configuration than in the KrF one. There is essentially no need for any correction, apart from the O_3 auto-correction (by the lidar), in the Nd:YAG configuration and the KrF one requires a small correction. For the “urban” case, the SO_2 contribution is the main one, under the concentration given in Table1, and the total correction to be applied is bigger for the Nd:YAG case than for the KrF one.

Both of these corrections, for O_3 and H_2O concentrations can be exported in an Excel file to the LabVIEW data treatment program. It provides the scattering and absorption corrections to the retrieved quantities.

3.Experimental description

3.1. The Raman lidar

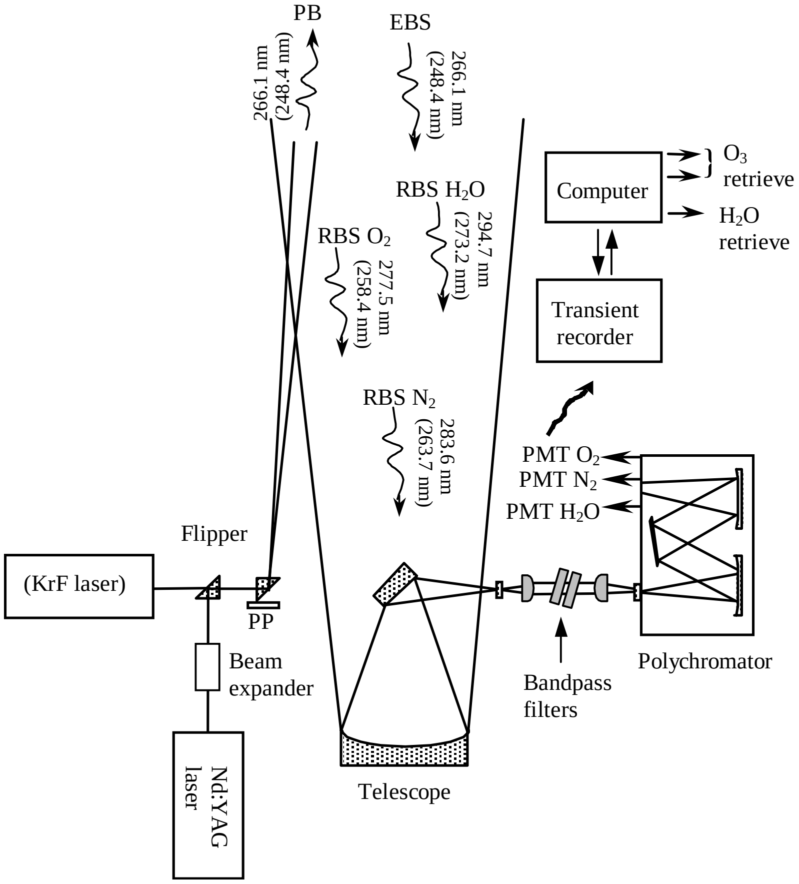

Figure 8. Experimental layout of the Raman lidar

The Raman lidar for the O_3 concentration and H_2O mixing ratio measurements was operated with two different laser sources, a 4th harmonic Nd:YAG and a KrF one. The experimental layout is shown in Figure 8. The KrF was used with a positive branch unstable resonator for reducing the beam divergence. The Nd:YAG beam was expanded three times before emitting to reduce the initial 0.50 mrad divergence to 0.17 mrad. The laser beam selection is made with a right angle prism mounted on a flipper. The selected beam is then emitted into the atmosphere via a right angle prism mounted on a piezo electric controlled stage. In the KrF configuration, the laser beam goes straight through this final prism, but for the Nd:YAG configuration, another right angle prism mounted on a piezo electric controlled stage was used before the flipper. This ensures an independent alignment of both emitting systems and the ability to move from one to the other more rapidly and without major realignments.

After atmospheric interactions, the backscattered signals are collected by a Newtonian-type telescope based on an off-axis paraboloid primary mirror. The optical reception part, ensures the spectral separation of the elastic backscattered signal and also the O_2, N_2 and H_2O Raman backscattered ones.

First separation is made with a 45° oriented fused silica window which allows to inject a fraction of the elastic backscattered signal into a PMT. This elastic signal permits to make a comparison with the Raman signals in case of clouds (test for elastic leakage in the Raman channels) or gives the possibility to retrieve the aerosol extinction coefficient.

To separate the O_2, N_2, H_2O Raman signals, a more complicate system has to be used. The main problems are the rejection of the strong elastic backscattered signal and the very weak Raman signals. To fit the numerical apertures (F numbers) of the receiving telescope and of the polychromator, a system of two lenses (positive plano convex) is used. The bandpass filters are placed into the parallel beam between these two lenses and, to ensure a good rejection of the elastic part, two identical bandpass filters are used together. A circular diaphragm in front of the entrance lens and near to the focal plane of the telescope defines the field of view of the receiver. A second diaphragm placed at the entrance of the polychromator slit reduces the level of the scattered light leaking into the polychromator. After this first filtering, the received signal passes through a solar blind filter for an additional suppression of the daylight background and then enters the polychromator. This latter performs a spectral separation, allowing to detect separately the three Raman backscattered signals. It also acts as a filter to additionally reject the residual elastic signal and daylight. The three Raman signals are detected simultaneously by three Hamamatsu photodetector modules and acquired by three transient recorders.

Each PMT can be displaced linearly of $\pm$ 3 mm from a central position, calculated for the Nd:YAG configuration. This allows: - a fine alignment of the Raman signal intensities,- the possibility to pass from the Nd:YAG configuration to the KrF one (due to the different pump wavelengths, the resulting Raman signals are not at the same place). Each PMT uses a special optical configuration in front of it, to overcome its spatial uniformity problem [*Simeonov et al.*, 1999].

The transient recorders are controlled via a NiDAQ card installed in a PC and working under a LabVIEW program. The trig used to monitor the different transient channels is given by a photodiode which takes the scattering light from the last prism before it is emitted in the atmosphere. This initial pulse then goes through two pulse generators (two channels each) which ensure suitable TTL levels for triggering the transient recorders. The advantage of the pulse generator use stands in the possibility to accurately tune the position and width of the transient channel trigs, and then to have identical ones. The acquisition program allows to visualize in real time the signals, criteria parameters and raw retrieves for the ozone concentration and the water vapor mixing ratio.

3.2.The tethered Balloon System

As an independent validation data set we measured O_3 and H_2O concentration profiles with a tethered balloon system from Atmospheric Instrumentation Research (A.I.R., Inc., Boulder, CO, U.S.A.), model TMT-5A, which carried a meteosonde, an ozonesonde, and an Infrared Gas Analyzer (IRGA). The meteosonde (A.I.R. model TS-5A-SEN) measured atmospheric pressure, air temperature, relative humidity, wind speed and wind direction at 2 second temporal resolution and transmitted data digitally to an A.I.R. IS-5A-RCR receiver (frequency range 395-410 MHz) connected to a Texas Instruments TI Extensa 460T laptop running the A.I.R. TS5A (version 4.2) software which stored the data on hard disk. The meteosonde had three analog spare channels to which the other two instruments were connected.

The ozonesonde (A.I.R. model OZ-3A-T) uses a bubbler system where ambient air is drawn into a $Na_2HPO_4 \cdot$ 12H2O and $NaH_2PO_4 \cdot H_2O$ buffered KI solution. It produces an electronic current between a Pt cathode and an Ag wire anode that is converted to a voltage where 1 ppb of ozone corresponds to approximately 1 mV. The ozone sonde was calibrated with a DASIBI 1008-PC (DASIBI Environmental Corp., Glendale, CA, U.S.A.) ozone generator/analyzer at 100 ppb O_3 (accuracy according to manufacturer: ±2 ppb) and with pressurized zero air from a gas bottle. Whenever the KI solution in the bubbler was changed a post-calibration with the old solution and a pre-calibration with the new solution were performed. The response of the KI solution to O_3 was typically quite stable up to over four hours of operation, before it was changed on a routinely basis. The estimated absolute accuracy of the ozonesonde measurements is ± 2-5 ppb of O_3 . Because of the cross-sensitivity of the KI solution to other oxidants in the air there might be unknown systematic errors if high concentrations of other oxidants exist. This is normally not the case in rural environments of Switzerland, but may not be of some, yet unknown, relevance in the urban/suburban atmosphere where this study was performed.

The IRGA was a CO_2/H_2O analyzer (PP Systems, Haverhill, MA, U.S.A., model P-CIRA-SCCIRAS-SC in a special light-weight aluminum enclosure) with internal pressure and temperature correction (accuracy according to manufacturer: ± 0.2 ppm CO2, ± 0.02-0.03 hPa vapour pressure). Every 30 minutes the IRGA performed an automatic zero calibration with ambient air from which CO_2 and H_2O were removed in a soda lime and magnesium perchlorate scrubber. The H_2O concentration range of the IRGA was calibrated with a LI-COR portable dew point generator (LI-COR, Inc., Lincoln, NB, U.S.A., model LI-610) with an accuracy of ± 0.2 °C. At a temperature of 20 °C and a pressure of 1013 hPa this accuracy corresponds to ± 0.3 hPa of the vapor pressure or ± 0.2 g/kg of the mixing ratio. Due to the slow response of the IRGA to changes in H_2O concentration, the absolute accuracy of the profile measurements is probably not better than ± 0.5 g/kg if there are steep changes of concentration with altitude. The response of the ozone sonde to such changes is much quicker so that even steep changes in O_3 concentration with altitude are well captured by this instrumentation.

3.3. The simulation models

3.3.1. Metphomod model

The *Metphomod* model (METeorology and PHOtochemistry MODel) [*Perego*, 1999] is a prognostic three-dimensional Eulerian model for the simulation of summer smog for complex terrain [*Liu et al.*, 1997]. The model includes modules for atmospheric dynamics, atmospheric turbulence, transport, gas-phase chemistry, short- and long-wave radiation transfer, and surface interactions, including emissions and deposition of trace gases. *Metphomod* uses a Cartesian grid with a rectangular coordinate system. With this grid structure most of the physical parameters are stored in the center of the respective grid cells, and only turbulence parameters and fluxes are stored at the faces. Topography is considered in two category of grid cells which are normal grid cells and underground grid cells. Fluxes at the boundaries of the underground grid cells are set to zero.

The calculation domain was chosen taking into consideration the topography. The rectangular grid has a dimension of 100 x 80 km, with a grid resolution of 2 km. GTOPO30 is used as the topography data set and GLCC as the land cover data set. Atmospheric initial and lateral boundary conditions are provided from the ISM model, which has a grid resolution of 14 km and gives predictions twice a day.

3.3.2. RAMS model

ClimRAMS [*Liston and Pielke*, 2000] is a climate version of the widely used CSU-RAMS non-hydrostatic mesoscale model (Regional Atmospheric Modeling System developed at the Colorado State University in Fort Collins, CO).

The domain of study was set up to contain the entire lake of Geneva, and an important portion of the mountains surrounding the region, i.e. the Alps and the Jura ranges.

ClimRAMS uses an oblique polar stereographic projection, with the pole put on the center of the domain, here at (46.2, 6.2) latitude/longitude coordinates, for minimizing the projection distortion errors on the domain area. Vertical levels are in a σ_z terrain-following coordinate system, with a first level at 50 m and a stretch of 1.2. First grid is a 13*13 grid, with 50 km cell width. Scaling down to the next grid is done with a ratio of 5, to obtain a cell width of 10 km, on a domain of 27*27 cells.

GTOPO30 is used as the topography data set. It is a global digital elevation model (DEM) with an horizontal grid spacing of 30 arc seconds (approximately 1 km), available through the United States Geological Survey's (USGS) Earth Resources Observation System (EROS) Data Center. The elevation values are averaged over the grid cells, from fine to coarser grid to keep higher resolution in finer grids. Also available through USGS EROS, is the 1 km resolution Global Land Cover Characteristics database. The data used for this study is the Biosphere-Atmosphere Transfer Scheme (BATS) classification of the 1.2 database version. As for the elevation values, the finer grid has an higher resolution. The land cover type is defined with a block-majority method, assigning the dominant land cover type to the entire cell. Sea-surface temperatures are derived from the global one-degree weekly database provided by the United States National Oceanic and Atmospheric Administration (NOAA). The values are interpolated to fit to the ClimRAMS grids and transformed to daily data. They are used in ClimRAMS for any water surface temperature, in this case, for the lake of Geneva. Atmospheric initial and lateral boundary conditions, as air temperature, horizontal wind components, relative humidity and geopotential height, are provided by the United States National Centers for Environmental Prediction (NCEP) reanalysis data in a six-hourly base, available through the NOAA-CIRES Climate Diagnostics Center (CDC). They are gridded on 17 pressure levels and on a global 2.5° * 2.5° latitude- longitude scale. The variables are interpolated in time and space to the coarsest grid. The nudging is only performed on the two outer-boundary grid cells of the coarser grid.

4. Results

4.1 General situation

The presented data are from an intercomparison campaign between the Raman lidar, set in the Nd:YAG configuration, and the tethered balloon. It occurred the 8th and 9th of April 2000 in the EPFL area. This campaign took advantage of extremely good weather conditions, with almost no wind at all altitudes. It permitted tethered balloon flights between 1400 and 1500 m during the entire measurement campaign.

The general weather situation was the following. Before the soundings, 7th of April, the center of the high pressure system was situated over the east coast of England. We were on its south rim and in a east-northeast oriented wind field ("bise"). As the cold front and the low pressure over Italy disappeared into the Mediterranean sea, wind ceased. On 8th of April there was hardly any pressure gradient over Switzerland, and as a consequence winds were only weak (local wind systems). A cold front system at the east of Switzerland was blocked by the high pressure. This front will disappear from the weather maps on the following days. On 9th of April overnight a high pressure bridge form Scandinavia to Sicily built up. We were on its west rim. Upper air winds increased in strength and turned to south and later southwest. In morning hours weather became overcast, winds increased and during the day a warm front crossed the lake of Geneva.

4.2 Comparisons

4.2.1. Water vapor comparisons

For the water vapor, the lidar spatial resolution is 22.5m and temporal resolution is 30 min. The first point of measurement is at 172.5 m agl. The analog detection is used for signal below 510 m for water vapor Raman lidar, while photon counting detection is used above this altitude. The lidar calibration constants are calculated using the values from the balloon descent. As the water vapor Raman lidar signal is also influenced by the ozone optical absorption, its effect is cancelled using each of the three Raman returns from O_2, N_2 and H_2O.For comparison with the lidar and balloon water vapor mixing ratio measurements, a run was made with the Metphomod and ClimRAMS models over the region of the lake of Geneva.

The Metphomod run was performed from the 6th of April to the 10th of April 2000.

The ClimRAMS run was performed with explicit cloud and precipitation microphysics representations [*Walko et al.*, 1995], from the 5th of April 2000 to the 10th of April 2000. Comparison between the calculations and the measurements is done with the results of April 8th as it corresponds to the 11 a.m. local time, in the cell (17,18) of the second grid. This cell is 100 km^2 large, covered with crop and 6% of water at 596m over sea level.

The result of this comparison is plotted in Figure 9 for the descent flight of the tethered balloon (11h30-12h on 08th of April 2000).

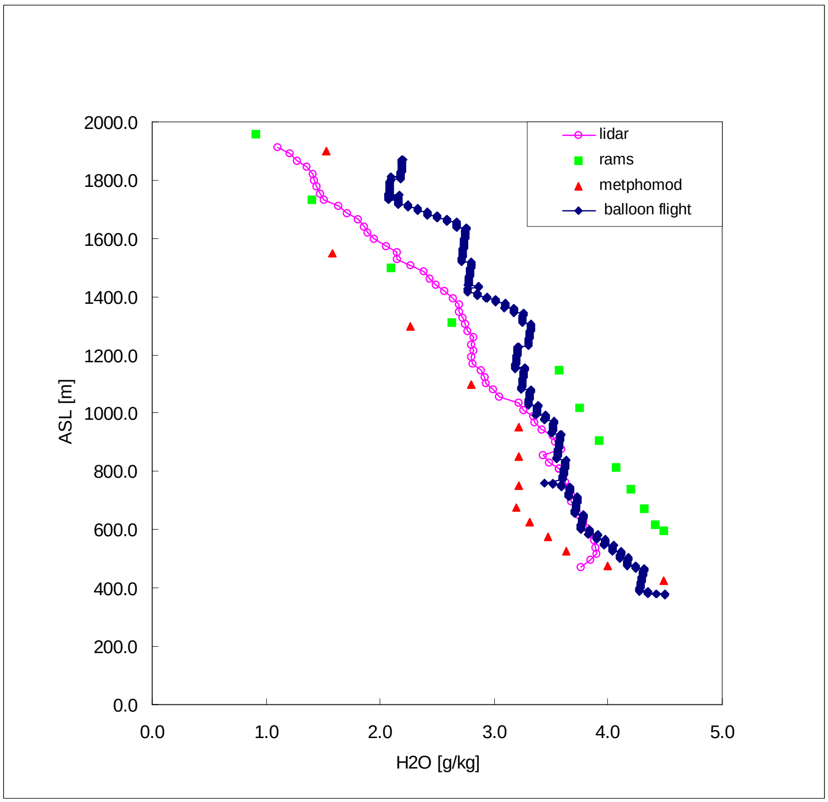

Figure 9. Comparison of the water vapor mixing ratio retrieved by Raman lidar, tethered balloon, METPHOMOD model and ClimRAMS model. 11h00 - 12h00 UTC the 8th of April 2000.

The H_2O mixing ratio tendency shown by the models and the measurements are the same. They all show a wet air flow between 1000 and 1800 m above sea level (asl). The two simulation profiles have a slope break at 1000-1200m height which indicates the top of the boundary layer. They are consistent with the balloon flight and the lidar profiles. Water vapor mixing ratio values, as well as boundary layer height, given by ClimRAMS are very sensitive to soil moisture conditions and vegetation type in the grid cell. Given an integration time so short and initial soil conditions so crudely defined, comparison has to be made on the tendencies and not on absolute values. Note that lower soil moisture initial conditions values would lead to improve ClimRAMS simulation of the boundary layer moisture conditions, with minimal change in the moisture conditions above the top of the boundary layer. For a complete analysis of simulation versus measurements values of water vapor mixing ratio, other variables like temperatures and winds should be compared (and integrated longer time series). Nevertheless, this first result shows consistent tendencies in water vapor mixing ratio profiles between different measurements and different simulations, even with crude parameterisation.

A temporal H_2O mixing ratio comparison was also made between the lidar and the Metphomod model. The result is shown in Figure 10, with a similar H_2O development.

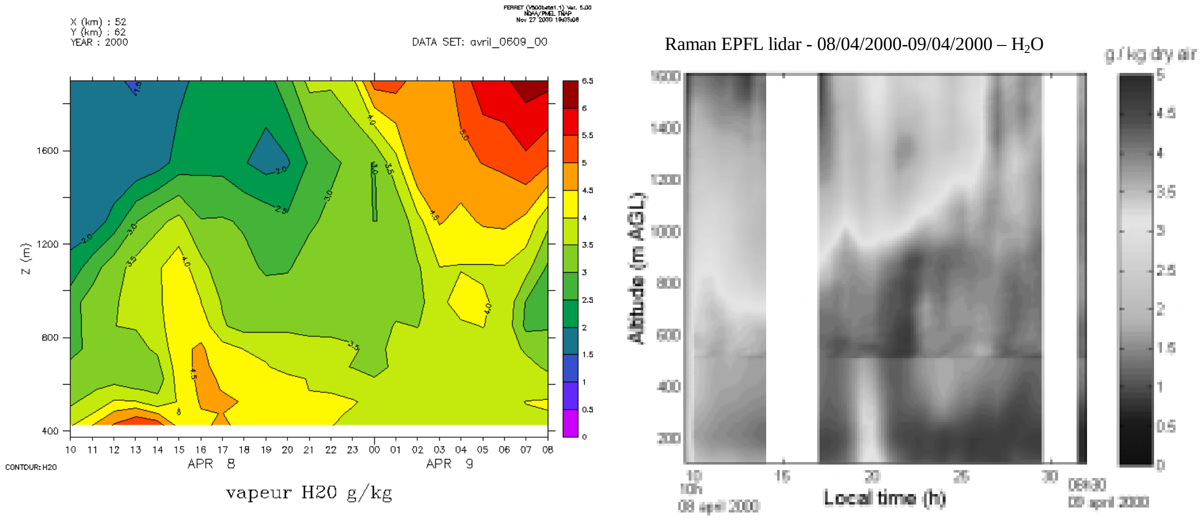
Raman EPFL lidar - 08/04/2000-09/04/2000 – H_2O

Figure 10. Relative humidity calculation and measurement between the 8th and the 9th of April 2000. On the left side is shown the resulting temporal series from MEDPHOMOD calculation and on the right side the one derived from the Raman lidar.

4.2.2. The ozone comparisons

In case of the ozone retrieval, the lidar spatial resolution is 78.75m, temporal resolution is 30 min and the first point of measurement is at 350m agl. The analog detection is used for signal below 600 m for O_3 Raman DIAL while photon counting detection is used above those respective altitudes

As the numerical models Metphomod and RAMS do not contain the O_3 capability retrieve, only comparison with the tethered balloon is possible. The result is shown in Figure 11.

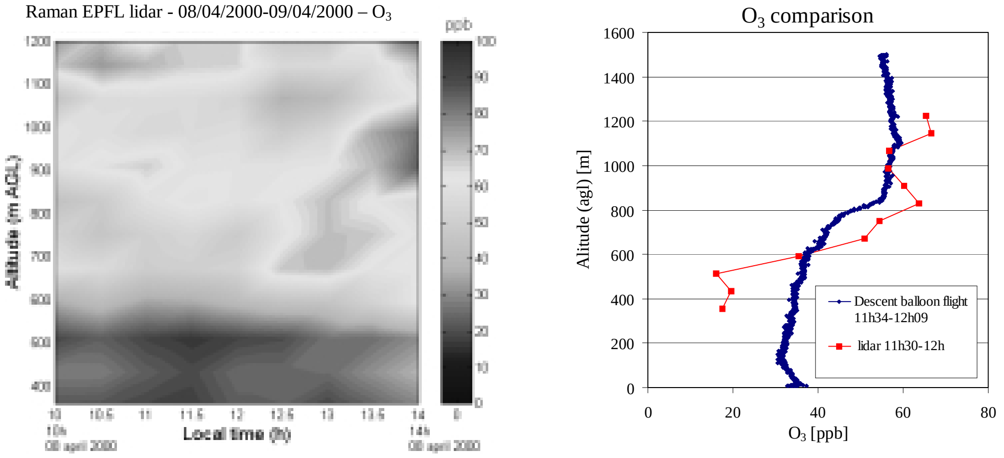
Raman EPFL lidar - 08/04/2000-09/04/2000 – O_3

O_3 comparison

Figure 11. O_3 concentration retrieves. On the left side a lidar temporal series made during the 08th and 09th of April is shown. On the right side a comparison between the lidar and the tethered balloon measurements, for the 11h30-12h00 descending flight on 08th April is shown.

The lidar temporal series shows values that are typical for the season with an expected increase tendency during the day, for a given altitude. The comparison with the tethered balloon shows a better O_3 retrieve in the photon counting mode than in the analog one.

6. Conclusion

The principle and design of a single wavelength excitation Raman-DIAL for the ozone concentration and the water vapor mixing ratio measurements in the planetary boundary layer, during day and night-time, was demonstrated. An extensive development of the corrective terms was performed and analyzed in both KrF and Nd:YAG configurations. Taking advantage of the KrF wavelength tuning capability, the optimum pump wavelength was given for a minimum SO_2 influence on the ozone concentration and water vapor mixing ratio retrieves. Inter-comparisons from a measurement campaign between the Raman lidar in the Nd:YAG configuration, a tethered balloon and two different numerical models were done. They showed good agreement in the H_2O mixing ratio retrieve and an expected worse one for the O_3 concentration retrieve. Further developments have to be made for an increased altitude covering, such as the combination with a classic elastic DIAL for higher altitudes, and a better O_3 concentration retrieve, with the help of an higher laser repetition rate or more sensitive PMTs. Nevertheless, and despite this difficulty, the approach we used appears to be convenient to give the essential O_3 integrated values necessary for the H_2O mixing ratio correction.

7. Acknowledgements

The EPFL lidar research was supported by the Swiss National Science Foundation under contract n° 21-50861.97 and the Federal Office for Science and Education under contract n° 97.0377. The KLIMET team was supported by a Hans-Sigrist fellowship grant from the University of Bern.

The authors are grateful to all the people who actively participated to the measurement campaigns.

8. Bibliography

Bates, D.R., Rayleigh scattering by air, *Planetary Space Science, 32*, 785-790, 1984.

Bernath, P., M. Carleer, S. Fally, A. Jenouvrier, A.C. Vandaele, C. Hermans, M.F. Mérienne, and R. Colin, The Wulf band of Oxygen, *Chemical Physics letters, 297,* 293-299, 1998.

Bischel, W.K., and G. Black, Wavelength dependence of Raman scattering cross sections from 200-600nm, in *AIP conference proccedings n°100 : eximer lasers,* edited by A.I.o. Physics, 1983.

Bösenberg, J., EUROTRAC / TESLAS (Tropospheric Environmental Studies by Laser Soundings), Max Planck Institute for Meteorology, Hamburg / Germany, 1996.

Burkholder, J.B., R.K. Talukdar, A.R. Ravishankara, and S. Solomon, Temperature dependence of the HNO_3 uv absorption cross sections, *Geophysical Research Letters, 98,* 22937-22948, 1993.

Cox, R.A., and R.G. Derwent, The ultraviolet absorption spectrum of gaseous nitrous acid, *Journal of Photochemistry, 6,* 23-24, 1976.

Daumont, D., J. Brion, J. Charbonnier, and J. Malicet, Ozone UV Spectroscopy I: Absorption Cross-Section at Room Temperature, *Journal of Atmospheric Chemistry*, *15*, 145-155, 1992.

Edlén, B., The Refractive Index of Air, *Metrologia*, *2* (2), 71-80, 1966.

Finlayson-Pitts, B.J., and J.N.J. Pitts, *Atmospheric Chemistry : Fundamentals and Experimental Techniques*, 1098 pp., Wiley Interscience, 1986.

Kuebler, J., Personnal communication on typical vertical distributions in remote and urban swiss places, 2000.

Lazzarotto, B., Ozone and water vapor measurements by Raman lidar in the planetary boundary layer, lidar thesis, EPFL, Lausanne, 2000.

Lazzarotto, B., M. Frioud, G. Larchevêque, V.M. Mitev, P. Quaglia, V. Simeonov, A. Thompson, H. Van den Bergh, and B. Calpini, Ozone and Water Vapor Measurements by Raman Lidar in the Boudary Layer : Error Sources and Field Measurements, *accepted in Applied Optics*, 2000.

Liston, G.E., and R.A. Pielke, A climate version of the regional atmospheric modeling system, *Theoretical and Applied Climatology*, *66*, 29-47, 2000.

Liu, R., P. Turco, and M.Z. Jacobson, An integrated air pollution modelling system for urban and regional scales: 1. Structure and performance, *Journal of Geophysical Research-Atmospheres*, *20* (D5), 6063-6079, 1997.

Measures, R.M., *Laser Remote Sensing. Fundamentals and Applications*, 510 pp., Krieger, New-York, 1992.

Meller, R., Private communication, *MPI Mainz / Germany*, 1992.

Mérienne, M.F., A. Jenouvrier, B. Coquart, M. Carleer, S. Fally, R. Colin, A.C. Vandaele, and C. Hermans, Fourier Transform Spectroscopy of the O_2 Herzberg Bands. (II. Band Oscillator Strengths and Transition Moments), *Journal of Molecular Spectroscopy*, *202*, 171-193, 2000.

Nicolet, M., and W. Peetermans, The Production of Nitric Oxide in the Stratosphere by Oxidation of Nitrous Oxide, *Ann. Geophys.*, *28*, 751-762, 1972.

NOAA, NASA, and USAF, U.S. standard atmosphere (76), U.S. government Printing Office, Washington / USA, 1976.

Penndorf, R., Tables of the refractive index for standard air and the Rayleigh scattering coefficient for the spectral region between 0.2 and 20.0 µm and their application to atmospheric optics, *Journal of the Optical Society of America*, *47*, 176-182, 1957.

Perego, S., A numerical mesoscale model for simulation of the regional photosmog in complex terrain: model description and application during POLLUMET 1993 (Switzerland), *Meteorological Atmospheric Physics*, *70*, 43-49, 1999.

Renaut, D., J.C. Pourny, and R. Capitini, Daytime Raman-lidar measurements of water vapor, *Optics Letters*, *5* (6), 233-235, 1980.

Schneider, W., G.K. Moortgat, G.S. Tyndall, and J.P. Burrows, Private communication, *MPI Mainz / Germany*, 1986.

Schoulepnikoff, L., H. Van den Bergh, B. Calpini, and V.M. Mitev, Tropospheric air pollution monitoring, lidar, in *Encyclopedia of environmental analysis and remediation*, John Wiley & Sons, 1998.

Schrötter, H.W., and H.W. Klöckner, Raman spectroscopy of gases and liquids, in *Topics in current physics n°11*, edited by A. Weber, Springer-Verlag, 1979.

Seinfeld, J.H., and S.N. Pandis, *Atmospheric Chemistry and Physics*, 1326 pp., Wiley Interscience, 1998.

Shemansky, D.E., CO_2 Extinction Coefficients 1700-3000 A, *J. Chem. Phys.*, *56*, 1582-1587, 1972.

Simeonov, V., G. Larchevêque, P. Quaglia, H. Van den Bergh, and B. Calpini, The influence of the photomultiplier spatial uniformity on lidar signals, *Applied Optics*, *38*, 5186-5190, 1999.

Trost, B., Benzene, Toluene absorption spectra, edited by I.f. Umweltphysik, Heidelberg, 1994.

Vandaele, A.C., P.C. Simon, J.M. Guilmot, M. Carleer, and R. Colin, SO_2 absorption cross section measurement in the UV using a Fourier transform sectometer, *Journal of Geophysical Research-Atmospheres*, *99* (12), 25599-25605, 1994.

Walko, R.L., W.R. Cotton, M.P. Meyers, and J.H. Harrington, New RAMS cloud microphysics parametrization, part 1: the single moment scheme., *Atmospheric Research*, *38*, 29-62, 1995.

Warneck, P., *Chemistry of the Natural Atmosphere*, Academic Press, 1988.

Yung, Y.L., and W.B. DeMore, *Photochemistry of Planetary Atmospheres*, Oxford University Press, 1999.

Chapter 8

Conclusion and perspectives

This work takes place in a long series of research, conducted by means of this technique since the 60's, aiming at a better understanding of the complicated phenomenons that occur in the atmosphere.

We proposed here to focus on the O_3 concentration and H_2O mixing ratio retrieves in the planetary boundary layer, by means of a Raman technique. The needed theoretical background to explain and understand the various phenomena was exposed in details all along this thesis. The system was described and essential tests to be performed were exposed.

First measurements of the O_3 concentration with two Raman signals were performed at the beginning of 1998 and were followed by important technical modifications intended to make possible the simultaneous detection of the O_3 concentration and the H_2O mixing ratio. A theoretical research on the corrective quantities and on the different noises, such as cross-talk, was carried out. It pointed out that in our case the optical cross-talk as well as the after pulse effect may be neglected. In typical atmospheric conditions, the corrections which have to be applied to O_3 concentration and to H_2O mixing ratio were discussed and higher correcting values in the KrF configuration were found. Above all, we confirmed that the most important correction for the H_2O mixing ratio is due to the O_3 absorption contribution and an auto-correction by means of the lidar appeared to be the best approach.

Although this work has allowed to reach some good results concerning the H_2O mixing ratio, the precise knowledge of the O_3 concentration retrieve still need further efforts. Nevertheless, and despite this difficulty, the appoach we used appears to be convenient to give the essential O_3 integrated values necessary for the H_2O mixing ratio correction. To be competitive with the classic DIAL approach , in case of the O_3 concentration retrieve, the Raman lidar method has to be improved on both technical and theoretical fields.

From a practical point of view, the laser repetition rate experiment made with the KrF configuration showed better results with higher repetition rate values, and appreciable progress should be expected with a Nd : YAG laser having a higher repetition rate. The other important element to be improved is the PMT, especially concerning its spatial homogeneity. Intensive research on these fields should be carried out whose results will determine the future solution of the many problems still pending.

From a theoretical point of view, one problem to be solved is the aerosol contribution value. Apart from the use of complicated numerical simulations, the retrieval method proposed in our work suffers from the Angström approximation. Recent methods taking advantage of well choosed wavelengths succeeded to overcome the systematic error introduced by the Angström's parameter k in the standard case [*Gathen*, 1995] or eliminate the differential transmis-

sion effects that are causing systematic errors [*Moosmüller and Wilkerson*, 1997].
The use of statistical methods allowing a better precision in the calculation of the derivative of the logarithm of two quantities ratio can also be an interesting way to explore [*Whiteman*, 1999], in order to increase the accuracy of the final result. Mathematical methods which permit a better signal binning and an accurate derivative calculation can also be investigated [*Godin*, 1987].

All these researches for technical and theoretical improvements have to be done in an unique aim: let a better earth to our childrens with a clean and respirable atmosphere.

Chapter 9

Annex

This chapter, apart the first and last paragraphs, is dedicated to calculations and constants that are usually well known.

In the first paragraph is presented a method different from the Ansmann's one to retrieve the aerosol backscattering coefficient. This purely theoretical investigation takes advantage of the last configuration of the Raman lidar with three Raman backscattered signals (from the atmospheric O_2, N_2 and H_2O) and one elastic backscattered signal at the pump wavelength. A calculation procedure to retrieve the unknown constants is also proposed.

In the last paragraph are shown and explained the different programs used, in their last version, for either the acquisition procedure or the data treatment one. The procedure for the data treatment is more detailed and will permit, in principle, the data treatment of a set of signals by a non-specialist.

The classical units as well as the unit conversions of interest in this thesis are summarized in two tables. It permits the person familiar to the domain to refresh his knowledge, but also to teach the neophyte one the quantities and relations that he may be not familiar with.

Some calculations which are used in the other chapters of this thesis are also placed here. It concerns the calculation of the Raman shifted wavelengths and the temperature independence of the ozone absorption cross-section and of the Raman one. Showing the results here allows a better understanding of the approximations that are made.

9.1. A new method for the aerosol backscattering coefficient calculation

Another procedure to retrieve the phase function P_π , for the aerosol case, will be developed here after. This function links the atmospheric attenuation coefficient and the atmospheric volume backscattering coefficient and is defined by:

$$ {}^{\pi}\beta^{aer}(\lambda_L, r) = P_\pi \alpha^{aer}(\lambda_L, r) \qquad \text{(EQ 9.1)}$$

As the aerosol extinction coefficient $\alpha^{aer}(\lambda_L, r)$ can be calculated, the phase function P_π can then be retrieved if the determination of the aerosol backscatter coefficient ${}^{\pi}\beta^{aer}(\lambda_L, r)$ can be performed. This latter can be retrieved by the analytical inversion of the lidar equation [*Fernald*, 1984], [*Klett*, 1981], [*Browell et al.*, 1985], but this is a difficult approach. Here we use both Raman and elastic channels to solve the problem.
In the elastic case the lidar equation can be written as [*Measures*, 1992]:

$$P_L(\lambda_L, R) = P_L(\lambda_L) K_L \frac{A(R)}{R^2} \Delta R\, ({}^{\pi}\beta^{gaz} + {}^{\pi}\beta^{aer})(\lambda_L, R)\, T(\lambda_L, R)\, T(\lambda_L, R) \qquad \text{(EQ 9.2)}$$

With the calculation for the transmission terms made in the chapter “Theory”, p 27 it gives:

$$P_L(\lambda_L, R) = P_L(\lambda_L) K_L \frac{A(R)}{R^2} \Delta R \left({}^{\pi}\beta^{molec} + {}^{\pi}\beta^{aer}\right)(\lambda_L, R) \times \exp\left\{ -2 \int_0^R \left[\alpha^{molec}(\lambda_L, r) + \alpha^{aer}(\lambda_L, r)\right] dr \right\} \qquad \text{(EQ 9.3)}$$

The aerosol extinction coefficient was already calculated, but for a region of full overlap. We have to keep in mind that now, because of the integral domain [0,R], the overlap term is not constant in the zero region and has to be kept. We then have a modified (EQ 4.34) p 76, valid for r in a region of full overlap or not:

$$\alpha^{aer}(\lambda_L, r) = \frac{\dfrac{\partial}{\partial r} \ln\left(\dfrac{A(r) n_X(r)}{r^2 P_X(\lambda_L, \lambda_X^{Ram}, r)} \right) - \left(\alpha^{molec}(\lambda_L, r) + \alpha^{molec}(\lambda_X^{Ram}, r) \right)}{1 + \left(\dfrac{\lambda_X^{Ram}}{\lambda_L} \right)^k} \qquad \text{(EQ 9.4)}$$

(EQ 9.3) and (EQ 9.4) then give:

$$\begin{aligned} P_L(\lambda_L, R) = {} & P_L(\lambda_L) K_L \frac{A(R)}{R^2} \Delta R \left({}^{\pi}\beta^{molec} + {}^{\pi}\beta^{aer}\right)(\lambda_L, R) \\ & \times \exp\left\{ -2 \int_0^R \left[\frac{\dfrac{\partial}{\partial r} \ln\left(\dfrac{A(r) n_X(r)}{r^2 P_X(\lambda_L, \lambda_X^{Ram}, r)} \right) - \left(\alpha^{molec}(\lambda_L, r) + \alpha^{molec}(\lambda_X^{Ram}, r) \right)}{1 + \left(\dfrac{\lambda_X^{Ram}}{\lambda_L} \right)^k} + \alpha^{molec}(\lambda_L, r) \right] dr \right\} \end{aligned} \qquad \text{(EQ 9.5)}$$

The first term inside the integral, countaining the overlap function, gives:

$$\int_0^R \frac{\partial}{\partial r}\ln\left(\frac{A(r)n_X(r)}{r^2P_X(\lambda_L,\lambda_X^{Ram},r)}\right)dr=\ln\left(\frac{A(R)n_X(R)}{R^2P_X(\lambda_L,\lambda_X^{Ram},R)}\right)-\ln\left(\frac{A(r)n_X(r)}{r^2P_X(\lambda_L,\lambda_X^{Ram},r)}\right)_{r=0} \qquad \text{(EQ 9.6)}$$

For the second term inside the (EQ 9.6), where r = 0, we have to go back to the Raman lidar equation (EQ 2.6) p 38 and extract the term of interest:

$$\frac{A(r)n_X(r)}{r^2P_X(\lambda_L,\lambda_X^{Ram},r)}=\frac{1}{P_L(\lambda_L)\;K_X\;\;\Delta R\;{}^{\pi}\beta_X^{Ram}\,T(\lambda_L,r)T(\lambda_X^{Ram},r)} \qquad \text{(EQ 9.7)}$$

The limit, approaching 0 gives:

$$\lim_{r\to 0^+}\frac{A(r)n_X(r)}{r^2P_X(\lambda_L,\lambda_X^{Ram},r)}\to\frac{1}{P_L(\lambda_L)\;K_X\;\;\Delta R\;{}^{\pi}\beta_X^{Ram}} \qquad \text{(EQ 9.8)}$$

and then by substitution we have:

$$\begin{aligned}P_L(\lambda_L,R)&=P_L(\lambda_L)\,K_L\,\frac{A(R)}{R^2}\Delta R\left({}^{\pi}\beta^{molec}+{}^{\pi}\beta^{aer}\right)(\lambda_L,R)\\&\times\exp\left\{-2\frac{\ln\left(\dfrac{A(R)n_X(R)}{R^2P_X(\lambda_L,\lambda_X^{Ram},R)}\right)+\ln\left(P_L(\lambda_L)\,K_X\,\Delta R\,{}^{\pi}\beta_X^{Ram}\right)}{1+\left(\dfrac{\lambda_X^{Raman}}{\lambda_L}\right)^k}-2\int_0^R\left[\frac{\left(\dfrac{\lambda_X^{Ram}}{\lambda_L}\right)^k\alpha^{molec}(\lambda_L,r)-\alpha^{molec}(\lambda_X^{Ram},r)}{1+\left(\dfrac{\lambda_X^{Ram}}{\lambda_L}\right)^k}\right]dr\right\}\end{aligned} \qquad \text{9.9)}$$

If we suppose (now) to be at full overlap, i.e. A(R) = 1, we have then the final expression of the aerosol backscattering coefficient:

$$\begin{aligned}{}^{\pi}\beta^{aer}(\lambda_L,R)&=\frac{P_L(\lambda_L,R)\,R^2}{P_L(\lambda_L)K_L\;\Delta R}\left(\frac{n_X(R)\,P_L(\lambda_L)\,K_X\;\;\Delta R\;{}^{\pi}\beta_X^{Ram}}{R^2\,P_X(\lambda_L,\lambda_X^{Ram},R)}\right)^{\frac{2}{1+\left(\frac{\lambda_X^{Ram}}{\lambda_L}\right)^k}}\\&\times\exp\left\{2\int_0^R\left[\frac{\left(\dfrac{\lambda_X^{Ram}}{\lambda_L}\right)^k\alpha^{molec}(\lambda_L,r)-\alpha^{molec}(\lambda_X^{Ram},r)}{1+\left(\dfrac{\lambda_X^{Ram}}{\lambda_L}\right)^k}\right]dr\right\}-{}^{\pi}\beta^{molec}(\lambda_L,R)\end{aligned} \qquad \text{(EQ 9.10)}$$

The aerosol backscattering term can be calculated for the O_2 and N_2 Raman signals (n_{N_2} and n_{O_2} are well known), which gives us a system of two equations with four unknowns:

$$\begin{cases}{}^{\pi}\beta^{aer}(\lambda_L,R)=f(K_L,K_{N_2})\\{}^{\pi}\beta^{aer}(\lambda_L,R)=g(K_L,K_{O_2})\end{cases} \qquad \text{(EQ 9.11)}$$

A relation between the system constants K_L , K_{N_2} and K_{O_2} has then to be found. As the wavelengths $\lambda_{N_2}^{Ram}$, $\lambda_{N_2}^{Ram}$ and $\lambda_{O_2}^{Ram}$ are close, we can make the assumption that the only linking factors are the relative sensibilities of the different PMTs in case of the Raman PMTs, with an additional optical constant for the elastic case (the elastic PMT doesn't have the same optical path):

$$K = \gamma_L K_L = \gamma_{N_2} K_{N_2} = \gamma_{O_2} K_{O_2} \tag{EQ 9.12}$$

where the factors γ_L, γ_{N_2} *and* γ_{O_2} take into account these PMT relative sensibilities.
The retrieve in the Raman case, i.e. the relation between γ_{N_2} *and* γ_{O_2} has been made in the paragraph 3.4.3. “Relative sensitivity of the PMTs”, p 57.
To find a relation between the factor for the elastic and a Raman PMT, the following procedure can be achieved:

- Like for the Raman case, part of the laser beam is taken with an optical fiber and injected inside the receiver part.
- The grating is turned in order to inject this signal inside the N_2 (or O_2) PMT.
- Then by recording the intensity of the elastic PMT and the N_2 (or O_2) one we can deduce the factor of interest.

We then have a system of two equations with two unknowns, that can then be resolved:

$$\begin{cases} {}^{\pi}\beta^{aer}(\lambda_L, R) = f(K\ ) \\ {}^{\pi}\beta^{aer}(\lambda_L, R) = g(K\ ) \end{cases} \tag{EQ 9.13}$$

To calculate ${}^{\pi}\beta_{Rayl}^{molec}(\lambda_L, R)$ *[cm^{-1}.sr^{-1}]*, the atmospheric volume (Rayleigh) backscattering coefficient, we make a similar procedure as for (EQ 2.10) p 40:

$${}^{\pi}\beta^{gas}(\lambda_L, R) \equiv {}^{\pi}\beta_{Rayl}^{molec}(\lambda_L, R) = n_{atmos}\,{}^{\pi}\sigma_{Rayl}^{molec}(\lambda_L, R) \tag{EQ 9.14}$$

In the paragraph 4.2.1. “The extinction term due to molecular scattering”, p 66, the Rayleigh molecular backscattering cross-section ${}^{\pi}\sigma_{Rayl}^{molec}(\lambda_L, R)$ *[cm^2.sr^{-1}.molec^{-1}]* was already calculated. Taking into account the simple relation given by (EQ 4.26) p 72 we then immediately have:

$${}^{\pi}\beta^{gas}(\lambda_L, R) \equiv {}^{\pi}\beta_{Rayl}^{molec}(\lambda_L, R) = \frac{3}{8\pi}\alpha_{Rayl}^{molec}(\lambda_L, R) \tag{EQ 9.15}$$

We see that (EQ 9.1) p 164 is in fact a generalization of the Rayleigh case, where $P_\pi = \frac{3}{8\pi}$.

Another possible method is to calculate these system constant terms with the different elements efficiencies. It will give us an order of magnitude for these constants, but great care has to be taken about the reality of it.
As a conclusion we wanted to mention the way proposed by Ansmann [*Ansmann et al.*, 1992] for this aerosol backscattering coefficient retrieve. They plot the aerosol extinction coefficient $\alpha_{\lambda_L}^{aer}(R)$ and deduce the regions with less aerosols, i.e. where it is possible to make a molec-

ular approximation. At this altitude, as there is no aerosol backscattering, $\beta_{\lambda_L}^{aer}(R_0) = 0$ and it is then possible to retrieve the unknown constants.
In our case the limitant problem concerns the low altitude of the measurements which doesn’t allow us, in principle, to apply this method.

9.2. Raman shifted wavelengths calculation

For a given excitation wavelength the Raman scattering will give birth to a shifted spectra characteristic to the excited molecule. Here was just computed the resulting shifted wavelength of the first Stokes, i. e. the most important one, and the one used in this work.
The paragraph 3.5. “Raman lidar specifications table”, p 60 shows a fixed emitted wavelength for the Nd:YAG laser and tunable one for the KrF. The quadrupled Nd:YAG wavelength, as the linewidth FWHM is less than 0.014 nm, is taken equal to 266.04 nm (no need to take 266.0375 nm).
These possibilities were then taken into account and introduced inside the calculation. Also a comparison of the different Raman displacements that can be found in the literature was exposed
From a theoretical point of view we have the following development. The wavelength λ is linked to the frequency ν and the wavenumber $\tilde{\nu}$ by:

$$\lambda = \frac{c}{\nu} = \frac{1}{\tilde{\nu}} \qquad \text{(EQ 9.16)}$$

where c is the speed of the light.

The Raman displacement $\Delta\tilde{\nu}$ is then given by:

$$\Delta\tilde{\nu} = \tilde{\nu}_L - \tilde{\nu}_X^{Ram} \quad (\tilde{\nu}_L > \tilde{\nu}_X^{Ram} \quad : \quad \lambda_X^{Ram} > \lambda_L) \qquad \text{(EQ 9.17)}$$

where $\lambda_L = \frac{1}{\tilde{\nu}_L}$ is the laser pump wavelength and $\lambda_X^{Ram} = \frac{1}{\tilde{\nu}_X^{Ram}}$ is the Raman shifted wavelength (of the first Stokes) for the molecule X. With (EQ 9.16) we then can deduce the relation of interest:

$$\lambda_X^{Ram} = \frac{\lambda_L}{1 - \Delta\tilde{\nu} \cdot \lambda_L} \qquad \text{(EQ 9.18)}$$

This equation is at the basis of the following two tables, Table 9-1 and Table 9-2, and was derived for the O_2, N_2 and H_2O molecules.

TABLE 9-1. Raman shifted wavelengths for O_2, N_2

	O_2	O_2	O_2	N_2	N_2
# ref	1, 2	3	4	1, 2	3, 4
Raman Displacement [cm^{-1}]	1555.0	1556.0	1554.7	2331.0	2330.7
Exitation wavelength [nm]	Shifted wavelength [nm]				
Nd:YAG					
266.04	**277.52**	**277.53**	**277.52**	**283.63**	**283.63**
KrF					
248.40	258.38	258.39	258.38	263.67	263.66
248.45	258.43	258.44	258.43	263.72	263.72
248.50	258.49	258.50	258.49	263.78	263.78
248.55	258.54	258.55	258.54	263.84	263.83
248.60	258.60	258.60	258.59	263.89	263.89
248.65	258.65	258.66	258.65	263.95	263.95
248.70	**258.70**	**258.71**	**258.70**	**264.00**	**264.00**
248.75	258.76	258.77	258.76	264.06	264.06
248.80	258.81	258.82	258.81	264.12	264.12
248.85	258.87	258.87	258.87	264.17	264.17
248.90	258.92	258.93	258.92	264.23	264.23
248.95	258.98	258.98	258.97	264.29	264.28
249.00	259.03	259.04	259.03	264.34	264.34
249.05	259.08	259.09	259.08	264.40	264.40
249.10	259.14	259.14	259.14	264.46	264.45

TABLE 9-2. Raman shifted wavelengths for H_2O

	H_2O ν_1 band	H_2O ν_1 band	H_2O ν_1 band
# ref	1	3	4
Raman Displacement [cm^{-1}]	3652.0	3651.7	3654.5
Exitation wavelength [nm]			
Nd:YAG			
266.04	**294.67**	**294.67**	**294.69**
KrF			
248.40	273.18	273.18	273.20
248.45	273.24	273.24	273.26
248.50	273.30	273.30	273.32
248.55	273.36	273.36	273.38
248.60	273.42	273.42	273.44
248.65	273.48	273.48	273.50
248.70	**273.54**	**273.54**	**273.56**
248.75	273.61	273.60	273.62
248.80	273.67	273.66	273.68
248.85	273.73	273.72	273.74
248.90	273.79	273.78	273.81
248.95	273.85	273.84	273.87
249.00	273.91	273.91	273.93
249.05	273.97	273.97	273.99
249.10	274.03	274.03	274.05

With ref 1: [*Schrötter and Klöckner*, 1979], ref 2: [*Bischel and Black*, 1983], ref 3: [*Inaba and Kobayashi*, 1972], ref 4: [*Herzberg*, 1946].

This calculations show no significant differences between the different calculations made with the different Raman displacements. The Raman displacement values from references 1 and 2 were chosen, which gives for the following Raman displacements:

$1555\ cm^{-1}$ for O_2, $2331\ cm^{-1}$ for N_2 and $3652\ cm^{-1}$ for H_2O.

The corresponding values of the Raman shifted wavelengths can be found in Table 9-1 and Table 9-2.

9.3. The temperature (in)dependence of the Raman and O_3 absorption cross-section

9.3.1. Introduction

According to the atmospheric profile model chosen in the chapter 4 “Corrections and errors analysis”, p 65 [*NOAA et al.*, 1976] we can see that, in the troposphere, the temperature gradient is approximately -0.65 *[K]* / 100 *[m]* in case of wet air (-1 *[K]* / 100 *[m]* for dry air).

The measurements made with the Raman system reach a maximum of 1500 m above ground level, which gives a temperature difference of approximately 10 K. If we also take into account the season temperature difference which is in the order of 30 K, we then have an idea of the temperature difference that can be encountered: 40 K.

This model shows a link between altitude (and so the range) and temperature. So, establishing a temperature independence for a given quantity will imply a range independence.

9.3.2. The Raman backscattering cross-section

For the Raman differential scattering cross-section in the vibrational case we have the following temperature dependence [*Schrötter and Klöckner*, 1979]:

$$^{\pi}\beta_X^{Ram} \equiv \frac{d\,^{\pi}\sigma_X^{Ram}}{d\Omega} \propto \frac{1}{1-\exp\left(-\frac{hc\upsilon_X}{k_B T}\right)} \qquad \text{(EQ 9.19)}$$

where $h = 6.626 \times 10^{-34}$ *[J.s]* is the Planck constant, $c = 2.998 \times 10^{8}$ *[m.s⁻¹]* is the light speed, ν_X *[cm^{-1}]* is the Raman shift of the molecule X, $k_B = 1.381 \times 10^{-23}$ *[$J.K^{-1}$]* is the Boltzmann constant and T *[K]* is the temperature.

As before, it makes sense to take a temperature difference of 40 K. The results for our three molecules of interest O_2, N_2 and H_2O are summarized in Table 9-3.

This table shows a relative error always smaller than 4×10^{-2} %, and so we can reasonably cancel the temperature dependence of the Raman backscattering cross-section.

As a useful consequence the Raman backscattering cross-section can be considered independent to altitude in our experimental conditions.

TABLE 9-3. Temperature dependence of the Raman backscattering cross-section

	O_2	N_2	H_2O
Raman displacement [cm-1]	1555	2331	3652
Relative error	-4.199E-04	-1.273E-05	-2.744E-08
Relative error in %	**-4.20E-02**	**-1.27E-03**	**-2.74E-06**

Temperature difference	40

9.3.3. The ozone absorption cross-section

Calculations have been made for the Nd:YAG case taking the ozone absorption cross-section spectrum at two different temperatures: 243 K and 298 K [*Daumont et al.*, 1992].
The Table 9-4 shows the relative error calculation on the ozone concentration and the water vapor mixing ratio.

TABLE 9-4. Temperature dependence of the ozone absorption cross-section

		Temperature [K]	243	298	228
Nd:YAG wavelength [nm]	266.04	spectra resolution [nm]	0.03	0.01	0.01
λ_{O2} calculation [nm]	277.52	λ_{O2} taken [nm]	*277.53*	277.52	277.52
		σ_{O3} abs [cm^2.$molec^{-}1$]	4.790E-18	4.870E-18	4.780E-18
λ_{N2} calculation [nm]	283.63	λ_{N2} taken [nm]	*283.62*	283.63	283.63
		σ_{O3} abs [cm^2.$molec^{-1}$]	2.830E-18	2.900E-18	2.820E-18
λ_{H2O} calculation [nm]	294.67	λ_{H2O} taken [nm]	*294.66*	294.67	294.67
		σ_{O3} abs [cm^2.$molec^{-1}$]	7.610E-19	8.070E-19	7.480E-19
		$\sigma_{O3}(\lambda_{O2})-\sigma_{O3}(\lambda_{N2})$ abs [cm^2.$molec^{-1}$]	1.960E-18	1.970E-18	1.960E-18
		$[\sigma_{O3}(\lambda_{H2O})-\sigma_{O3}(\lambda_{N2})]$ / $[\sigma_{O3}(\lambda_{O2})-\sigma_{O3}(\lambda_{N2})]$ abs	1.056	1.062	1.057

	O_3	H_2O
Temperature difference	298-243	298-243
relative error	-5.10E-03	-1.97E-03
relative error in %	**-0.51**	**-0.20**

Supposing to have a lidar signal ratio $PO_2/PN_2=0.75$

In the given range of 40 K, the relative error for both retrieves is always smaller than 0.5 %. The temperature dependence, and then the range dependence, on the ozone absorption cross-section can be neglected here. This behavior has been used in the paragraph 2.3.1. “The Raman lidar equation”, p 38 and was of essential interest in the retrieve of the ozone integrated term for the water vapor correction given by (EQ 2.25) p 44.

9.4. Classical physical constants and useful unit conversions

9.4.1. Introduction: Physical constants, units and relations between them

A small compilation [*Cohen and Taylor*, 1995], [*Seinfeld and Pandis*, 1998], [*Swiss_Metrology_Office*, 1993], [*Lide*, 1992-1993], [*Matthieu et al.*, 1985], [*Ernst*, 1982] for the quantities of interest will be exposed. As confusion or forgetting often occur, it motivates such elaboration.

Atmospheric properties of interest

In Table 9-5 is listed the main constants that are used in this work.

TABLE 9-5. Physical constants and atmospheric properties

	Name	Symbol	Value	SI unit	Relation / condition
Fundamental physical constants	Velocity of light in the vacuum	c	$2.997925\ 10^{8}$	$m.s^{-1}$	
	Electron charge	e	$1.60219\ 10^{-19}$	C	
	Planck's constant	h	$6.62618\ 10^{-34}$	$J.s^{-1}$	
	Molar gas constant	R	8.31441	$J.mol^{-1}.K^{-1}$	
	Avogadro's number	N_A	$6.0221367\ 10^{23}$	mol^{-1}	
	Boltzmann constant	k_B	$1.38066\ 10^{-23}$	$J.K^{-1}$	$k_B=R/N_A$
	Molar volume of an ideal gas at standard temperature and pressure	V_M	$22.4141\ 10^{-3}$	$m^3.mol^{-1}$	$V_M=RT_0/P_0$
Atmospheric properties	Standard temperature	T_0	273.15	K	
	Standard pressure	P_0	101325	Pa	
	Loschmidt number		$2.69\ 10^{19}$	$molec.cm^{-3}$	concentration of molecules of an ideal gas at 0 °C and 1atm
	Common air concentrations		$2.688\ 10^{19}$@ 273K $2.463\ 10^{19}$@ 298K	$molec.cm^{-3}$	ideal gas at 1atm
	Molecular weight of dry air		28.966	$g.mol^{-1}$	
	Air volume mass		$1.2928\ 10^{-3}$	$g.cm^{-3}$	273 K and 1atm

Units and linking relations

Table 9-6 shows the basic SI units, as a reminder, and other useful units with their interlinking.

TABLE 9-6. The different units

	Physical quantity	**Name**	**Symbol**	**Relations**
SI base units	Length	Meter	m	
	Plane angle	Radian	rad	
	Solid angle	Steradian	sr	
	Mass	Kilogram	kg	
	Time	Second	s	
	Electric current	Ampere	A	
	Thermodynamic temperature	Kelvin	K	
	Amount of substance	Mole	mol	
	Luminous intensity	Candela	cd	
SI derived units	Pressure	Pascal	Pa	1 Pa = 1 N.m^{-2}
	Energy / Work / Heat quantity	Joule	J	1 J = 1 N.m = 1 W.s
	Power / Energetic rate / Thermic rate	Watt	W	1 W = 1 J.s^{-1} = 1 N.m.s^{-1} = 1 V.A
Non SI units	Pressure	Bar	bar	1 bar = 10^{5} Pa (->1 mbar = 1 hPa)
		Hg millimeter	mmHg	1mmHg = 1.33322 10^{2} Pa
	Energy / Work / Heat quantity	Kilowatt hour	kW.h	1 kW.h = 3.6 10^{6} J
		Electron Volt	eV	1 eV = 1.60217733 10^{-19} J
	Thermodynamic temperature	Celsius degree	°C	T[°C] = T[K] - 273.15 ΔT[°C] = ΔT[K]
		Fahrenheit degree	°F	T[°C] = 5/9(T[°F] - 32) ΔT[°F] = 5/9 ΔT[°C]= 5/9 ΔT[K]

TABLE 9-6. The different units

	Physical quantity	Name	Symbol	Relations
Non SI units	Length	Inch	in	1 in = 25.54 mm
		Angström	Å	1 Å = 10^{-10} m
	Pressure	Physical (or standard) atmosphere	atm	1 atm = 1.01325 10^5 Pa = 760 mmHg = 760 torr = 1.01325 bar
		Technical atmosphere	at	1 at = 0.980665 10^5 Pa
		Torr	torr	1 torr = 1.33322 10^2 Pa
		Barye	barye	1 barye = 0.1 Pa
		Pieze	pz	1 pz = 10^3 Pa
		mmH_2O	mmH_2O	$1mmH_2O$ = 9.80665 Pa
	Energy / Work / Heat quantity	Calorie	cal	1 cal = 4.1868 J
		Horsepower hour	hph	1 hph = 2.6478 10^6 J
		Erg	erg	1 erg = 10^{-7} J
		Thermie	th	1 th = 4.1855 10^6 J
	Power / Energetic rate / Thermic rate	KiloCalorie by hour	kcal/h	1 kcal/h = 1.163 W
		Horsepower	hp	1 hp = 0.735499 kW

9.4.2. Conversions between concentration and mixing ratio

Concentration is defined as an amount, like a number of molecules or moles (or a mass), of a substance in a given volume divided by this volume. In terms of equation it gives:

$$C_X = \frac{\text{Substance X amount}\big|_{\text{given volume}V}}{V} \qquad \text{(EQ 9.20)}$$

C_X can then represent a volume concentration (of molecules or moles) or a mass concentration, depending on how the substance amount is described. This representation implies a pressure and temperature dependence through the ideal gas law.

Mixing ratio, which is just a fraction of identical units, is better suited than concentration to describe abundance of species in air, specially when spatial and temporal variation occurr. It is defined as the ratio of the amount of a substance, like a number of molecules or moles (or a mass), in a given volume to the total amount (or mass) of all constituents (including water vapor but not including particulate matter or condensed phase water) in that volume.

Often the term "all constituents" does not include the water vapor, and then the mixing ratio is related to dry air as it was done in the water vapor mixing ratio retrieve in the paragraph 2.3.3. “The water vapor retrieve (first formulation)”, p 42. This permits to cancel the variation

of the mixing ratio, which can amount to several percent, if the water vapor is included in the "all constituents" term.
In terms of equation we have:

$$\xi_X = \frac{\text{Substance X amount}\big|_{\text{given volume}V}}{\text{"Total" amount}\big|_{\text{given volume}V}} = \frac{C_X}{C_{total}} \qquad \text{(EQ 9.21)}$$

As in the concentration definition, ξ_X can represent a volume mixing ratio (by mean of a molecules or moles number) or a mass mixing ratio depending on how the different amounts are described. The first one, used in atmospheric chemistry, is expressed as part of volume and denoted by ppmv for example, where "v" denotes the volumic dependence. The second one, used in the water chemistry, is of less interest for us and is expressed relatively to mass and denoted by ppmm for example, where "m" denotes the mass dependence.
In the atmospheric field it is common to take the first solution and to omit the last "v" term, considered as obvious.
The mixing ratio unit is usually declined in three possibilities:

ppm	for parts per million (10^{-6})
ppb	for parts per billion (10^{-9})
ppt	for parts per trillion (10^{-12})

molec.cm^{-3}* <-> *ppm(v)

The ozone concentration retrieved by mean of the lidar, and given by (EQ 2.19) p 42, is expressed in terms of *molec.cm*$^{-3}$. To convert this value in a *ppm* one the following calculation has to be made.
From the ideal gas law we have:

$$P[Pa]V[m^3] = \eta[molec]k_B[J.K^{-1}]T[K] \rightarrow C[molec.m^{-3}] = \frac{\eta}{V} = \frac{P}{k_BT} \qquad \text{(EQ 9.22)}$$

We also have:

$$1[ppm] = 10^{-6} \equiv 1\,\mu[molec].[molec]^{-1} \qquad \text{(EQ 9.23)}$$

It then gives, because 1 ppm represents 10^{-6} molecule X for one molecule of air:

$$\begin{aligned} 1[ppm] &= 10^{-6} \times \frac{P}{k_BT}[molec.m^{-3}] \times 10^{-6}\frac{[m^3]}{[cm^3]} \\ &= 10^{-12} \times \frac{P}{k_BT}[molec.cm^{-3}] \end{aligned} \qquad \text{(EQ 9.24)}$$

For example we have at a pressure of 1 atm = 1.01325 10^5 Pa and a temperature of 298 K:
1ppm = 2.463 10^{13} molec.cm^{-3}
This value changes with temperature and pressure and care as to be taken about this.

μg.m^{-3} <-> ppm

For an element X, the mass concentration ρ_X is linked to the molar concentration $\tilde{C}_X$ by:

$$\rho_X\ [g.m^{-3}] = \tilde{C}_X[mol.m^{-3}]M_X[g.mol^{-1}] \qquad \text{(EQ 9.25)}$$

Where M_X represents the molar mass of the constituent X.
The mixing ratio is then given by:

$$\xi_X\ [ppm] = 10^{-6}\frac{\tilde{C}_X[mol.m^{-3}]}{\tilde{C}_{tot}[mol.m^{-3}]} = 10^{-6}\frac{\frac{\rho_X}{M_X}}{\frac{P_{tot}}{RT_{tot}}} = 10^{-6}\frac{RT_{tot}}{M_XP_{tot}}\rho_X[g.m^{-3}] = \frac{RT_{tot}}{M_XP_{tot}}\rho_X[\mu g.m^{-3}] \qquad \text{(EQ 9.26)}$$

and finally:

$$\xi_X\ [ppm] = \frac{R[J.mol^{-1}.K^{-1}]T_{tot}[K]}{M_X[g.mol^{-1}]P_{tot}[Pa]}\rho_X[\mu g.m^{-3}] \qquad \text{(EQ 9.27)}$$

For example we have at a pressure of 1 atm = 1.01325 10^5 Pa and a temperature of 298 K, in case of the ozone molecule (M_{O3}=48 g.mol^{-1}):

$$\xi_X\ [ppm] = 5.094\times10^{-4}\times\rho_X[\mu g.m^{-3}] \qquad \text{(EQ 9.28)}$$

Recommendation

As said before, the mass mixing ratio is generally used to describe the mixing ratios in the solid or liquid phases of particles suspended in the air.
The mass mixing ratio is given by:

$$\xi_{X,mass}\ [ppm] = 10^{-6}\frac{\rho_X[g.m^{-3}]}{\rho_{tot}[g.m^{-3}]} = 10^{-6}\frac{\rho_X}{\frac{M_{tot}P_{tot}}{RT_{tot}}} = \frac{RT_{tot}}{M_{tot}P_{tot}}\rho_X[\mu g.m^{-3}] \qquad \text{(EQ 9.29)}$$

This expression differs from the mixing ratio given in (EQ 9.27) and the mass and volume mixing ratio are linked by:

$$\xi_{X,mass}\ [ppm(m)] = \frac{M_X}{M_{tot}}\times\xi_{X,volume}\ [ppm(v)] \qquad \text{(EQ 9.30)}$$

9.4.3. Conversion of a relative humidity into a water vapor mixing ratio

We will develop calculations that enable the comparison between a measurement giving results in *[g / g_dry air]* (typically given by the lidar) and another one giving results in *[%]* (as given by a humidity sonde, mounted on a balloon).
As we have seen with (EQ 2.20) p 42, the water vapor mixing ratio in *[g H_2O / g_dry air]*, is defined by:

$$\xi_{H_2O} = \left.\frac{\text{Mass of } H_2O}{\text{Mass of dry air}}\right|_{\text{given volume}} = \frac{\rho_{H_2O}}{\rho_{N_2}} \qquad \text{(EQ 9.31)}$$

Where ρ_X *[g.m^{-3}]* denotes the volumic mass of the element X.

ξ_{H_2O} is directly given by the lidar but, often, comparison is made with other types of analyzers (punctual ones or on a sonde balloon for example) giving a relative humidity measurement in %. We then have to calculate the conversion factor to convert g / g_dry air into %, and vice versa.
From the ideal gas law we have:

$$P_{H_2O}\, V_{H_2O} = N_{H_2O} R\,T \xrightarrow{\times M_{H_2O}} M_{H_2O} P_{H_2O} = \underbrace{\frac{N_{H_2O} M_{H_2O}}{V_{H_2O}}}_{\rho_{H_2O}} R\,T \qquad \text{(EQ 9.32)}$$

The water vapor volumic mass ρ_{H_2O} is then given by:

$$\rho_{H_2O} = \frac{M_{H_2O} P_{H_2O}}{R\;T} \qquad \text{(EQ 9.33)}$$

and in a similar way for the one of the dry air:

$$\rho_{\text{dry air}} = \frac{M_{\text{dry air}} P_{\text{dry air}}}{R\;T} = \frac{M_{\text{dry air}} \left(P_{\text{tot}} - P_{H_2O}\right)}{R\;T} \qquad \text{(EQ 9.34)}$$

The water vapor mixing ratio, defined in (EQ 9.31), then gives with(EQ 9.33) and (EQ 9.34):

$$\xi_{H_2O} = \frac{M_{H_2O}\, P_{H_2O}}{M_{\text{dry air}} \left(P_{\text{tot}} - P_{H_2O}\right)} \qquad \text{(EQ 9.35)}$$

The relative humidity RH *[%]* describes the water vapor partial pressure P_{H_2O} in term of the saturation vapor pressure $P^0_{H_2O}$ and is defined as:

$$RH = \frac{P_{H_2O}}{P^0_{H_2O}} \times 100 \qquad \text{(EQ 9.36)}$$

The final equation linking the water vapor mixing ratio and the relative humidity RH is then given by the combination of (EQ 9.36) and (EQ 9.39):

$$\xi_{H_2O} = \frac{M_{H_2O}}{M_{dry\ air}} \frac{RH \cdot P^0_{H_2O}}{100 \cdot \left(P_{tot} - \dfrac{RH \cdot P^0_{H_2O}}{100}\right)} \qquad \text{(EQ 9.37)}$$

With the water vapor mixing ratio ξ_{H_2O} in *[g / g_dry air]* and the relative humidity RH in *[%]*.

The molar mass of dry air is retrieved by taking the values from the Table 1-1, “. International values for dry air”, p 10, and the one of water vapor which is well known. If we also choose to express the result in *[g / kg_dry air]* it gives:

$$\xi_{H_2O} = 6.22 \frac{RH \cdot P^0_{H_2O}}{\left(P_{tot} - \frac{RH \cdot P^0_{H_2O}}{100} \right)} \qquad \text{(EQ 9.38)}$$

The saturation vapor pressure dependence in temperature is retrieved with an "empiric" formula [*Quaglia*, 1999] rather than a classical table listing all the values [*Lide*, 1992-1993]:

$$P^0_{H_2O} = 10^{\left\{ \begin{array}{l} -7.90298 \cdot (Y-1) + 5.02808 \cdot \log_{10}(Y) - 1.3816 \cdot 10^{-7} \cdot \left(10^{11.344 (1 - \frac{1}{Y})} - 1 \right) \\ +8.1328 \cdot 10^{-3} \cdot \left(10^{-3.49149 (Y-1)} - 1 \right) + \log_{10}(1043.246) \end{array} \right\}} \qquad \text{(EQ 9.39)}$$

In a temperature range of -100 °C to +100 °C and with $Y = \frac{373.16}{T_K\,[\mathrm{K}]} = \frac{373.16}{273.15 + T_{\circ C}\,[°\mathrm{C}]}$.
The main advantage, apart its accuracy, is in a possible automatic calculation in Excel files for example.

All those calculations have to be linked with the water vapor mixing ratio given by the lidar way and expressed in (EQ 2.26) p 44 for the ozone corrected case. Two solutions are possible depending on how the unknown constants are retrieved.
First one is given by an external calibration, giving then the value of the calibration constant. With this method there is no need to keep all the different constant terms which can be replaced by an overall constant $K^{N_2}_{cal}$:

$$\xi^{(N_2)}_{H_2O}(R) = \underbrace{K^{N_2}_{cal} \cdot \Psi(R)}_{\text{lidar}} = 6.22 \underbrace{\frac{RH \cdot P^0_{H_2O}}{\left(P_{tot} - \frac{RH \cdot P^0_{H_2O}}{100} \right)}}_{\text{calibration instument (sonde...)}} \qquad \text{(EQ 9.40)}$$

This constant $K^{N_2}_{cal}$ will be determined by an external calibration point.
The second solution supposes that all constant terms in the lidar retrieve are known, in order to calculate the constant $K^{N_2}_{cal}$ given by (EQ 2.27) p 45. This is particularly difficult as this constant term includes all the optic and electronic specifications of the lidar. An approximated calculation can be made but great care has to be taken about the validity of the result.

9.5. Acquisition and data treatment programs

9.5.1. The LabVIEW environment

LabVIEW, which is a National Instrument product, is a graphical programming that combines graphical development with the flexibility of a programming language. It offers an intuitive environment, tightly integrated with measurement hardware, to produce solutions for data acquisition, analysis and representation. All LabVIEW applications execute at compiled speed for optimal performance.

The "LabVIEW choice" is due to the fact that all software developments on the transient recorder control, made by Licel, were made under a LabVIEW configuration. It is nowadays the best, and quite unique, solution in this field of instrument control. Apart the libraries furnished by Licel to drive the transient recorder, specific ones have been made to permit the data acquisition and (pre) treatment.

Here after will be shown and discussed only the two main programs in their last version: the acquisition and the treatment one, this latter being much more elaborated and sophisticated.

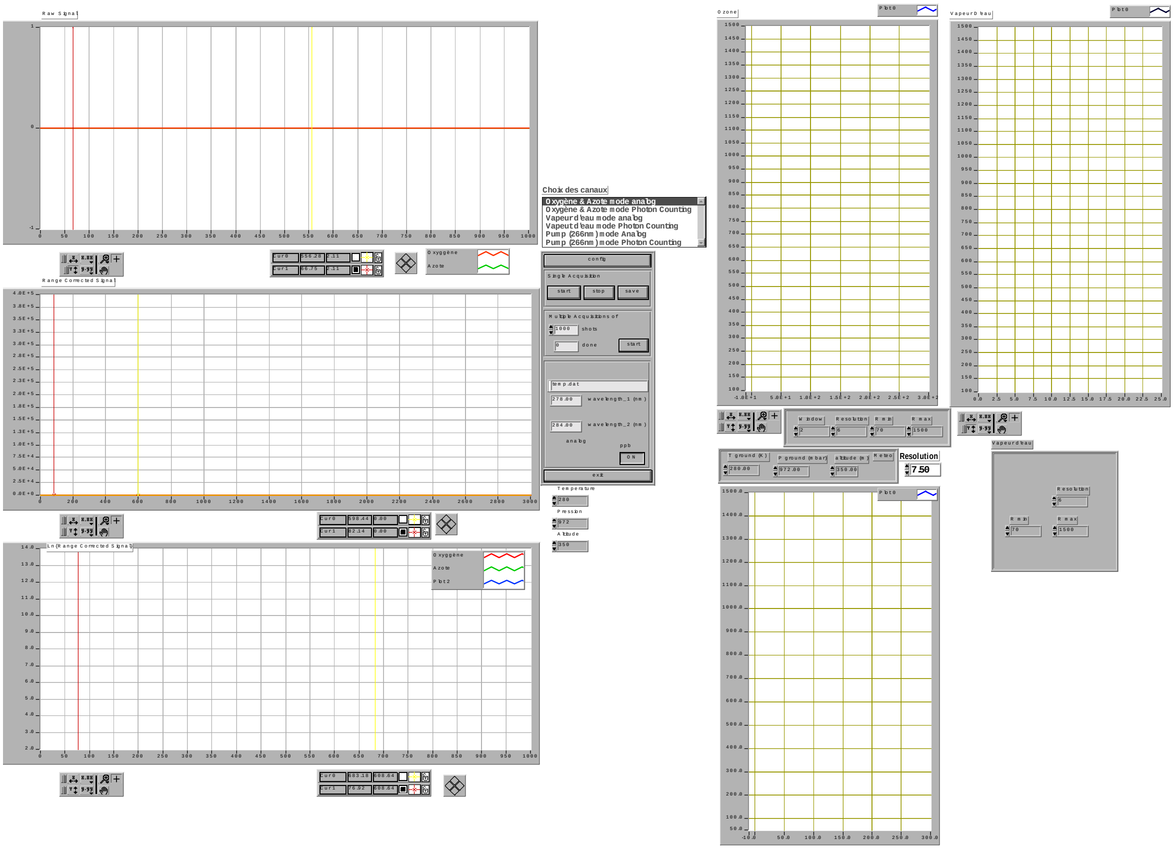

Choix des canaux
- Oxygène & Azote mode analog
- Oxygène & Azote mode Photon Counting
- Vapeur d'eau mode analog
- Vapeut d'eau mode Photon Counting
- Pump (266nm) mode Analog
- Pump (266nm) mode Photon Counting

1000 shots
0 done
temp.dat
278.00 wavelength_1 (nm)
284.00 wavelength_2 (nm)
analog
ppb ON
Temperature 280
Pression 972
Altitude 350
Window 2
Resolution 6
R min 70
R max 1500
T ground (K) 280.00
P ground (mbar) 972.00
altitude (m) 350.00
Resolution 7.50

FIGURE 9-1. Data acquisition front panel

Figure 9-1 shows the data acquisition front panel program used to acquire the lidar signals in case of the Nd:YAG configuration. The main characteristics of the lidar signals can be visualized, such as the raw, the range corrected and the logarithm of range corrected signals. The curve display selection is made with a dialog box. For example, oxygen & nitrogen Raman signals in the analog mode or the water vapor in the photon counting mode can be displayed. A simple version, without corrections, for the ozone concentration and water vapor mixing ratio are also incorporated in order to visualize the on line result.

Concerning the data treatment, the first step is made under LabVIEW. The related front panel and diagram are shown in Figure 9-2 and Figure 9-3.

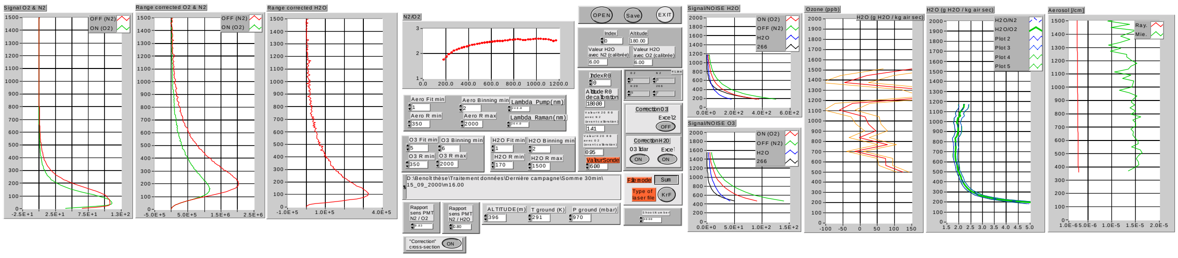

FIGURE 9-2. Data treatment front panel

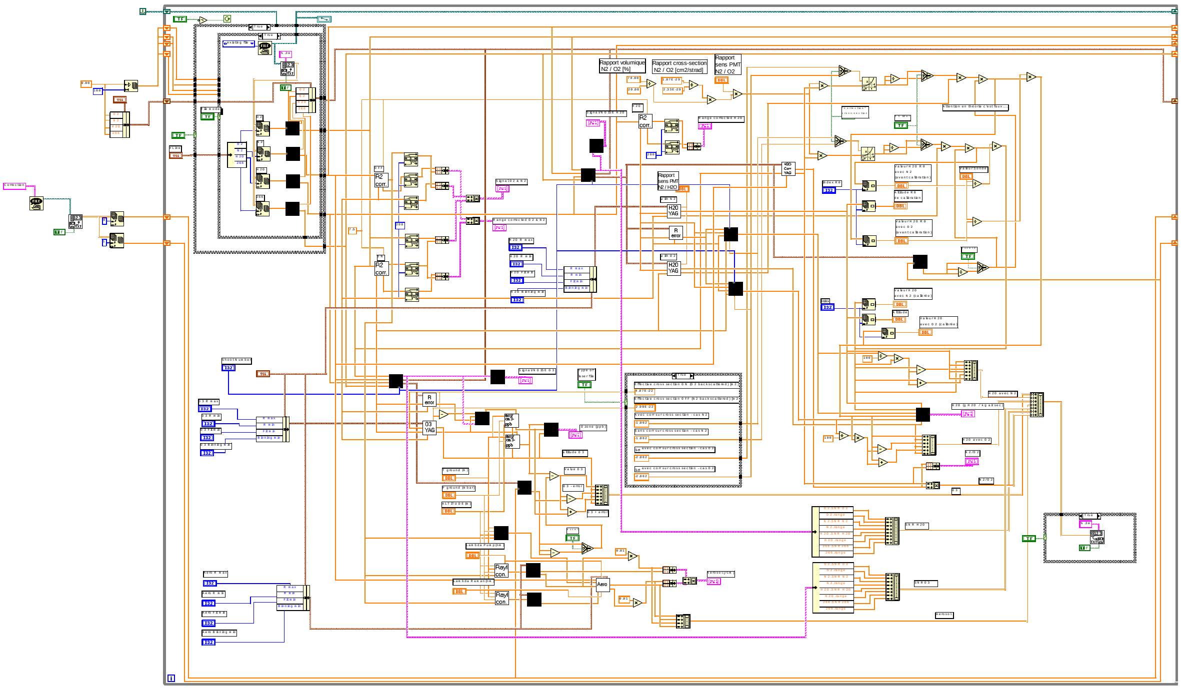

FIGURE 9-3. Data treatment diagram

This program enables to treat a variety of files, like:-a single (4000 shots) file or a 30 minutes summed file, - a file made with the Nd:YAG or KrF configuration. The output gives:

- the ozone concentration
- the water vapor mixing ratio (calibrated with an external point)
- the aerosol extinction coefficient
- the relative errors for the ozone and water vapor cases
- the signal to noise ratio of the different signals.

A correction (absorption, Rayleigh and Mie) of the ozone concentration retrieve can be made,

with an external computed Excel file. For the water vapor mixing ratio retrieve a similar procedure is available and, additionally, it is possible to correct this retrieve with the ozone integrated concentration retrieved by mean of the lidar.
A series of dialog boxes permit to set parameters such as the binning, the minimum and maximum altitudes, the atmospheric conditions, the desired analyzed channels (to see the analog or photon counting part for example)... and more.
Visualizations of the oxygen, nitrogen and water vapor Raman raw and range corrected signals are available. It gives a first look at these signals and permits to see where the total overlap height is, giving then the height region for the first retrieve.

The data treatment procedure is the following.
First step is made with a careful analysis of the 4000 shots single files with the data treatment program in the mode "single file". This enables to detect the bad files and to keep a series of 4 good files for each 30 minutes. The selected files are then compiled in a program (not shown) to make a "30 min. averaged file".
Going back to the data treatment program, the 30 minutes summed files are then treated and saved in the available modes: analog and / or photon counting one. For this treatment, the parameters are set at the beginning and then are not modified. This is valid for the analog and photon counting mode which requires different parameters (for example the beginning altitude "Rmin" which is bigger for the photon counting case). The result is a big matrix that will be treated and plotted under a matlab program.

9.5.2. Matlab programming

Because of the lack of potential for data treatment from the LabVIEW program, a matlab routine was developed to make 2D temporal series. It takes advantage of the powerful possibilities in term of treatment (smoothing for example) and graphic representation.
The program is listed below to show its structure.

```
%Lecture de données
%Juin 2000, GL
clear;
close all

%lecture données
load Final_traitement_campagne_2_bis.txt;
data=Final_traitement_campagne_2_bis;

n=size(data,2)/3;

Range_O3=data(2:end,1);
O3=data(2:end,2:n);
time_O3=data(1,2:n);

Range_H2O=data(2:end,n+1);
H2O=data(2:end,n+2:2*n);
time_H2O=data(1,n+2:2*n);

Range_H2O_corr=data(2:end,2*n+1);
H2O_corr=data(2:end,2*n+2:end);
time_H2O_corr=data(1,2*n+2:end);
```

```
%convolution pour le lissage
b=[1];
%b=[0 0 0 0 ; 0 .2 .1 .1 ; 0 .1 .1 .1; 0 .1 .1 .1];
%b=[0.2 .2 .2 ; .1 .1 .05 ; 0.05 .05 .05];
O3_conv=conv2(O3,b,'same');
H2O_conv=conv2(H2O,b,'same');

[X_O3,Y_O3]=meshgrid(time_O3,Range_O3);
[X_H2O,Y_H2O]=meshgrid(time_H2O,Range_H2O);
[X_H2O_corr,Y_H2O_corr]=meshgrid(time_H2O_corr,Range_H2O_corr);

figure(1);
pcolor(X_O3,Y_O3,O3_conv);
shading interp;
hold off
%contourf(X_O3,Y_O3,O3_conv, [0 10 20 30 40 50 60]);
colormap(jet);
axis([10 14 360 1200]);
caxis([0 100]);
set(colorbar, 'xtick', [0 10 20 30 40 50]);
xlabel('Local time (h)','fontsize',[14])
ylabel('Altitude (m AGL)','fontsize',[14])
title('Raman - EPFL Lidar - 31/03/99-01/04/99 - O3','fontsize',[14])
set(gca,'box','on')

figure(2)
pcolor(X_H2O,Y_H2O,H2O_conv);
shading interp;
hold off
%contourf(X_H2O,Y_H2O,H2O_conv, [0 1 2 3 4 5 6 7 8 9 10]);
colormap(jet);
axis([10 18 360 1200]);
caxis([0 5]);
colorbar;
xlabel('Local time (h)','fontsize',[14])
ylabel('Altitude (m AGL)','fontsize',[14])
title('Raman - EPFL Lidar - 31/03/99-01/04/99 - H2O','fontsize',[14])
set(gca,'box','on')

% fichier de sortie
heure_choisie=16.5;
heure_depart=time_O3(1);
m=((heure_choisie-heure_depart)*2)+1;
if m<=size(time_O3,2)
   length=size(Range_O3,1)+1;
   s=ones(length,4)*NaN;
   s(1,1)=-1;
   s(1,3)=-1;
   s(1,2)=time_O3(m);
   s(1,4)=time_H2O(m);
   s(2:end,1)=Range_O3;
   s(2:end,3)=Range_H2O;
   s(2:end,2)=O3_conv(:,m);
   s(2:end,4)=H2O_conv(:,m);
   figure(3);
   plot(O3_conv(:,m),Range_O3);
   axis([0 80 0 1400]);
   xlabel('O3','fontsize',[14]);
```

```
   ylabel('Altitude (m AGL)','fontsize',[14]);
   title(['Raman - EPFL Lidar ',num2str(time_O3(m))],'fontsize',[14]);
   set(gca,'box','on');
   figure(4);
   plot(H2O_conv(:,m),Range_H2O);
   axis([0 5 200 1600]);
   xlabel('H2O','fontsize',[14]);
   ylabel('Altitude (m AGL)','fontsize',[14]);
   title(['Raman - EPFL Lidar ',num2str(time_H2O(m))],'fontsize',[14]);
   set(gca,'box','on');
   save sortie s -ascii -tabs;
else
   disp('out of range');
end
```

Bibliography

Résumé / Summary

Bösenberg, J., EUROTRAC / TESLAS (Tropospheric Environmental Studies by Laser Soundings), Max Planck Institute for Meteorology, Hamburg / Germany, 1996.

Measures, R.M., *Laser Remote Sensing. Fundamentals and Applications*, 510 pp., Krieger, New-York, 1992.

Schoulepnikoff, L., H. Van den Bergh, B. Calpini, and V.M. Mitev, Tropospheric air pollution monitoring, lidar, in *Encyclopedia of environmental analysis and remediation*, John Wiley & Sons, 1998.

Chapter 1. Introduction

Ancellet, G., and J. Bösenberg, Methodology, in *Instrument development for atmospheric research and monitoring*, Springer-Verlag, Berlin, Germany, 1996.

Arshinov, Y.F., S.M. Bobrovnikov, V.E. Zuev, and V.M. Mitev, Atmospheric-Temperature Measurements Using a Pure Rotational Raman Lidar, *Applied Optics*, *22* (19), 2984-2990, 1983.

Browell, E., S. Ismail, and S.T. Shipley, Ultraviolet DIAL measurements of O_3 profiles in regions of spatially inhomogeneous aerosols, *Applied Optics*, *24*, 2827-2836, 1985.

Browell, E., T.D. Wilkerson, and T.J. McIlrath, Water vapor differential absorption lidar development and evaluation, *Applied Optics*, 1979.

Calpini, B., V. Simeonov, F. Jeanneret, J. Kuebler, V. Sathya, and H. Van den Bergh, Ozone lidar as an analytical tool in air pollution management: the Geneva 1996 campaign, *Chimia*, *51*, 700-704, 1997.

Cooney, J., Measurements of the Raman component of Laser Atmospheric backscatter, *Applied Physics Letters*, *12* (2), 40-42, 1968.

Crutzen, P.J., A discussion of the photochemistry of some minor constituents in the stratosphere and troposphere, *Pure App. Geophys.*, *106-108*, 1385-1399, 1973.

Crutzen, P.J., Photochimical reactions initiated by and infuencing ozone in unpolluted tropospheric air, *Tellus*, *26*, 47-57, 1974.

Daumont, D., J. Brion, J. Charbonnier, and J. Malicet, Ozone UV Spectroscopy I: Absorption Cross-Section at Room Temperature, *Journal of Atmospheric Chemistry, 15*, 145-155, 1992.

Dockery, D.W., C.A. Pope, and X. Xu, An association between air pollution and mortality in six US cities, *N. Engl. J. Med., 329*, 1753-1759, 1993.

Elterman, L., Seasonal trends of temperature, density and pressure to 67,6 km, obtained with the searchlight probing technique, *Journal of Geophysical Research-Atmospheres, 59* (3), 351-358, 1954.

Fiocco, G., and L.D. Smullin, Detection of Scattering Layers in the Upper Atmosphere (60-140 km) by Optical Radar, *Nature, 199*, 1275-1276, 1963.

Fiorani, L., B. Calpini, L. Jaquet, and H. Van den Bergh, A combined determination of wind velocities and ozone concentrations for a first measurement of ozone fluxes with a DIAL instrument during the Medcaphot Trace campaign, *Atmospheric Environment, 32*, 2151-2159, 1998.

Hauchecorne, A., M.L. Chanin, and P. Keckhut, Climatology and trends of the middle atmospheric temperature (33-87 km) as seen by Rayleigh lidar over the south of France, *Journal of Geophysical Research-Atmospheres*, 1991.

Hochenbleicher, J.G., W. Kiefer, and J. Brandmüller, A laboratory for a resonance Raman lidar system, *Applied Spectroscopy, 30* (5), 528-531, 1976.

Inaba, H., and T. Kobayashi, Laser-Raman Radar for Chemical Analysis of Polluted Air, *Nature, 224*, 170-172, 1969.

Jeanneret, F., F. Kirchner, A. Clappier, H. Van den Bergh, and B. Calpini, Total VOC reactivity in the Planetary Boundary Layer, *Journal of Geophysical Research-Atmospheres, In Press*, 2000.

Junge, C.E., Global ozone budget and exhange between stratosphere and troposphere, *Tellus, 14*, 363-377, 1962.

Junge, C.E., *Air Chemistry and Radioactivity*, Academic Press, New York, 1963.

Köhler, H., The nucleus in and the growth of hygroscopic droplets, *Trans. Faraday. Soc., 33*, 1152-1162, 1936.

Leonard, D.A., Observation of Raman Scattering from the Atmosphere using a Pulsed Nitrogen Ultraviolet Laser, *Nature, 216*, 142-143, 1967.

Ligda, M.G.H., Conf. Laser Technol. , 1st, San Diego Californie, 1963.

Maiman, T.H., Stimulated Optical Radiation in Ruby, *Nature, 187*, 493-494, 1960.

Mc Clung, F.J., and R.W. Hellworth, Giant Optical Pulsations from Ruby, *Journal of Applied Physics, 33*, 828-829, 1962.

Measures, R.M., *Laser Remote Sensing. Fundamentals and Applications*, 510 pp., Krieger, New-York, 1992.

Melfi, S.H., J.D. Lawrence, and M.P. McCormick, Observation of Raman Scattering by Water Vapor in the Atmosphere, *Applied Physics Letters, 15* (9), 295-297, 1969.

Pruppacher, H.R., and J.D. Klett, *Microphysics of clouds and precipitation,* Reidel, Dordrecht. The Netherlands, 1980.

Rabinowitz, J., P. Miller, and H. Greppin, Les oxydants photochimiques, *Médecine et Hygiène, 43,* 3466-3478, 1985.

Renaut, D., and R. Capitini, Boundary-Layer Water Vapor Probing with a Solar-Blind Raman Lidar: Validations, Meteorological Observations and Prospects, *Journal of Atmospheric and Oceanic Technology, 5* (5), 585-601, 1988.

Rosen, H., P. Robrish, and O. Chamberlain, Remote detection of pollutants using resonance Raman scattering, *Applied Optics*, *14* (11), 2703-2706, 1975.

Schawlow, A.L., and C.H. Townes, Infrared Optical Masers, *Physical Review, 112*, 1940-1949, 1958.

Schwartz, J., Air pollution and daily mortality, *Environmental Research, 64*, 36-52, 1994.

She, C.Y., J.R. Yu, H. Latifi, and R.E. Bills, Observed thermal structure of a midlatitude mesopause, *Applied Optics,* 1992.

Skarby, L., and G. Sellden, The effects of ozone on crops and forests, *Ambio*, *13,* 68-72, 1984.

Uchiumi, M., O. Choo Chee, K. Muraoka, M. Maeda, and O. Uchino, DIAL measurement of CH_4, CO_2, CO and NO_2 using a tunable IR source based on the Ti:Sapphire laser, in *17th ILRC*, Sendai, Japan, 1994.

W.M.O., Scientific assesment of ozone depletion:1994, in *WMO global ozone research and monitoring project,* Geneva, 1995.

Chapter 2. Theory

Bischel, W.K., and G. Black, Wavelength dependence of Raman scattering cross sections from 200-600nm, in *AIP conference proccedings n°100 : eximer lasers*, edited by A.I.O. Physics, 1983.

Bribes, J.L., R. Gaufres, M. Monan, M. Lapp, and C. Penney, Raman band contours for water vapor as a function of temperature, *Applied Physics Letters*, *28*, 336-337, 1976.

Brodersen, S., High-resolution rotation-vibrational Raman spectroscopy, in *Topics in current physics n°11,* edited by A. Weber, pp. 7-69, Springer-Verlag, 1979.

Burris, J., T. McGee, and W. Heaps, UV Raman cross sections in Nitrogen, *Applied Spectroscopy*, *46* (6), 1076, 1992.

Chevallier, P., *Interaction du Rayonnement avec la Matière*, Techniques de l'Ingénieur, A 214, 1986.

Faris, G.W., and R.A. Copeland, Ratio of oxygen and nitrogen Raman cross sections in the ultraviolet, *Applied Optics / technical note, 36* (12), 2684-2685, 1997.

Gouesbet, G., and G. Grehant, *Diffusion des faisceaux laser par des particules*, Techniques de l'Ingénieur, AF 3460, 1998.

Herzberg, G., *Molecular Spectra and Molecular Structure, vol. 2 : Infared and Raman Spectra of Polyatomic Molecules*, 632 pp., Van Nostrand Company, New-York, 1946.

Herzberg, G., *Molecular Spectra and Molecular Structure, vol. 1 Spectra of Diatomic Molecules*, 658 pp., Van Nostrand Reinhold Company, New-York, 1950.

Herzberg, G., *Molecular Spectra and Molecular, vol.3 : Electronic Spectra and Electronic Structure of Polyatomic Molecules,* 745 pp., Van Nostrand Reinhold Company, New-York, 1966.

Hinkley, E.D., *Laser Monitoring of the Atmosphere*, Springer-Verlag, 1976.

Horvath, H., *Atmospheric Environment*, *5*, 171, 1971.

Inaba, H., and T. Kobayashi, Laser-Raman Radar for Chemical Analysis of Polluted Air, *Nature*, *224*, 170-172, 1969.

Inaba, H., and T. Kobayashi, Laser-Raman Radar -Laser-Raman scattering methods for remote detection and analysis of atmospheric pollution-, *Opto-Electronics*, *4*, 101-123, 1972.

Measures, R.M., *Laser Remote Sensing. Fundamentals and Applications,* 510 pp., Krieger, New-York, 1992.

Middleton, W.E.K., *Vision through the atmosphere*, University of Toronto Press, 1952.

Placzek, G., Rayleigh -streuung und Raman-effekt, in *Handbuch der radiologie,* edited by G. Marx, pp. 205, 1934.

Placzek, G., and E. Teller, *Z. Physik*, *81*, 209, 1933.

Renaut, D., J.C. Pourny, and R. Capitini, Daytime Raman-lidar measurements of water vapor, *Optics Letters*, *5* (6), 233-235, 1980.

Schrötter, H.W., and H.W. Klöckner, Raman spectroscopy of gases and liquids, in *Topics in current physics n°11,* edited by A. Weber, Springer-Verlag, 1979.

Teller, E., and D. Jahrb, *Chemical Physics, 9* (2), 43, 1934.

Whiteman, D., S.H. Melfi, R. Ferrare, and K. Evans, Daytime Measurements of Water Vapor Mixing Ratio using Raman Scattering- Techniques and Assessment, in *17th ILRC,* pp. 137-140, Sendaï / Japan, 1994.

Chapter 3. Experimental part

dos Santos, J.M.F., J.F.C.A. Veloso, J.A.M. Lopes, and R.E. Morgado, A simple method to improve the spatial uniformity of venitian-blind photomultiplier tubes, *Ieee Transactions of Nuclear Science, 43* (3), 1335-1340, 1996.

Lazzarotto, B., M. Frioud, G. Larchevêque, V.M. Mitev, P. Quaglia, V. Simeonov, A. Thompson, H. Van den Bergh, and B. Calpini, Ozone and Water Vapor Measurements by

Raman Lidar in the Boudary Layer : Error Sources and Field Measurements, *accepted in Applied Optics*, 2000.

Lide, D.R., *Handbook of Chemistry and Physics, 73 rd edition*, 1992-1993.

Measures, R.M., *Laser Remote Sensing. Fundamentals and Applications*, 510 pp., Krieger, New-York, 1992.

Simeonov, V., G. Larchevêque, P. Quaglia, H. Van den Bergh, and B. Calpini, The influence of the photomultiplier spatial uniformity on lidar signals, *Applied Optics*, *38*, 5186-5190, 1999.

Spectrogon_manual, Optical Interference Filters, 16th edition.

Chapter 4. Corrections and errors analysis

Angström, A., On the atmospheric transmission of sun radiation and on dust in the atmosphere, *Geogr. Ann.*, *11*, 156-166, 1929.

Ansmann, A., M. Riebesell, and C. Weitkamp, Measurement of Atmospheric Aerosol Extinction Profiles with a Raman Lidar, *Optics Letters*, *15* (13), 746-748, 1990.

Ansmann, A., U. Wandinger, M. Riebesell, C. Weitkamp, and W. Michaelis, Independent Measurement of Extinction and Backscatter Profiles in Cirrus Clouds by Using a Combined Raman Elastic-Backscatter Lidar, *Applied Optics*, *31* (33), 7113-7131, 1992.

Barrell, H., and J.E. Sears, The refraction and Dispersion of Air for the Visible Spectrum, *Phil. Trans. Roy. Soc. London*, *A238*, 1-64, 1939.

Bates, D.R., Rayleigh scattering by air, *Planetary Space Science*, *32*, 785-790, 1984.

Bernath, P., M. Carleer, S. Fally, A. Jenouvrier, A.C. Vandaele, C. Hermans, M.F. Mérienne, and R. Colin, The Wulf band of Oxygen, *Chemical Physics letters*, *297*, 293-299, 1998.

Bodhaine, B.A., On Rayleigh Optical Depth Calculations, *American Meteorological Society*, *16*, 1854-1861, 1999.

Bösenberg, J., B. D., and P.C. Simon, Part 1: tropospheric environmental studies by laser sounding, in *Instrument development for atmospheric research and monitoring*, Springer Verlag, 1997.

Bucholtz, A., Rayleigh-scattering calculations for the terrestrial atmosphere, *Applied Optics*, *34*, 2765-2773, 1995.

Burkholder, J.B., R.K. Talukdar, A.R. Ravishankara, and S. Solomon, Temperature dependence of the HNO_3 uv absorption cross sections, *Geophysical Research Letters*, *98*, 22937-22948, 1993.

Cox, R.A., and R.G. Derwent, The ultraviolet absorption spectrum of gaseous nitrous acid, *Journal of Photochemistry*, *6*, 23-24, 1976.

Daumont, D., J. Brion, J. Charbonnier, and J. Malicet, Ozone UV Spectroscopy I: Absorption Cross-Section at Room Temperature, *Journal of Atmospheric Chemistry, 15*, 145-155, 1992.

Edlén, B., The Dispersion of Standard Air, *Journal of the Optical Society of America, 43*, 339-344, 1953.

Edlén, B., The Refractive Index of Air, *Metrologia, 2* (2), 71-80, 1966.

Elterman, L., *UV, visible, and IR attenuation for altitudes to 50 km,* Air Force Cambridge Research Laboratories, 1968.

Ferrare, R.A., S.H. Melfi, D.N. Whiteman, K.D. Evans, and R. Leifer, Raman lidar measurements of aerosol extinction and backscattering - 1. Methods and comparisons, *Journal of Geophysical Research-Atmospheres, 103* (D16), 19663-19672, 1998.

Finlayson-Pitts, B.J., and J.N.J. Pitts, *Atmospheric Chemistry : Fundamentals and Experimental Techniques,* 1098 pp., Wiley Interscience, 1986.

Fiorani, L., Une première mesure lidar combinée d'ozone et de vent, à partir d'une instrumentation et d'une méthodologie coup par coup, Lidar development thesis, EPFL, Lausanne, 1996.

Gathen, P., Aerosol extinction and backscatter profiles by means of a multiwavelength Raman lidar: a new method without a priori assumptions, *Applied Optics, 34* (3), 463-466, 1995.

Karmazin, S.E., V.M. Klimkin, S.F. Luk'ynenko, M.M. Makogon, I.N. Potaokin, I.S. Tyryshkin, V.N. Fedorishchev, and A.L. Tsvetkov, A new absorption band of water vapor H_2O : a fresh exctinction channel radiation in the near-ultraviolet, in *15th ILRC,* Tomsk, Russia, 1990.

Klimkin, V.M., and V.N. Fedorishchev, A new atmospheric absorption band in the ultraviolet, *Atmospheric Optics, 2,* 174-175, 1989.

Kuebler, J., Personnal communication on typical vertical distributions in remote and urban swiss places, 2000.

Mc Cartney, E.J., *Optics of the Atmosphere,* 408 pp., Wiley, 1976.

Measures, R.M., *Laser Remote Sensing. Fundamentals and Applications,* 510 pp., Krieger, New-York, 1992.

Meller, R., Private communication, *MPI Mainz / Germany,* 1992.

Mérienne, M.F., A. Jenouvrier, B. Coquart, M. Carleer, S. Fally, R. Colin, A.C. Vandaele, and C. Hermans, Fourier Transform Spectroscopy of the O_2 Herzberg Bands. (II. Band Oscillator Strengths and Transition Moments), *Journal of Molecular Spectroscopy, 202,* 171-193, 2000.

Nicolet, M., and W. Peetermans, The Production of Nitric Oxide in the Stratosphere by Oxidation of Nitrous Oxide, *Ann. Geophys., 28*, 751-762, 1972.

NOAA, NASA, and USAF, U.S. standard atmosphere (76), U.S. government Printing Office, Washington / USA, 1976.

Owens, J.C., Optical Refractive Index of Air : Dependence on Pressure, Temperature and Composition, *Applied Optics*, *6* (1), 51-59, 1967.

Peck, E.R., and K. Reeder, Dispersion of Air, *Journal of the Optical Society of America*, *62*, 958-962, 1972.

Penndorf, R., Tables of the refractive index for standard air and the Rayleigh scattering coefficient for the spectral region between 0.2 and 20.0 µm and their application to atmospheric optics, *Journal of the Optical Society of America*, *47*, 176-182, 1957.

Renaut, D., and R. Capitini, Boundary-Layer Water Vapor Probing with a Solar-Blind Raman Lidar: Validations, Meteorological Observations and Prospects, *Journal of Atmospheric and Oceanic Technology*, *5* (5), 585-601, 1988.

Schneider, W., G.K. Moortgat, G.S. Tyndall, and J.P. Burrows, Private communication, *MPI Mainz / Germany*, 1986.

Seinfeld, J.H., and S.N. Pandis, *Atmospheric Chemistry and Physics*, 1326 pp., Wiley Interscience, 1998.

Shemansky, D.E., CO_2 Extinction Coefficients 1700-3000 A, *J. Chem. Phys.*, *56*, 1582-1587, 1972.

Trost, B., Benzene, Toluene absorption spectra, edited by I.f. Umweltphysik, Heidelberg, 1994.

Valero, F.P.J., and P. Pilewski, Latitudinal survey of spectral optical depths of the Pinatubo aerosol cloud-derived particle sizes, columnar mass loadings and effects on planetary albedo, *Geophysical Research Letters*, *19*, 163-166, 1992.

van de Hulst, H.C., Light scattering by small particles, pp. 414-439, Dover, New York, 1981.

Vandaele, A.C., P.C. Simon, J.M. Guilmot, M. Carleer, and R. Colin, SO_2 absorption cross section measurement in the UV using a Fourier transform sectometer, *Journal of Geophysical Research-Atmospheres*, *99* (12), 25599-25605, 1994.

Warneck, P., *Chemistry of the Natural Atmosphere*, Academic Press, 1988.

Young, A.T., Revised depolaritation corrections for atmospheric exctinction, *Applied Optics*, *10*, 3427-3428, 1980.

Young, A.T., On the Rayleigh-scattering optical depth of the atmosphere, *Journal of Applied Meteorology*, *20*, 328-330, 1981.

Yung, Y.L., and W.B. DeMore, *Photochemistry of Planetary Atmospheres*, Oxford University Press, 1999.

Chapter 8. Conclusion

Gathen, P., Aerosol extinction and backscatter profiles by means of a multiwavelength Raman lidar: a new method without a priori assumptions, *Applied Optics*, *34* (3), 463-466, 1995.

Godin, S., Etude expérimentale par télédétection laser et modélisation de la distribution verticale d'ozone dans la haute stratosphère, Lidar development thesis, Université Paris 6, 1987.

Moosmüller, H., and T.D. Wilkerson, Combined Raman-elastic backscatter lidar method for the measurement of backscatter ratios, *Applied Optics, 36* (21), 5144-5147, 1997.

Whiteman, D.N., Application of statistical methods to the determination of slope in lidar data, *Applied Optics, 38* (15), 3360-3369, 1999.

Chapter 9. Annex

Ansmann, A., U. Wandinger, M. Riebesell, C. Weitkamp, and W. Michaelis, Independent Measurement of Extinction and Backscatter Profiles in Cirrus Clouds by Using a Combined Raman Elastic-Backscatter Lidar, *Applied Optics, 31* (33), 7113-7131, 1992.

Bischel, W.K., and G. Black, Wavelength dependence of Raman scattering cross sections from 200-600nm, in *AIP conference proccedings n°100 : eximer lasers,* edited by A.I.O. Physics, 1983.

Browell, E., S. Ismail, and S.T. Shipley, Ultraviolet DIAL measurements of O_3 profiles in regions of spatially inhomogeneous aerosols, *Applied Optics*, *24*, 2827-2836, 1985.

Cohen, E.R., and B.N. Taylor, The fundamental physical constants, *Physics today*, BG9-BG16, 1995.

Daumont, D., J. Brion, J. Charbonnier, and J. Malicet, Ozone UV Spectroscopy I: Absorption Cross-Section at Room Temperature, *Journal of Atmospheric Chemistry, 15*, 145-155, 1992.

Ernst, R., *Dictionnaire français / anglais (& anglais / français) des techniques industrielles*, Editions de l'usine nouvelle, 1982.

Fernald, F.G., Analysis of atmospheric lidar observations: some comments, *Applied Optics, 23*, 652-653, 1984.

Herzberg, G., *Molecular Spectra and Molecular Structure, vol. 2 : Infared and Raman Spectra of Polyatomic Molecules*, 632 pp., Van Nostrand Company, New-York, 1946.

Inaba, H., and T. Kobayashi, Laser-Raman Radar -Laser-Raman scattering methods for remote detection and analysis of atmospheric pollution-, *Opto-Electronics, 4,* 101-123, 1972.

Klett, J.D., Stable analytical inversion solution for processing lidar returns, *Applied Optics, 20*, 211-220, 1981.

Lide, D.R., *Handbook of Chemistry and Physics, 73 rd edition*, 1992-1993.

Matthieu, J.P., A. Kastler, and P. Fleury, *Dictionnaire de Physique*, Masson & Eyrolles ed, 1985.

Measures, R.M., *Laser Remote Sensing. Fundamentals and Applications*, 510 pp., Krieger, New-York, 1992.

NOAA, NASA, and USAF, U.S. standard atmosphere (76), U.S. government Printing Office, Washington / USA, 1976.

Quaglia, P., Personal communication on the saturation vapor pressure formula, 1999.

Schrötter, H.W., and H.W. Klöckner, Raman spectroscopy of gases and liquids, in *Topics in current physics n°11*, edited by A. Weber, Springer-Verlag, 1979.

Seinfeld, J.H., and S.N. Pandis, *Atmospheric Chemistry and Physics*, 1326 pp., Wiley Interscience, 1998.

Swiss_Metrology_Office, *Les unités de mesure légales en Suisse*, 30 pp., Office fédéral de Métrologie, 1993.

Curriculum Vitae

LAZZAROTTO Benoît
Chemin des berges, 6
1022. CHAVANNES-PRES-RENENS
SUISSE / SWITZERLAND

530, avenue de la creusaz
74500. NEUVECELLE
FRANCE

May 1st, 1969.
Swiss **and** French citizenships.
Married, one daughter born 10th of January 2000.

(March 2001)

PhD thesis EPFL
Engineer in Physics EPFL

CURSUS

2001-1996:	Ph.D. thesis work, atmospheric remote sensing by laser. Institute of environmental engineering, Air pollution laboratory, Swiss Federal Institute of Technology (EPFL, Switzerland). Thesis title: Ozone and water vapor measurement by Raman lidar in the planetary boundary layer and free troposphere.
1996-1995:	**Military**, french army. « 27th battalion of alpine chasseurs » (Annecy, France).
1995-1990:	**Graduate in Physics**. EPFL.
1990-1987:	**Preparatory classes to engineer schools**. Berthollet school (Annecy, France).

DIPLOMAS

March 2001:	**PhD thesis EPFL**. Environmental science and technology. LPAS / DGR.
March 1995:	**Engineer in Physics EPFL**.
Oct. 1992:	**Federal scientific maturity** (swiss), obtained in parallel of the EPFL studies.
July 1987:	**Leaving-certificate in science** (Thonon, France).

PROFESSIONAL AND EXTERNAL EXPERIENCES

2000-1996: **Participation in international field campaigns.** Kolimbary / Crete: *Saharan dust transport* (may 1999), Seregno / Italy: *Air pollution episode over densely urbanized area* (may-june 1998), Obwald / Switzerland: *Ozone smog in the alpine region* (june 1997), Sodankylä / Finland: *Polar stratospheric clouds studies* (4 times during the 1999–1996 period). **Practical work** to 3rd year students (2000-1998). EPFL, lidar group.

1993-1992: **Adaptation of a Czech software** for educational purposes. Prof. C. Gruber, DP-EPFL.

1993-1988: Music and audio material **selling agent**. Techtra Co(Evian-France).

1993-1990: **Active member** of the EPFL student association (AGEPOLY). **Co-founder** of the EPFL CD-thèque (1993-1992). **Founder, president and accountant** of a new association (1992-1991). **Staff member** of the European “nautical” meeting (1991-1990).

LANGUAGES

French: Mother language.
English: Read, written, spoken.
German: Good notions.

INFORMATIC KNOWLEDGE

Languages: Pascal and Turbo-Pascal, Fortran, Basic.
Softwares: Labview, Matlab, Word, Excel, Power point …..
Machines: PC, Macintosh.

LEISURE TIME

Sports: High mountaineering ascents, climbing (rock & ice), jogging, ski, windsurfing.
Others: Music, reading.

Personal publications

Publications

Jimenez, R., C. Dubois, F. Jeanneret, G. Larchevêque, B. Lazzarotto, V. Simeonov, and B. Calpini, Assessment of Air Quality in the Canton of Obwald. Field Measurement Campaign 1997, preliminary experimental report, Lausanne, 1997.

Matthey, R., V.M. Mitev, B. Lazzarotto, B. Calpini, M. Morandi, F. Castagnoli, P. Agostini, A. Antonelli, B. Stein, and C. Wedekind, Depolarisation Backscatter Lidar for Stratospheric Studies, *SPIE Europto series "Lidar Atmospheric Monitoring", 3104* (2-11), 1997.

Kivi, R., E. Kyrö, L. Rontu, C. Wedekind, B. Stein, H. Wille, A. Dörnbrack, V.M. Mitev, R. Matthey, J.M. Rosen, V. Rizi, B. Lazzarotto, B. Calpini, L. Stefanutti, and M. Del Guasta, Polar Stratospheric Cloud Measurements by Lidar and Balloon Borne Sondes at Sodankylä in 1996/1997, *Annales Geophysicae*, *suppl.III to vol. 16,* 929-, 1998.

Kivi, R., E. Kyrö, C. Wedekind, L. Rontu, A. Dörnbrack, B. Stein, H. Wille, V.M. Mitev, R. Matthey, J.M. Rosen, N.T. Kjome, V. Rizi, G. Redaelli, B. Lazzarotto, B. Calpini, M. Del Guasta, M. Morandi, L. Stefanutti, P. Agostini, A. Antonelli, M. Rummukainen, T. Turunen, and J. Karhu, SAONAS Activities at Sodankylä in Winter 1996/1997, in *4th European Workshop on Polar Stratospheric Ozone, Air Pollution Research Report 66,* pp. 135-138, 1998.

Calpini, B., A. Clappier, R. Jimenez, G. Larchevêque, B. Lazzarotto, A. Martilli, F. Pasi, P. Quaglia, V. Simeonov, and H. Van den Bergh, Photo-Oxydant Formation in the Milan Metropolitan Area, in *Eurotrac Symposium 98*, pp. 875-880, 1999.

Lazzarotto, B., V. Simeonov, P. Quaglia, G. Larchevêque, H. Van den Bergh, and B. Calpini, Retrieval of Ozone and Water Vapor in the Lower Troposphere by Raman DIAL., in *Extended Abstract of the 19th ILRC*, 1998.Lazzarotto, B., G. Larchevêque, P. Quaglia, V. Simeonov, H. Van den Bergh, and B. Calpini, Raman DIAL Measurement of Ozone and Water Vapor in the Lower Troposphere, *SPIE Europto series "Environmental Sensing and Applications", 3821,* 54-61, 1999.

Lazzarotto, B., V. Simeonov, P. Quaglia, G. Larchevêque, H. Van den Bergh, and B. Calpini, A Raman Differential Absorption Lidar for Ozone and Water Vapor Measurement in the Lower Troposphere, *International Journal of Environmental Analytical Chemistry, 74*, 255-261, 1999.

Simeonov, V., B. Lazzarotto, G. Larchevêque, P. Quaglia, and B. Calpini, UV Ozone DIAL based on a Raman Cell Filled with Two Raman Actives Gases, *SPIE Europto series "Environmental Sensing and Applications", 3821*, 54-61, 1999.

Couach, O., J. Balin, R. Jimenez, P. Quaglia, V. Simeonov, G. Larchevêque, B. Lazzarotto, J. Kuebler, V. Sathya, A. Martilli, M. Junier, Y.-A. Roulet, F. Kirchner, A. Clappier, B. Calpini, and H. Van den Bergh, Campagne de mesure intensives 1999 sur la région grenobloise. Eensemble des résultats et Analyse des Périodes d'Observations Intensives (POI), EPFL-ASCOPARG, 2000.

Lazzarotto, B., M. Frioud, G. Larchevêque, V.M. Mitev, P. Quaglia, V. Simeonov, A. Thompson, H. Van den Bergh, and B. Calpini, Ozone and Water Vapor Measurements by Raman Lidar in the Boudary Layer : Error Sources and Field Measurements, *accepted in Applied Optics*, 2000.

Lazzarotto, B., V. Simeonov, P. Quaglia, G. Larchevêque, H. Van den Bergh, and B. Calpini, Ozone and Water Vapor by Raman Lidar in the PBL, in *Extended Abstract of the 20th ILRC*, 2000.

Quaglia, P., O. Couach, J. Balin, V. Simeonov, B. Lazzarotto, H. Van den Bergh, and B. Calpini, Air Pollution Measurements During the Grenoble 1999 Campaign, in *Extended Abstract of the 20th ILRC*, 2000.

Quaglia, P., G. Larchevêque, R. Jimenez, B. Lazzarotto, V. Simeonov, G. Ancellet, H. Van den Bergh, and B. Calpini, Planetary Boundery Layer Ozone Fluxes from Combined Airborne, Ground Based Lidars and Wind Profilers Measurements, *Analusis*, *27* (4), 304-310, 1999.

Simeonov, V., B. Lazzarotto, P. Quaglia, H. Van den Bergh, and B. Calpini, Three Wavelength UV Ozone DIAL based on a Raman Cell Filled with Two Raman Active Gases, in *Extended Abstract of the 20th ILRC*, 2000.

Lazzarotto, B., S. Brönnimann, R. Cattin, O. Couach, W. Eugster, N. Hasler, G. Larchevêque, G. E. Liston, V. Simeonov, H. Van den Bergh, and B. Calpini, Vertical profiles of O_3 and H_2O by Raman lidar, compared with tethered balloon and numerical simulation, *To be submitted*, 2001.

Participation

Schoulepnikoff, L., H. Van den Bergh, B. Calpini, and V. Mitev, Tropospheric Air Pollution Monitoring Lidar, in *Encyclopedia of Environmental Analysis and Remediation*, edited by R.A. Meyers / Wiley, pp. 4873-4909, 1998.

Index